

**Development & use of site-directed
labeling methods to study the structure,
dynamics, and interactions of GPCRs
with their affiliate proteins arrestin and
rhodopsin kinase.**

A DISSERTATION

Presented to The department of Biochemistry and Molecular Biology

Oregon Health & Science University

In Partial Fulfillment of the Requirements for the Degree

Doctor of Philosophy

Amber M Jones Brunette

May 2016

School of Medicine
Oregon Health and Science University

CERTIFICATE OF APPROVAL

This is to certify that the PhD dissertation of

Amber M Jones Brunette

has been approved



Dr. David L Farrens, PhD, Thesis Advisor



Dr. Michael Chapman, PhD, Committee Chair



Dr. Ujwal Shinde, PhD, Committee Member



Dr. Francis Valiyaveetil, PhD, Committee Member



Dr. Matt Whorton, PhD, Committee Member

Acknowledgments

First, I would like to thank my mentor, Dr. Dave Farrens, for giving me valuable lessons in how science is done, both at the bench and in the lecture hall. Dr. Farrens has led me to be a better biochemist and critical thinker, as well as helping me form questions and develop innovative ways to answer them. Thank you, Dave, for your leadership, encouragement, and mentorship. I would also like to thank the members of my dissertation committee, Dr. Michael Chapman, Dr. Ujwal Shinde, Dr. Francis Valiyaveetil, Dr. Matt Whorton, and Dr. Bill Skach (former).

Graduate school would have been an altogether different experience if not for the support of my hubby, Clark—my darling, thank you for your encouragement and unbelievable support. My life truly would not be the same without you. I also want to thank my parents, Margot and Ree for their love, encouragement, and for forgiving me my absence over the last 6 years.

I am thankful for the collaboration and friendship of my fellow Farrens lab members (past and present), Dr. Jon Fay, Dr. Abhinav Sinha, Dr. Steve Mansoor, and especially Chris Schafer who will defend his dissertation in the coming weeks. I also benefitted and am eternally grateful for the friendship and comradery of my PMCB cohort, Dr. Jessica Martin, Dr. Johannes Elferich, and Nathalie Javidi-Sharifi. Finally, I must thank Crystal Paredes for always being my advocate, and the women of the ARCS foundation who support basic science by supporting science students. Thank you in particular to Cornelia & Bill Stevens and Barbara & Phil Silver.

Table of Contents

List of Tables	xii
List of Figures	xiii
List of Abbreviations	xvii
Chapter 1: Introduction.	1
Opening statement.	1
G protein coupled receptors.....	1
Emerging signaling paradigms.	4
Rhodopsin is ideal for studying GPCR activation and attenuation.....	4
Introduction to G-protein coupled receptor kinases.....	7
GRK1—rhodopsin kinase.....	8
GRK7—cone opsin kinase.....	10
GRK2/3— β -adrenergic receptor kinase 1 & 2.	10
GRK 4/5/6.....	11
Role of GRKs in biased signaling.....	12
Working with GRKs: classical methods for purifying GRKs are not optimal.	13
Introduction to the TrIQ method.....	13
A brief introduction to fluorescence.	14
Discovery of Tryptophan induced quenching of fluorescence.	15
Dissertation overview.	17
List of publications.	17
Figures.	18
Chapter 2: Distance Mapping in Proteins Using Fluorescence Spectroscopy: Tyrosine, like Tryptophan, Quenches Bimane Fluorescence in a Distance Dependent Manner	38
Abstract.....	38

Introduction.....	39
Materials & Methods.....	41
Materials.....	41
Buffers.....	41
Construction, expression, and purification of T4 lysozyme mutants.....	41
Purification and fluorescent labeling of proteins.....	42
Hydrolysis of peptidoglycan bound to the active site of the T4L T26E mutants.....	43
Fluorescence intensity measurements.....	43
Quantum yield measurements.....	44
Fluorescence lifetime measurements.....	44
Calculation of the fraction of fluorophore in a static complex with quencher.....	46
Analysis of the pH-dependence of the TrIQ and TyrIQ effects.....	46
Arrhenius analysis of hinge-bending and temperature dependence of the TrIQ and TyrIQ effects.....	46
Results.....	48
Phenylalanine is a structurally similar control residue for TyrIQ and TrIQ studies that shows minimal bimane quenching.....	48
Tyrosine can quench the fluorescence intensity of bimane in a distance-dependent fashion, but does so over a shorter range than Tryptophan.....	49
Unlike Tryptophan, Tyrosine does not show substantial quenching of BODIPY 507/545 fluorescence.....	50
The degree of intensity quenching does not always match the degree of lifetime quenching for both quenchers, Trp and Tyr.....	50
Differences in the ratio of the fluorescence intensity and lifetime quenching indicate static quenching complexes form in some of the Trp- and Tyr-quenched samples.....	51

Assessment of pH and temperature on the efficiency of quenching for both Trp and Tyr.....	52
Both TrIQ and TyrIQ can detect a hinge-bending movement in T4L that accompanies substrate binding.	53
Both TrIQ and TyrIQ can be used to assess the energetics of a protein movement through Arrhenius analysis of dynamic quenching rates.....	55
Discussion.....	55
Both Tyr and Trp show distance-dependent quenching of bimane.	56
Tyr does not substantially quench BODIPY 507/545 in a distance dependent manner, whereas Trp does.	59
Both TrIQ and TyrIQ can detect a hinge bending movement in T4L that occurs with substrate binding.	60
Arrhenius analysis of the TrIQ and TyrIQ data suggest a low energy barrier for hinge-bending motion in T4L.	62
Tables.....	65
Figures.	68
Chapter 3: Rapid Purification of full-length GRK1.....	86
Summary.....	86
Introduction.....	87
Materials & Methods.	90
Materials.	90
Buffers.....	91
Cloning of rhodopsin kinase.	91
Expression and Purification of Profinity-tagged rhodopsin kinase.	92
Isolation of ROS membranes and preparation of urea stripped ROS.	93
Preparation of phospholipid/DDM rhodopsin mixed micelles.	93
Rhodopsin kinase activity assay.	94
Kinetics parameters.....	95

Whole protein mass spectroscopy analysis.....	95
Phosphorylation of CB ₁ by GRK1.....	96
Results.....	97
The Profinity eXact purification method can be used to rapidly purify tag-free, full-length farnesylated rhodopsin kinase.....	97
Purified wild type GRK1 is functional and can phosphorylate DDM-solubilized USR.....	98
GRK1 S488D/T489D phosphorylates rhodopsin to the same degree and with the same affinity of wildtype GRK1 and has nearly undetectable levels of autophosphorylation.....	99
Kinetics parameters for GRK1 purified using the Profinity exact method.....	100
Phosphorylation of human CB ₁ by GRK1.....	101
Discussion.....	101
The Profinity eXact purification method yields full-length tag-free purified recombinant rhodopsin kinase in 1 day.....	101
Purified full-length GRK1 has wildtype-like functionality.....	103
Comparison of GRK1 purified using the Profinity method with GRK1 purified using other methods.....	105
GRK1 phosphorylates purified human CB ₁ in an agonist dependent manner... ..	106
Conclusion.....	107
Tables.....	108
Figures.....	109
Chapter 4: Evidence that the rhodopsin kinase (GRK1) N-terminus and the Transducin Gα C-terminus interact with the Same “Hydrophobic Patch” on Rhodopsin TM5.....	123
Abstract.....	123
Introduction.....	124
Materials & Methods.....	126

Materials.....	126
Buffers.....	127
Cloning of rhodopsin kinase.....	127
Expression and Purification of Profinity-tagged rhodopsin kinase.....	127
Isolation of ROS membranes and preparation of urea stripped ROS.....	129
Expression and Purification of wild-type and mutant rhodopsin.....	129
Rhodopsin kinase activity assay.....	130
Kinetics parameters.....	131
Whole protein mass spectroscopy analysis.....	131
G _{ta} C-terminal peptide inhibition of phosphorylation.....	132
GRK1 N-terminal peptide inhibition of phosphorylation.....	132
Retinal Release Assay.....	132
Assessing visual arrestin binding to rhodopsin via retinal trapping experiment.....	133
Measurement of G _t activation.....	133
PyMPO labeling V250C.....	134
Sequence analysis and modeling of GRK1-rhodopsin binding.....	134
Results.....	135
The Profinity eXact purification method can be used to rapidly purify tag-free, full-length farnesylated rhodopsin kinase.....	135
Purified wild type GRK1 is functional and can phosphorylate DDM-solubilized USR rhodopsin.....	136
GRK1 phosphorylates DDM-purified bovine rhodopsin almost as efficiently as DDM-solubilized USR.....	137
Both the G _{ta} C-terminal and the GRK1 N-terminal peptides block efficient GRK1 phosphorylation of rhodopsin.....	137

Site-directed labeling studies suggest the G_{α} C-terminus and GRK1 N-terminus share the same binding site.	139
Mutations in a conserved hydrophobic patch used for G_t and visual arrestin binding block GRK1-mediated receptor phosphorylation.	140
Discussion.	141
A rapid way to purify fully functional GRK1.	141
GRK1 shares a common site of binding on rhodopsin with the G_{α} C-terminus.	143
GRK1 requires residues L226 and V230 on the rhodopsin cytoplasmic face for efficient receptor phosphorylation.	144
Modeling studies incorporating our data suggest that the GRK1 N-terminus binds in the same location and orientation as the G_{α} C-terminus.	146
Conclusion—rhodopsin uses a common binding pocket and hydrophobic residues to bind all three affiliate signaling proteins; G_t , visual arrestin and GRK1.	149
Tables.	150
Figures.	152
Chapter 5: Conclusions and Future Directions.	164
Improvement and expansion of the TrIQ/TyrIQ method for mapping interactions within and between proteins.	164
A rapid method for GRK1 purification that produces highly function kinase, and enables future GRK-GPCR studies.	168
Identification of a shared binding site on rhodopsin, used by the G protein transducin, arrestin, and rhodopsin kinase.	171
Figures.	175
Bibliography.	178
Appendix 1: Supplementary Results and Discussion for TyrIQ.	197
Opening statement.	197
The fluorescence decay curves can be fit with a Lorentzian Distribution kinetic model.	198

Lifetime decays analyzed using a Lorentzian distribution kinetic model provide insights into the dynamic quenching component in TrIQ and TyrIQ studies.	199
Analysis of two fluorophores well suited for fluorescence imaging, Atto488 or Oxa11.....	200
Tables.....	204
Figures	205
Appendix 2: Preliminary GRK1:rhodopsin crosslinking experiments.	211
Introduction.....	211
Materials & Methods.	213
Preparation of rhodopsin mutants.	213
Purification and activity assays of site-directed GRK1 cysteine mutants.	213
Copper phenanthroline crosslinking.	213
BMOE crosslinking.	214
SDS-Page and silver staining.....	215
Western blot transfer and dual antibody labeling.	215
Results.....	216
Purified GRK1 L6C has wild type-like activity.	216
GRK1 T8C and S13C are less active than wild type GRK1.....	217
GRK1 T8C and V9C were not crosslinked to rhodopsin T242C ₀ in the presence of 10 or 50 μ M BMOE.....	217
GRK1 T8C and V9C were not crosslinked to rhodopsin T242C ₀ in the presence of copper phenanthroline.....	218
Discussion and future directions.....	218
GRK1 N-terminal cysteine mutant L6C has WT activity towards rhodopsin and rhodopsin mutants.....	218
GRK1 N-terminal cysteine mutants T8C and S13C have reduced activity towards rhodopsin and rhodopsin mutants.	219

Attempts to crosslink rhodopsin T242C ₀ were unsuccessful, but our binding model suggests sites for future crosslinking experiments.....	220
Tables.....	222
Figures	223

List of Tables

Table 2.1: Results of fitting lifetime decay of bimane attached to T4 lysozyme at multiple sites with and exponential decay model	65
Table 2.2: TrIQ and TyrIQ effect on bimane attached to the same site of T4L in various substrate binding modes.....	66
Table 2.3: Fluorescence quantum yield, intensity, and bimane maximal absorbance for T4L N116X/N132B comparing Phe, Tyr, and Trp at position 116 to the native residue, Asn.....	67
Table 3.1: Comparison of kinetic parameters published for GRK1 over the last ~30 years	108
Table 4.1: GRK1 activity parameters for WT rhodopsin and rhodopsin constructs.....	150
Table 4.2 Solvent accessibility* of rhodopsin site V250 when bound to G _{ta} CT and GRK1 NT peptides.	151
Table A1.1: Results of fitting bimane decay data with a Lorentzian distribution kinetic model*	204
Table A2.1: Kinetic parameters of GRK1 cysteine mutants for rhodopsin mutants.	222

List of Figures

Figure 1.1 Classes of GPCRs and canonical activation scheme.	18
Figure 1.2 G protein-mediated signaling by GPCRs.	20
Figure 1.3 Arrestin-mediated GPCR signaling.	22
Figure 1.4 Comparison of arrestin family domain structure.	24
Figure 1.5 Architecture of rod cells, location of rhodopsin within the rod outer segment, and structure of rhodopsin.	25
Figure 1.6 Rhodopsin activation involves isomerization of 11-cis retinal, leading to multiple transition states that have distinct spectroscopic states.	27
Figure 1.7 Retinal release from the rhodopsin binding pocket can be measured using fluorescence.	29
Figure 1.8 Insight in to GPCR activation from crystal structures of rhodopsin.	30
Figure 1.9 Comparison of domain structure among G protein coupled receptor kinases.	31
Figure 1.10 Sequence specificity for protein isoprenoid transferases.	33
Figure 1.11 Crystal structures of GRKs 1/2/6 reveal conservation of kinase RGS- homology and catalytic domains.	34
Figure 1.12 The quantum mechanical process of fluorescence illustrated in a Jablonski diagram.	36
Figure 1.13 Examples of fluorescence emission spectra and TCSPC fluorescence decay data.	37
Figure 2.1 Model showing the fluorophores, quenching residues, and sites of attachment on T4 lysozyme used in this study.	68
Figure 2.2 Models illustrating the three different quencher-fluorophore conformations that can be quantified using fluorescent measurements, and how their fluorescence emission intensity and lifetime decay differ.	70

Figure 2.3 Absorbance spectra of Bimane incorporated in T4L showing a shift in peak absorbance.....	72
Figure 2.4 Tryptophan quenches the fluorescence emission of T4 lysozyme labeled with either bimane or BODIPY 507/545, while tyrosine only quenches bimane.	73
Figure 2.5 Examples of bimane fluorescence decay and Exponential decay fitting.....	75
Figure 2.6 Comparison of the distance-dependent effect of Trp and Tyr quenching of bimane emission, fluorescence lifetime, and the calculated relative components of fluorescent quenching.	77
Figure 2.7 BODIPY 507/545 is quenched by Trp but not by Tyr.	79
Figure 2.8 Measurements of the pH and temperature sensitivity of TrIQ and TyrIQ.	80
Figure 2.9 SDS-PAGE analysis of T4L active site mutants shows peptidoglycan binding.	82
Figure 2.10 TrIQ and TyrIQ can be used to measure the magnitude and energetics of a hinge bending motion in T4L that occurs upon substrate binding.....	83
Figure 3.1 Design and protocol for rapid purification of Rhodopsin kinase (GRK1) in a functional, tag-free form using the Profinity eXact Fusion Tag method.....	109
Figure 3.2 Wildtype GRK1 purified using the Profinity eXact method is highly pure, properly farnesylated, and elutes in the non-autophosphorylated form.....	111
Figure 3.3. Whole protein mass spectra analysis of WT GRK1 indicates that it is properly farnesylated and not autophosphorylated.	113
Figure 3.4 Profinity eXact purified GRK1 is highly functional and can phosphorylate rhodopsin in a light dependent manner.	115
Figure 3.5 Presence of acidic phospholipids restores full phosphorylation of DDM-purified rhodopsin by full length, Profinity-purified GRK1.....	117
Figure 3.6 GRK1 mutant lacking the primary autophosphorylation sites, GRK1 S488D/T489D, is fully functional.....	119
Figure 3.7 Whole protein mass spectra analysis of GRK1 S488D/T489D indicates that it is farnesylated.	120

Figure 3.8 Profinity-purified GRK1 can phosphorylate a ligand-binding GPCR, the human cannabinoid receptor, CB1, in an agonist-dependent manner.....	122
Figure 4.1 Design and protocol for rapid purification of Rhodopsin kinase (GRK1) in a functional, tag-free form using the Profinity eXact Fusion Tag method.....	152
Figure 4.2 The ability of GRK1 to phosphorylate rhodopsin is not dramatically impacted by presence of 1D4 peptide, but is blocked by the presence of 500 μ M GRK1 NT peptide and 100 μ M $G_{t\alpha}$ C-terminal peptide ($G_{t\alpha}$ CT), suggesting both affiliate proteins need access to the same sites on the receptor.....	154
Figure 4.3 Site-directed labeling studies of rhodopsin mutant V250C suggest the N-terminus of GRK1 binds to the same site on rhodopsin as the $G_{t\alpha}$ C-terminus and requires similar interactions with a key hydrophobic residue, L226.	157
Figure 4.4 Functional evidence that GRK1, G_t , and visual arrestin all require some of the same “hydrophobic patch” residues for optimal activity.....	159
Figure 4.5 Sequence analysis and structural modeling support the hypothesis that GRKs, G-proteins and arrestins all interact with GPCRs through hydrophobic interactions within a conserved “hydrophobic patch” on TM5 of the receptor.....	161
Figure 5.1 Model of full length visual arrestin fused to opsin (PDB 4ZWJ) shows that a monomeric interaction between the two proteins simultaneously satisfies the distance restraints produced from our TrIQ study.	175
Figure 5.2 The cytoplasmic face of active rhodopsin can accommodate starkly different binding angles of the α -helices of the $G_{t\alpha}$ C-terminal peptide and visual arrestin finger loop.	177
Figure A1.1: Results from fitting Bimane decays with a Lorentzian distribution model.	205
Figure A1.2 Ability of Tyrosine and Tryptophan to quench Atto 488 fluorescence.	207
Figure A1.3 Ability of Tyrosine and Tryptophan to quench Oxa 11 fluorescence	209
Figure A2.1 Crosslinking studies used copper phenanthroline for direct crosslinking and BMOE for an 8 Å linker arm.	223

Figure A2.2 SDS-PAGE analysis shows that the Profinity eXact purification method yields highly pure GRK1 L6C, T8C, and S13C.	224
Figure A2.3 Addition of DOPS to DDM-purified θ rhodopsin increases the activity of GRK1 cysteine mutants.	225
Figure A2.4 Cysteine substitutions at sites V139 and V250 do not affect the phosphorylation of these DDM-DOPS purified rhodopsins by GRK1 cysteine mutants.	226
Figure A2.5 GRK1 T8C and GRK1 V9C did not crosslink to rhodopsin T242C ₀ with BMOE.	227
Figure A2.6 GRK1 T8C and GRK1 V9C did not crosslink to rhodopsin T242C ₀ using copper phenanthroline.	229
Figure A2.7 A model of the GRK1 N-terminus bound to the cytoplasmic face of rhodopsin predicts that GRK1 L6 and V9 bind near rhodopsin site V250 and T243.	230

List of Abbreviations

11-CR	11-cis retinal
ATP	adenosine triphosphate
ATR	all trans retinal
β ARK	beta adrenergic receptor kinase
BL21 DE3	<i>E. coli</i> strain used for production of proteins of interest from plasmid DNA
BMOE	Bis-maleimide o-ethyl
BODIPY	N-(4,4-difluoro-1,3,5,7-tetramethyl-4-bora-3a,4a-diaza-s-indacene-2-yl)iodoacetamide <i>aka</i> BODIPY 507/545 IA
CHAPS	3-[(3-cholamidopropyl)dimethylammonio]-1-propanesulfonate
CHS	Cholesterol Hemisuccinate
CuP	Copper phenantroline
DAG	Diacyl glycerol
DDM	n-dodecyl β -D-maltoside
DH5 α	<i>E. coli</i> strain used for amplification of plasmid DNA
DMEM	Dulbecco's modified eagle medium
DMSO	dimethyl sulfoxide
DOPA	1,2-dioleoyl-sn-glycero-3-phosphate
DOPC	1,2-dioleoyl-sn-glycero-3-phosphatyl choline
DOPS	1,2-dioleoyl-sn-glycero-3-phospho-L-serine
DTT	Dithiothreitol
EDTA	<i>N,N'</i> -1,2-ethanediylbis[<i>N</i> -(carboxymethyl)glycine] disodium salt
EGTA	Ethylene glycol tetraacetic acid
FBS	Fetal bovine serum
FRET	Forster resonance energy transfer
FWHM	Full width at half maximum
GDP	guanosine diphosphate
GPCR	G protein coupled receptor
GRK	G protein coupled receptor kinase

GRK1	Rhodopsin kinase
GRK1 NT	Peptide comprising the N-terminal sequence of GRK1
Gt	Transducin
Gt CT	High-affinity transducin alpha-subunit C-terminal peptide 23SV
GTP	guanosine triphosphate
GTP γ S	guanosine 5'-O-[gamma-thio]triphosphate
G α	Transducin alpha-subunit
G $\beta\gamma$	Transducin beta/gamma subunits
HEPES	4-(2-hydroxyethyl)-1-piperazineethanesulfonic acid
IANBD	N,N-dimethyl-N-(iodoacetyl)-N-(7-nitrobenz-2-oxa-1,3-diazol-4-yl)ethylenediamine
IP3	Inositol triphosphate
IPTG	Isopropyl β -D-1-thiogalactopyranoside
IRF	Instrument response function
mBBr	monobromo bimane
MES	2-(N-morpholino)ethanesulfonic acid
MI	Meta I rhodopsin
MII	Meta II rhodopsin
MIII	Meta III rhodopsin
MOPS	3-(N-morpholino)-propanesulfonic acid
NEM	N-ethyl maleimide
PBSSC	Phosphate-buffered saline
PCR	Polymerase chain reaction
PDB	Protein databank
PDE	Phosphodiesterase
PEI	polyethyleneimine
PET	Photo-induced electron transfer
PH	Pleckstrin homology domain
PKA	Protein kinase A
PKC	Protein kinase C
PMSF	Phenylmethylsulfonyl fluoride
POPC	1-Palmitoyl-2-oleoylphosphatidylcholine

POPS	1-Palmitoyl-2-oleoyl- <i>sn</i> -glycero-3-phospho-L-serine
PTI	Photon technology international
PVDF	polyvinylidene difluoride
PyMPO	1-(3-carboxybenzyl)-4-(5-(4-methoxyphenyl)oxazol-2-yl)pyridinium bromide
RGS	Regulator of G protein signaling domain
RH	RGS homology domain
RK	Rhodopsin Kinase
ROS	Rod Outer Segments
SDFL	Site-directed fluorescence labeling
SDSL	Site-directed spin labeling
SDS-PAGE	Sodium Dodecyl Sulfate Polyacrylamide Gel Electrophoresis
TCA	Trichloro acetic acid
TCSPC	Time correlated single photon counting
TM	Transmembrane helix
Tris	2-Amino-2-hydroxymethyl-propane-1,3-diol
USR	urea-stripped rod outer segments
UV	Ultraviolet
WT	wild type

Chapter 1: Introduction.

Opening statement.

This dissertation describes my work on two main projects, first to expand and calibrate a site-directed fluorescence labeling method that can assess distance relationships between discrete sites within or between two proteins, and second to study the interactions of rhodopsin kinase with its substrate, rhodopsin. In this chapter, I will discuss the background of these subjects, and then give an overview of the entitled thesis.

G protein coupled receptors.

G protein coupled receptors (GPCRs) comprise a large class of membrane proteins that together represent the largest class of receptors in the human genome, with ~800 family members, ~400 of which are non-olfactory. The broad family, shown in Figure 1.1A, is divided into multiple classes based on similarity: Class A (rhodopsin like), Class B1 (secretin like), Class B2 (adhesion-like receptors), Class C (glutamate-like receptors), Class F (frizzled-like receptors). Note that there are still ~40 GPCRs in “others” groups according to the GPCR database (1-3).

The broad family of GPCRs differ in the relative size and nature of the N- and C-termini, and the loops that connect the helices together (intra- and extra-cellular loops). Even more varied are the ligands for the known GPCR family, which show incredible

chemical diversity, from small molecules, to peptides, small proteins, fatty acids, and light (4). Despite these differences, all GPCRs are thought to share a common, basic structure of 7 transmembrane alpha helices (5).

Historically, this family of receptors was identified by their ability to couple to and activate heterotrimeric G proteins (comprising three subunits called α , β , and γ).

Recently, however, it has become clear that among the receptors sharing 7 transmembrane helices, there is a variety of efficacies for activating G proteins, and even signaling through other pathways, which is why some in the field are transitioning to referring to this family as 7TMRs (7 transmembrane receptors). For consistency, I will continue to use the term GPCR in this dissertation.

Classically, GPCR signaling involves activation of the receptor by binding of an agonist. Once turned “on” the active receptor then induces a heterotrimeric G protein to exchange GDP for GTP and transduce the appropriate signaling cascade (6) (Figure 1.1B). GPCRS signal through combinations of 16 G protein α subunits and 5 β and 13 γ subunits, although only a subset of the theoretically possible heterotrimers have been reported. In general, the “type” of signaling cascade a GPCR activates depends on the subtype of the $G\alpha$ subunit (reviewed in (7, 8)). As outlined in Figure 1.2, the “stimulatory” $G\alpha_s$ increases the activity of adenylyl cyclase which results in increased production of cyclic AMP (cAMP), which is an important regulatory cofactor for multiple proteins such as protein kinase A (PKA), and cyclic nucleotide gated channels. The “inhibitory” $G\alpha_i$ inhibits adenylyl cyclase activity. The $G\alpha_q$ subunit activates phospholipase C- β (PLC β), which hydrolyzes phosphatidyl inositol lipids to release inositol(1,4,5)triphosphate (IP₃) and diacyl glycerol (DAG) that go on to increase protein

kinase C activity and intracellular calcium ions. Finally, the $G\alpha_{12/13}$ enzymes regulate the cytoskeleton by activating a guanine nucleotide exchange factor (GEF) for the RhoA small GTP-binding protein.

GPCRs are also turned “off” by a conserved process – they become phosphorylated by one or more of the 7 GPCR-kinase (GRK) family members, typically at multiple serine and threonine sites on the C-terminus of the receptor, as discussed later in this chapter. The phosphorylated receptor can then bind a protein called arrestin, which was named for its role in sterically preventing additional G protein activation and subsequently initiating either receptor recycling or degradation (Figure 1.3). Four types of arrestins are known, arrestin 1 (rod arrestin, also known as visual arrestin), arrestins 2 & 3 (also called β -arrestin 1 & 2, respectively), and arrestin 4 (cone arrestin). These all share a conserved domain structure (Figure 1.4) comprising an N- and C- domain that fold to create two lobes of curved antiparallel β -sheets. The rod visual arrestin is discussed later in this chapter. The β arrestins contain additional clathrin and AP2 binding domains, both of which allow the β arrestins to mediate GPCR internalization for subsequent receptor recycling or degradation.

Despite the large number of and diversity in ligands, the broad array of nonvisual GPCR signaling regimes are attenuated by a startlingly small number of subtypes, just 2 arrestins and 5 GRKs. The limited and conserved nature of signal attenuation machinery strongly suggests there are common features shared by active GPCRs recognized by GRKs and arrestins.

Emerging signaling paradigms.

Historically, pharmacology has classified GPCR ligands as either agonist or antagonist solely by their effects on G protein activation. However, this paradigm is shifting. Recent work has demonstrated that GPCR interactions with arrestins are capable of initiating ERK signaling cascades in their own right (Figure 1.3), typically from endocytosed vesicles (9, 10) or from clathrin-coated structures that have formed a pit on the cell surface but have not been fully endocytosed (11).

These new realizations require a new model of understanding about GPCR signaling, and will require a new vocabulary for the classification of ligands that bind specific GPCRs. Emerging from these discoveries is the concept of ligand-directed signaling or biased agonism, wherein specific ligands can activate primarily G protein mediated signaling pathways, while others are biased for arrestin-mediated signaling pathways (reviewed in (12)). In fact, some ligands that have been classified as antagonists for G protein signaling are, instead, agonists for arrestin signaling, leading to even more complexity in the GPCR signaling paradigm.

Rhodopsin is ideal for studying GPCR activation and attenuation.

The dim light sensing GPCR in the retina is called rhodopsin (13, 14). Rhodopsin has historically been one of two canonical GPCRs for understanding GPCR structure and function, along with the β_2 adrenergic receptor, which has served a similar foundational role for studying “ligand-binding” GPCRs. Rhodopsin is found in retinal rod cells, which are typically found on the peripheries of the retina in humans and are associated with night and peripheral vision. Rod cells, which get their name due to their unique shape,

form a synapse with a neuron via the synaptic body on one end, the nucleus and inner segment follow. Past the inner segment is found the outer segment (rod outer segment, ROS) that is comprised on stacked disks containing densely packed rhodopsins whose “extracellular face” is, in fact exposed to the intradiskal space (Figure 1.5)

As noted above, rhodopsin is unique in having a dedicated G protein (transducin), kinase (rhodopsin kinase a.k.a. GRK1), and arrestin (visual arrestin), making it a powerful model system with which to study and define the physical interactions between a GPCR and its intracellular binding partners.

Rhodopsin is particularly tractable because of its light-sensitive ligand and its mode of activation, light absorption, which results in distinct activation states that can be observed with absorbance spectrometry using ultra violet (UV) and visible light (13, 15, 16). Rhodopsin is kept in an “off” state by binding of 11-cis retinal, which keeps rhodopsin in an inactive form in the dark. In fact, the rhodopsin dark state is so stable that it induces almost zero aberrant signaling ensuring that it is extremely sensitive to even small amounts of light. In its unbound form, 11-cis retinal has a maximal absorbance at 380 nm. When it is bound to rhodopsin, 11-cis retinal forms a protonated Schiff base with lysine 296 in the receptor binding pocket, shifting the maximal absorbance of the 11-cis retinal to 500 nm. These characteristics are so well documented that the ratio of the 500 nm absorbance peak (from 11-cis retinal) to the 280 nm absorbance peak (from the protein) can be used to assess the purity of rhodopsin spectrophotometrically, without the need to use methods like SDS-PAGE analysis, making the assessment of the purity and quality of rhodopsin purification procedures relatively rapid and straightforward (17, 18).

Photons within its absorbance range activate rhodopsin by causing the 11-cis retinal to isomerize to all trans retinal. Subsequently, the Schiff base hydrolyzes and the all trans retinal is released from rhodopsin's ligand binding pocket and returns to 380 nm maximal absorbance (Figure 1.6). Several photo-intermediates are then produced in femto-to-microseconds, each with characteristic absorbances (Figure 1.6) that are associated with a strained retinal that maintains its protonated Schiff base linkage to the rhodopsin. These intermediate states can be observed by time-resolved measurements (19) or be trapped by cryogenic cooling, as shown in Figure 1.6 (15, 20). The metarhodopsin I (MI) state is associated with a retinal that has been fully isomerized to all trans retinal but still maintains the protonated Schiff base. The deprotonation of the Schiff base converts MI to metarhodopsin II (MII), the active state of rhodopsin that activates transducin, is phosphorylated by GRK1, and can bind visual arrestin (once MII is phosphorylated). Finally, cleavage of the deprotonated Schiff base allows all trans retinal to exit the binding pocket leaving an apo-opsin. Thus, characterization of rhodopsin has contributed to the understanding that GPCRs can have multiple conformations between fully inactive and fully active.

In addition to identifying multiple activation states, spectroscopy can also be used to monitor the ligand binding dynamics in rhodopsin. Along with the absorbance shifts noted above, when retinal is bound in rhodopsin's ligand binding pocket it quenches the fluorescence of the nearby tryptophan residues, due to transfer of energy to the retinal via a Forster Resonance Energy Transfer (FRET) mechanism. Thus, as the retinal leaves the binding pocket, the fluorescence signal from tryptophans at 330 nm increases (21), as shown in Fig 1.7. This method was used to show the interconnectedness between the

cytoplasmic face of rhodopsin and the ligand binding site when it was observed that arrestin binding blocked retinal release (22). This method is used in Chapter 4 to demonstrate that specific mutations made to the cytoplasmic face of rhodopsin do not affect the light-induced activation and release of retinal.

How does ligand binding result in GPCR activation? In the case of rhodopsin, light isomerization of 11-cis retinal chromophore changes the shape of retinal, which is translated to a conformational change on the cytoplasmic face of rhodopsin (Figure 1.8). Specifically, after light isomerization of the chromophore, transmembrane helices (TMs) 5&6 swing outward on the cytoplasmic face of rhodopsin (23), although in rhodopsin, the magnitude of this movement remains controversial: the degree of movement in crystal structures is smaller than the movement observed using other spectroscopic methods. This movement has since also been observed in other GPCRs.

Just as much of what is known about the shared structure and activation of GPCRs was initially observed in rhodopsin, many aspects of signal attenuation have also been first discovered using the rhodopsin:visual arrestin interaction. Thus, in this vein, we are using the rhodopsin:GRK1 interaction to understand the fundamental interaction between GPCRs and their kinases. Next, I will introduce GRKs and briefly cover what is known about the individual GRK family members.

Introduction to G-protein coupled receptor kinases.

It should be noted that, for the purposes of this dissertation, I will be focusing on GRK-mediated GPCR phosphorylation, although there are additional kinases that act on GPCRs in their own distinct way and as part of other feedback mechanisms, like protein

kinase A (PKA), but importantly, these other kinases do not phosphorylate GPCRs in an agonist dependent manner.

The first GRK that was identified acted on rhodopsin, or as it was referred to at the time “opsin kinase” (24-26), now referred to as GRK1. Only a few years later it was found that the β_2 -adrenergic receptor was also desensitized through the same phosphorylation process (27, 28), which led to the discovery of β -adrenergic receptor kinase (β -ARK), now known as GRK2. Since then, a total of 7 GRK family members have been identified. The 7 GRKs share a basic domain structure, shown in Figure 1.9 and all are serine/threonine kinases. The initial N-terminal residues contain some strictly conserved residues (Figure 1.9), while the broader N-terminal regions vary. The catalytic domain of all GRKs are also well conserved, comprising a Regulator of G protein Signaling (RGS) homology (RH) domain followed by a Protein Kinase domain, although to date only GRK2 has been definitively shown to bind-to and regulate $G\alpha$ subunits (29-31).

Below, the similarities and differences of the individual GRK family members are briefly reviewed.

GRK1—rhodopsin kinase.

GRK1 is expressed primarily in the rod outer segments of the retina, and in the pineal gland—the latter is thought to be ancestral optical tissue and houses melanopsin. GRK1 is regulated by compartmentalization, protein-protein interactions, and phosphorylation. In the rod outer segments, GRK1 is attenuated by binding of a calcium-sensitive protein called recoverin, and is unable phosphorylate rhodopsin and alter signaling until the local

calcium concentration is sufficiently reduced as a result of downstream closure of $\text{Na}^+/\text{Ca}^{2+}$ ion channels such that the recoverin (a calcium-binding protein) is released.

GRK1 is also regulated by phosphorylation, and undergoes autophosphorylation, primarily at sites S488 and T489 (indicated by asterisks in the C-domain of GRK sequences shown in Figure 1.9), and to a lesser extent at S8 (32-35). Studies from the Palczewski group have shown that autophosphorylated GRK1 has the same affinity for light-activated rhodopsin as non-autophosphorylated GRK1, but when GRK1 is autophosphorylated it has a lower affinity for phosphorylated rhodopsin which might indicate a mechanism that could attenuate high-gain rhodopsin phosphorylation. GRK1 is also trans-phosphorylated at S21 by PKA, which reduces the ability of GRK1 to phosphorylate rhodopsin (36, 37).

Another level of regulation is context-dependent spatial separation of the kinase from its membrane-bound substrate—GRK1 is post-translationally modified with a farnesyl isoprenoid (38, 39). Isoprenylation is indicated by a C-terminal CAAX motif, wherein the “A” residues are various aliphatic amino acids, and the “X” residue specifies between addition of a farnesyl group (alanine, methionine, serine, cysteine, or glutamine) or a geranylgeranyl group (leucine or phenylalanine) (40-42), shown in Figure 1.10. This farnesyl group allows GRK1 to be found in either the cytosol or be membrane bound, an equilibrium that is dependent on activation of rhodopsin (43). Farnesylation is not only critical for membrane localization, but is also required for full GRK1 activity (38).

While GRK1 is primarily expressed in the same cell type as rhodopsin, GRK1 can also function to phosphorylate other class A GPCRs. Notably, early work showed that GRK1 phosphorylates the β_2 -adrenergic receptor in an agonist dependent manner (44), though it

is unclear if the amount and location of the phosphorylation is the same between the GRK1-mediated and GRK2/3-mediated phosphorylation.

GRK7—cone opsin kinase.

GRK7, or cone opsin, is the most recently identified member of this family; publication of its identification in amphibians came in 1998 (45), and it was subsequently confirmed to be present in humans (46-48). GRK7 shares 45% identity and 75% similarity with GRK1. GRK7 is primarily expressed in cone cells, indicating that its primary substrates *in vivo* are cone opsins (responsible for bright-light vision), and is reported to have kinetic values similar to GRK1 for phosphorylating rhodopsin (36). Given the relatively recent discovery of this kinase, much is unknown about its regulation and it is not yet known if there are proteins that regulate GRK7 analogous to recoverin-regulation of GRK1.

GRK7 appears to undergo PKA-mediated phosphorylation at sites S23 and S36 *in vitro* (36). It is also capable of autophosphorylation but neither the role of this autophosphorylation on kinase activity nor the specific sites of phosphorylation have been identified (48). GRK7 is isoprenylated with a geranylgeranyl group, which causes GRK7 to be membrane anchored (45).

GRK2/3— β -adrenergic receptor kinase 1 & 2.

GRKs 2 & 3 are ubiquitously expressed (49) and have much in common, sharing 85% sequence identity and many aspects of regulation. GRK2 is the most well studied GRK. They are assumed to be generally responsible for agonist-dependent non-visual class A

GPCR phosphorylation, and thus will be the primary subject of the description that follows. Importantly, while less studied, GRK3 does seem to be responsible for phosphorylation of olfactory receptors, which represent the largest type of GPCRs in the human genome by number, as well as the human cannabinoid receptor, CB₁.

GRK2 is regulated by binding calmodulin, a broadly expressed calcium binding protein (50), which binds the N-terminus of GRK2 akin to the recoverin binding and inhibition of GRK1. GRK2 activity is regulated by phosphorylation by protein kinase C (PKC) (51, 52).

Membrane localization of both GRK2 & 3 is regulated by a phosphatidyl inositol diphosphate (PIP₂)-binding domain called pleckstrin homology (PH) domain located in the C-terminus (Figure 1.9 and 1.11). The PH domain acts in combination with a G_{βγ}-binding domain for spatial and temporal control of membrane localization. Interestingly, this binding domain acts as an alternative to direct isoprenylation of GRKs 2&3, because the G_γ subunit itself is isoprenylated, typically with a geranylgeranyl group (reviewed in (53)).

In addition to being highly regulated, GRK2 also plays a role in cell regulation, reviewed in (49, 54).

GRK 4/5/6.

The GRK4 family has differential tissue distribution, with GRK4 being expressed in a limited number of tissues, while GRKs 5 & 6 are more broadly expressed. As such, GRKs 5 & 6 are better understood. In general, GRKs 4/5/6 all contain calmodulin-binding domains at their N-terminus, while GRK5 has a second calmodulin binding site

at its C-terminus. This second calmodulin site at the C-terminus of GRK5 might be an important regulatory strategy—GRK5 is constitutively membrane-bound (55) due to electrostatic interactions between positively charged residues at the GRK5 C-terminus and phospholipids (56), thus calmodulin binding to this region may block this interaction. GRK5 is also regulated by autophosphorylation at sites analogous to the C-terminal sites of autophosphorylation in both GRK1 & 7. Both GRK4 & 6 are palmitoylated at C-terminal cysteine residues, which is a reversible post-translational modification and allows for cell-level regulation of GRK4 & 6 membrane association (reviewed in (57)).

Intriguingly, a certain level of constitutive activity has been noted for GRK5 since its discovery (55). Recently, this observation has been directly studied and it was found that both GRK5 & 6 phosphorylate inactive GPCRs (58). In fact, GRK5 showed robust phosphorylation of opsin (apo rhodopsin) and dark state rhodopsin, although both GRK5 & 6 also robustly phosphorylated the agonist-bound GPCRs tested, as well.

Role of GRKs in biased signaling.

Biased GPCR signaling, strictly speaking, involves the initiation of signaling cascades by either a G-protein or an arrestin protein after interaction with an active GPCR. However, arrestins do not typically bind non-phosphorylated GPCRs, even those in an “active” state, and only bind a GPCR after the action of kinases, further suggesting that GRKs might also be involved. So what role do GRKs play in biased signaling? The role of GRKs in GPCR biased signaling is unclear, but it has been demonstrated that the position and relative level of GRK phosphorylation influence the cellular outcomes (59-62). In fact, it appears that, at least in some cases, individual GRK subtypes are capable

of creating distinct phosphorylation patterns on a GPCR in a ligand dependent manner, as in the case of the V2 vasopressin, AT1A angiotensin, follicle stimulating, and β_2 adrenergic receptors. In these receptors, certain ligands preferentially result in GRK5/6 phosphorylation of the receptor while other ligands result in GRK2/3 phosphorylation of the receptor (61, 63-66).

Working with GRKs: classical methods for purifying GRKs are not optimal.

The biochemical study of individual GRK subtypes is critical to understand and manipulate biased signaling, but these methods are still evolving. The interaction between GRKs and GPCRs is not well understood, partially due to the technical challenges of purifying fully functional kinase, and much work still needs to be done in order to glean structural information about this interaction. For example, in order to utilize site-directed labeling techniques to study full-length GRK1, mutagenic studies will need to first show that the mutation is well tolerated by the kinase. In this dissertation I describe my efforts to calibrate a fluorescence method for detecting interactions between proteins that utilizes site directed fluorescent labeling, but I was not able to use this method to study the GRK1:rhodopsin interaction. I was able to expand and calibrate one such method, however, which I introduce below.

Introduction to the TrIQ method.

Below I describe my contribution to a spectroscopic method that uses fluorescence to assess distances within and between proteins. This method, called Tryptophan Induced Quenching (TrIQ), uses a genetically encoded tryptophan residue paired with an

introduced cysteine residue that has been labeled with a fluorophore to approximate the distance between the tryptophan residue and the fluorophore based on the former's ability to quench the fluorescence of the latter. My work, described in Chapter 2 and Appendix 1 of this dissertation, expands the TriQ method by defining the ability to tyrosine to also quench the fluorescence of a fluorophore called bimane.

A brief introduction to fluorescence.

Fluorescence occurs after a molecule absorbs a photon of a certain energy (or wavelength) then emits a lower energy photon, at a different wavelength (Figure 1.12). Before, I discuss the results of fluorescence intensity, quantum yield, and fluorescence lifetime experiments, I will briefly introduce these concepts below.

The amount or intensity of the emitted fluorescence can be measured using a spectrophotometer, and by exciting at one wavelength and scanning the emission across many wavelengths, one can obtain fluorescence spectra that has wavelength on the x axis and fluorescence intensity as counts per second on the y-axis (Figure 1.13A). It is important to note that this intensity measurement is entirely relative, that is, it is dependent on the concentration of fluorophores in the sample as well as the brightness of the exciting light and numerous other mechanical aspects of the optical path. Thus, it is important to match the concentration of fluorophores in each sample in one's set of experiments as well as monitor the instruments parameters, be careful to maintain them during the course of your experiments, and create internal standards to enable comparisons between data sets.

One way to compare the fluorescence emission intensity between experiments is to calculate and compare the quantum yield of the fluorophores. This value, called ϕ , reflects the efficiency of the fluorophore, and is directly related to the number of photons emitted divided by the number of photons absorbed. As this is not trivial to determine, for ease, quantum yields are typically defined by comparison to a known standard for which the quantum yield is well established.

Fluorescence lifetime describes the average amount of time a fluorophore, after absorbing a photon, remains in the excited state before emitting a photon. In my work, I used a time-correlated single photon counting (TCSPC) instrument from PicoQuant that has maximal time resolution of ~ 28 picoseconds. Briefly, TCSPC works by repetitive short bursts of excitatory light. Electronics precisely measure the length of time between excitation and emission, in a process that can be thought of as analogous to a stopwatch. The instrument cycles through excitation and emission detection many times, and creates a histogram with the time to emission on the x-axis, and the number of photons counted on the y-axis (Figure 1.13B). After collection this fluorescence decay data is fit using software to determine the optimal decay curve, and thus the lifetime of the fluorophore.

Discovery of Tryptophan induced quenching of fluorescence.

Perturbations to the environment of a fluorophore can affect its fluorescence, a fact that makes fluorophores excellent reporters of structural changes in proteins. For example, the fluorescence of the fluorophore bimane, the main focus of Chapter 2, shifts significantly in different dielectric environments, as catalogued by a previous member of Dr. Farrens' lab, Dr. Steve Mansoor (67). In fact, it was in the course of an effort to use

bimane as a reporter of protein structure analogous to spin probes used for EPR (electron paramagnetic resonance) measurements that Dr. Mansoor and Dr. Farrens noticed that, while absorbance and fluorescence maximal wavelengths correlated with the local dielectric environment, drastic differences in quantum yield did not follow an obvious pattern. Their investigation into the underlying cause of this anomaly identified nearby tryptophans as potential culprits, a hypothesis that was tested and confirmed in subsequent manuscripts (68-70).

In the course of defining the quenching relationship between tryptophan residues and fluorophores conjugated to cysteine residues, those authors proposed that the quenching could be described in simple terms, discussed in detail in Chapter 2, and briefly below.

The first type of quenching, called “static quenching,” arises from a physical interaction between the tryptophan quenching residue and the fluorophore. Static quenching is indicated by a reduction of fluorescence emission intensity without a concomitant reduction in observed fluorescence lifetime. Importantly, the presence of static quenching indicates that the quencher and fluorophore are close enough to physically interact with each other at the moment of light absorption.

The other form of quenching, called “dynamic quenching,” arises from a photo-induced electron transfer event, and is thus distance dependent. For tryptophan, the range of dynamic quenching is $\sim 5\text{-}15$ Å between the $C\alpha$'s of the quencher and fluorophore positions, and the relative degree of dynamic quenching is higher at closer distances and lower at further distances. Dynamic quenching is indicated when there is an observed reduction in fluorescence emission intensity as well as a reduction in fluorescence lifetime.

Dissertation overview.

In this dissertation I present my efforts to further expand and characterize the TrIQ method to include the amino acid residue tyrosine as a distance-dependent quencher of bimane. This work was published in the journal *Biochemistry* in 2014 (71) and has been reformatted in Chapter 2, with the supplemental results and discussion from the publication presented in Appendix 1. Next I present our efforts to develop a method to purify and characterize full length and functional GRK1 in Chapter 3. Chapter 4 is the recently published manuscript detailing efforts to map the interaction between rhodopsin and GRK1 using biochemical and site directed fluorescence labeling approaches. Finally, Appendix 2 presents unpublished work with cysteine mutant GRK1 expression, purification, and analysis as well as initial attempts to crosslink rhodopsin and GRK1.

List of publications.

Sinha*, A., **Jones Brunette***, A. M., Schafer, C. T., Fay, J. F., Farrens, D. L. (2014). "Rhodopsin TM6 can interact with two separate and distinct sites on arrestin: evidence for structural plasticity and multiple docking modes in arrestin-rhodopsin binding." *Biochemistry* 53(20): 3294-3307.

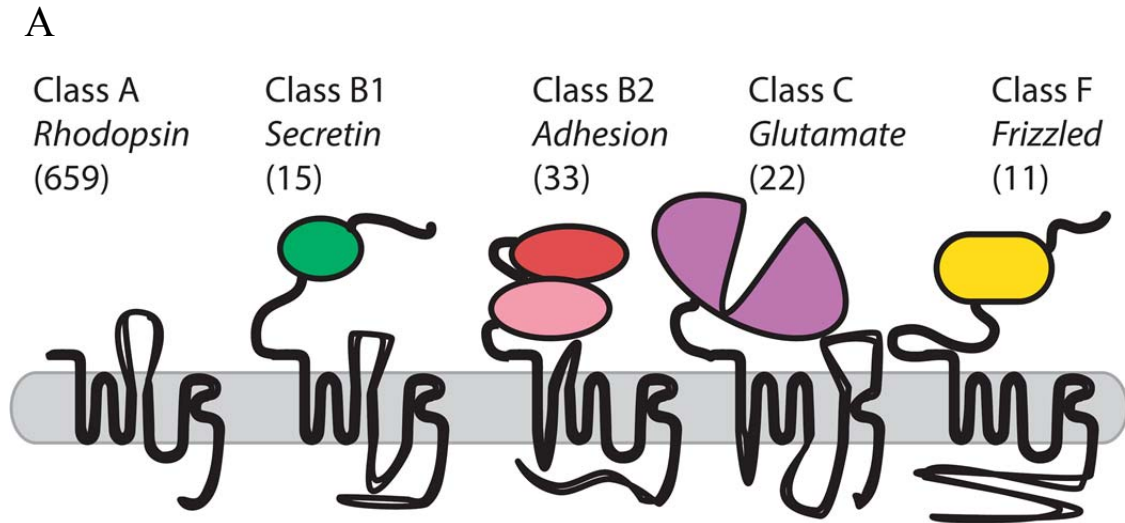
Jones Brunette, A. M. and Farrens, D. L. (2014). "Distance mapping in proteins using fluorescence spectroscopy: tyrosine, like tryptophan, quenches bimane fluorescence in a distance-dependent manner." *Biochemistry* 53(40): 6290-6301.

Jones Brunette, A. M., Sinha, A., David, L. L., Farrens, D. L. (2016). "Evidence that the Rhodopsin Kinase (GRK1) N-terminus and the Transducin α C-terminus interact with the Same "Hydrophobic Patch" on Rhodopsin TM5." *Biochemistry* *in press*.

Cambronne, X. A., Stewart, M. L., Kim, D., **Jones Brunette, A. M.**, Morgan, R. K., Farrens, D. L., Cohen, M. S., Goodman, R. H. (2016) NAD⁺ biosensor reveals multiple sources for mitochondrial NAD⁺. *Science* *in press*.

Figures.

Figure 1.1 Classes of GPCRs and canonical activation scheme.



B Agonist binding/activation

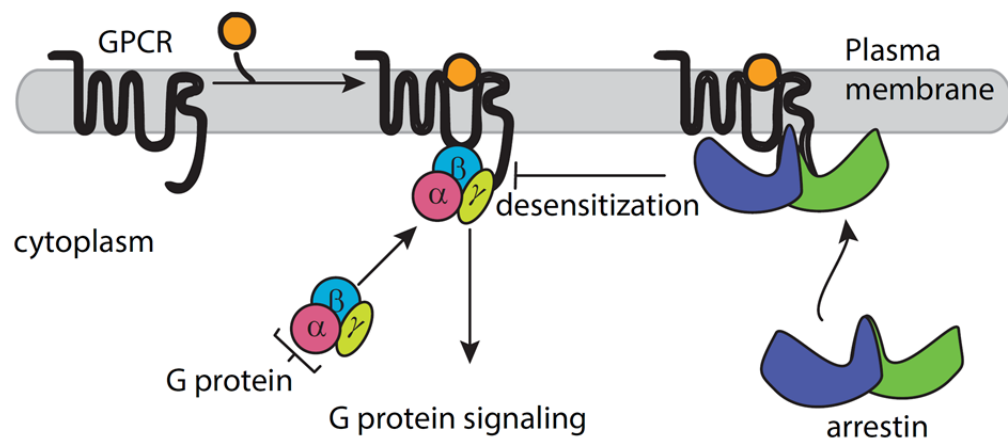


Figure 1.1 Classes of GPCRs and canonical activation scheme. (A) Class A GPCRs are by far the largest class, with 659 family members in humans. Class A GPCRs have relatively short N-termini and bind ligands such as odorants, chromophores, biological amines, lipids, purines, chemokines, and peptides. Class B1 GPCRs have 15 family members in humans, and contain an extracellular domain (depicted in green) that participates in binding peptide ligands. Class B2 GPCRs have 33 family members in humans, and contain both an adhesion domain and a GPCR autoproteolysis-inducing domain (depicted in pink and red). Class C GPCRs have 22 family members in humans and form functional dimers, such that each functional unit contains 2 Venus fly trap domains (depicted in purple), which bind ligands such as biological amines, glutamate, and calcium ions. Class F GPCRs have 11 family members in humans and contain an N-terminal cysteine-rich domain (depicted in yellow) that binds lipid-modified glycoprotein ligands for this class. Figure adapted from Tesmer 2016 Nature Reviews (72). (B) The shared, general, mode of GPCR activation starts when the GPCR binds to an agonist (represented as an orange circle). Once active, the GPCR can activate a heterotrimeric G protein $G\alpha$ subunit to release GDP and bind a GTP. GPCRs are desensitized by phosphorylation by a GPCR kinase and then bound by an arrestin molecule that mediates receptor recycling or degradation. Figure adapted from Ghosh et al 2015 Nature Reviews (73).

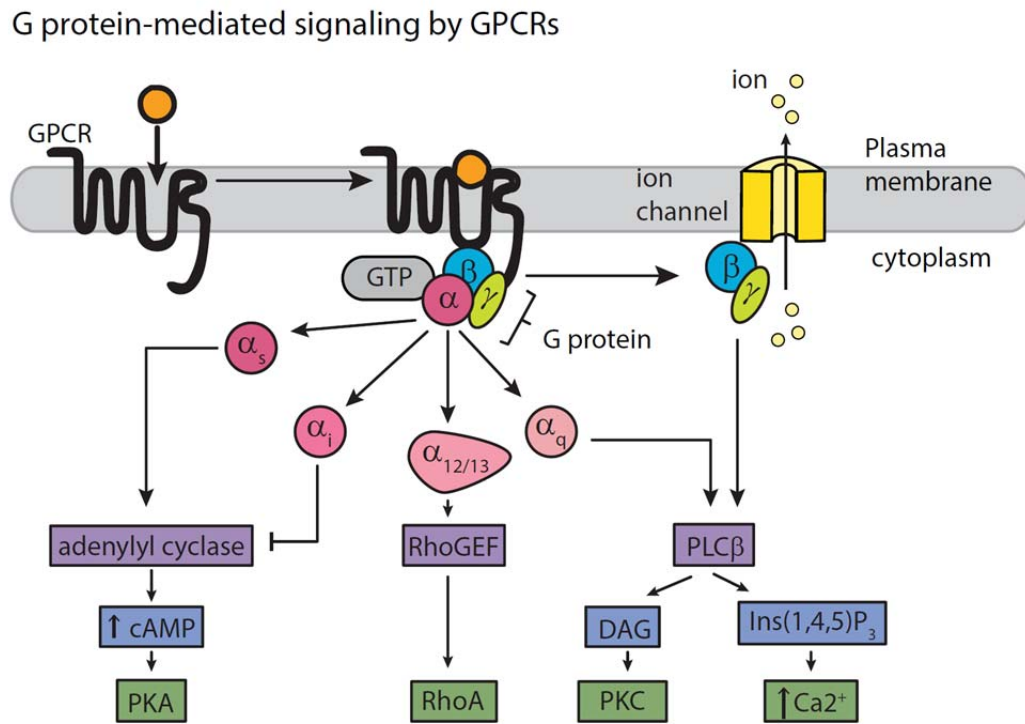
Figure 1.2 G protein-mediated signaling by GPCRs.

Figure 1.2 G protein-mediated signaling by GPCRs. When GPCRs activate a heterotrimeric G protein, the G_{α} subunit releases GDP and binds a GTP, and typically separates from the $G_{\beta\gamma}$ subunit. G_{α} subunits belong to different subfamilies based on what signaling pathway they initiate. The $G_{\alpha s}$ subfamily stimulates adenylyl cyclase to increase intracellular cyclic AMP (cAMP) levels, which activates protein kinase A (PKA). The $G_{\alpha i}$ subfamily inhibits this pathway, and the inhibitory $G_{\beta\gamma}$ subunit has been shown to interact directly with ion channels (74-76). The $G^{\alpha 12/13}$ subfamily stimulates a guanine nucleoside exchange factor that increases the activity of RhoA GTPases that go on to affect several cellular responses like cytoskeleton remodeling. Finally, the $G_{\alpha q}$ subfamily activates phospholipase C- β (PLC β) that cleaves phosphatidyl inositol lipids to release inositol (1,4,5) triphosphate (IP₃) and diacyl glycerol (DAG), which results in increased cellular Ca²⁺ and protein kinase C (PKC) activity. Figure adapted from Ritter and Hall 2009 Nature Reviews (77)

Figure 1.3 Arrestin-mediated GPCR signaling.

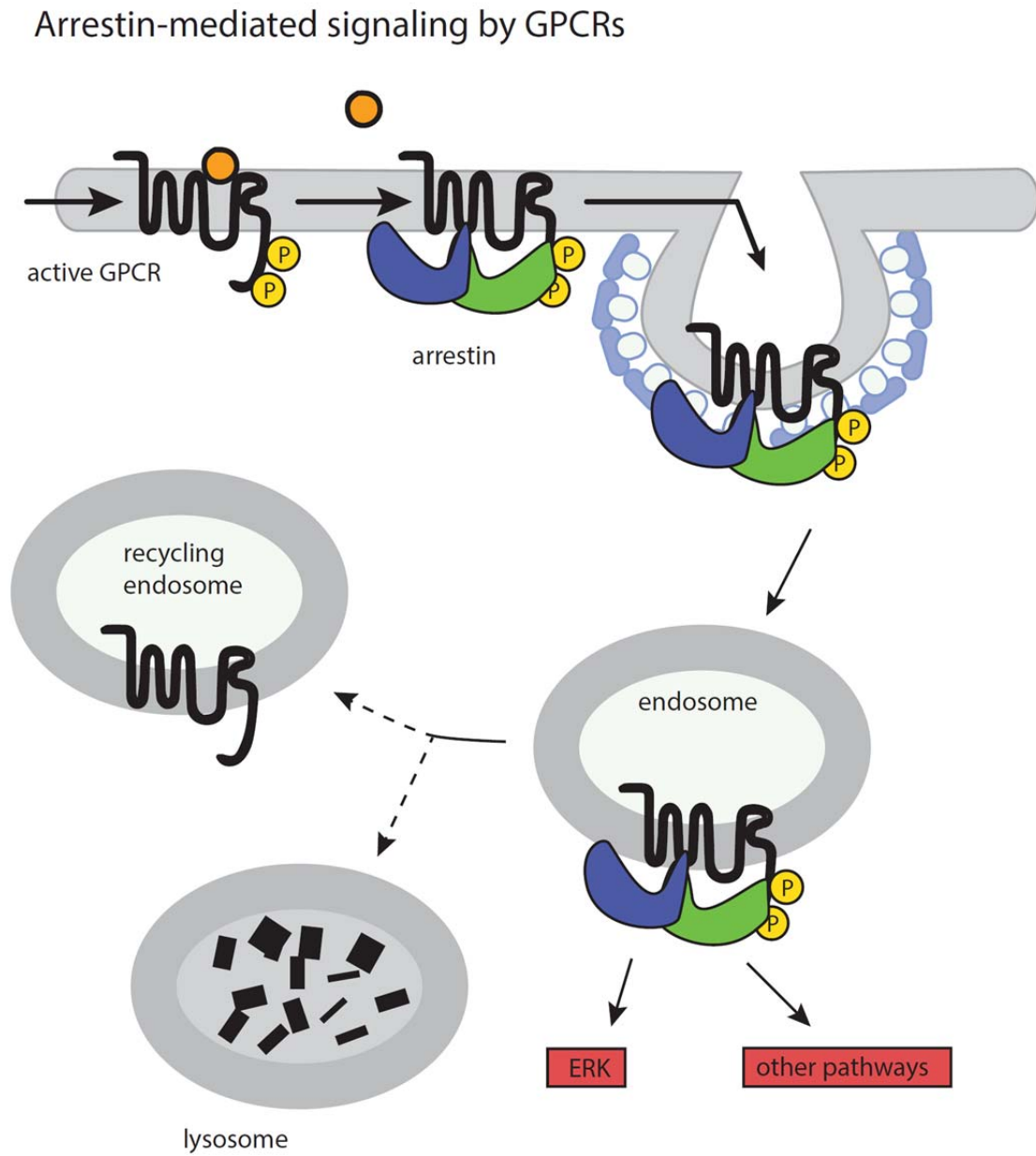


Figure 1.3 Arrestin-mediated GPCR signaling. Arrestin mediated signaling from GPCRs is initiated after a ligand-bound GPCR has been phosphorylated by various kinases, including GPCR kinases. Once bound by arrestin, the arrestin-GPCR complex can associate with clathrin coated structures using the clathrin and AP2 binding domains of the β arrestins. There is growing evidence that arrestin can activate ERK pathways from either the non-internalized clathrin coated structures at the membrane (11) and after internalization in to an endosome. From there, the arrestin dissociates and the unliganded GPCR can be recycled to the membrane surface or degraded. Figure adapted from Ritter and Hall 2009 Nature Reviews (77)

Figure 1.4 Comparison of arrestin family domain structure.

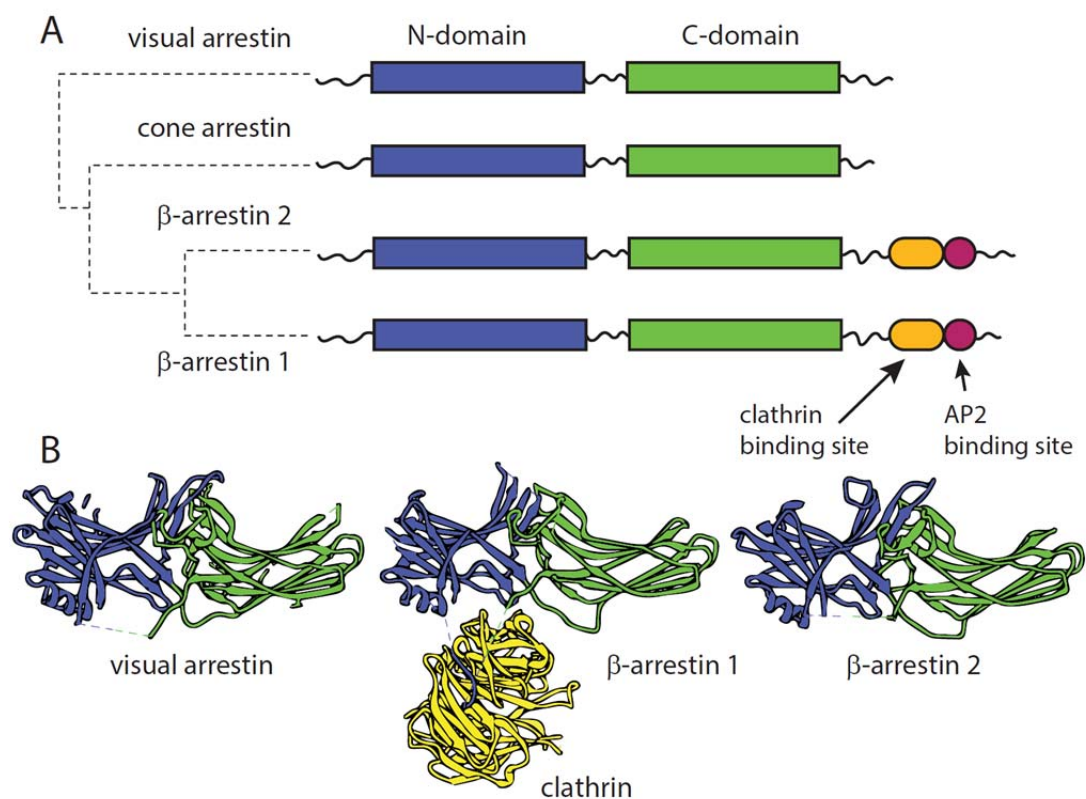


Figure 1.4 Comparison of arrestin family domain structure. (A) All of the visual/ β arrestin family members share similar domain structures, an N- and C-domain shown in blue and green, respectively. The two β arrestins contain additional domains at their C-terminus for binding clathrin and AP2, depicted in yellow and pink, respectively. (B) Crystal structures of visual arrestin (PDB:3UGX), β -arrestin 1 (co-crystallized with clathrin in yellow, PDB:3GC3), and β -arrestin 2 (PDB:3P2D) show the N-domain (blue) and C-domain (green) are comprised of primarily antiparallel β -sheets, with a conserved α -helix in the N-domain.

Figure 1.5 Architecture of rod cells, location of rhodopsin within the rod outer segment, and structure of rhodopsin.

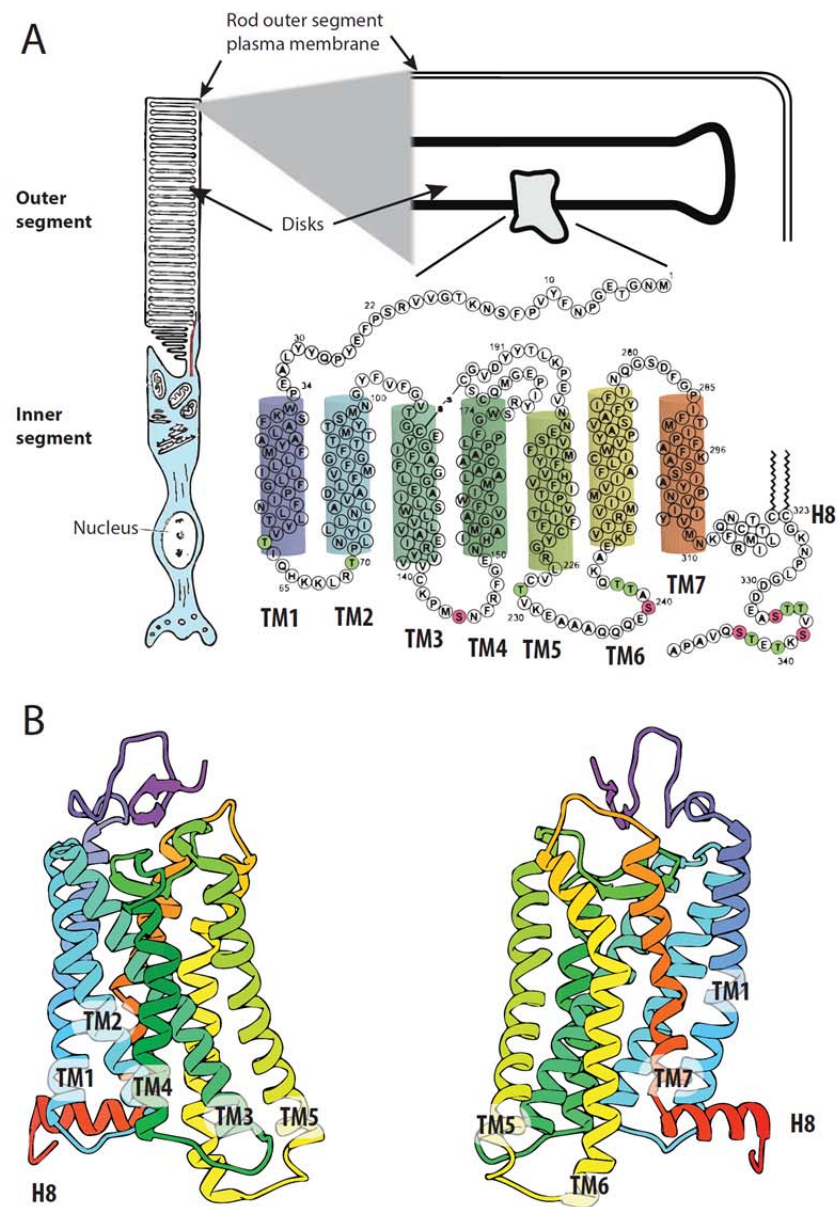
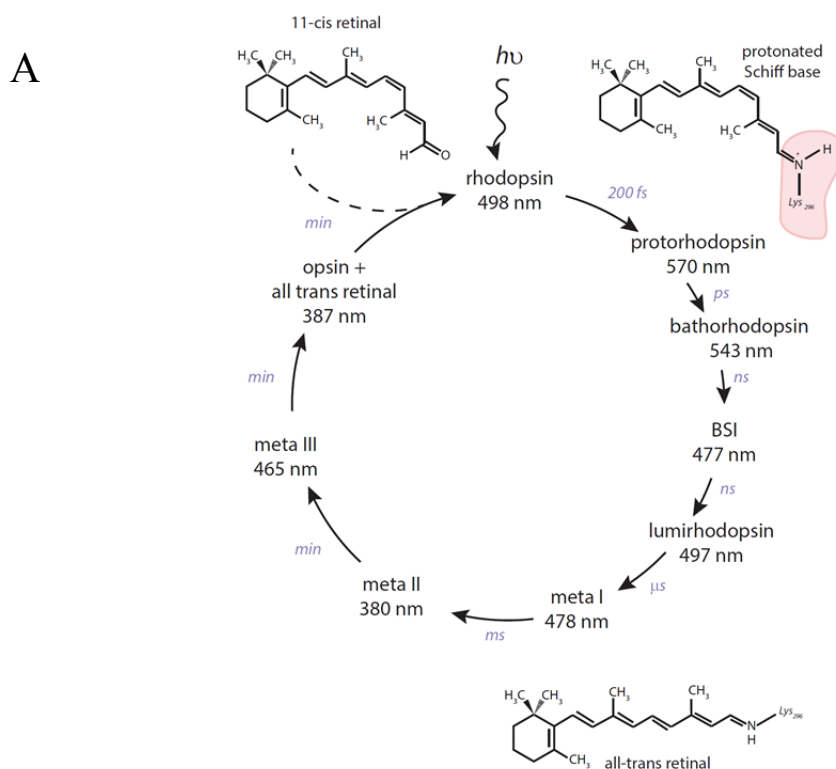


Figure 1.5 Architecture of rod cells, location of rhodopsin within the rod outer segment, and structure of rhodopsin. (A) Rhodopsin, the dim light visual pigment, is found in the rod cells of the retina, whereas the bright light sensors are found in cone cells. Rod cells are elongated, specialized cells in which visual pigment rhodopsin densely packed in the outer segment in stacked disks. The N-terminus is found in the intradiskal space and the C-terminus is on the intracellular side. The primary and secondary structures are displayed as an inset bubble diagram. Transmembrane (TM) helices 1-7 are indicated. Potential serine/threonine residues are highlighted in pink and green. Figure adapted from (78) and augmenting the structure of a rod cell openly available in the public domain on Wikipedia. (B) The crystal structure of rhodopsin (PDB:3C9L) (79) has been colorized to highlight the placement of the transmembrane helices (TMs1-7) as well as helix 8 (H8) that is associated with the membrane on the cytoplasmic side.

Figure 1.6 Rhodopsin activation involves isomerization of 11-cis retinal, leading to multiple transition states that have distinct spectroscopic states.



B

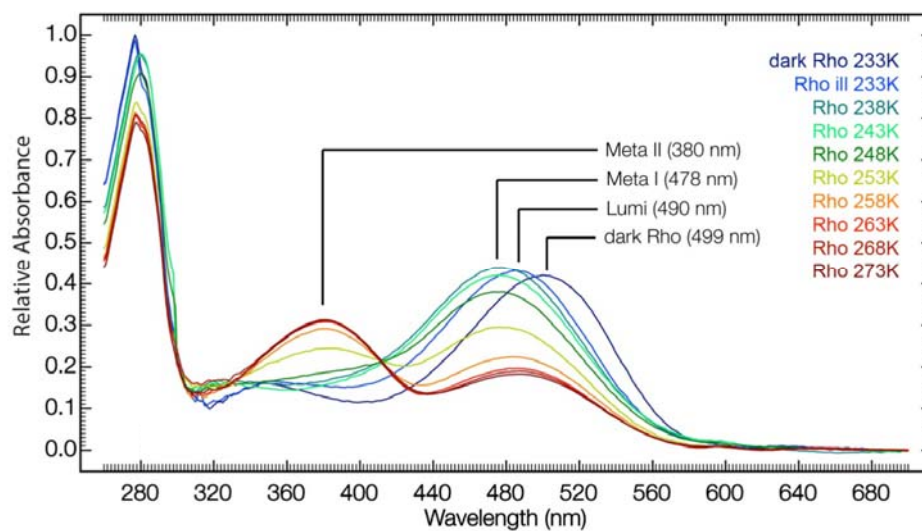


Figure 1.6 Rhodopsin activation involves isomerization of 11-cis retinal, leading to multiple transition states that have distinct spectroscopic states. (A) After absorption of a photon of an appropriate energy, the 11-cis retinal bound to rhodopsin via a protonated Schiff base undergoes rapid transitions through several “photo-intermediate” states. These early states are a result of the cis→trans isomerization of the retinal. The meta rhodopsin state MI is a result of a full isomerized, all trans retinal that is still bonded to the rhodopsin in a protonated Schiff base. Meta rhodopsin II (MII) is a result of a deprotonated Schiff base, and is also the form of active rhodopsin that is associated with G protein activation, phosphorylation by GRKs, and arrestin binding. The meta rhodopsin III (MIII) state reflects a cleaved Schiff base, but all trans retinal still in the binding pocket of rhodopsin, and the current understanding is that MIII is formed from MI, not MII. (B) UV-vis spectroscopy of rhodopsin activation states stabilized by cryogenic temperatures demonstrates the distinct differences in maximal absorbance for these photo-intermediate states. Figure taken from Sandberg et al (15).

Figure 1.7 Retinal release from the rhodopsin binding pocket can be measured using fluorescence.

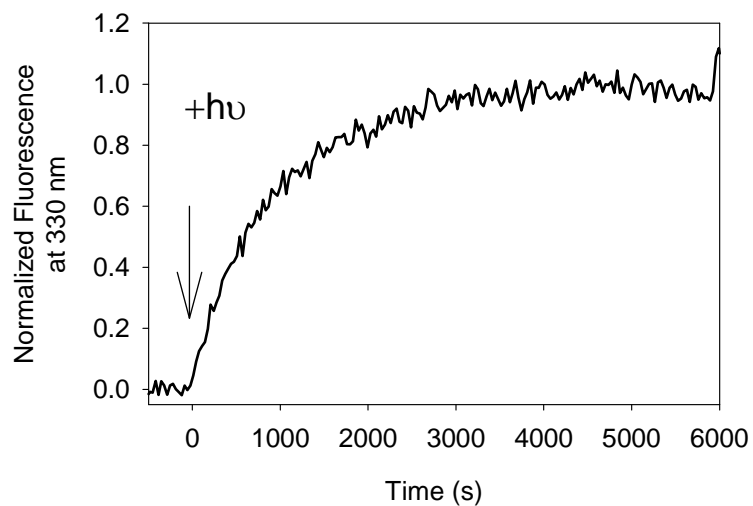


Figure 1.7 Retinal release from the rhodopsin binding pocket can be measured using fluorescence. Rhodopsin tryptophan residue fluorescence in the dark state is quenched by the bound 11-cis retinal. After light isomerization of 11-cis retinal and subsequent hydrolysis of the protonated Schiff base, the chromophore leaves rhodopsin and the quenching of tryptophan fluorescence is relieved. Thus, one can observe the rate of retinal release by monitoring an increase of fluorescence at 330 nm (21).

Figure 1.8 Insight in to GPCR activation from crystal structures of rhodopsin.

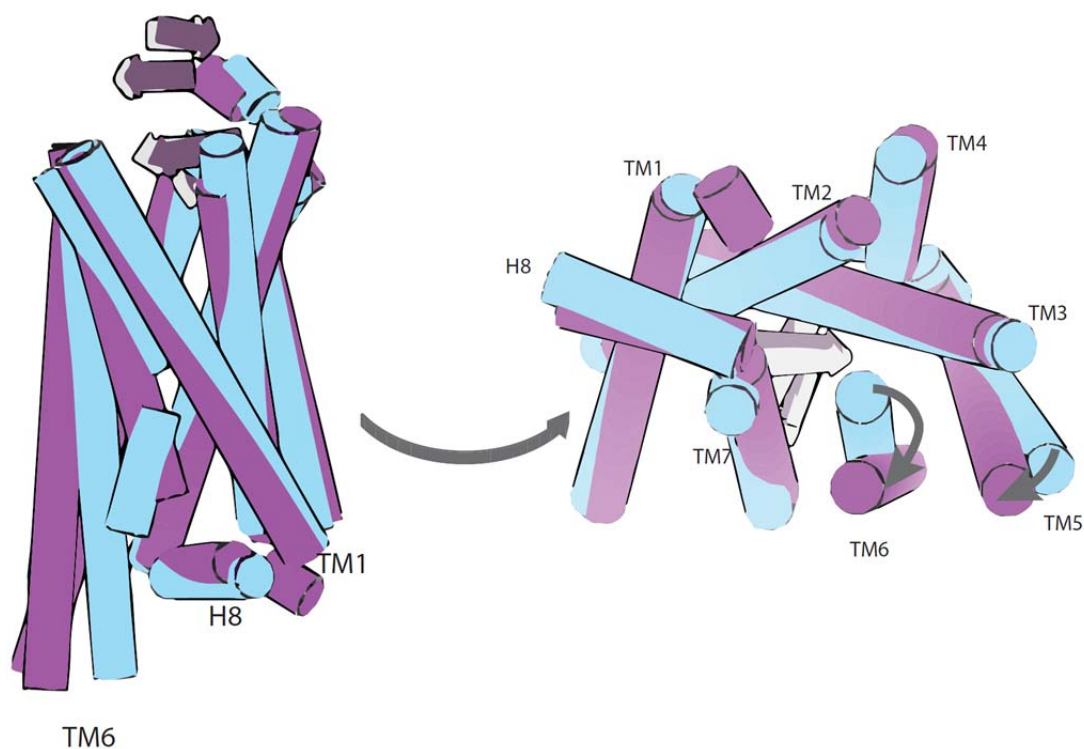


Figure 1.8 Insight in to GPCR activation from crystal structures of rhodopsin. Crystal structures of rhodopsin in different conformational states (inactive, blue 3C9L (79); purple, active 4X1H (80)) confirms that TM5&6 swing away from the helical bundle of rhodopsin upon light activation, as had been shown using biochemical and spectroscopic approaches (23).

Figure 1.9 Comparison of domain structure among G protein coupled receptor kinases.

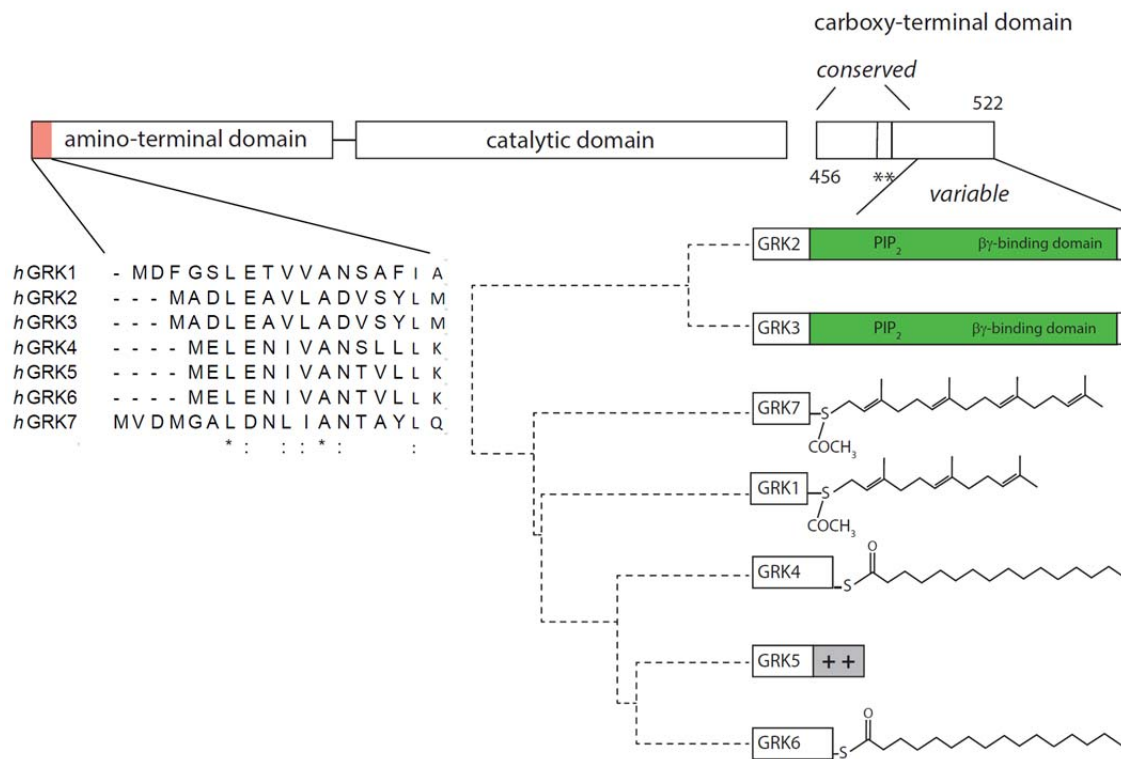


Figure 1.9 Comparison of domain structure among G protein coupled receptor kinases.

Figure adapted from (81, 82). Comparison of overall domain organization of the 7 GRK family members. An alignment of the sequences of all human GRKs, as well as bovine GRK1 is shown at the top, indicating the conservation of some residues, including some hydrophobic residues that have been implicated in receptor binding (83-87). The catalytic domains are fairly well conserved among the 7 GRKs. The C-terminal domain is comprised of a conserved domain and a variable domain. The conserved domain contains the primary sites of autophosphorylation for GRK1, GRK5, and GRK4. The variable domain is the site of farnesylation for GRK1, $G\beta\gamma$ and PIP2 binding domain in GRK2 and GRK3 (green), palmitoylation of GRK4 and GRK6, positively charged residues of GRK5 (grey), and geranylgeranylation of GRK7—all strategies for membrane association.

Figure 1.10 Sequence specificity for protein isoprenoid transferases.

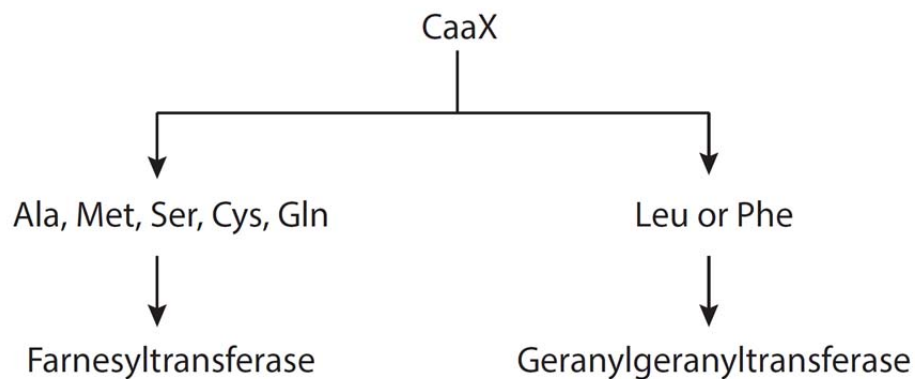


Figure 1.10 Sequence specificity for protein isoprenoid transferases. The signal sequence for isoprenylation is a C-terminal CaaX, where the “a” residues are aliphatic (40). The X residue defines which isoprenyltransferase acts to modify the protein (41, 42). When X is an A, M, S, C, or Q, the farnesyltransferase will add a farnesyl group. When X is a L or P, the geranylgeranyltransferase will add a geranylgeranyl group.

Figure 1.11 Crystal structures of GRKs 1/2/6 reveal conservation of kinase RGS-homology and catalytic domains.

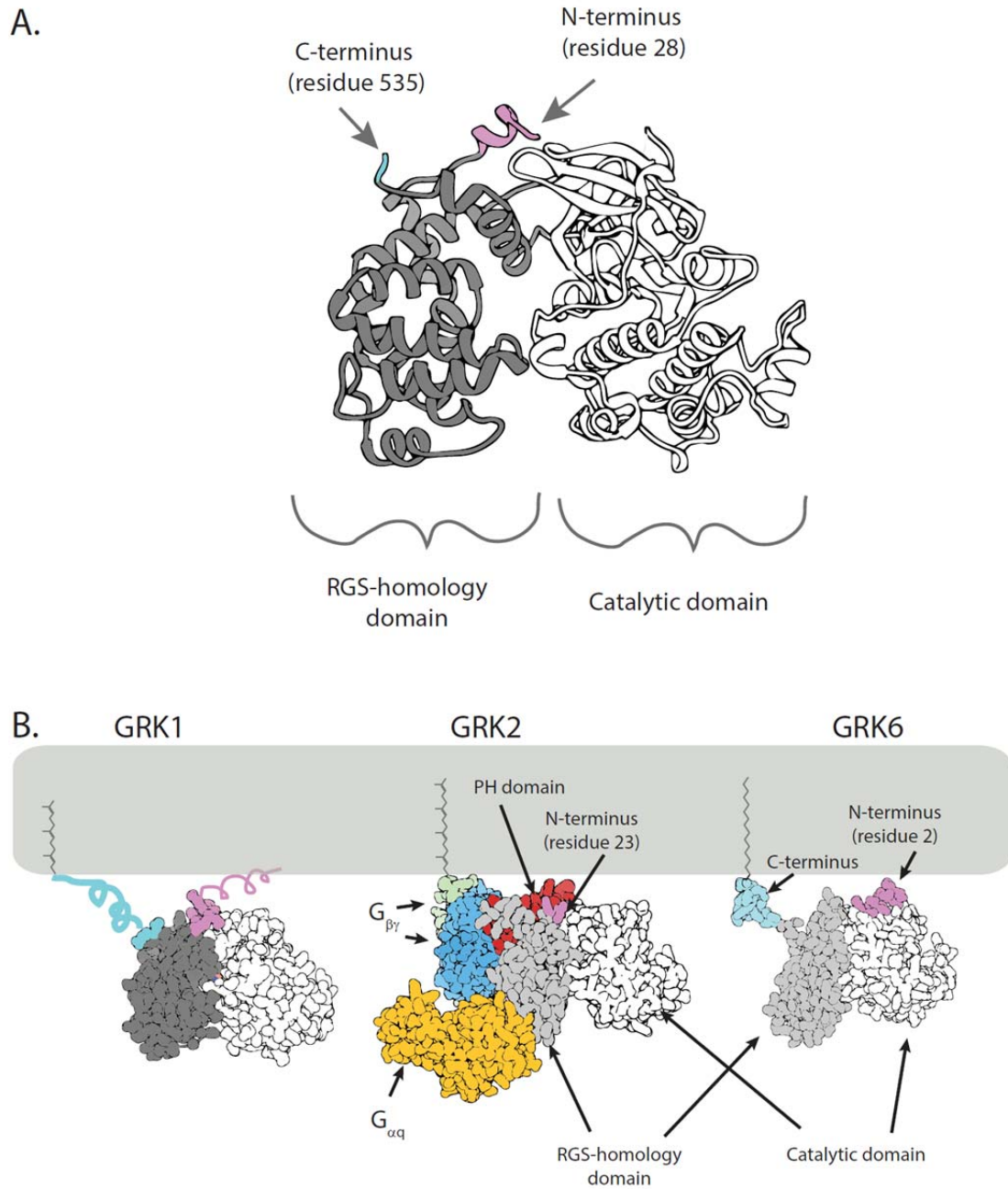


Figure 1.11 Crystal structures of GRKs 1/2/6 reveal conservation of kinase RGS-homology and catalytic domains. (A) Crystal structure of GRK1 (PDB:4PNI) (88), shows density starting at residue 28 of the N-terminus, and ends at residue 535 (full length GRK1 is 561 residues) due to the author's use of a shortened GRK1 mutant. The conserved regulator of G protein signaling (RGS) homology domain is shown in grey, and the catalytic domain is shown in white. (B) Comparison of the GRK1 crystal structure, shown with the side chains shown in spheres, with the N-terminus (purple) and C-terminus (teal) imagined as cartoon helices, including a farnesyl group on the C-terminus inserted in a membrane bilayer (grey). A crystal structure of GRK2 complexed with a $G\alpha_q$ enzyme (yellow) associated with the GRK2 RGS-homology domain (grey), as well as a $G\beta\gamma$ (blue and green) anchored to a membrane using the $G\gamma$ geranylgeranyl post translational modification. The GRK2 catalytic domain is shown in white and the pleckstrin homology (PH) domain is shown in red, which is positioned on the projected membrane-interacting plane (PDB:2BCJ) (89). The crystal structure of GRK6 shows similar structure to GRK1, but is the first crystal structure of a GRK with a resolved N- and C-terminus, shown in purple and teal, respectively. The precise location of the reversible post translational palmitoylation is hypothetical, and has been added and inserted in to a membrane (grey) by me (PDB:3NYN) (83).

Figure 1.12 The quantum mechanical process of fluorescence illustrated in a Jablonski diagram.

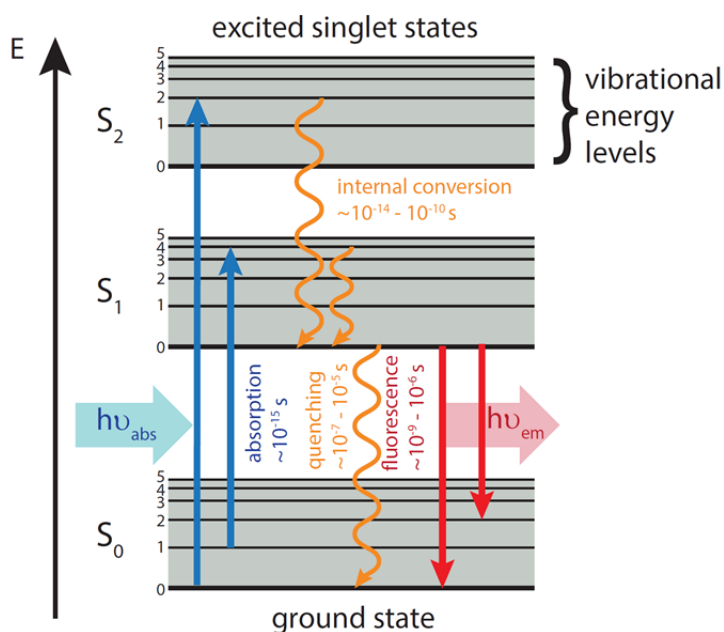


Figure 1.12 The quantum mechanical process of fluorescence illustrated in a Jablonski diagram. Fluorescence is a quantum mechanical process in which an electron in the ground state of a molecule absorbs a photon of light (blue solid arrow) with sufficient energy to excite the electron. Within the excited singlet states (S_1 , S_2) there are multiple vibrational energy levels, and the excited electron can relax within the vibrational states in a non-radiative manner (orange squiggly lines). From the excited state, light can relax in a non-radiative manner (labeled as quenching in orange squiggly line) or as light (red arrows) of defined wavelengths.

Figure 1.13 Examples of fluorescence emission spectra and TCSPC fluorescence decay data.

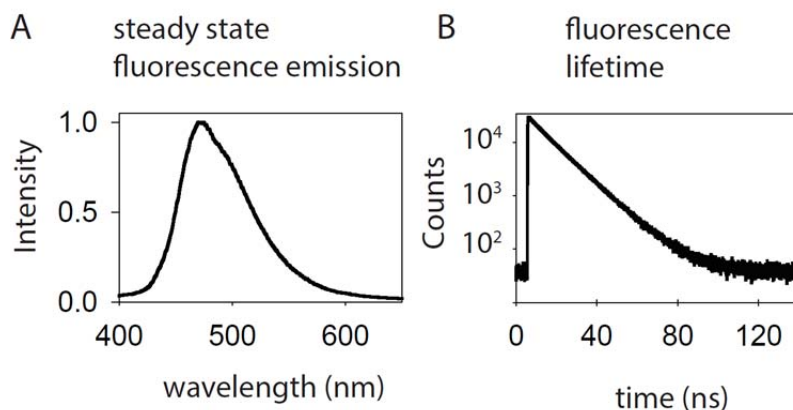


Figure 1.13 Examples of fluorescence emission spectra and TCSPC fluorescence decay data. (A) Steady state fluorescence emission is measured by exciting a fluorophore at a defined wavelength and monitoring the fluorescent emission, typically over a range of emission wavelengths as shown above. Importantly, the signal intensity is dependent on both the amount of fluorophore in the cuvette and a number of instrumental optical parameters. Thus, in order to compare fluorescence emission intensity, one should match fluorophore concentrations between samples and utilize an internal control to be able to compare intensities between experiments. (B) In this dissertation, fluorescence decay is measured using a time-correlated single photon counting lifetime instrument from PicoQuant. Sophisticated electronics measure the amount of time it takes for a fluorophore in the excited state to emit a photon, and after many rounds a histogram is produced with number of photons on the y-axis and time-to-emission on the x-axis. Lifetime of the fluorophore is calculated by fitting the decay to kinetic models using software called FluoFit.

Chapter 2: Distance Mapping in Proteins Using Fluorescence Spectroscopy: Tyrosine, like Tryptophan, Quenches Bimane Fluorescence in a Distance Dependent Manner.

The work presented in this chapter was well received by the reviewers for the ACS journal *Biochemistry* and accepted upon review in May 2014, and published in August of 2014. I, Amber M Jones Brunette performed all of the experiments and prepared the manuscript with the help and guidance of my mentor Dr. David L. Farrens. The publication contained a large supporting information file that contained additional figures pertaining to the main text as well as additional results and discussion. I have incorporated the supporting figures pertaining to the main text in this chapter, and retained the supporting results and discussion as appendix 1 of this dissertation.

Abstract.

Tryptophan-Induced Quenching of fluorophores, or TrIQ, uses intramolecular fluorescence quenching to assess distances in proteins too small (<15 Å) to be easily probed by traditional FRET methods. A powerful aspect of TrIQ is its ability to obtain an ultrafast snapshot of a protein conformation, by identifying “static quenching” (contact between the Trp and probe at the moment of light excitation). Here we report new advances to this site-directed fluorescence labeling (SDFL) approach, gleaned from recent studies of T4 lysozyme (T4L). First, we show that like TrIQ, Tyrosine induced

quenching (TyrIQ) occurs for the fluorophore bimane in a distance dependent fashion, although with some key differences: the Tyr “sphere of quenching” for bimane is smaller than for Trp ($\leq 10\text{\AA}$ vs. $\leq 15\text{\AA}$, C α -C α distance), and the size difference between quenching residue (Tyr) and control (Phe) differs by only a hydroxyl group. Second, we show how TrIQ and TyrIQ can be used together to assess the magnitude and energetics of a protein movement. In these studies, we placed a bimane (probe) and Trp or Tyr (quencher) on opposite ends of a “hinge” in T4L, and carried out TrIQ and TyrIQ measurements. Our results are consistent with a $\sim 5\text{\AA}$ change in C α -C α distances between these sites upon substrate binding, in agreement with the crystal structures. Subsequent Arrhenius analysis suggests the activation energy barrier (E_a) to this movement is relatively low (~ 1.5 - 2.5 kcal/mol). Together, these results demonstrate that TyrIQ, used together with TrIQ, significantly expands the power of and reach of distance-mapping SDFL studies.

Introduction.

Methods for studying protein dynamics still lag behind those for determining structure, although alternative methods, like site-directed fluorescence labeling (SDFL) are showing increasing promise and use (90-103). Our lab and others have been developing SDFL methods that exploit the small size and excellent spectral properties of the fluorophore bimane, with the goal of expanding the resolution and ability of SDFL methods to study protein structure and dynamics. One especially powerful method we have developed, called Tryptophan Induced Quenching (TrIQ), can map interactions

within and between proteins as well as assess protein movements in real time, by monitoring changes in the distance-dependent quenching of certain fluorophores caused by a nearby Trp residue (68-70, 104-112). TrIQ has some unique advantages that make it complementary to FRET – it only operates over relatively short distances ($<15 \text{ \AA}$), and does not require labeling a sample with two different fluorescent probes. TrIQ also does not require quantitative label incorporation, since the quencher—Trp—is always encoded in the protein (see Figure 2.1). Perhaps the most powerful aspect of TrIQ lies in its ability to identify and quantify “static quenching” (68-70, 113), a situation in which the fluorophore/Trp pairs are so close they are already touching when the photon is absorbed (see Figure 2.2). Such data provides a near-instant snapshot of a given protein conformation.

Here we set out to expand this SDFL approach by testing if the amino acid tyrosine (Tyr) can also be used as a quenching residue, and if it could, determine how the use of Tyr as a quencher could enhance protein studies. To do this, we calibrated the distance-dependent ability of Tyr to quench the fluorophores bimane and BODIPY 507/545 while attached to T4 Lysozyme (T4L). This work was spurred by previous observations from Kosower (and subsequently our lab) that free tyrosine methylester can quench bimane fluorescence in solution (68, 107, 114) as well as our growing realization that the increasing use of bimane derivatives in SDFL studies (68-70, 104-112, 115-118) requires that the effect of Tyr on bimane be fully defined to enable proper interpretation of SDFL data.

As discussed below, our results show Tyr-induced quenching (TyrIQ) has intriguing similarities, as well as clear differences with Trp-induced quenching (TrIQ). We also

show how these differences could be exploited to study the magnitude and energetics underlying a “hinge bending” movement in T4L that occurs upon substrate binding (119, 120). Together, our data highlight unique aspects of using Tyr as a quencher, and demonstrate how a combined use of TrIQ and TyrIQ in parallel significantly enhances the resolution and ability of these SDFL methods to study protein dynamics and energetics.

Materials & Methods.

Materials.

Chemicals and buffer components were purchased from Fischer, except monobromobimane, which was purchased from Molecular Probes.

Buffers.

Buffer A 50 mM MOPS, 50 mM Tris, and 1mM EDTA, pH 7.6. *Cell-pellet Wash Buffer* 50 mM Tris-PO₄ pH 7.2, 50 mM Sodium Acetate. *Lysis Buffer* 50 mM Tris-PO₄ pH 7.2. 50 mM Na Acetate, 5 mM β-mercaptoethanol, 0.1 mM PMSF, 1X Complete Protease Inhibitor tablet. *Binding/Wash Buffer* 100 mM Sodium Phosphate, pH 7.2. *Elution Buffer* 100 mM Sodium Phosphate, 100 mM Sodium Fluoride, pH 7.2. *Regeneration Buffer* 100 mM Phosphoric Acid. *Storage Buffer* 100 mM Sodium Phosphate pH 7.2, 0.02% Sodium Azide.

Construction, expression, and purification of T4 lysozyme mutants.

T4Lysozyme was cloned into the pG58 vector (121), and overlap-extension PCR was used to introduce point mutations into the protein. All mutant sequences were confirmed

by DNA sequencing. Hereafter, mutants are referred to by first naming the native amino acid residue, then the residue number followed by the new residue, respectively. For example, a mutant called N116F has a phenylalanine residue replacing the asparagine residue at position 116.

Mutant T4 Lysozyme was expressed in BL21 (DE3) cells, using fresh transformants. BL21 (DE3) cultures were grown to $OD_{595} = 0.9$ at 18°C with shaking. Expression was induced by IPTG at a final concentration of 1 mM, and the culture incubated at 37°C for 2 hours with shaking, then harvested by centrifugation, washed with cell-pellet wash buffer and re-pelleted in order to remove as much chloride from the cell pellet as possible. Pellets were then stored at -20° C for up to two weeks, until use.

Purification and fluorescent labeling of proteins.

Typically, the cell pellets for six different mutants were prepared simultaneously. Cell pellets were resuspended in Lysis buffer and lysed using a Fisher French Pressure cell. For the T4L T26E active site mutants, wild type T4L lacking the Profinity tag (from Sigma Aldrich) was added to the bacterial homogenate to help hydrolyze the peptidoglycan, since the active-site mutant T4L covalently binds their substrate and does not turn over. Major cell debris was removed by centrifugation at 14 krpm for 45 minutes in a Beckman JA20 rotor. The supernatant was decanted and passed through a 0.8 µm filter to remove insoluble lysate and then loaded on an equilibrated Profinity eXact resin (which will only bind the tagged lysozyme mutants), and washed with at least 15 column volumes of binding/wash buffer, in a gravity flow apparatus.

Fluorescent labeling of the T4L samples was done while the proteins were bound to the purification column. First, the resin-bound T4L was incubated with an estimated 5X

molar excess monobromobimane label in binding/wash buffer or 5X excess BODIPY 507/545 iodoacetamide in binding/wash buffer containing 10% DMSO for two hours at room temperature with nutation. Subsequently, the labeling buffer was drained, and the column washed with 15 column volumes of binding/wash buffer for bimane labeled samples, when labeling with BODIPY 507/545 the first 5 column volumes of wash also contained 10% DMSO in order to remove unreacted label. Fluorescently-labeled T4L was eluted by incubating the column in elution buffer over night at room temperature with nutation. Eluate was concentrated and buffer exchanged with Buffer A with an Amicon Ultra centrifugal filter (0.5 mL, 10 kDa), for a final exchange-dilution of >1/3000, which also removed free-fluorescent label (to <1%) and allowed for buffer exchange from Elution buffer to Buffer A.

Hydrolysis of peptidoglycan bound to the active site of the T4L T26E mutants.

The peptidoglycan bound to the active site of the T4L T26E mutants was acid-hydrolyzed essentially as described by *Kuroki et al.* when first describing this mutation (119). Samples were buffer exchanged with an Amicon Ultra centrifugal filter (0.5 mL, 10 kDa) to a buffer containing 50 mM NaH₂PO₄, 50 mM Na Acetate pH 3 and incubated for an hour at 37°C. The samples were then returned to Buffer A, also using Amicon Ultra centrifugal filters.

Fluorescence intensity measurements.

To enable direct comparison of the data, sample concentrations were adjusted by dilution so they had matching fluorophore maximum absorbance for bimane (typically

$A_{bs} = 0.05$, and absorbance maxima ranged from 386-397 nm depending on bimane location), and for BODIPY 507/545 at 507 nm. Fluorescence intensity measurements were carried out using a PTI Quanta Master fluorometer (PTI, New Jersey). Bimane excitation was at 380 nm (1 nm slits), while emission was scanned from 400 nm to 650 nm (8 nm slits using a 0.2-second integration time per 1 nm step size). Total bimane fluorescence was obtained by integrating the fluorescence from 400 nm to 650 nm for each bimane-labeled sample. BODIPY 507/545 excitation was at 480 nm (1 nm slits), while emission was scanned from 500 nm to 700 nm (3 nm slits using a 0.2-second integration time per 1 nm step size). Total BODIPY 507/545 fluorescence was obtained by integrating the fluorescence from 500 nm to 700 nm for each BODIPY 507/545-labeled sample.

Quantum yield measurements.

The quantum yield of bimane was calculated by comparing its absorbance and fluorescent intensity at 360 nm to that of Quinine Sulfate, a common fluorescent standard that has a quantum yield of 0.54 in 1N H_2SO_4 , using the equation below.

$$\Phi_{\text{sample}} = \Phi_{\text{std}} * \frac{F_{\text{sample}}}{F_{\text{std}}} * \frac{Abs_{\text{std}}}{Abs_{\text{sample}}}$$

Quantum yields were calculated for T4L N116/N132B, N116F/N132B, N116Y/N132B, and N116W/N132B in order to test the merits of using Phe as the non-quenching control residue instead of the native residue, as previously used.

Fluorescence lifetime measurements.

Fluorescence lifetime measurements were made using a PicoQuant FluoTime 200 time correlated single photon counting instrument (PicoQuant, Berlin), outfitted with a

Hamamatsu micro-channel plate detector, using polarizers at magic angle and 1.0 nm emission slits. Excitation was achieved using a pulsed diode laser of 405 nm, which yielded an Instrument Response Function (IRF) of 64-128 ps (FWHM) measured using a Ludox solution. Emission from the samples was collected using a stack of two 470 nm long-pass filter on the detector side of the sample holder using the same slits, same polarization. The fluorescence decay curves were fitted with PicoQuant software using an exponential decay model [$I(t) = \sum_{i=1}^n A_i e^{-t/\tau_i}$], where A_i is the amplitude of the i^{th} components, in counts, in the first range fitting channel and τ_i is the lifetime of the i^{th} component]. The quality of each fit was assessed by considering the χ^2 value, the residuals, and the autocorrelation function. In some cases fits with higher χ^2 were chosen because the residuals and autocorrelation functions were more randomly distributed and had lower values.

The amplitude-weighted lifetime ($\langle \tau \rangle$) measurements resulting from the best fit were used in calculations as discussed below. The lifetime decay data were also fit with a Lorentzian distribution model [$I(t) = \int_{-\infty}^t IRF(t') \int_{-\infty}^{\infty} \rho(\tau) e^{-\frac{t-t'}{\tau}} d\tau dt'$ $\rho(\tau) = \sum_{i=1}^n \frac{A_i}{\pi} \frac{\frac{\Delta_{FWHM} i}{2}}{(\tau - \tau_i)^2 + (\frac{\Delta_{FWHM} i}{2})^2}$], where A_i is the amplitude of the i^{th} distribution components, in counts, in the first range fitting model, τ_i is the center lifetime of the i^{th} distributed component, and $\Delta_{FWHM} i$ is the distribution width (full width at half maximum) of the i^{th} distributed component]. The results and discussion for the distribution fitting can be found in the Supporting Information.

Calculation of the fraction of fluorophore in a static complex with quencher.

The fluorescence contribution of each quencher-fluorophore pair was calculated as described previously (68-70). Briefly, using this analysis, the relative fraction of quencher and fluorophore in an open, non-static conformation, called γ , is calculated by $\gamma = \frac{F}{F_0} \cdot \frac{\tau_0}{\tau}$, where F is the fluorescence intensity and τ is the lifetime, the subscript O refers to the Phe-containing unquenched measurement and the subscript Q refers to the Trp or Tyr-containing quenched sample. It is also possible to further separate γ into the contribution by dynamic quenching, $\gamma_{DQ} = \left(1 - \frac{\tau}{\tau_0}\right)\gamma$, and the contribution from unquenched fluorescence, $\gamma_0 = \frac{\tau}{\tau_0} \cdot \gamma$. The relative fraction of quencher-fluorophore pairs in a static (non-fluorescent) complex at the moments of light excitation is then simply determined as $1 - \gamma$.

Analysis of the pH-dependence of the TrIQ and TyrIQ effects.

The purified and labeled T4L mutants N116F/N132B, N116Y/N132B, and N116W/N132B were buffer exchanged into a 50 mM Na PO₄, 50 mM Na Acetate buffer at each pH 3, pH 7.5, and pH 10. The fluorescence intensity and lifetime decay were measured, as described above, for each of the mutants at each of the 3 pH conditions at 20°C. The fraction of the fluorophore in static complex with the quencher was calculated for each pH condition as described above.

Arrhenius analysis of hinge-bending and temperature dependence of the TrIQ and TyrIQ effects.

The fluorescence intensity and lifetime decay were measured as described above but with the F4/K60B, F4Y/K60B, and F4W/K60B mutants at 10, 15, 20, 25, and 30°C in order to evaluate the temperature dependence of the TrIQ effect and were used for Arrhenius analysis.

The same measurements were also carried out on mutants containing the T26E active site mutation, which traps the substrate by making a non-catalytically relevant covalent bond between the T4L to the peptidoglycan. For these studies, the bound substrate was hydrolyzed prior to measurements described above, lifetime decays were fit with an exponential decay, and the amplitude-weighted average lifetime ($\langle \tau \rangle$) from the best fits were used to calculate the dynamic quenching rate $k_q = \left(\frac{1}{\tau} - \frac{1}{\tau_0}\right)$. The natural log of k_q was plotted on the y-axis against the reciprocal of the sample temperature in Kelvin on the x-axis. The slope of the resulting line is taken to be the activation energy divided by the gas constant, $-\frac{E_a}{R}$, from the Arrhenius equation.

The average lifetime $\langle \tau \rangle$ was used for simplicity in the dynamic quenching rate calculations because multiple apparent lifetimes are detected in the TrIQ and TyrIQ data, especially ultrashort lifetimes in samples with extensive quenching (see Supporting Table 1). We attribute the latter very fast quenching events to quenchers that are next to, but not touching, the fluorophore at the moment of light excitation. Such phenomenon are not due to multiple distinct probe environments, but rather occur because the limited diffusional volume space for the fluorophore and quencher (due to their being covalently attached to the protein) results in a very high apparent quencher concentration (see discussion in chapter 9.6 of Lakowicz (122)).

Results.

Our goal was to determine if the amino acid Tyr, like Trp, could be used as an internal quenching molecule in SDFL studies for mapping proximity in proteins. To do this, we compared the extent of Trp-induced quenching (TrIQ) and Tyr-induced quenching (TyrIQ) on the emission from the fluorophores bimane and BODIPY 507/545 (Fig 2.1), while these probes were attached to the sites on the protein T4L indicated in Figure 1B. These sites provided varying probe-to-quencher distances, ranging from ~ 7 to 11 \AA ($C\alpha$ - $C\alpha$ distances). The data from these studies could be analyzed to determine the relative fraction of fluorescence present in each sample (non-quenched, dynamically quenched, and statically quenched, as described in Figure 2.2). The results are discussed below.

Phenylalanine is a structurally similar control residue for TyrIQ and TrIQ studies that shows minimal bimane quenching.

We tested if Phe, a structurally similar residue to Tyr and Trp, could act as a better “control” (non-quenching residue) for TyrIQ and TrIQ studies, rather than our previous approaches that simply used whatever native residue was at the site under investigation. To do this, we studied T4L mutants containing a Phe, Tyr, Trp or Asn (the native residue) at position 116, and a bimane fluorophore at position 132. The 116/132 sites shows the largest amount of Trp quenching, and represents the closest quencher-fluorophore pair in the present study ($C\alpha$ - $C\alpha$ distance = 7.5 \AA). The results of absorbance and fluorescence measurements on these samples are reported in Table 2.3 and Figure 2.3. As can be seen in Fig 2.3, the bimane absorbance maximum is red-shifted for the Phe, Tyr and Trp samples compared to the sample containing the native Asn residue ($\sim 386 \text{ nm}$ for the

N116/132B sample compared to ~397 nm for the others). Such a shift in absorbance indicates a ground-state complex formation (contact) between the residue and bimane fluorophore, as we have noted and discussed previously (67-70).

However, even with this contact, bimane quenching by Phe is minimal, as indicated in the comparison of intensity quenching ratios, calculated using N116/N132B as the unquenched control, 1.3 for the Phe containing sample (N116F/N132B) versus ~14.0 for the Tyr containing sample (N116Y/N132B) and ~27.0 for the Trp containing sample (N116W/N132B). These values, along with the measured quantum yields, and relative changes in fluorescence lifetimes are reported in Table 2.3. Together, these studies demonstrate Phe is an excellent control residue for TyrIQ and TrpIQ studies, due to its structural similarity for both Tyr and Trp, and because it causes limited quenching even when physically in contact with bimane.

Tyrosine can quench the fluorescence intensity of bimane in a distance-dependent fashion, but does so over a shorter range than Tryptophan.

We measured the ability of both Tyr and Trp to quench bimane in our present studies in parallel, both for comparison purposes, and to test the efficacy of our new streamlined purification and fluorescence labeling strategy for T4L, shown in scheme presented in Figure 2.1. As expected, the results re-confirm our previous findings that Trp quenches bimane in a distance-dependent manner (Figure 2.4, top). The data show Tyrosine also quenches the emission intensity of bimane, but does so less efficiently and over a shorter range of distance (Figure 2.4). For example, whereas Tryptophan quenching of bimane is

seen to extend to the 11.0 Å C α -C α distance, Tyrosine exhibits essentially no quenching for C α -C α separations greater than 10 Å.

Unlike Tryptophan, Tyrosine does not show substantial quenching of BODIPY 507/545 fluorescence.

We previously established that Trp can also efficiently quench the fluorescence of the probe BODIPY 507/545 in a distance-dependent way (68). Interestingly, we find here that Tyr does not show substantial quenching of BODIPY 507/545 fluorescence (Figure 2.4, bottom, Figure 2.7). Since these samples exhibited no dramatic fluorescence intensity quenching they were not studied further.

The degree of intensity quenching does not always match the degree of lifetime quenching for both quenchers, Trp and Tyr.

Figure 2.6 shows how the ratio of the Trp and Tyr induced quenching of bimane ($\frac{F_0}{F}$) measured in Figure 2.4 decreases as a function of C α -C α distance. The quenching mechanism occurring in these samples was further investigated by measuring their fluorescence lifetimes (rates of fluorescence decay after excitation) using a PicoQuant FluoTime 200 time-correlated single photon counting instrument with a ~ 50 ps time resolution. Representative fits of the decay data can be found in Figure 2.5. The amplitude-weighted average lifetime $\langle \tau \rangle$ from the exponential fits of this decay data were used to calculate the lifetime quenching ratio, ($\frac{\langle \tau_0 \rangle}{\langle \tau \rangle}$), as shown in Figure 2.6B.

For the unquenched bimane-labeled samples (Phe residue at the “quenching” position) the $\langle \tau \rangle$ values ranged from 7.9 to 13.4 ns (Table 2.1), depending on the environment

of the probe (123), similar to previous reports (67-70). For the Trp containing T4L mutants, the $\langle \tau \rangle$ lifetime was observed to decrease for all of the Trp-Bimane distances (7.5, 8.4, 10.1, 10.7, and 11.0 Å), with the most dramatic changes in lifetime occurring at the shorter distances. In contrast, the Tyr containing T4L samples showed a dramatic decrease in lifetime for the 8.4 Å Tyr-Bimane distances and the closest and intermediate distances (7.5, and 10.1 Å), and no decrease in the longest distances (10.7 and 11.0 Å) compared to the unquenched (Phe) samples. A similar pattern is observed when the decay data is fit using a lifetime distribution model, as discussed in Appendix 1 of this dissertation.

Differences in the ratio of the fluorescence intensity and lifetime quenching indicate static quenching complexes form in some of the Trp- and Tyr-quenched samples.

We next used the combination of intensity and lifetime quenching ratios to calculate the relative amount of static quenching, dynamic quenching, and unquenched fluorescence components (Figure 2.6C). This analysis shows that Trp can statically quench bimane for the 7.5, 8.4, and 10.1 Å C α -C α distances, whereas the quenching observed at the 10.7 and 11 Å distances is primarily dynamic in nature. These Trp quenching values for bimane show the same range of distances as our previously reported results but a higher quenching ratio. We surmise this difference in quenching ratio is due to our improved purification and labeling method (which resulted in lower amounts of free bimane and presumably less misfolded protein).

In contrast to the Trp samples, the Tyr-containing samples only showed a large amount of static quenching at the shortest distance (7.5 Å), with much lower static quenching at the 8.4 Å sample. The longer C α -C α distance separations show no static quenching for Tyr.

Assessment of pH and temperature on the efficiency of quenching for both Trp and Tyr.

We next tested the effect of pH and temperature on both the fluorescence intensity and lifetime decay using the N116X/N132B series of T4L mutants, where X=F, W, or Y. For both Tyr & Trp containing samples, both the intensity ($\frac{F_O}{F}$) as well as the lifetime ($\frac{\langle\tau_O\rangle}{\langle\tau\rangle}$) quenching ratios were measured, where an O-subscript indicates data from the unquenched, Phe containing sample.

The data show a relatively small pH-dependency for both quenchers (Figure 2.8A). When Trp is the quenching residue, the intensity quenching ratio slightly increases with increasing pH, ~14% per pH unit, while the lifetime quenching ratio is constant at the pH values tested. The intensity-quenching ratio when Tyr is the quenching ratio also follows the pattern of increasing with pH, although to a lesser extent than Trp, ~7% per pH unit. Interestingly, the lifetime quenching ratio of Tyr does not follow a pattern, as the ratio (or decrease in lifetime of the quenched probe relative to the unquenched probe at the same pH) is higher at pH 3 and pH 10 than the pH 7.5 sample. When these quenching ratios are used to calculate the relative presence of static and dynamic quenching, Trp shows a constant relative amount of each component of fluorescence (Figure 2.8), but the relative

contributions of static and dynamic quenching when Tyr is the quencher vary only slightly across the pHs tested (Figure 2.8A).

We also assessed the temperature dependence of TrIQ and TyrIQ for bimane-labeled samples, using a temperature range of 30, 25, 20, 15, and 10°C. The resulting quenching ratios ($\frac{F_0}{F}$) as well as the lifetime quenching ratios ($\frac{\langle\tau_0\rangle}{\langle\tau\rangle}$) are shown in Figure 2.8B, both ratios show a slight increase with temperature for both Trp and Tyr (~1-2% per degree). The relative components of fluorescence, however, show consistent ratios of static and dynamic quenching across all of the temperatures measured for both quenchers (Figure 2.8B).

Both TrIQ and TyrIQ can detect a hinge-bending movement in T4L that accompanies substrate binding.

We next tested the ability of TrIQ to measure dynamic structural changes in T4L, specifically, a hinge-bending motion that occurs in T4L upon substrate binding (124, 125). These studies placed a probe and quencher on opposite sides of this “hinge,” with the probe at K60B and the quencher at site F4X, where X is a Trp, Tyr or a Phe residue to act as the unquenched control. In the substrate-free state, the quencher and probe C α -C α distances are closer (~10.5Å apart) and move farther apart (~14.5Å) when T4L binds substrate (Figure 2.10A). Thus, one would expect more quenching in the apo state and less quenching upon substrate binding.

As expected, the results showed considerable TrIQ for the substrate-free form of the Trp containing sample (F4W/K60B), with an intensity quenching ratio ($\frac{F_0}{F}$) of ~3.5, and the amplitude-weighted average lifetime quenching ratio ($\frac{\langle\tau_0\rangle}{\langle\tau\rangle}$) of ~2. This trend is

repeated with Tyr as the quencher, (F4Y/K60B), although the amount of quenching is much less pronounced, with a $\left(\frac{F_0}{F}\right)$ of ~ 1.5 (Figure 2.10B) and $\left(\frac{\langle\tau_0\rangle}{\langle\tau\rangle}\right)$ of ~ 1.2 (Table 2.2), as would be expected given the decreased apparent “reach” of Tyr as a quencher.

To measure the effect of substrate binding on the structure of T4L, the same studies were carried out on samples containing an active site mutation, T26E, in the F4X/K60B background. The T26E mutation causes the peptidoglycan substrate to be covalently bound, and thus traps the protein in a distinct conformation (119) with these two distances separated by $\sim 14.5\text{\AA}$ (C α -C α). For these samples, both the Trp and Tyr containing proteins showed decreased quenching (Figure 2.10B). We attribute the changes in TrIQ and TyrIQ in these samples as being due to the samples containing covalently attached peptidoglycan from the cell walls of bacteria. This was confirmed by SDS-PAGE, which shows a smear for these samples (due to the incorporation of heterogeneous lengths of peptidoglycan polymers, see Figure 2.9).

We then confirmed these differences in TrIQ and TyrIQ were due to bound peptidoglycan by incubating the T4L T26E samples for one hour at pH 3 and 37°C in order to hydrolyze the peptidoglycan-lysozyme covalent bond (119). After returning these samples to the original experimental conditions of pH 7.6, the substrate-free (acid-hydrolyzed) proteins show intensity and lifetime quenching ratios similar to the non-active site mutant, indicating their return to the empty conformation (Figure 2.10B). Finally, adding back purified peptidoglycan to the acid-hydrolyzed T26E samples returned the amount of quenching to that of the static peptidoglycan-bound protein (Figure 2.10B).

Both TrIQ and TyrIQ can be used to assess the energetics of a protein movement through Arrhenius analysis of dynamic quenching rates.

We next tested the ability of both TrIQ and TyrIQ to assess the energetics underlying the hinge-bending movement, by measuring the fluorescence intensity and lifetime decay of the samples described above as a function of temperature. Samples with and without the active site mutation T26E were measured, at different temperatures (30, 25, 20, 15, and 10°C), and the data then subjected to Arrhenius analysis.

The results indicate a slight temperature dependent change in dynamic quenching rate, from which we calculated the activation energy for the hinge bending motion by assuming the slope of the line resulting from an Arrhenius plot of the data was equal to the activation energy divided by the gas constant, $-\frac{E_a}{R}$. This analysis resulted in activation energies ranging from ~1.5-2.5 kcal/mol (Figure 2.10C). The implications of these results are discussed below.

Discussion.

We set out in this work to expand and calibrate an SDFL method that enables mapping distances in proteins and studying protein dynamics and conformational changes. Specifically, we sought to determine if Tyr, like Trp, could also be used as an internal quencher in SDFL studies, as Tyr has been reported to quench bimane fluorescence in the free amino acid form (68, 114). We also tested how well these internal quenching methods (TrIQ and TyrIQ) could assess the dynamics and energetics of a protein

structural change, in this case, the hinge bending motion in T4L that occurs upon substrate binding.

In the process of carrying out this work, we also developed a new way to purify and label the proteins (see scheme in Figure 2.1), with the goal of increasing throughput and enabling future automation, as we proposed previously (69). Briefly, this involved using a BioRad Profinity eXact fusion purification method and on-column labeling of the proteins. Together, with these modifications, we could substantially scale-up and increase the throughput of our SDFL studies. The reduced sample handling and the ability to label and purify samples in parallel resulted in a 6-fold increase in the sample throughput and decreased the required time from three days to one. In the future, it should be possible to automate this purification and labeling approach, significantly simplifying the production of multiple samples for SDFL TrIQ and TyrIQ experiments.

Both Tyr and Trp show distance-dependent quenching of bimane.

We find that both Tyr and Trp quench bimane fluorescence in a distance-dependent manner, but there are clear differences in their abilities to do so, with Trp showing more quenching over a longer range than Tyr. Before discussing these results in detail below, we first briefly review how different types of fluorescence can be quantified in a TrIQ and TyrIQ study, followed by a discussion of the results when this analysis was applied to our samples.

There are several possible fates for a fluorophore in a TrIQ or TyrIQ study (see Figure 2.2). One possibility is that after absorbing light, the fluorophore is not quenched at all, and thus the fluorescence intensity and fluorophore lifetime are unaffected.

Alternatively, the fluorophore may be dynamically quenched after absorbing a photon (i.e., the quenching event occurs after photon absorption by the fluorophore), which results in a change in both the fluorescence intensity and lifetime. The third possibility, static quenching, is especially interesting and informative because it indicates a fluorophore and quencher are in contact with each other at the moment of light excitation (126). Static quenching also causes a decrease in the fluorescence intensity, but no similar relative change to the fluorescence lifetime τ values (because these non-fluorescent complexes emit no light, they are not detected in the lifetime measurement). Importantly, the relative amounts of each type of quenching and the relative fraction of sample in each state can be calculated as described in Figure 2.2 and the Methods section.

Subjecting our data to this analysis demonstrates that the ability of Tyr, like Trp, to exhibit static quenching of bimane depends on the distance of separation between the quencher and bimane (Figure 2.6). Both quenchers show the largest relative amount of static quenching for the N116X/132B sample, the shortest C α -C α distance separation (7.5 Å) measured here, and the Trp results reproduce our previous observations (68-70). Static quenching due to ground-state complex formation between bimane and the quencher in these samples is also indicated by shifts in their absorbance spectra. As shown in Figure 2.3, the absorbance λ_{max} for the bimane probe at site 132 is ~386nm when an Asn is at site 116 (the native residue). This absorbance λ_{max} shifts to ~397 nm for the Tyr, Trp and Phe samples, a strong indicator of ground-state complex formation. Importantly, these data also show that Phe causes minimal quenching of bimane, even when it is in contact with the fluorophore at the moment light excitation (Table 2.3).

Interestingly, the data show Tyr has a smaller “maximal sphere of static quenching” than Trp, that is, Tyr has a smaller apparent reach than Trp. In fact, Tyr exhibits no static quenching at $C\alpha$ - $C\alpha$ distances greater than ~ 10 Å, consistent with the smaller size of Tyr compared to Trp, although the shorter apparent reach for Tyr quenching could be due to different intrinsic properties and not a difference in length. In either case, the shorter range of Tyr quenching can be used to increase resolution in mapping studies, and we show in the next section that the different ranges of quenching by Trp and Tyr can be used to resolve the magnitude of a protein conformational change, such as the hinge-bending motion in T4L that occurs upon substrate binding (Figure 2.10).

We also explored the possibility that new information could be obtained from different analysis of the dynamic quenching component. This involved fitting the fluorescent decay data with a lifetime distribution model. Our working hypothesis was that quencher-probe pairs in very close proximity—but not touching—at the moment of light excitation would exhibit ultrafast lifetimes (resulting from “pseudo static quenching”) and that separating this variable might enable further probing of the dynamic quenching component reflected in the longer lifetime component, and the results show an intriguing pattern. As shown in Appendix 1 (Figure A2.1), unquenched samples were well fit by a single distribution. However, quenched species required a bimodal distribution, with an ultrafast lifetime and a longer lifetime. Intriguingly, the longer lifetime component decreases as the distance from the quencher decreases (except for the case of extreme static quenching).

We also tested the effect of pH and temperature and found that although the magnitude of intensity quenching in TrIQ and TyrIQ are somewhat sensitive to different

pHs and temperatures (Figure 2.8), the effect of these parameters on the relative amount of different types of quenching are not greatly affected (Figure 2.8). Only Tyr showed a slight difference in the relative contributions to static and dynamic quenching at low pH for reasons that are not presently clear but are likely due to changes in the redox state of Tyr at different pHs. Despite these slight differences, we have shown here that one can still detect the presence and relative contribution of static quenching, which will allow both TrIQ and TyrIQ to be used under a range of pH and temperature conditions.

Tyr does not substantially quench BODIPY 507/545 in a distance dependent manner, whereas Trp does.

Previously, we established that Trp also quenches a number of other fluorophores besides bimane in a distance dependent fashion, thus expanding the palette of probes that can be used in TrIQ studies (68). Here, we reconfirmed that Trp can quench BODIPY 507/545, a red shifted fluorophore with excellent quantum yield. Surprisingly, we find that Tyr does not show obvious distance dependence quenching of BODIPY 507/545 (Figures 2.4 and 2.7), despite previous reports that free Tyrosine-methyl ester can cause some slight quenching of BODIPY 507/545 in solution (68). In fact, analysis using a form of the Rehm-Weller equation and published redox potentials for Trp, Tyr, and BODIPY-FL (127, 128) suggests that both Trp and Tyr might be able to quench some BODIPY fluorophores in a PET-fashion. Unfortunately, it was not possible to carry out these calculations on the BODIPY 507/545 used here, due to a lack of published E_{red} values. Interestingly, although BODIPY 507/545 shares the same basic structure as the other BODIPY fluorophores, its linkage group does not contain a methylene “spacer”

between the iodoacetamide reactive group and the fluorophore. This difference might account for its inability to be significantly quenched by Tyrosine, and the possibility remains that some other BODIPY fluorophores may still show Tyrosine-induced quenching, as has been reported in studies using free Tyr amino acid and BODIPY-FL (129).

The observation that Tyr does not significantly quench BODIPY 507/545, whereas Trp does, suggests several possible uses. For example, when studying a protein of unknown structure or conformation one could rapidly determine if some observed bimane quenching in an experiment is due to Trp or Tyr by simply re-labeling the same protein with BODIPY 507/545. A lack of BODIPY 507/545 quenching would indicate the cause of the initial bimane quenching was due to a Tyr residue. Similarly, one could exploit the different quenching profiles obtained using Trp and Tyr to glean orientation information about how two interacting proteins dock with each other.

Both TrIQ and TyrIQ can detect a hinge bending movement in T4L that occurs with substrate binding.

Crystal structures show substrate binding to T4L involves a large domain movement between two lobes that results in the exposure of the active site. We attempted to measure this movement by putting a quencher (Trp or Tyr) on one side of the active site cleft (residue 4) and a fluorescent probe on the other side (residue 60). Crystal structures show the C α -C α distances between these two sites are closer (~ 10.5 Å) in the empty state (130), and then move apart (~ 14.5 Å C α -C α) upon binding substrate (119). The latter distances were determined using a T4L active-site mutant T26E, which covalently binds

and traps the substrate peptidoglycan (119). This active site mutant has been used in numerous previous studies focused on defining this hinge bending (120, 124), thus here we tested if this hinge bending could be detected using TrIQ or TyrIQ, which would result in decreased quenching upon substrate binding.

Indeed, the TrIQ and TyrIQ data reflect the movements seen in the crystal structures. As seen in Figure 2.10, the Trp containing sample shows significant quenching in the absence of substrate, but almost no quenching for the substrate-bound T26E mutant. In contrast, Tyr shows a very small amount quenching for the substrate-free T4L, and no quenching upon substrate binding to the T26E mutant.

These changes are exactly as one would expect based on the distance-dependent constraints reported in the Results section. As shown in Figures 2.4 and 2.6, the maximal reach Trp is ~ 15 Å, but only ~ 10 Å for Tyr. Thus, significant Trp quenching and minimal Tyr quenching is expected for T4L in the apo, freely hinge-bending, state, as is observed (Figure 2.10). In contrast, no significant quenching should be expected for either Trp or Tyr in the substrate bound state in the T26E mutant, as the two sites move to 14.5 Å apart outside of the maximal reach of either quenching residue.

Together, these observations show how including Tyr quenching increases the resolution of an internal quenching study, by enabling the separation of “close” interaction distances (less than ~ 10 Å) and those that are between ~ 10 and ~ 15 Å.

Arrhenius analysis of the TrIQ and TyrIQ data suggest a low energy barrier for hinge-bending motion in T4L.

We also assessed the energetics of the hinge-bending movement, described above, by carrying out studies at different temperatures and subjecting the results to Arrhenius analysis. Specifically, we calculated a dynamic quenching rate, k_q , at each temperature from the amplitude-weighted average lifetime, $\langle\tau\rangle$, as described previously in the Methods section, and used these values for Arrhenius analysis (112, 131). The similar low E_a values resulting from this analysis of both the TrIQ and TyrIQ data (~1.5-2.5 Kcal/mole) are consistent with the idea that hinge-bending movement between empty and substrate-bound T4L conformations occurs in the protein (124, 125) and is not impeded by a high activation energy barrier. The E_a values obtained from TrIQ and TyrIQ differ by ~ 1 kcal, and it is not yet clear if difference is truly significant, as the different physical properties of Trp and Tyr could cause subtle difference in this dynamic movement in T4L. Moreover, the amount of quenching is low in the Tyr samples and thus the data could potentially contain significant error due to the low signal and increased noise.

In summary, in the present work we expanded the tool set for characterizing and quantifying dynamic structural movements in proteins by establishing and calibrating how Tyr can be used in internal quenching SDFL studies. We find that TrIQ and TyrIQ of bimane is measurable across a range of pHs and temperatures, and we show how the use of these two approaches together increases the resolution of structural and dynamics information that can be obtained, thus significantly expanding the scope of this SDFL approach.

Some caveats need be mentioned regarding TrIQ and TyrIQ. First, in contrast to FRET, neither method has a straightforward and experimentally verified theory for mathematically calculating precise distances between quencher and fluorophore. However, it is possible to identify and quantify quencher-probe pairs that are in near proximity (dynamic quenching) and those in contact at the moment of light excitation (static quenching), although we are using these terms in an operational sense. It can also be difficult to separate “true” static quenching from “pseudo” static quenching, the latter which occurs when ultra-fast quenching events (due to excited state collisions between proximal quencher-probe pairs immediately after light excitation) introduce ultra-short lifetime components in the data. Thus, in these calculations, it is critical to take into account the time resolution of the instrument and scattering propensity of the sample when calculating the fluorescence lifetimes and differentiating between light scattering and ultra-fast quenching events. Second, for the bimane probe used here, both TrIQ and TyrIQ only work over a limited distance ($< 15 \text{ \AA}$), although this limitation can also be considered a strength and used to increase the precision of a given measurement. Third, the use of $C\alpha$ - $C\alpha$ distance as a calibration metric is non-ideal because it does not account for parameters like probe-quencher orientations. In the future, a key step to advancing the TrIQ and TyrIQ methods will be to include Molecular Dynamic simulations in the analysis of the data to model the quencher-probe interactions, as Ladhokin and colleagues have done using two Trp residues to approximate the Trp-bimane pair (47).

Importantly, TyrIQ introduces new advantages to this internal quenching approach. For one thing, TyrIQ works over a smaller range than TrIQ, and thus can be used to provide higher distance resolution. Furthermore, the fact that Tyr (the quencher) only

differs by an –OH group from the control (Phe) means that TyrIQ studies will be optimal for use to minimize proteins sensitive to changes in steric volume. Previously, bimane TrIQ has been used to assess movements within GPCRs (*104, 112, 132-134*), and we have recently used this approach to map the interactions between the GPCR opsin and visual arrestin (*108*).

Tables.

Table 2.1: Results of fitting lifetime decay of bimane attached to T4 lysozyme at multiple sites with and exponential decay model

C α -C α Dist. (Å)	Quenching Residue	A ₁	τ_1	A ₂	τ_2	A ₃	τ_3	χ^2	< τ >	Site Average
7.5	<i>Phe</i>	9338.1	13	21945	9.27	-	-	1.031	10.5	11.1 \pm 0.56
	<i>Phe</i>	17599	15	14502	8.13	-	-	1.038	11.6	
	<i>Tyr</i>	1037.1	9.9	1237.7	4.85	964	0.32	1.028	5.11	
	<i>Tyr</i>	100.6	12	402.55	6.61	254	1.6	0.956	5.63	
	<i>Trp</i>	762.4	9.1	1118	1.7	4428	0.53	0.985	1.78	
	<i>Trp</i>	713.9	11	1038.5	4.57	7840	0.71	0.954	1.89	
8.4	<i>Phe</i>	27721	15	5497	6.42	-	-	0.965	13.3	13.4 \pm 0.14
	<i>Phe</i>	27989	14	4407	7.69	-	-	1.014	13.5	
	<i>Tyr</i>	4302.4	11	9050	4.99	26370	0.53	1.035	2.64	
	<i>Tyr</i>	7356.4	6.3	4583	1.57	27118	0.31	1.085	2.03	
	<i>Trp</i>	600	7.2	458.5	3.06	2004	0.25	1.085	2.03	
	<i>Trp</i>	1091.8	7.9	1285.9	4.03	1543	0.5	0.977	3.71	
10.1	<i>Phe</i>	47.51	12	539.4	9.05	-	-	1.022	9.3	9.28 \pm 0.02
	<i>Phe</i>	6705.3	10	2913.8	6.85	-	-	0.974	9.26	
	<i>Tyr</i>	1289.7	11	5735.5	7.99	1681	1.34	0.955	7.16	
	<i>Tyr</i>	8915.7	9.8	21241	6.73	8658	1.73	0.985	6.32	
	<i>Trp</i>	30.3	11	196.4	4.02	280	0.77	1.018	2.62	
	<i>Trp</i>	6377.6	10	13598	3.88	30162	1.15	0.987	3.02	
10.7	<i>Phe</i>	254.8	13	567.1	11.2	-	-	1.098	11.8	11.5 \pm 0.26
	<i>Phe</i>	580.5	13	317.7	8.81	-	-	0.949	11.3	
	<i>Tyr</i>	5155.6	12	1765.4	7.12	-	-	0.899	10.8	
	<i>Tyr</i>	59751	12	7136	5.81	-	-	1.032	11	
	<i>Trp</i>	4750	10	4049	4.31	-	-	1.025	7.48	
	<i>Trp</i>	30377	9.6	8953	5.02	11480	0.34	1.054	6.72	
11	<i>Phe</i>	3849.4	8.7	992.9	1.62	-	-	0.976	7.22	7.93 \pm 0.72
	<i>Phe</i>	18236	9.4	5439	6.19	-	-	0.934	8.65	
	<i>Tyr</i>	32399	8.6	15700	1.73	-	-	1.049	6.38	
	<i>Tyr</i>	23033	9.1	2901	5.12	-	-	1.01	8.69	
	<i>Trp</i>	25945	6.6	7226	1.89	10490	0.33	1.026	4.3	
	<i>Trp</i>	1863.7	9.9	15135	6.43	4489	1.35	1.919	5.67	

C α -C α Distance (Å) is from PDB 1L63. A_i is the amplitude of the ith component. τ_i is the lifetime of the ith component. χ^2 is the reduced chi-squared. < τ > is the amplitude-weighted average lifetimes, which are combined to give an average lifetime, values are given \pm standard deviation from 2 experiments.

Table 2.2: TrIQ and TyrIQ effect on bimane attached to the same site of T4L in various substrate binding modes

Quenching Residue	State of the binding site	Intensity Quenching (F ₀ /F)		Lifetime Quenching (τ ₀ /τ)			Components of Fluorescence•					
							<i>Static</i>		<i>Dynamic</i>		<i>Unquenched</i>	
<i>Trp</i>	Open	3.4	+/- 0.1	1.9	+/- 0.0	43.5	+/- 1.8	27.2	+/- 1.1	29.3	+/- 0.7	
	Closed	1.0	+/- 0.0	1.0	+/- 0.0	1.3	+/- 3.0	3.1	+/- 1.6	95.6	+/- 1.6	
	Acid-treated	3.7	+/- 0.5	1.9	+/- 0.2	47.5	+/- 4.7	22.7	+/- 6.1	29.9	+/- 6.8	
	Peptidoglycan added back	1.3		1.1		16.5		5.9		77.6		
<i>Tyr</i>	Open	1.4	+/- 0.0	1.3	+/- 0.0	10.5	+/- 0.8	18.0	+/- 0.2	71.5	+/- 0.6	
	Closed	1.0	+/- 0.0	1.0	+/- 0.0	-0.2	+/- 2.5	1.0	+/- 0.9	98.6	+/- 2.1	
	Acid-treated	1.7	+/- 0.2	1.3	+/- 0.1	23.9	+/- 9.4	16.5	+/- 4.2	59.5	+/- 7.5	
	Peptidoglycan added back	1.0		1.0		-6.6		4.6		102.0		

* Values are given ± standard deviation from 2 measurements where indicated.

•Amplitude-weighted average lifetimes from an exponential fit using FluoFit software from PicoHarp were used to calculate lifetime quenching ratios.

•The components of fluorescence were calculated as follows: static quenching is defined as $1 - \gamma$, dynamic quenching is $\gamma_{DQ} =$

$\left(1 - \left(\frac{\tau}{\tau_0}\right)\right) * \gamma$, and the unquenched fluorescence is calculated using $\gamma_0 = \left(\frac{\tau}{\tau_0}\right) * \gamma$, where the relative component, gamma is

$\gamma = \left(\frac{F}{F_0}\right) * \left(\frac{\tau_0}{\tau}\right)$. Components are given as a percentage and thus multiplied by 100.

Table 2.3: Fluorescence quantum yield, intensity, and bimane maximal absorbance for T4L N116X/N132B comparing Phe, Tyr, and Trp at position 116 to the native residue, Asn.

	Quantum Yield*	Peak Bimane Absorbance	F ₀ /F	τ ₀ /τ
T4L N116 N132B	0.22	386	1.0	1.0
T4L N116F N132B	0.16 ± 0.003**	397	1.4	1.1
T4L N116Y N132B	0.02	398	14.1	3.4
T4L N116W N132B	0.008	395	27.5	4.0

* Quantum yields were calculated by comparing bimane absorbance and fluorescent intensity at 360 nm to that of quinine sulfate as described in material and methods.

** Average and standard deviation from 3 measurements are reported where indicated, otherwise measurements were made once.

Figures.

Figure 2.1 Model showing the fluorophores, quenching residues, and sites of attachment on T4 lysozyme used in this study.

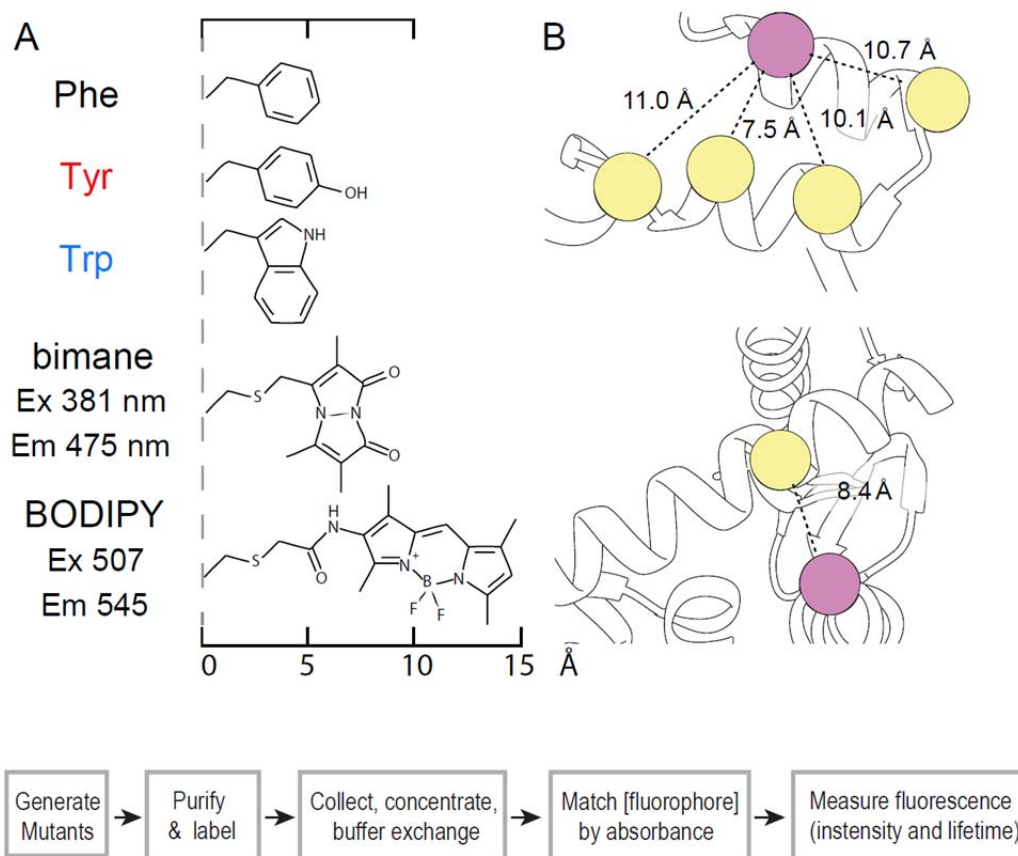


Figure 2.1 Model showing the fluorophores, quenching residues, and sites of attachment on T4 lysozyme used in this study (A) Structures and abbreviations for the quenching and non-quenching residues (Trp, Tyr, and Phe) and fluorophores (bimane and BODIPY 507/545). The spectral qualities of the fluorophores are listed below the name. (B) Top, a model of T4 lysozyme highlighting the location of the C α atom of the cysteines used for fluorophore incorporation using SDFL at sites 123, 128, 132, and 135 (yellow spheres). The location of the 5th cysteine site, at 68, is shown below. The pink spheres indicate the C α carbons of sites N116X (top) and F4X (bottom), where X is Phenylalanine (F), Tryptophan (W), or Tyrosine (Y). The different C α -C α distances between probe and quencher site are also indicated. The models were generated using coordinates from PDB 1L63 and the UCSF Chimera package.

Figure 2.2 Models illustrating the three different quencher-fluorophore conformations that can be quantified using fluorescent measurements, and how their fluorescence emission intensity and lifetime decay differ.

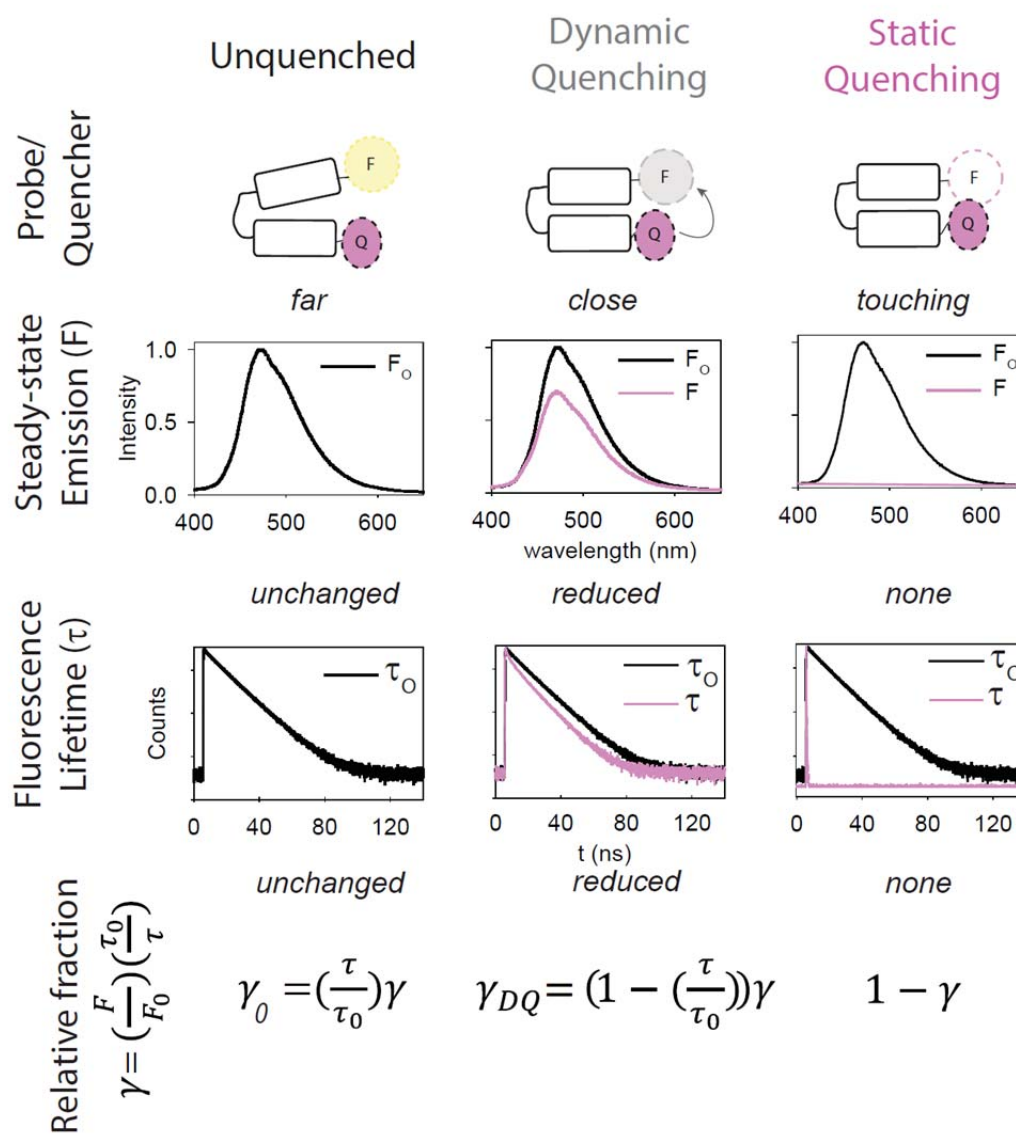


Figure 2.2 Models illustrating the three different quencher-fluorophore conformations that can be quantified using fluorescent measurements, and how their fluorescence emission intensity and lifetime decay differ (Top Row). As shown, at the moment of light excitation the quencher and fluorophore can either be far apart from each other and unable to quench (Top, left), close enough for the quencher to dynamically quench the fluorophore after excitation (Top, middle), or so close that the pair touch before light excitation, resulting in a nonfluorescent complex (Top, right). The effect of these different conformations on the fluorescence emission and decay are shown in the second and third rows, respectively. Note that both dynamic and static quenching results in a decrease in fluorescence intensity, yet their fluorescence decay results are drastically different. Dynamic quenching results in a faster fluorescent decay (shorter lifetime), whilst fluorophores that are statically quenched have no lifetime and do not contribute to this analysis. The relative contribution of each quenching state can be elucidated from the fluorescence intensity ($\frac{F_0}{F}$) and lifetime quenching ratios ($\frac{\langle\tau_0\rangle}{\langle\tau\rangle}$) to calculate using the equations in the final row, as described in Materials and Methods.

Figure 2.3 Absorbance spectra of Bimane incorporated in T4L showing a shift in peak absorbance.

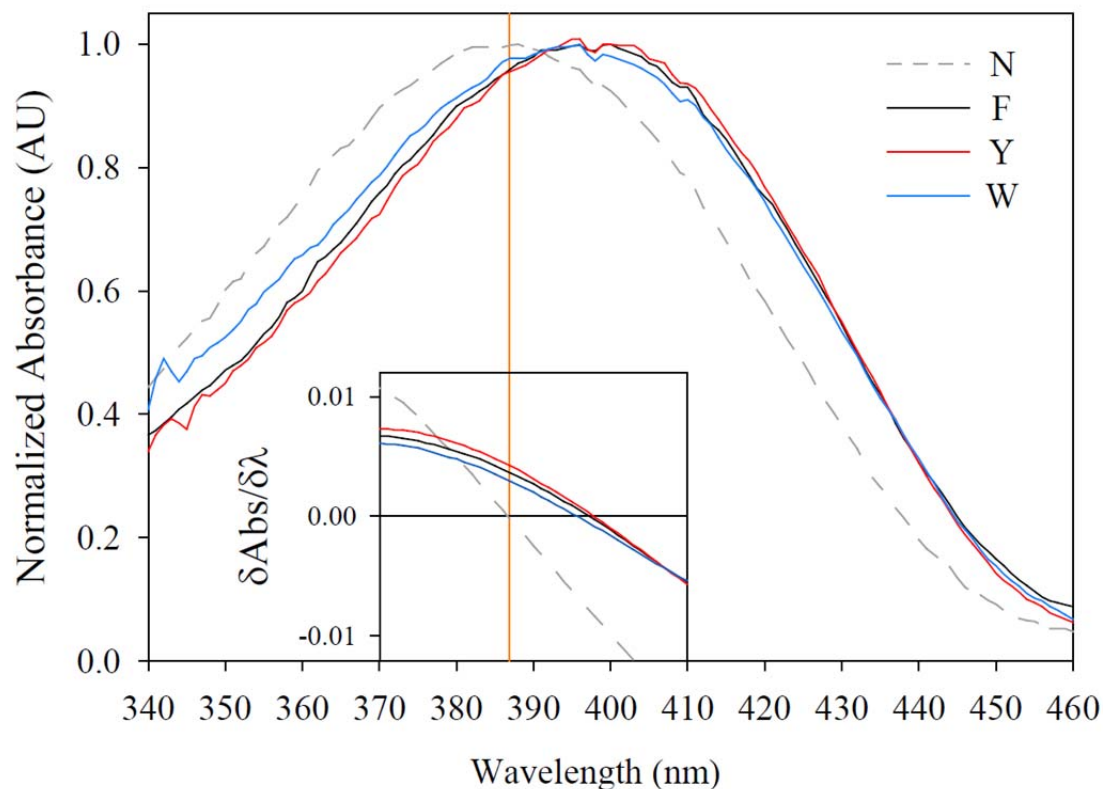


Figure 2.3 Absorbance spectra of Bimane incorporated in T4L showing a shift in peak absorbance. Bimane absorbance spectra for T4L N116X/N132B, where X is N, F, Y, or W. The bimane in T4L containing an N at the “quenching position” has maximal absorbance at 386 nm, highlighted with the orange vertical line. T4L containing an F, Y, or W at the “quenching position” has maximal bimane absorbance at ~397 nm. Inset shows the first derivative of absorbance spectra ($\delta Abs/\delta \lambda$) for each quenching residue, which helps identify the peak absorbance wavelength.

Figure 2.4 Tryptophan quenches the fluorescence emission of T4 lysozyme labeled with either bimane or BODIPY 507/545, while tyrosine only quenches bimane.

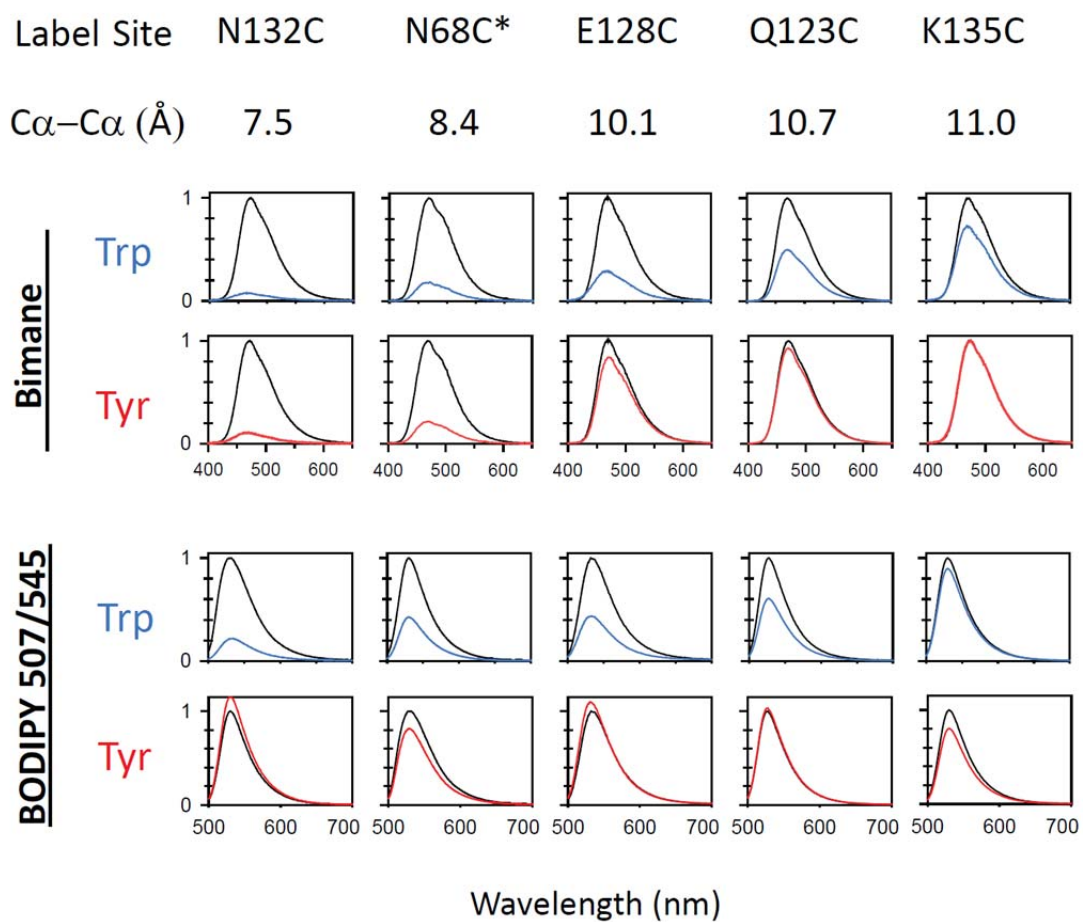


Figure 2.4 Tryptophan quenches the fluorescence emission of T4 lysozyme labeled with either bimane or BODIPY 507/545, while tyrosine only quenches bimane. Fluorescence emission intensity for Phe containing, unquenched samples (black) and samples quenched by Trp (blue) or Tyr (red) for the fluorophores bimane (top) and BODIPY 507/545 (bottom). In all cases the Phe, Tyr, or Trp was incorporated at one of the indicated locations on T4L (site 116 or site 4 for N68C, indicated by *) and a fluorophore was covalently attached to unique cysteines at multiple locations on T4L indicated in Figure 1, resulting in the different C α -C α distances separating the quencher and probe indicated. The data show Trp can quench bimane fluorescence, to some degree, at all distances measured, with the best quenching observed at the shortest distance, and the least quenching at the longest distance. Tyr can also quench bimane at close distances but, in contrast to Trp, is unable to considerably quench bimane further than $\sim 10\text{\AA}$ separation. Trp also quenches BODIPY 507/545 in a distance dependent manner, whereas Tyr does not dramatically quench BODIPY 507/545 at any of the distances measured.

Figure 2.5 Examples of bimane fluorescence decay and Exponential decay fitting for bimane when unquenched (Phe containing samples, black traces) and quenched (Tyr or Trp containing samples, red and blue traces, respectively). The decay curves were fit with a multiexponential decay function using FluoFit software as described in the Methods section of the main text. The resulting lifetimes can be found in Table 2.1, along with the χ^2 for each fit. Here we show the additional metrics to assess quality of the fit: the residuals (directly below each decay trace), and the autocorrelation functions of the weighted residuals (directly below the residuals trace) for each of the example bimane fluorescent decays. Here we show a single data set for each of the bimane-quencher distances measures, C α -C α distance 7.5 Å (first column), 8.4 Å (second column), 10.1 Å (third column), 10.7 Å (fourth column), and 11.0 Å (fifth column).

Figure 2.6 Comparison of the distance-dependent effect of Trp and Tyr quenching of bimane emission, fluorescence lifetime, and the calculated relative components of fluorescent quenching.

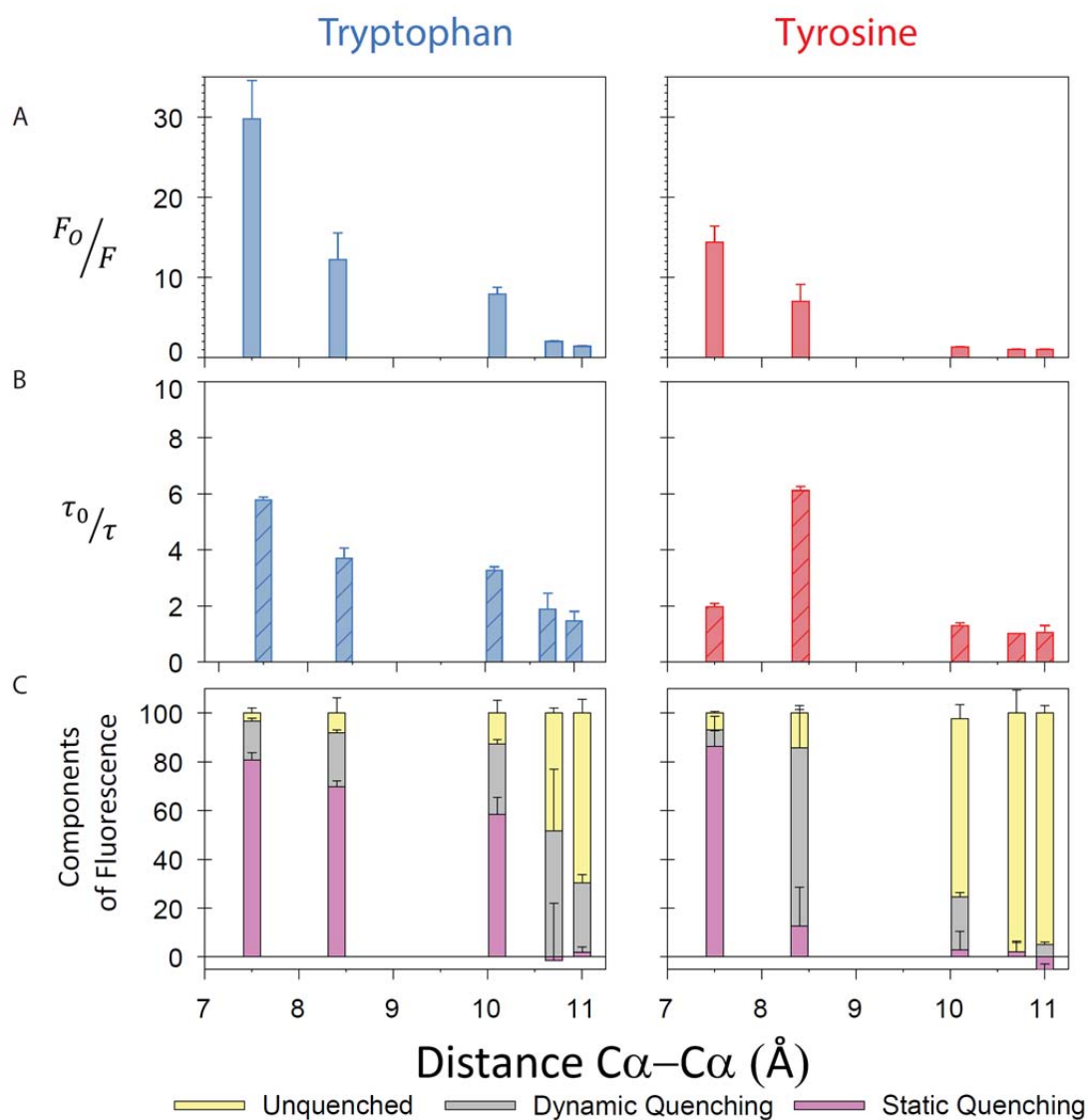


Figure 2.6 Comparison of the distance-dependent effect of Trp and Tyr quenching of bimane emission, fluorescence lifetime, and the calculated relative components of fluorescent quenching. (A) Ratio of the fluorescence intensity of bimane-labeled T4L samples with the probe at different C_α - C_α distances from a Phe (F_0) or either of the quenching residues Trp or Tyr (F). The data indicate the $\frac{F_0}{F}$ for Trp (blue bars, top left) is greater than for Tyr (red bars, top right), and drops off faster as a function of C_α - C_α distance separation. The quenching ratios at each C_α - C_α distance were measured in quadruplet, except for the 8.4Å sample, which was measured in triplicate. (B) Comparison of the ratio of average fluorescence lifetimes of ($\langle \tau \rangle$) of bimane-labeled T4L containing a Phe at the quenching position, $\langle \tau_0 \rangle$, to samples containing a quenching Trp (blue cross hatched bars, middle left) or Tyr (red cross hatched bars, middle right) ($\langle \tau \rangle$) residue at the indicated C_α - C_α distance.

(C) The relative fraction of probe-quencher pairs in static complex (and thus in direct physical contact) can be calculated using respective F_0 and F_Q , and $\langle \tau_0 \rangle$ and $\langle \tau \rangle$ values. To do this, the fraction of quencher-probe pairs in a static complex is calculated by $1 - \gamma$, where γ describes the fraction of quencher-probe pairs in the “open” conformation and is given by $\gamma_{DQ} = \frac{F}{F_0} \cdot \frac{\tau_0}{\tau}$. For the “open” (non-static) quencher-probe pairs, the fraction that are not quenched is given by $\gamma_0 = \frac{\tau}{\tau_0} \cdot \gamma$, and within this group, the fraction of dynamically quenched pairs is given by $\gamma_{DQ} = \left(1 - \frac{\tau}{\tau_0}\right) \gamma$.

Figure 2.7 BODIPY 507/545 is quenched by Trp but not by Tyr.

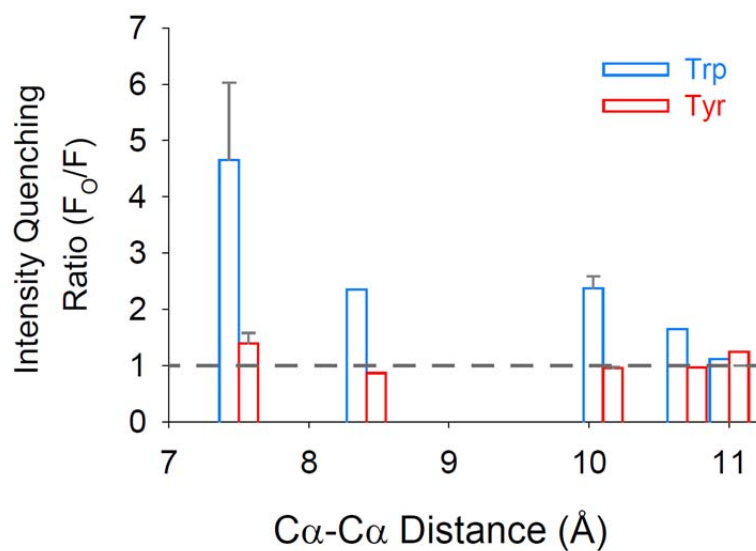


Figure 2.7 BODIPY 507/545 is quenched by Trp but not by Tyr. Comparison of the intensity quenching ratio for BODIPY 507/545 indicates that Trp substantially quenches BODIPY 507/545 in a distance dependent manner whereas Tyr does not. Grey dashed reference line is at $y=1$, which indicates a lack of quenching.

Figure 2.8 Measurements of the pH and temperature sensitivity of TrIQ and TyrIQ.

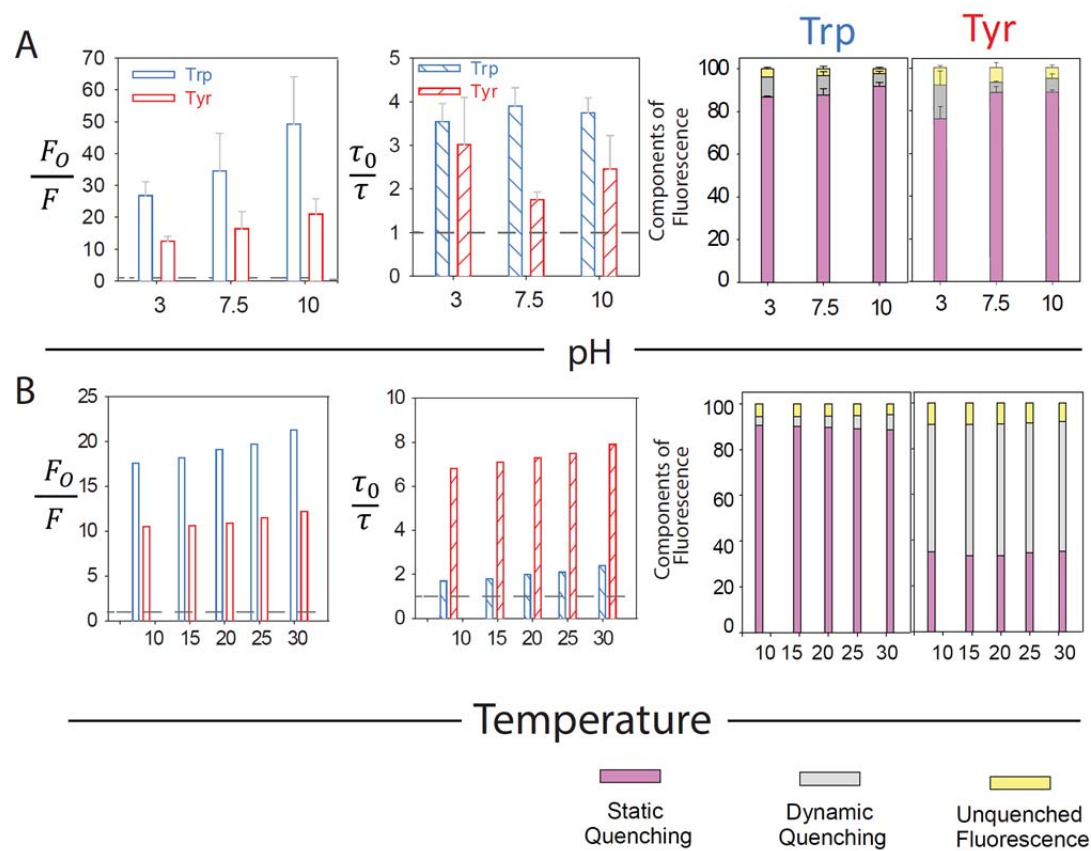


Figure 2.8 Measurements of the pH and temperature sensitivity of TrIQ and TyrIQ. (A) Sensitivity of TrIQ and TyrIQ to changes in pH were assessed using N116X/N132B samples. The extent of TrIQ and TyrIQ intensity quenching ($\frac{F_0}{F}$) is pH dependent (left), with the quenching ratio increasing ~12% per pH unit for TrIQ and ~10% per pH unit for TyrIQ. The extent of TrIQ and TyrIQ intensity quenching ($\frac{\langle\tau_0\rangle}{\langle\tau\rangle}$) is about steady for TrIQ and is only somewhat pH dependent for TyrIQ (middle). Grey dashed reference line is at $y=1$, which would indicate a lack of quenching. Components of bimane fluorescence were calculated for N116X/N132B samples at three different pHs (right) when quenched by Trp and Tyr. Importantly, the relative amount of static quenching is consistent across the pH values tested. (B) The effect of multiple temperatures were also assessed using F4X/N68B samples across 5 temperatures with both Trp and Tyr as quenching residues. The ($\frac{F_0}{F}$) values show the extent of TrIQ (blue bars) and TyrIQ (red bars) are moderately effected by Temperature (left), with TrIQ showing a ~1% ($\frac{F_0}{F}$) change per $^{\circ}\text{C}$ and TyrIQ showing ~0.7% change per $^{\circ}\text{C}$. The ($\frac{\langle\tau_0\rangle}{\langle\tau\rangle}$) values show the extent of TrIQ (blue bars) and TyrIQ (red bars) are also moderately effected by temperature, with TrIQ showing a ~2% ($\frac{\langle\tau_0\rangle}{\langle\tau\rangle}$) change per $^{\circ}\text{C}$ and TyrIQ showing ~0.7% change per $^{\circ}\text{C}$. As with changes in pH, the components of fluorescence of TrIQ and TyrIQ (right) are consistent across the temperatures tested.

Figure 2.9 SDS-PAGE analysis of T4L active site mutants shows peptidoglycan binding.

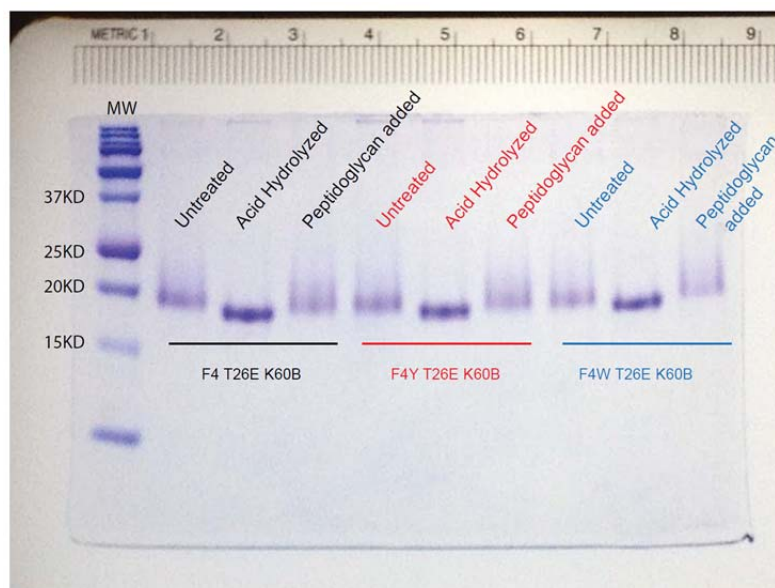


Figure 2.9 SDS-PAGE analysis of T4L active site mutants shows peptidoglycan binding.

SDS-PAGE analysis of T4L active site mutants both before and after acid-hydrolysis of the covalently bound peptidoglycan and subsequent addition of purified peptidoglycan. The lane containing the untreated active site mutants show a smearing of the T4L band, presumably due to nonhomogeneous peptidoglycan polymer length. Acid treatment of these samples is seen to condense back to a single band indicating the loss of the previously covalently bound substrate. When each sample is incubated with purified peptidoglycan, the “smear band” is again observed, supporting the idea peptidoglycan is covalently bound to the T26E T4L mutant, resulting in the varied mobility on SDS-PAGE. The single gel was visualized with Coomassie staining.

Figure 2.10 TrIQ and TyrIQ can be used to measure the magnitude and energetics of a hinge bending motion in T4L that occurs upon substrate binding.

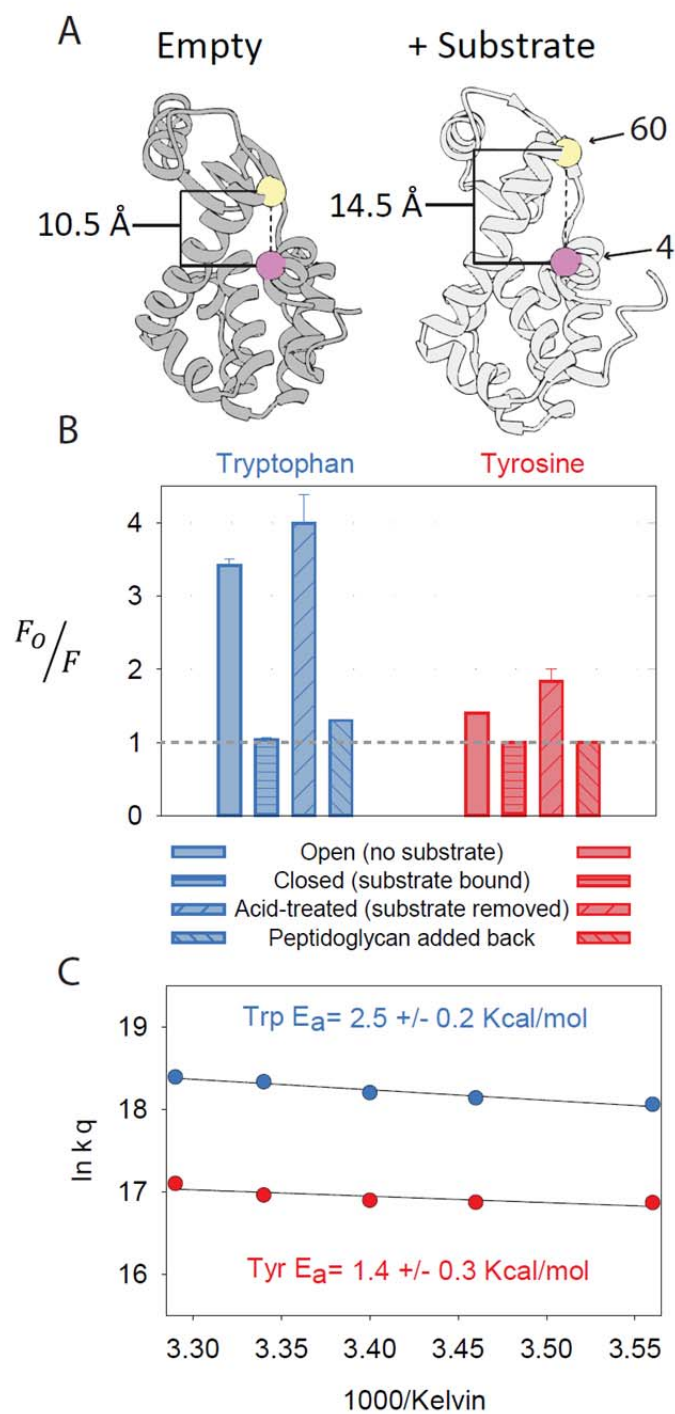


Figure 2.10 TrIQ and TyrIQ can be used to measure the magnitude and energetics of a hinge bending motion in T4L that occurs upon substrate binding. (A) Models of T4L both with (left) and without (right) peptidoglycan bound to the active site (PDB 150L and 2LZM, respectively). To monitor this change, TrIQ and TyrIQ were employed, placing the bimane probe at site 60 and the quenching residue (Trp or Tyr) or non-quenching (Phe) at site 4. With no substrate present, the C_{α} - C_{α} distance (\AA) separating the quenching residue and probe is only $\sim 10.5 \text{\AA}$. Upon binding the substrate peptidoglycan, the C_{α} - C_{α} distance increases to $\sim 14.5 \text{\AA}$, too far for either Trp or Tyr to show substantial quenching.

(B) Ratio of fluorescence emission intensity for samples containing a quenching Trp (blue line) or Tyr (red line) residue (F) compared to samples containing the non-quenching Phe residue (F_0), in either presence or absence of bound substrate. The T4L sample F4W/K60B (without substrate, open bars) shows $\frac{F_0}{F} \sim 3.5$ amount of TrIQ, which is abolished in the active site (T26E) mutant that contains peptidoglycan from the purification (horizontal hatch bars). When the bound peptidoglycan is removed by acid hydrolysis, the quenching is observed again (positive slope hatched bars), and this effect can be reversed by adding back peptidoglycan to the acid hydrolyzed samples (negative slope hatched bars). A similar but less extensive trend in TyrIQ is also observed for the T4L F4Y/K60B samples (right). Inset- SDS-PAGE of the respective samples show the covalently attached peptidoglycan substrate as indicated by the slower mobility and smear in the band. (I) T4L F4Y/T26E/K60B with peptidoglycan bound, (II) when peptidoglycan is released after pH 3 incubation, and (III) after incubation with purified peptidoglycan (see Supporting Figure 7 for full gel) (C) Arrhenius analysis of the dynamic quenching rate (k_q) from Trp and Tyr induced quenching of bimane in the T4L

F4X/K60B mutants as a function of temperature show similar low E_a values using either TrIQ or TyrIQ (~1.5-2.5 Kcal/mol), suggesting the energy barrier for the hinge-bending movement is small. The dynamic quenching rates were calculated as described in the methods section.

Chapter 3: Rapid Purification of full-length GRK1.

Dr. Abhinav Sinha, a previous graduate student of Dr. Farrens, designed the application of the Profinity eXact™ purification approach from BioRad to the purification of GRK1, having recognized that existing methods for expression and purification of recombinant GRK1 was overly laborious, by modern standards, and that these existing approaches yielded GRK1 that was either C-terminally truncated or simply low-activity. Thus, he began this project by sub-cloning the full-length GRK1 gene in to a plasmid containing the Profinity eXact domain and also devised a purification scheme. This project was also helped by the contributions of Dr. Larry David, who conducted the whole protein mass spec analyses. Some of the work presented in this Chapter is also contained in Chapter 4 of this dissertation, which was accepted as a manuscript in the ACS journal Biochemistry.

Summary.

Phosphorylation of G protein coupled receptors (GPCRs) is a key step in terminating their ability to couple with and activate G proteins. Unfortunately, detailed information regarding how G-protein coupled receptors (GPCRs) interact with their kinases (GRKs) is limited, due in part to the fact that established protocols for purifying GRKs are relatively cumbersome and time-consuming processes by modern standards. Moreover, purified recombinant GRKs often exhibit lower activity than enzymes extracted from

their native sources. To overcome these problems, we have optimized a method for rapidly expressing and purifying rhodopsin kinase, GRK1. The method employs transient expression in COS-1 cells, followed by a rapid “one step” purification using the Profinity eXact Fusion-Tag method, a process that results in tag-free and functional, high activity kinase with minimal autophosphorylation. Mass spec analysis indicates the kinase thus produced is properly isoprenylated. We used this method to generate a previously described autophosphorylation-mutant, GRK1 S488D/T489D, which was also purified in its properly isoprenylated form.

Introduction.

G protein coupled receptors (GPCRs) comprise a large class of membrane proteins that share a basic mode of signaling; once turned “on” (activated by a ligand), they induce heterotrimeric G proteins to exchange GDP for GTP and transduce the appropriate signaling cascade. GPCRs are also turned “off” by a conserved process, involving phosphorylation by a GPCR-kinase (GRK), then binding by a protein called arrestin, which sterically blocks further G protein binding and activation. The first GRK identified phosphorylates rhodopsin, the dim-light sensing GPCR in the retina (*135*). This GRK, called rhodopsin kinase or GRK1, is a soluble enzyme that becomes associated with the membrane when rhodopsin is light activated (*24, 43, 136*) and subsequently phosphorylates the rhodopsin C-terminal tail at up to seven Ser/Thr phosphorylation sites (*137, 138*).

While both the structure of rhodopsin (*139-143*) and inactive GRK1 have been solved (*84, 144-146*), how the two proteins interact is still not well defined. In the absence of high-resolution co-structures of various rhodopsin-GRK1 complexes, our lab has begun studying how these two proteins interact using other approaches, primarily mutagenesis coupled with site-directed fluorescence labeling (SDFL) approaches.

Unfortunately, methods for purifying GRK1 are relatively cumbersome and time consuming by modern standards. Typically, the approaches have employed expression of the kinase in insect or mammalian cells, followed by several rounds of chromatographic purification, first using nickel affinity chromatography, then cation exchange chromatography, and finally size exclusion chromatography (*145, 147*). Compounding this involved process is the fact that after purification, the GRK1 thus purified rapidly loses activity (*135, 147*). Moreover, most methods for purifying recombinant GRK1 often lack the extreme C-termini (*84, 138, 145, 148, 149*), which is the site of a post-translational isoprenylation required for full kinase activity (*38, 39*) and employ an N- or C-terminal hexahistidine tag on the protein (*145, 147, 150*) which, if left on the protein, might alter interactions between this critical region of GRK1 with the receptor.

Another obstacle has been that during kinase activation GRK1 autophosphorylates itself, primarily at residues S388/T489 (*32, 34, 35*). Autophosphorylated GRK1 has a lower affinity for light-activated phospho-rhodopsin and is thought to dampen high-gain receptor phosphorylation. Traditional methods of GRK1 purification can result in a mix of autophosphorylated enzyme with 2, 1, or 0 phosphates (referred to as α , β , or γ , respectively), and these must be separated by an additional chromatographic step using a

heparin affinity column or cleaved from the kinase by incubation with a protease in the course of kinase purification.

To address these issues, we set out to optimize the expression and purification of recombinant GRK1. Our goal was to develop a process that would take less time, produce a full-length kinase and leave no remaining affinity tags on the kinase to impair interactions with the GPCR. For our purposes, we wanted to use a transient transfection approach, employing mammalian system to shorten time from DNA mutagenesis to protein expression, and to optimize proper enzyme folding and ensure proper post-translational protein processing. Moreover, our purification method needed to be fast and scalable, capable of processing proteins in parallel to enable higher throughput for site-directed mutagenesis studies and the SDFL and SDSL studies mentioned above.

Here we report our success in meeting these goals. Our approach employs transient expression of GRK1 in COS-1 cells. Purification is achieved using the *Profinity eXact* Fusion-Tag method (121), which exploits the picomolar affinity with which subtilisin binds a prosubtilisin tagged target protein (151-153). The chromatography employed in this method is relatively elegant yet simple – the tagged GRK1 is bound to a column containing an immobilized mutant subtilisin, and then washed extensively to remove non-bound proteins. After this, the GRK1 is obtained simply by activating the immobilized subtilisin (achieved by adding halides to the elution buffer). This allows the subtilisin to cleave the prosubtilisin tag off of the GRK1, and release pure, tag-free kinase in the elution.

In our hands, this approach offers a quick and simple way to purify functional GRK1, as it has previously been shown for transducin (121) and arrestin (152, 154). Our

analysis of kinase produced this way indicates the GRK1 is functional, with full activity, on par with native GRK1 isolated from bovine retinas, has proper farnesylation at the C terminus, and is purified in the non-autophosphorylated state. We have determined this GRK1 can phosphorylate rhodopsin in membranes as well as a detergent-solubilized, purified rhodopsin obtained from either bovine retina or COS-1 cell expressed, purified recombinant rhodopsin mutants to high levels (up to ~ 9 phosphates/receptor), and retains its activity for several weeks when stored at 4 °C.

We used this fully functional GRK1 to phosphorylate the human cannabinoid receptor CB1, a ligand-binding GPCR, and found that it phosphorylate CB1 in an agonist-dependent manner. Here we also report the successful expression and purification of the autophosphorylation-mutant GRK1 S488D/T489D in the farnesylated form. Aligned with a previous report of this mutant (35), we found that GRK1 S488D/T489D is fully functional against DDM-solubilized USR rhodopsin. These findings are promising for future work to investigate whether GRK1 can be used to query the ligand-dependent phosphorylation pattern of non-visual GPCRs.

Materials & Methods.

Materials.

All restriction enzymes, ligase and DNA polymerase were from New England Biolabs. Tissue culture media was purchased from HyClone, while polyethyleneimine was from Polysciences, Inc. Dodecyl maltoside was purchased from Anatrace and 1,2-dioleoyl-*sn*-glycero-3-phospho-L-serine was from Avanti Polar Lipids. 1D4 antibody was obtained

from the Monoclonal Antibody Core at the Vaccine and Gene Therapy Institute of Oregon Health and Science University. Protease Inhibitor Cocktail (EDTA Free) was purchased from Roche Diagnostics. Profinity eXact™ column was from Bio-Rad. Amicon Ultra protein concentrator (10kD cut-off) was from Millipore. [³²P]-ATP was obtained from Perkin Elmer. Frozen bovine retinas were obtained from Lawson and Lawson, Inc. (Lincoln, NE). GBX red light filters were purchased from Eastman Kodak Co. Band pass filters and long pass filters were purchased from Oriel (Stratford, CT). All other chemicals and reagents were obtained from Sigma-Aldrich.

Buffers.

Solubilization buffer is 20 mM HEPES pH 7.5, 250 mM Na Acetate, 1 mM EGTA, 0.125% DDM, 1 mM Benzamidine, 20 µg/µL Leupeptin, 1X Complete protease inhibitor, and 1 mM PMSF. Wash Buffer 1 is 20 mM HEPES pH 7.5. Wash buffer 2 is 20 mM HEPES pH 7.5 and 200 mM Sodium Acetate. Wash buffer 3 is 20 mM HEPES pH 7.5 and 0.3% DDM. Wash buffer 4 is 20 mM HEPES pH 7.5 and 0.3% Tween-20. Wash buffer 5 is 20 mM HEPES pH 6.5. Wash buffer 6 is 20 mM HEPES pH 7.5 and 5 mM EGTA. Wash buffer 7 is 20 mM HEPES pH 7.5 and 1 mM Calcium Acetate. Wash buffer 8 is 20 mM HEPES pH 7.5 and 300 mM Ammonium Sulfate. GRK1 Reaction Buffer is 20 mM HEPES pH 7.5, 75 mM MgCl₂, and 2 mM EDTA.

Cloning of rhodopsin kinase.

To enable purification using the prosubtilisin affinity tag method, the Profinity-tagged GRK1 was created by sub-cloning the 77-amino acid long ProR8FKAM subtilisin BPN'

prodomain coding sequence (121, 151) into a pCMV5-GRK1(His)₆ plasmid obtained from the Khorana group (147). This involved removing the N-terminal hexahistidine tag from rhodopsin kinase, and replacing it with the ProR8FKAM sequence using overlap extension PCR, while maintaining the Kozak sequence (GCCACC) preceding the start codon of the prodomain.

Expression and Purification of Profinity-tagged rhodopsin kinase.

COS-1 cells were transfected with 30 µg pCMV5 Prosubtilisin- GRK1 construct and 100 µg polyethyleneimine (PEI) per 15 cm plate. To ensure proper posttranslational modification of the kinase (38), the transfected cells were given fresh media containing 4 mM (±) mevalonolactone 16-18 hours post transfection and allowed to grow for 36-48 hours. Subsequently, the transfected cells were harvested in solubilization buffer lacking detergent and protease inhibitors. Cell pellets were washed once in the same buffer, then resuspended in 2 mL of solubilization buffer per plate containing 20 units of DNaseI, 1 mM Mg SO₄, and protease inhibitors, and homogenized for 60 strokes using a Dounce homogenizer. Homogenates were solubilized for 1 hour by the addition of 0.125% DDM and nutated at 4°C. The lysates were clarified by centrifugation at 100,000 xg for 45 minutes, and the supernatants were passed through a 0.45 µm filter before the addition of 1 mM DTT.

The chromatographic purification step involved loading the sample prepared as described above onto a 1 mL Profinity eXact column, equilibrated with Wash Buffer 1. The column is washed with 30 mL Wash Buffer 3, and then washed successively with 15 mL of each of the following: Wash Buffers 4, 5, 6, 7, and 8, then 30 mL Wash Buffer 1,

15 mL Wash Buffer 2, and finally 15 mL Wash Buffer 1. GRK1 was eluted with wash Buffer 1 containing 100 mM Sodium Fluoride. Elution fractions containing purified GRK1 were identified by SDS-PAGE as a band at ~63000 Daltons. These fractions were pooled, concentrated and buffer exchanged into GRK1 Reaction Buffer with an Amicon ultra 10 kDa centrifugal filter, after which the concentration was calculated based on the absorbance at 280 nm and an extinction coefficient of 64455 (Protparam Swissprot), and stored at 4°C for use.

Isolation of ROS membranes and preparation of urea stripped ROS.

ROS were isolated from bovine retinas as described previously (155, 156). All steps were carried out under dim red light. Rhodopsin concentration was assessed by difference spectra in the presence of hydroxylamine. Stocks were snap-frozen and stored at -80 °C. Urea stripped ROS (USR) was prepared as described (157). Briefly, this involved washing ROS membranes consecutively with 5 M urea in 50 mM Tris pH 8 containing 50 mM EDTA. The membranes were then centrifuged at 13,000 x g for 15 min and washed five times with 50 mM Tris pH 7.4 before snap-freezing in liquid nitrogen.

Preparation of phospholipid/DDM rhodopsin mixed micelles.

Experiments incorporating phospholipids in the DDM micelles we prepared as described previously (154, 158). Briefly, 5 mM lipid stocks containing 1% DDM and 20 mM HEPES pH 7.4 and 140 mM NaCl were diluted to a final concentration of 0.3 mM in rhodopsin kinase reaction buffer, sonicated for 5 minutes, and placed on ice. Purified

rhodopsin was added to this mix and allowed to incubate on ice for 2 hours, or overnight at 4 °C.

Rhodopsin kinase activity assay.

Phosphorylation assays containing 1 μM of DDM-solubilized rhodopsin was incubated with 0.3 μM GRK1 in GRK1 Reaction Buffer, containing 0.2 mM ATP (with ³²P-ATP as a radioactive tracer) and 1 mM DTT, at room temperature (~24 °C), typical reaction volume was 50 μL. Assays were carried out by illuminating reactions with continuous light passed through a 500 nm long-pass filter, then removing aliquots at different time points (dark, 1, 3, 10, 30, or 90 min) to quench the reaction using either Applebury loading buffer (for analysis by SDS-PAGE), or by addition of TCA to 20% (for filter binding analysis). For the “dark” time points, an aliquot of the reaction is set aside before illumination and kept in the dark for the duration of the experiment, and quenched after 95 minutes in the dark.

Samples analyzed by SDS-PAGE were separated on 0.5 mm Tris-tricine gels, the dye front was removed, gels were dried, and finally imaged using a BioRad phosphor imager to detect the phosphorylated proteins, and the relative phosphorylation between the bands was determined from densitometry analysis using Quantity One software.

To determine the phosphorylation kinetics (described below) and the average number of phosphates incorporated on to each receptor, a filter-binding method was developed. This involved loading the TCA-precipitated samples onto a 96-well PVDF filter plate followed by washing with GRK1 Reaction Buffer. The filters were removed from the plate and incubated in scintillation fluid. After scintillation counting, the amount of ³²P

incorporation was determined by comparing the counts to a standard curve generated using known amounts of ^{32}P -ATP. The number of phosphates per receptor (# phosphates/receptor) was determined by adjusting for the ratio of $^{32}\text{P}/^{31}\text{P}$ -ATP used in the experiment and dividing total moles of P_i by moles of receptor present in the reaction mix. Autophosphorylation studies were carried out under the same experimental conditions lacking rhodopsin. In these experiments the calculation of total number of phosphates/kinase involved using the moles of kinase present.

Kinetics parameters.

Specific activity was calculated using the average number of phosphates per receptor at the final time point of 90 minutes and the amount of kinase used in each reaction. The total number of phosphates transferred at 1, 3, and 10 minutes were plotted and fit with a straight line, the slope of which is taken to be the initial rate. K_m and V_{\max} were calculated from the average of the initial rate of phosphoryl transfer by GRK1 in the presence of 1, 10, 20, or 40 μM DDM-solubilized USR from 3 separate experiments.

Whole protein mass spectroscopy analysis.

0.5 μg of the Profinity-purified rhodopsin kinase was injected at 20 $\mu\text{l}/\text{min}$ in mobile phase A containing water, 0.1% formic acid and bound to a 5 μl bed volume Opti-Trap protein trap (Optimize Technologies, Oregon City, OR). Following washing for 5 min, the trap was switched on-line to a 1.0 x 250 mm C4 column (214 MS C4, Vydac, Hesperia, CA) and protein eluted using a 30 min linear gradient of 7.5 to 60% mobile phase B containing acetonitrile, 0.1% formic acid. Protein masses were determined by

electrospray ionization mass spectrometry using a LTQ linear iontrap mass spectrometer (Thermo Scientific, San Jose, CA), and data collected in profile mode from m/z 400-2000 with averaging of 20 μ scans. Spectra from GRK1 eluting at 26 min into the gradient were averaged and processed using Protein Deconvolution 4.0 software (Thermo Scientific).

Phosphorylation of CB₁ by GRK1.

Human CB₁ with a “cys-less” (containing only C257 and C265), truncated N-terminus Δ N-88 CB₁, and containing a truncated C-terminus with the final 8 amino acid residues (TDTSAEAL) replaced with the 1D4 epitope (TETSQVAPA originating from the rhodopsin C-terminus) was expressed in HEK 293S GnTI- cells as described above, and purified as described previously (104, 159, 160). Briefly, cell pellets were solubilized in 50 mM Tris, 200 mM NaCl, 5 mM MgCl₂, 20% glycerol, 0.6% CHAPS, 0.1% CHS and 0.1% DDM, supplemented with Roche protease inhibitor cocktail, 5 μ g/ml Leupeptin, 10 mM Benzamidine, 0.5 mM PMSF, and 1 μ M SR141716A and gently nutated for 2-3 hours at 4°C. Samples were then centrifuged for 1 hour at 100,000 x g. The supernatant was added to an appropriate volume of 1D4 antibody-Sepharose beads, washed and eluted with buffer containing 0.12% CHAPS, 0.02% DDM, 0.02% CHS, and 200 μ M nonapeptide. Excess ligand and free peptide were removed by 3 passes over a 10kDa size exclusion spin column prior to phosphorylation experiments, described below.

Purified human CB₁ was incubated with either 20 μ M antagonist SR141716A, 20 μ M agonist CP55,940, 20 μ M allosteric ligand Org 27569, or in buffer “vehicle” control in GRK1 reaction buffer containing 0.2 mM ATP (containing 0.05 μ Ci/ μ L final

concentration of ^{32}P -ATP), 0.12% CHAPS, 0.02% DDM and 0.02% CHS for 20 minutes on ice. Phosphorylation experiments were initiated by addition of 1 μM GRK1 wildtype or GRK1 S488D/T489D. Samples were quenched as described above and analyzed thusly.

Results.

The Profinity eXact purification method can be used to rapidly purify tag-free, full-length farnesylated rhodopsin kinase.

GRK1 purified using the Profinity eXact method (Figure 3.1) results in >80% purity from a single step purification, as indicated by Coomassie-stained SDS-PAGE (Figure 3.2A) with a total yield of ~3-5 μg GRK1 per 15 cm plate of transfected COS-1 cells. GRK1 purified using the Profinity eXact method elutes from a heparin sepharose column with 300 mM and 500 mM NaCl (Figure 3.2B), which indicates it is almost exclusively GRK1 with no autophosphorylation (i.e. γ -GRK1) (32).

Mass spec analysis of the GRK1 (Figure 3.3) indicates a mass of 62843.5 Daltons. Isoprenylation is signaled by a CaaX motif at the extreme C-terminus, and involves cleavage of the 3-terminal amino acid residues. For GRK1, the farnesylation site is CVLS. Thus, removal of the VLS residues results in a loss of ~310 Daltons, and farnesylation and carboxymethylation adds back only ~220 Daltons, meaning that a properly modified GRK1 mass is expected to be ~ 90 Daltons less than the full-length GRK1. Indeed, the theoretical mass is calculated to be 62840.6 Daltons for farnesylated GRK1 and 62933.9 Daltons for non-farnesylated GRK1. Based on these results, we

conclude that GRK1 thus produced is fully farnesylated with minimal autophosphorylation.

Purified wild type GRK1 is functional and can phosphorylate DDM-solubilized USR.

As shown in Figure 3.4, the purified GRK1 is functional and causes robust light-dependent phosphorylation of DDM-solubilized, wild-type rhodopsin obtained from urea-stripped bovine ROS (USR), as indicated by autoradiograms of the SDS-PAGE-analyzed phosphorylation experiments (Figure 3.4A). Under these conditions, addition of excess all trans retinal did not appear to dramatically increase GRK1-mediate phosphorylation of light-activated rhodopsin in urea stripped ROS membranes or after DDM solubilization of those membranes (Figure 3.4B). Using a 96-well filter binding assay we developed (see methods), we find that WT GRK1 can phosphorylate DDM-solubilized USR with ~8 phosphates per receptor (Figure 3.4C). We also found that highly active preparations of GRK1 was stable for several weeks when stored at 4° C (Figure 3.4D)

We did observe an overall reduction in the amount of phosphorylation in the DDM-purified sample by ~50%, to ~ 5 phosphates/rhodopsin, presumably due to the loss of the ROS lipids (Figure 3.5). To test this hypothesis, we directly tested the effect of adding back phospholipids to the DDM micelles. We tested DOPS, DOPA, and DOPC as well as the effect of adding back cholesterol and a cholesterol-derived detergent called CHAPS (Figure 3.5A). We queried the phosphorylation results using SDS-PAGE separation rather than 96-well filter binding to control for possible lipid effect on binding to the

filters. We find that addition of the acidic phospholipids DOPS and DOPA restores phosphorylation to the DDM-purified rhodopsin, but that incorporation of the basic phospholipid DOPC does not restore normal phosphorylation levels.

Interestingly, we found that addition of CHAPS/CHS to the DDM micelles nearly completely blocks receptor phosphorylation. We checked the ability of this DDM/CHS/CHAPS-contained rhodopsin to light activate and found that light activation does result in a mix of MII and MI/MIII receptors, which suggests that the near complete loss of receptor phosphorylation is not caused simply from a lack of substrate (active MII rhodopsin) but rather to some other effect, possibly by direct interaction with some domain in the kinase.

GRK1 S488D/T489D phosphorylates rhodopsin to the same degree and with the same affinity of wildtype GRK1 and has nearly undetectable levels of autophosphorylation.

To reduce the amount of GRK1 autophosphorylation (see Figure 3.4A) we also made and purified a GRK1 mutant in which the primary sites of autophosphorylation, S488 and T489, were mutated to aspartate residues as initially reported by Palczewski and colleagues (34, 35). SDS-PAGE analysis of GRK1 S488D/T489D purification yields a protein that is ~80% pure kinase, producing ~2 µg of kinase per 15 cm plate of COS-1 cells (Figure 3.6A). Deconvolution of the whole protein mass spectra yields a measured mass of 62879.7 Daltons versus an expected (calculated) mass for unmodified GRK1 S488D/T489D of 62975.9 and 62882.6 Daltons for the farnesylated form (Figure 3.7).

We therefore conclude that this mutant GRK1 is also purified in the fully farnesylated form.

Initial experiments using GRK1 S488D/T489D to phosphorylate DDM-solubilized USR show the GRK1 S488D/T489D behaves similar to wt GRK1, producing comparable levels of receptor phosphorylation upon light activation (Figure 3.6C, compare results with Figure 3.4).

Importantly, as reported with the initial identification of sites S488 and T489 as the major autophosphorylation sites for GRK1 (35), GRK1 S488D/T489D shows no visible autophosphorylation when queried by autoradiographic analysis of an SDS-PAGE gel (Figure 3.6B), and exceedingly low phosphate incorporation when GRK1 S488D/T489D activity is measured in the absence of substrate and counted using filter binding and liquid scintillation counting of the result (not shown). Quantification of receptor phosphorylation by GRK1 S488D/T489D shows nearly identical levels of average phosphate incorporation per rhodopsin (Figure 3.6C).

Kinetics parameters for GRK1 purified using the Profinity exact method.

The Profinity-purified GRK1 shows a K_m for DDM-solubilized USR of $2.0 \pm 1.3 \mu\text{M}$, a V_{max} of $2200 \text{ nmole min}^{-1} \text{ mg}^{-1}$, and a K_{cat} is $39 \pm 11 * 10^{-3} \text{ s}^{-1}$, with a resulting in a K_{cat}/K_m of $20 \mu\text{M}^{-1} \text{ s}^{-1}$ (Table 3.1).

The GRK1 S488D/T489D showed comparable results to wt GRK1, with a K_m for DDM-solubilized USR of $1.6 \pm 0.24 \mu\text{M}$, a V_{max} of $1700 \pm 190 \text{ nmole min}^{-1} \text{ mg}^{-1}$, and a K_{cat} is $31 \pm 3.5 * 10^{-3} \text{ s}^{-1}$, resulting in a K_{cat}/K_m of $19 \pm 0.19 \mu\text{M}^{-1} \text{ s}^{-1}$ (Table 3.1). The values compare well with the original kinetic parameters for GRK1 S488D/T489D, a K_m

of $2 \pm 1 \mu\text{M}$ and V_{max} of 380 ± 63 nmole phosphate per minute per mg of kinase (35). Why the V_{max} for profinity-purified GRK1 S488D/T489D is ~5-fold higher than the previous report is unclear, perhaps our sample had a higher level of isoprenylation due to the addition of mevalonolactone during expression in COS-1 cells (161-163).

Phosphorylation of human CB1 by GRK1.

We also assessed the ability of our GRK1 to phosphorylate a ligand binding GPCR, specifically the cannabinoid receptor CB1. Our results show that WT GRK1-mediated CB1 phosphorylation is ~3-fold higher than the basal signal in the presence of the agonist CP, and incubation with the antagonist SR blocks basal phosphorylation by ~50% as measured by autoradiographic analysis from SDS-PAGE gels. We also found that incubation with the allosteric CB1 ligand, Org, shows similar phosphorylation as the vehicle control receptor. Importantly, these are initial results and must be repeated in order to reliably quantify the effect of different CB1 ligands on GRK1-mediated phosphorylation, but, these results indicate the purified GRK1 can act on CB1 in an agonist-dependent manner, as it can for other GPCRs.

Discussion.

The Profinity eXact purification method yields full-length tag-free purified recombinant rhodopsin kinase in 1 day.

A key advantage of using the ProFinity eXact method (Figure 3.1) is that the prosubtilisin tag acts as a high-affinity purification tag that remains on the column after proteolytic cleavage by the resin-bound protease during the elution step from the Bio-Rad

Profinity eXact column (121, 151-153) (Figure 3.1A). The resulting tag-free, full length GRK1 has unencumbered N- and C-termini that can interact with the receptor in a manner akin to native GRK1. This avoids possible complications that the hexahistidine tag could have on interactions with rhodopsin. Moreover, our unadulterated C-terminus contains its proper isoprenoid post-translational modification, avoiding the decreased activity that results from expressing a C-terminally shortened form of the protein that lacks a critical farnesylation site (38).

From the GRK1 purification gels, we estimate >80% purity from a single step purification (Figure 3.2A), with a yield of ~3-5 µg GRK1 per 15 cm plate. Importantly, this purification scheme (Figure 3.1B) is much faster than traditional GRK purification methods (which typically require at least two chromatographic steps with long incubation times that might affect enzyme activity (147)) and can be rapidly carried out in parallel for different GRK1 mutants, utilizing multiple small (1 mL, prepacked) Profinity columns. This latter point is key to enabling high-throughput SDFL studies.

Based on the deconvoluted whole protein mass spec result of 62843.5 Daltons (Figure 3.3), we conclude that the GRK1 expressed in the presence of mevalonolactone (147, 150, 164) and purified with the Profinity method is properly modified with a farnesyl group. Full length, unmodified GRK1 should have a mass of 62933.9 Daltons, and a mass of 62840.6 Daltons when properly isoprenylated, due to the addition of the farnesyl group and cleavage of proximal three amino acids and alpha carboxymethylation of the modified cysteine residue (38, 40). Thus, the use of the Profinity system avoids the lack of farnesylation seen in some purification approaches used for GRK1 (84, 145, 146, 148, 149).

Purified full-length GRK1 has wildtype-like functionality.

The Profinity-purified GRK1 has robust ability to phosphorylate wild-type rhodopsin, as determined from autoradiography (Figure 3.4A) We further analyzed these samples using a 96-well plate filter binding assay, which enabled rapid sample analysis as well as more direct quantification of the level of phosphate incorporation per receptor. This analysis shows the Profinity-purified GRK1 is able to incorporate ~8 phosphates per rhodopsin on average (Figure 3.4C), achieving well above the 3 phosphates required for high affinity arrestin binding (165-167).

The use of DDM detergent has been instrumental in the purification and analysis of membrane proteins. While critical for enabling functional studies of purified GPCRs, solubilization with DDM affects the activation pathway of GPCRs as well as their ability to interact with G protein, arrestin, and GRK. We have shown previously that the addition of certain phospholipids increases the ability of visual arrestin to bind to DDM-purified rhodopsin (158).

The activity of most GRK family members is dependent on the presence of negatively charged phospholipids (161-163, 168, 169), although the only previous report to test the sensitivity of GRK1 for acidic phospholipids found that negatively charged phospholipids did not enhance GRK1-mediated phosphorylation of rhodopsin in nanodiscs (49).

However, the latter work used the C-terminally truncated form of GRK1 Δ_{535} -His₆ and compared phosphorylation in the presence of POPC-containing nanodiscs with and without added POPS. Here we show that purified rhodopsin in DDM micelles resulted in decreased average phosphorylation than when in ROS lipids and sterols, but that addition of DOPS and DOPA restores the level of phosphorylation. Interestingly, addition of

acidic phospholipids to GRK2 and GRK3 experiments increased phosphorylation amounts by ~2-2.5 fold (162), similar to our results. Notably, addition of DOPC, which has a positively charged head group, does not restore the level of phosphorylation to that of DDM-Solubilized rhodopsin in ROS membranes. This could indicate that the full length isoprenylated GRK1 does, in fact, have a previously unappreciated preference for acidic phospholipids.

The relatively high activity of our GRK1 may also be because the Profinity eXact purification method results in GRK1 with low levels of autophosphorylation, in contrast to previous methods that sometimes require treatment of GRK1 with phosphatase to remove autophosphorylation (32, 34, 35). GRK1 primarily phosphorylates itself at residues S488 and T489, and this lowers its ability to phosphorylate rhodopsin (32, 34, 35). Analysis of our purified GRK1 by heparin chromatography shows most of the GRK1 elutes with 300 mM NaCl, indicating it is primarily non-phosphorylated, also referred to as γ - GRK1 (32, 34, 35) (fully autophosphorylated GRK1 elutes with 100 mM NaCl, and partially autophosphorylated GRK1 with 200 mM NaCl, see Figure 3.2B). The mass spectrometry analyses also support the conclusion that most of our GRK1 is not autophosphorylated, since the addition of each phosphate group would add ~80 Daltons and we observe the expected mass for non-phosphorylated GRKs. One caveat is that phosphate groups can be labile and are sometimes lost during ionization so the lack of this shift in mass alone does not definitively prove a lack of GRK1 autophosphorylation.

Comparison of GRK1 purified using the Profinity method with GRK1 purified using other methods.

GRK1 activity has primarily been reported using K_m and V_{max} , and more recently K_{cat} values (Table 3.1). The reported K_m for the substrate rhodopsin typically ranges from ~3-5 μM for GRK1 extracted from bovine retina (33, 135, 170), and K_m values for recombinantly expressed and purified C-terminally cleaved GRK1 range from 3.4-12 μM (84, 145, 148), and ~4 μM for the full-length wild type GRK1 purified from COS-7 cells (35). Wildtype GRK1 purified using the Profinity method shows a K_m affinity for DDM-solubilized USR of $2.0 \pm 1.3 \mu\text{M}$, which is within error of the values published for bovine GRK1.

Reported V_{max} values for GRK1 have varied more than affinity parameters, ranging from 650-700 nmole of phosphate per minute per mg of GRK1 purified from bovine retina (33, 135), to 450 ± 52 nmole of phosphate per minute per mg of WT recombinant GRK1 purified from COS-7 cells (35). In contrast, both the WT and C-terminally truncated constructs of GRK1 expressed in and purified from Sf9 (insect) cells have V_{max} values of 2300 and 1100 nmole of phosphate per minute per mg of kinase, respectively (145), whereas the WT GRK1 purified using the Profinity method has a V_{max} of 2200 ± 620 nmole phosphate per minute per mg of kinase, which is at the high-end of the range of maximal reaction velocities for bovine GRK1 in the literature.

The turnover number, or K_{cat} , for Profinity-purified GRK1 of $39 \pm 11 \cdot 10^{-3}$ per second while the K_{cat} of GRK1 purified from bovine retina has been reported as $\sim 0.8 \cdot 10^{-3}$ per second (135), and the C-terminally shortened construct of GRK1 has a reported K_{cat} of $25 \cdot 10^{-3}$ and $58 \cdot 10^{-3}$ per second (84, 148). Thus, the Profinity-purified GRK1 displays

kinetic parameters that are among the best reported values for both the bovine wildtype and recombinantly expressed and purified enzymes.

GRK1 phosphorylates purified human CB1 in an agonist dependent manner.

We wanted to test the ability to use GRK1 to sense activation states of a non-visual GPCR, the human cannabinoid receptor CB1, which has been reported to have 2 critical phosphorylation sites (S426 and S430) that dictate receptor internalization (60). Previous phosphorylation studies with CB1 have been limited due to the fact that purification of active CB1 has been challenging, and there is limited information about the phosphorylation of the native C-terminal residues, TDTSAEAL, which are remarkably similar in sequence to the residues in the same position on rhodopsin, TETSQVAPA. Our lab has developed a method to purify active CB1, which has enabled extensive ligand-binding characteristics for the agonist CP, antagonist SR, and an allosteric ligand called Org, as well as SDFL studies that have revealed that these three ligands bind to/induce distinct receptor conformations (104, 159, 160, 171).

One caveat of the work presented here is that we have shortened the C-terminus of the CB1 used in this work and replaced the native 8 amino acid residues with those of rhodopsin to enable purification using the 1D4 antibody, so this analysis might not reflect phosphorylation position accurately. Nevertheless, the differences in GRK1-mediated phosphorylation of CB1 observed for the active and inactive states suggest that the Profinity-purified GRK1 can sense the active states of CB1. Thus, future experiments should use the full length CB1 protein, and use the autophosphorylation GRK1 S488D/T489D, which, by eliminating the background, autophosphorylation signal from

the kinase itself, should enable 96-well filter binding experiments. Also, given the sensitivity of GRK1 to CHS/CHAPS when phosphorylating rhodopsin, it is possible that an even higher amount of activity could be observed for CB1 phosphorylation in a different detergent/lipid environment.

Conclusion.

In summary, we have developed a straightforward, rapid, simple way to obtain functional, tag-free rhodopsin kinase, GRK1. The method is ideal for the purification of recombinant and mutated GRKs, and it can be carried out in parallel, enabling purification of multiple enzyme mutants at once, which increases throughput considerably. Using this purified kinase, we demonstrate that a one-day purification of GRK1 yields a robustly functional and farnesylated kinase. We have also shown a previously unappreciated sensitivity of the full-length GRK1 to acidic phospholipids such as DOPS and DOPA. We also present preliminary studies that indicate GRK1 can be used to phosphorylate CB1 in an agonist-dependent manner.

Tables.

Table 3.1: Comparison of kinetic parameters published for GRK1 over the last ~30 years

Vmax <i>nmole min⁻¹ mg⁻¹</i>	Km (rho) <i>μM</i>	GRK	Purification method	Expression System	Kcat <i>*10⁻³ s⁻¹</i>	Kcat/Km <i>μM⁻¹ s⁻¹</i>	Year
—	~3	wt	DEAE/HA	Bovine retina	—	—	1988 (170)
700	4 ± 1.1	wt	DEAE/HA	Bovine retina	0.8	0.2	1988 (135)
650	4.4	wt	DEAE/Heparin sepharose	Bovine retina	—	—	1991 (33)
450 ± 52	4 ± 2	wt	Heparin sepharose	COS-7	—	—	1995 (35)
2300 ± 110	2.1 ± 0.4	wt	Ni ²⁺ affinity/TEV cleavage	Insect cells	—	—	2008 (145)
1100 ± 50	12 ± 1.5	wt Δ535-His ₆ •	Ni ²⁺ affinity	Insect cells	—	—	2008 (145)
—	4.7 ± 1.6	wt Δ535-His ₆ •	Ni ²⁺ affinity	Insect cells	58	12.3	2009 (148)
—	3.4 ± 1.7	wt Δ535-His ₆ •	Ni ²⁺ affinity	Insect cells	25 ± 4	7.2 ± 2.7	2011 (84)
2200 ± 620	2.0 ± 1.3	wt	Profinity	COS-1	39 ± 11	20 ± 0.73	
380 ± 63	2 ± 1	S488D/T489D	Heparin sepharose	COS-7	—	—	1995 (35)
1700 ± 190	1.6 ± 0.24	S488D/T489D	Profinity	COS-1	31 ± 3.5	19 ± 0.19	

• wt Δ535-His₆ indicates a GRK1 construct in which the C-terminus (residues 536-561) was truncated and replaced with a His₆ tag to enable Ni²⁺ affinity chromatographic purification.

Figures.

Figure 3.1 Design and protocol for rapid purification of Rhodopsin kinase (GRK1) in a functional, tag-free form using the Profinity eXact Fusion Tag method.

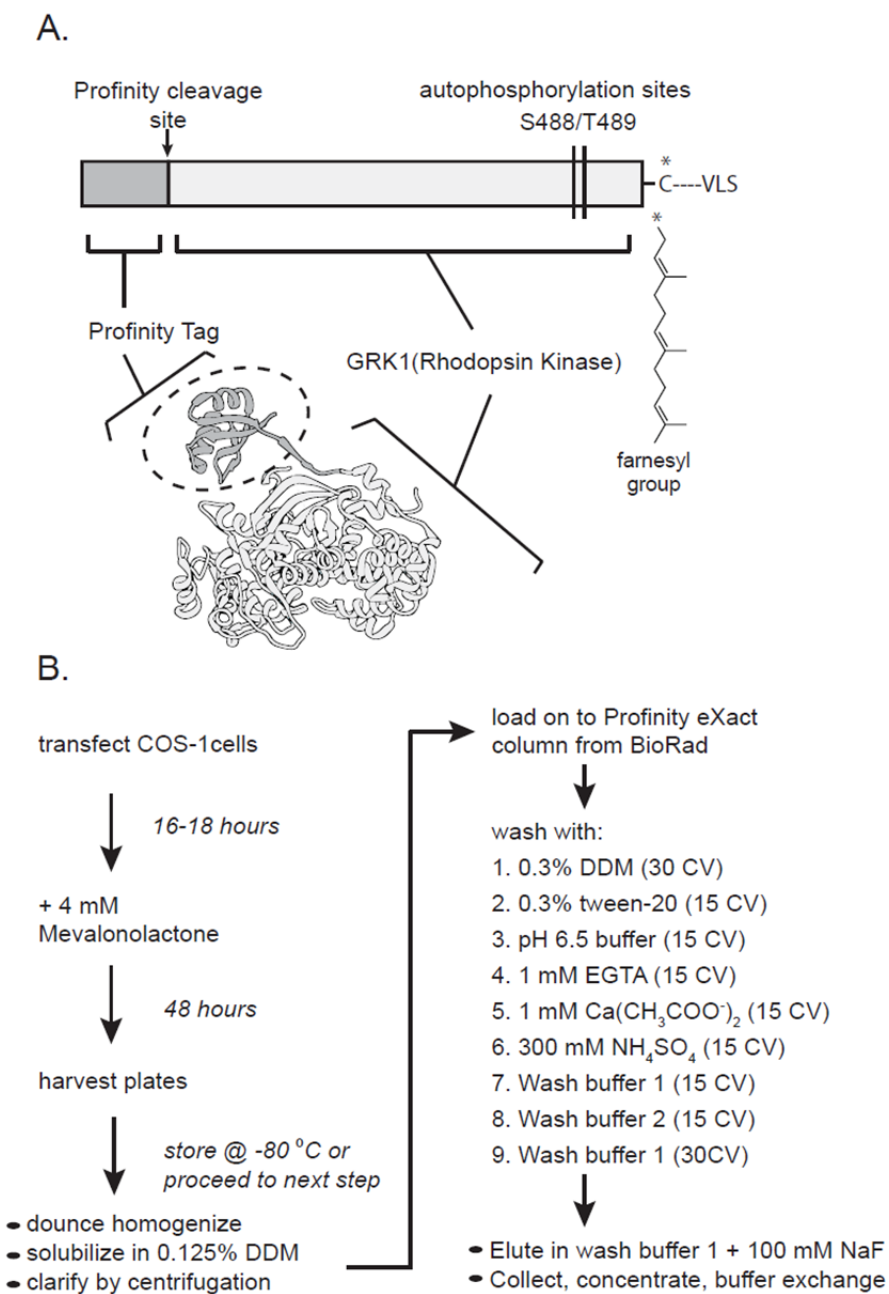


Figure 3.1 Design and protocol for rapid purification of Rhodopsin kinase (GRK1) in a functional, tag-free form using the Profinity eXact Fusion Tag method. (A) Schematic diagram (top) and structural model of GRK1 (bottom) show the N-terminal location of the “tag” (subtilisin prodomain, grey). Note that the subtilisin cleavage site is located between the prodomain tag and GRK1. The two major sites of GRK1 autophosphorylation, S488 and T489, and the CAAX farnesylation site are also indicated. (B) Schematic diagram of the expression and purification system used in the current work. Briefly, this involved transient transfection of the Profinity eXact-tagged GRK1 coding plasmid in COS -1 cells, supplemented with 4 mM mevalonolactone 16-18 hours after transfection (to ensure farnesylation). After harvest and solubilization, samples were applied to a BioRad Profinity eXact column, to which the Profinity tag on GRK1 binds. After extensive washing to remove contaminant proteins the immobilized subtilisin is activated (by addition of 100 mM NaF), whereupon it cleaves off (yet continues to bind) the Profinity tag, releasing purified, tag-free GRK1 in the elution volume. Models were made using UCSF Chimera, and PDB:3CO0 for the prodomain, and PDB:4PNI for GRK1.

Figure 3.2 Wildtype GRK1 purified using the Profinity eXact method is highly pure, properly farnesylated, and elutes in the non-autophosphorylated form.

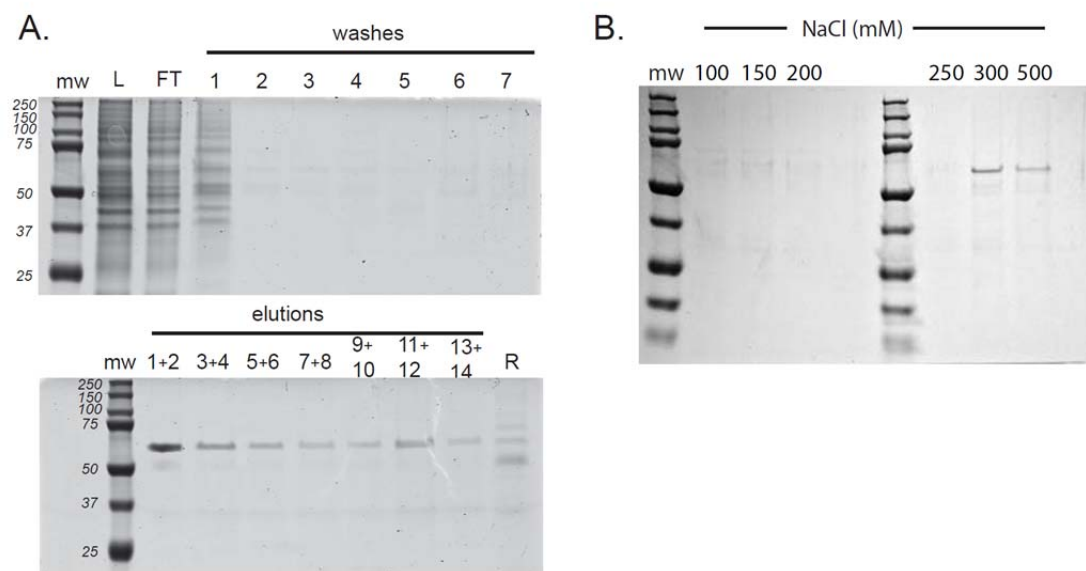


Figure 3.2 Wildtype GRK1 purified using the Profinity eXact method is highly pure, properly farnesylated, and elutes in the non-autophosphorylated form. (A) SDS-PAGE analysis indicates GRK1 purified using the Profinity eXact method produces >80% pure protein in one step. The gel on the left shows the BioRad precision plus protein standard molecular weight marker, MW. L is the fraction loaded on the column, FT is the flow through, and the numbered fractions (1-7) refer to column washes. The right gel shows combined elutions from the column and the results from regeneration of the column indicated by an R. (B) Heparin chromatography analysis of the Profinity eXact-purified GRK1 indicates minimal autophosphorylation has occurred. This analysis is based on previous work that has shown fully autophosphorylated GRK1 (2 phosphates) elutes with 100 mM NaCl, partially autophosphorylated GRK1 with 1 phosphate with 200 mM NaCl, and non-autophosphorylated GRK1 with 300 mM NaCl (32, 35). As shown in this Coomassie-stained SDS-PAGE, our GRK1 does not elute from the heparin column until 300 and 500 mM NaCl are used, confirming the mass spec results indicating that the Profinity eXact method yields GRK1 with little to no autophosphorylation.

Figure 3.3. Whole protein mass spectra analysis of WT GRK1 indicates that it is properly farnesylated and not autophosphorylated.

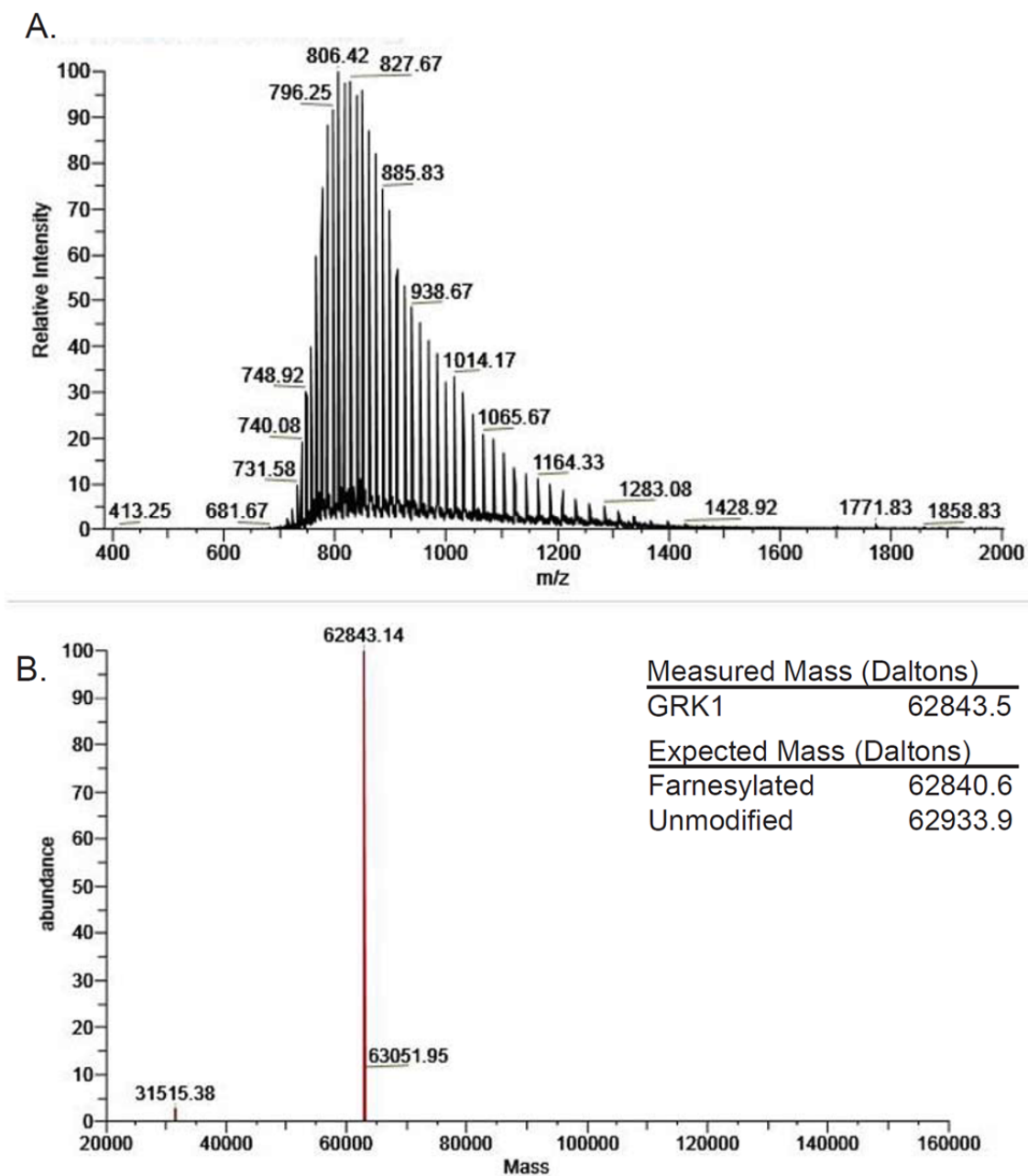


Figure 3.3. Whole protein mass spectra analysis of WT GRK1 indicates that it is properly farnesylated and not autophosphorylated. (A) Whole protein mass spectra for Profinity-purified GRK1 indicates an expected mass for fully farnesylated GRK1. The whole protein charged states with m/z ratios are indicated. (B) Deconvolution of the mass spec data result in a predominant peak at 62843 Daltons (~90%, with the minor deconvolution peak), in close agreement with an expected mass for a farnesylated, full length GRK of 62840.6 Daltons. In contrast, 62933.9 Daltons would be expected for the unmodified GRK1. These results indicate that the majority of our purified GRK1 is properly isoprenylated and non-phosphorylated.

Figure 3.4 Profinity eXact purified GRK1 is highly functional and can phosphorylate rhodopsin in a light dependent manner.

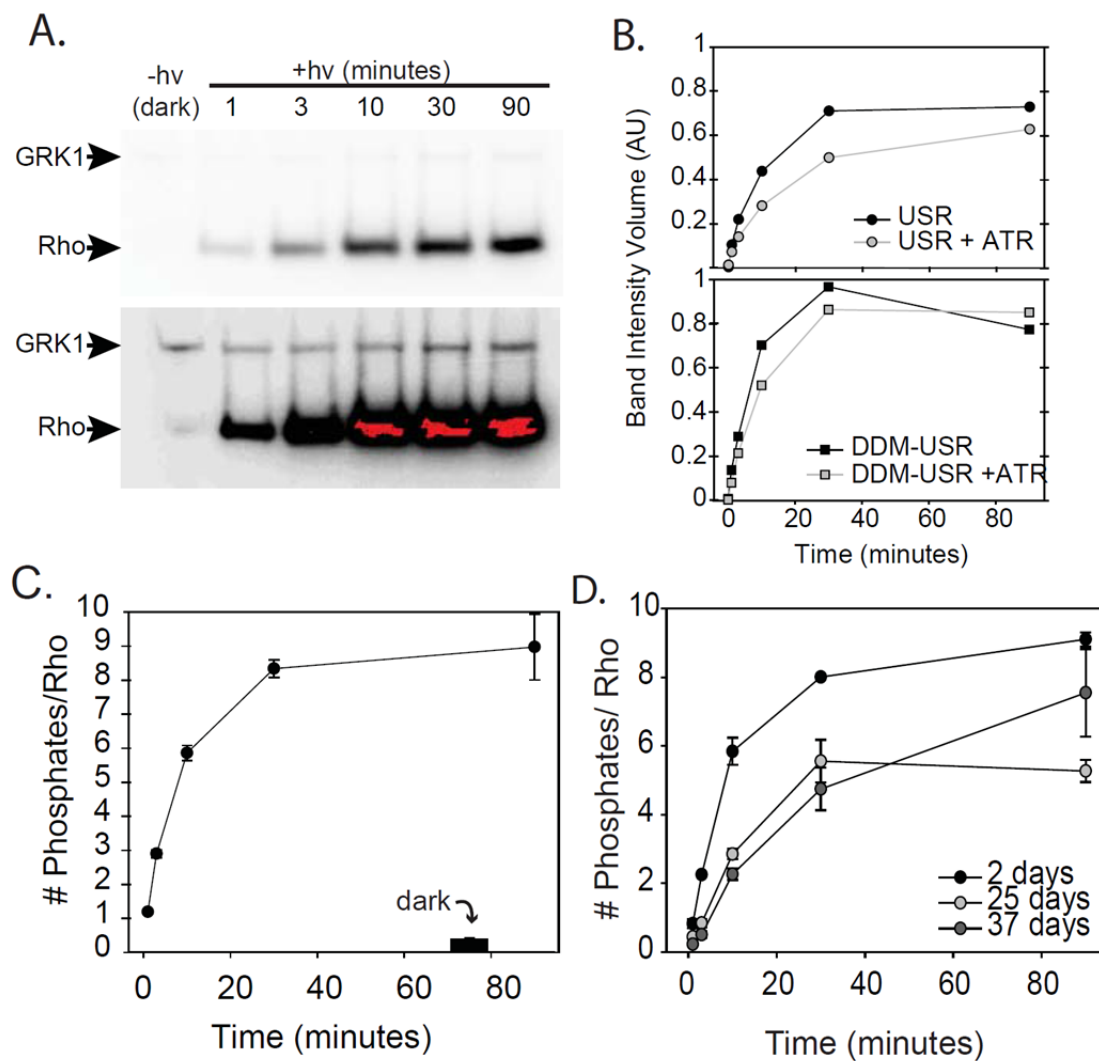


Figure 3.4 Profinity eXact purified GRK1 is highly functional and can phosphorylate rhodopsin in a light dependent manner. **(A)** GRK1 phosphorylation of DDM-solubilized, urea-stripped-ROS (USR) rhodopsin as determined from autoradiography of SDS-PAGE gels. GRK1 (0.3 μ M) was incubated with DDM-solubilized-USR rhodopsin (1 μ M) in the presence ATP (0.2 mM ATP containing trace 32 P-ATP). The samples were light activated, then aliquots removed and quenched in Applebury SDS-PAGE loading buffer at the indicated times (dark, 1, 3, 10, 30 or 90 min), and subjected to SDS-PAGE analysis, followed by 32 P autoradiography. Robust light-dependent phosphorylation of rhodopsin is indicated by the increasing dark bands. Note that trace amounts of GRK1 autophosphorylation are not visible in the properly exposed autoradiogram (top), but over-exposure of the phosphor screen (bottom) does reveal some trace amount of wild type GRK1 autophosphorylation. **(B)** Comparison of the ability of the purified GRK1 to phosphorylate urea-stripped rod outer segment (USR) rhodopsin containing membranes (left panel, black circles) and DDM-solubilized USR membranes (right panel, black squares). Intensities were calculated from autoradiogram band intensities of the SDS-PAGE gels using Quantity one software. The effect of 5-fold molar excess additional all-trans retinal (ATR) (white circles and squares) was also assessed, and did not appear to strongly effect receptor phosphorylation. **(C)** The Profinity eXact-purified GRK1 shows robust phosphorylation of DDM-solubilized USR in a light-dependent manner, with \sim 8 phosphates per receptor (black circles), and essentially no phosphorylation in the dark. **(D)** GRK1 purified using the Profinity eXact method remains active for up to 5 weeks when stored at 4°C in GRK1 reaction buffer (20 mM HEPES pH 7.5, 7.5 mM MgCl₂, 2 mM EDTA).

Figure 3.5 Presence of acidic phospholipids restores full phosphorylation of DDM-purified rhodopsin by full length, Profinity-purified GRK1.

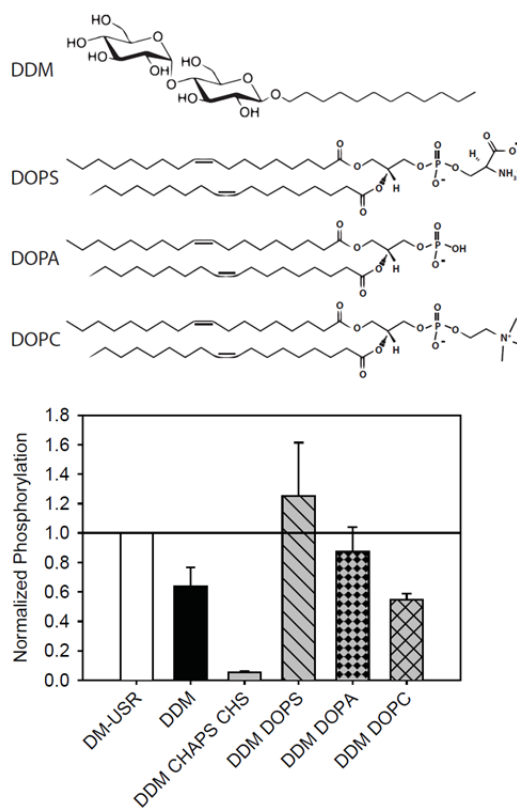


Figure 3.5 Presence of acidic phospholipids restores full phosphorylation of DDM-purified rhodopsin by full length, Profinity-purified GRK1. (A) The structure of DDM detergent and phospholipids used are shown. DOPS and DOPA have negatively charged, or acidic, head groups, while DOPC has a positively charged head group. (B) DDM purification of bovine rhodopsin reduces the ability of GRK1 to phosphorylate the receptor. We tested the effect of adding back certain phospholipids on GRK1 using the SDS-PAGE/autoradiography approach, and not the 96-well filter binding approach in order to ensure that any observed differences were not due to differential binding to the filters. The amount of phosphorylation has been normalized to the DDM-solubilized rhodopsin level. We find that incubation in CHS/CHAPS severely inhibits phosphorylation, which could be due to the destabilization of MII rhodopsin in this CHS/CHAPS environment. Addition of DOPS or DOPA to the DDM-purified rhodopsin restores native-like phosphorylation levels, while the addition of DOPC does not increase the phosphorylation above the DDM-purified level.

Figure 3.6 GRK1 mutant lacking the primary autophosphorylation sites, GRK1 S488D/T489D, is fully functional.

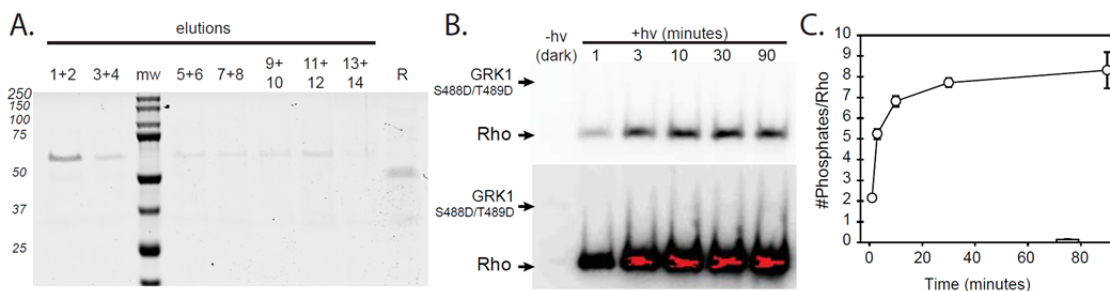


Figure 3.6 GRK1 mutant lacking the primary autophosphorylation sites, GRK1 S488D/T489D, is fully functional. (A) To limit GRK1 autophosphorylation, the two major autophosphorylation sites in GRK1, S488 and T489 were both mutated to D residues based on previous results from Palczewski et al (34, 35). The mutant expressed as well as the wildtype GRK1 in COS-1 cells, and could be purified using the Profinity method, as shown in SDS-PAGE gel. (B) The purified GRK1 S488D/T489D also showed robust light-dependent ability to phosphorylate DDM-solubilized USR, as indicated by increasingly dark bands. Note that the GRK1 S488D/T489D does not autophosphorylate in either the properly exposed autoradiogram (top) nor the overexposed autoradiogram (bottom), unlike the signal observed for wild type GRK1 (Fig 3.4A). (C) The GRK1 S488D/T489D phosphorylates DDM-solubilized with up to 8 phosphates/receptor, and shows very little dark-state receptor phosphorylation as determined using the filter binding assay.

Figure 3.7 Whole protein mass spectra analysis of GRK1 S488D/T489D indicates that it is farnesylated.

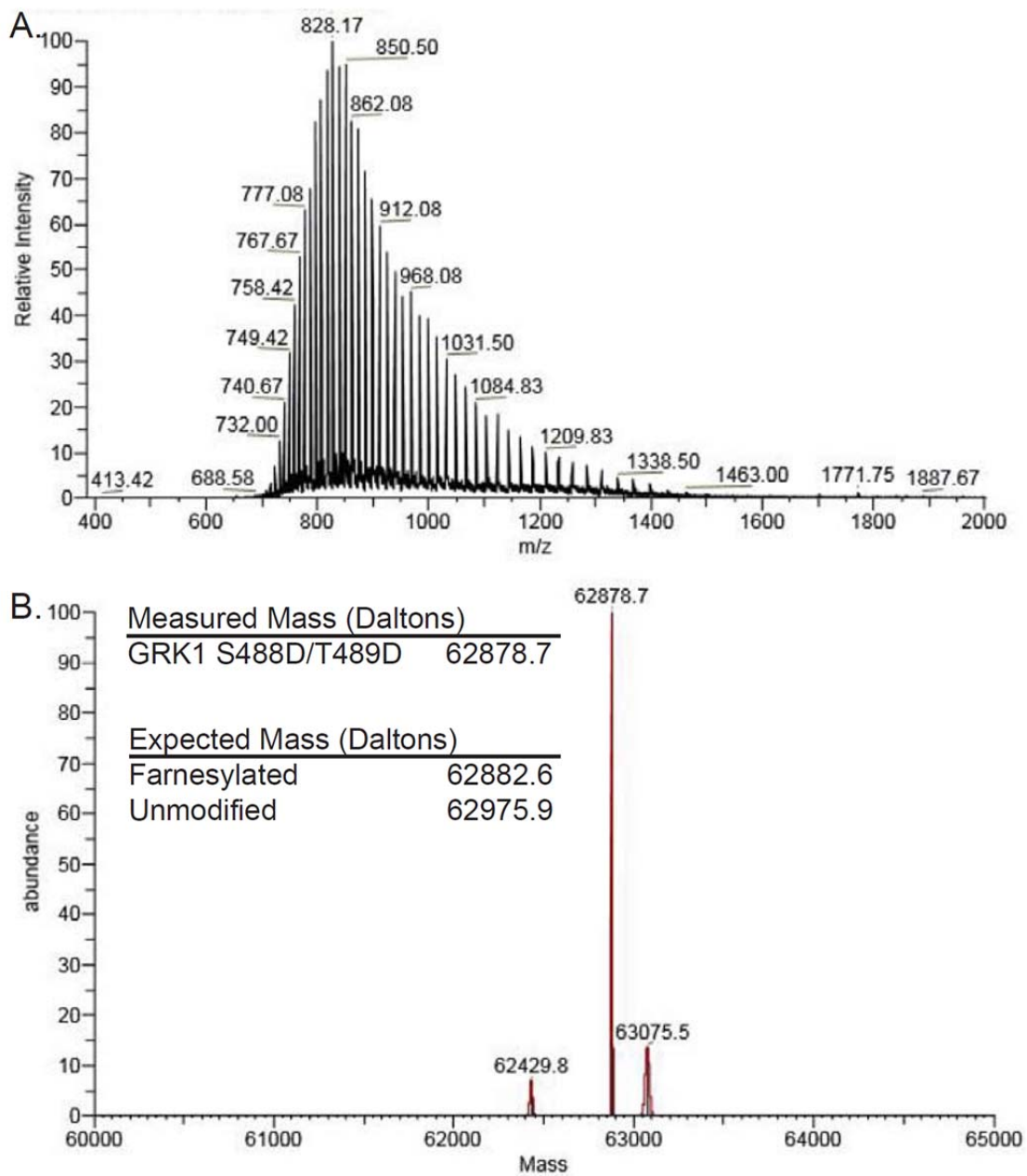


Figure 3.7 Whole protein mass spectra analysis of GRK1 S488D/T489D indicates that it is farnesylated. (A) Whole protein mass spectra for Profinity-purified GRK1 S488D/T489D indicate an expected mass for fully farnesylated GRK1 S488D/T489D. The whole protein charged states with m/z ratios are indicated. (B) Deconvolution of the mass spec data result in a predominant peak at 62879 Daltons (~82%, with the minor deconvolution peak), in close agreement with an expected mass for a farnesylated, full length GRK1 S488D/T489D of 628728.6 Daltons. In contrast, 62975.9 Daltons would be expected for the unmodified GRK1 S488D/T489D. These results indicate that the majority of our purified GRK1 S488D/T489D is properly isoprenylated and non-phosphorylated.

Figure 3.8 Profinity-purified GRK1 can phosphorylate a ligand-binding GPCR, the human cannabinoid receptor, CB1, in an agonist-dependent manner.

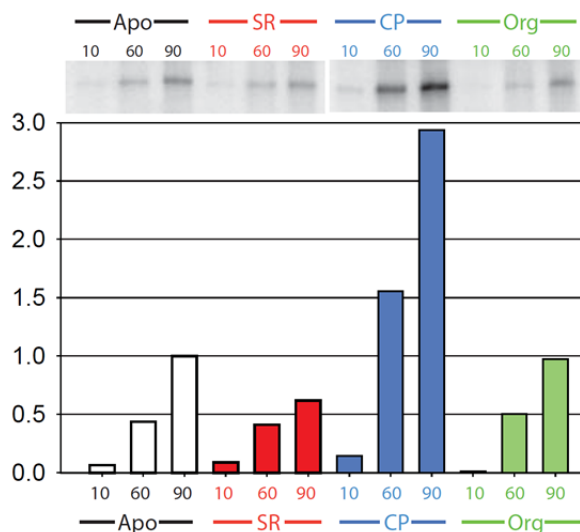


Figure 3.8 Profinity-purified GRK1 can phosphorylate a ligand-binding GPCR, the human cannabinoid receptor, CB1, in an agonist-dependent manner. Ligand-dependent phosphorylation of human CB1 by wild type GRK1 was monitored by SDS-PAGE autoradiography, with vehicle (labeled Apo on the autoradiogram and in black bars in the graph), 20 μ M of the antagonist SR141716 (labeled as SR in red in the autoradiogram and in red bars on the graph), 20 μ M of the agonist CP55,940 (labeled as CP in blue on the autoradiogram and in blue bars on the graph), or 20 μ M of the allosteric ligand Org 27569 (labeled as Org on the autoradiogram and in green bars on the graph). These data indicate GRK1 recognizes both the basal activity of CB1, as indicated by the decreased phosphorylation of the antagonist-containing experiment, as well as the agonist-activated state, as receptor phosphorylation is increased in the presence of CB1 agonist.

Chapter 4: Evidence that the rhodopsin kinase (GRK1) N-terminus and the Transducin G α C-terminus interact with the Same “Hydrophobic Patch” on Rhodopsin TM5.

This chapter has been accepted for publication in the ACS journal Biochemistry (April 13, 2016). Some of the work described in Chapter 3 is also discussed in this Chapter in order to establish that the full length kinase used in this manuscript had wild type activity. As with Chapter 3, Dr. Larry David performed the whole protein mass spectrometry, Dr. Abhinav Sinha designed the purification method and performed initial experiments on the function of GRK1 purified using the Profinity eXact method, although his results are not contained in this manuscript. Dr. David Farrens contributed to the design and analysis of experiments as well as preparation of the manuscript.

Abstract.

Phosphorylation of G protein coupled receptors (GPCRs) terminates their ability to couple with and activate G proteins by increasing their affinity for arrestins. Unfortunately, detailed information regarding how GPCRs interact with the kinases responsible for their phosphorylation is still limited. Here, we purified fully functional GPCR kinase 1 (GRK1), using a rapid method and used it to gain insights into how this important kinase interacts with the GPCR rhodopsin. Specifically, we find that GRK1 uses the same site on rhodopsin as the transducin (G_t) G α C-terminal tail and the arrestin

“finger loop”, a cleft formed in the cytoplasmic face of the receptor upon activation. Our studies also show GRK1 requires two conserved residues located in this cleft (L226 and V230) that have been shown to be required for G_t activation due to their direct interactions with hydrophobic residues on the G_α C-terminal tail. Our data and modeling studies are consistent with the idea that all three proteins (G_t, GRK1 and visual arrestin) bind, at least in part, in the same site on rhodopsin and interact with the receptor through a similar hydrophobic-contact driven mechanism.

Introduction.

G protein coupled receptors (GPCRs) comprise a large class of membrane proteins that share a basic mode of signaling; once turned “on” (activated by a ligand), they induce heterotrimeric G proteins to exchange GDP for GTP, and transduce the appropriate signaling cascade. GPCRs are also turned “off” by a conserved process that first involves phosphorylation by a GPCR-kinase (GRK), then binding by a protein called arrestin, which sterically blocks further G protein binding and activation. The first GRK identified, called rhodopsin kinase or GRK1, phosphorylates rhodopsin, the dim-light sensing GPCR in the retina (*135*). GRK1 is a soluble enzyme that becomes associated with the membrane when rhodopsin is light activated (*24, 43, 136*) and subsequently phosphorylates rhodopsin cytoplasmic residues at up to nine Ser/Thr phosphorylation sites (*137, 138*).

While the structures of rhodopsin (*139-143*) and GRK1 have been solved (*84, 144-146*), specifically how the two proteins interact is still not well defined. GRK family

members are thought to use their N-termini to recognize and bind cognate receptors (83, 172-175), in part through hydrophobic residues located in this region (83, 84, 149), analogous to how G proteins bind using the C-terminus of their G_{α} subunits (143, 176). The C-tail of the kinase has also been implicated in mediating receptor induced activation of GRKs, possibly by forming a receptor docking site in conjunction with the small lobe of the kinase domain (148). In the absence of high-resolution co-structures of various rhodopsin-GRK1 complexes, we have begun studying how these two proteins interact using biochemical methodologies, primarily mutagenesis coupled with site-directed labeling methods.

Here, we report new insights into how GRK1 interacts with rhodopsin. Specifically, we show that GRK1 binds to the same site on rhodopsin as does both the transducin (G_t) alpha C-terminal tail (106, 142, 177-179), and the visual arrestin “finger loop” (22, 109, 154, 158, 180-188), a cleft that is exposed in the cytoplasmic face of the receptor upon activation-induced movements of transmembrane helices 5 and 6 (TM5 and TM6). Our results indicate that GRK1 not only binds to this shared site but, like G_t and visual arrestin (154, 176), requires interactions with a “hydrophobic patch” found in this cleft, suggesting that a similar hydrophobic contact-driven mechanism may underlie the affinity of all three proteins.

Finally, we note that in the course of these studies, we developed a rapid way to purify GRK1. Our method was based on the Profinity eXact purification system, an approach that has been similarly used to streamline the purification of G_t (121) and arrestin (152, 154). Advantages of our new approach are numerous – the resulting purified GRK1 is tag-free, full length, and farnesylated (the latter required for GRK1 membrane association

and full kinase activity (38, 39)). As a result, the GRK1 produced using this method appears to be the most fully functional recombinant expressed GRK1 in comparison to other published methods (see Supporting Table 1). In our hands, this quick and simple way to purify GRK1 is well suited to multiplexing, a helpful feature for high-throughput site-directed labeling based studies (71).

Materials & Methods.

Materials.

All restriction enzymes, ligase, and DNA polymerase were from New England Biolabs. Tissue culture media was purchased from HyClone, while polyethyleneimine was from Polysciences, Inc. n-dodecyl β -D-maltoside (DDM) was purchased from Anatrace. 1D4 antibody was obtained from the Monoclonal Antibody Core at the Vaccine and Gene Therapy Institute of Oregon Health and Science University. Peptides were purchased from Genscript. Protease Inhibitor Cocktail (EDTA Free) was purchased from Roche Diagnostics. Profinity eXactTM column was from Bio-Rad. Amicon Ultra protein concentrator (10 kDa cut-off) was from Millipore. [³²P]-ATP was obtained from Perkin Elmer. Frozen bovine retinas were obtained from Lawson and Lawson, Inc. (Lincoln, NE). GBX red light filters were purchased from Eastman Kodak Co. Band pass filters and long pass filters were purchased from Oriel (Stratford, CT), while cuvettes were purchased from Starna. All other chemicals and reagents were obtained from Sigma-Aldrich.

Buffers.

Solubilization buffer is 20 mM HEPES pH 7.5, 250 mM Na Acetate, 1 mM EGTA, 0.125% DDM, 1 mM Benzamidine, 20 $\mu\text{g}/\mu\text{L}$ Leupeptin, 1X Complete protease inhibitor, and 1 mM PMSF. Wash Buffer 1 is 20 mM HEPES pH 7.5. Wash buffer 2 is 20 mM HEPES pH 7.5 and 200 mM Sodium Acetate. Wash buffer 3 is 20 mM HEPES pH 7.5 and 0.3% DDM. Wash buffer 4 is 20 mM HEPES pH 7.5 and 0.3% Tween-20. Wash buffer 5 is 20 mM HEPES pH 6.5. Wash buffer 6 is 20 mM HEPES pH 7.5 and 5 mM EGTA. Wash buffer 7 is 20 mM HEPES pH 7.5 and 1 mM Calcium Acetate. Wash buffer 8 is 20 mM HEPES pH 7.5 and 300 mM Ammonium Sulfate. GRK1 Reaction Buffer is 20 mM HEPES pH 7.5, 75 mM MgCl_2 , and 2 mM EDTA.

Cloning of rhodopsin kinase.

To enable purification using the prosubtilisin affinity tag method, the Profinity-tagged GRK1 was created by subcloning the 77-amino acid long ProR8FKAM subtilisin BPN¹ prodomain coding sequence (121, 151) into a pCMV5-GRK1(His)₆ plasmid obtained from the Khorana group (147). This involved removing the N-terminal hexahistidine tag from rhodopsin kinase, and replacing it with the ProR8FKAM sequence using overlap extension PCR, while maintaining the Kozak sequence (GCCACC) preceding the start codon of the prodomain.

Expression and Purification of Profinity-tagged rhodopsin kinase.

COS-1 cells were transfected with 30 μg pCMV5 Prosubtilisin- GRK1 construct and 100 μg polyethyleneimine (PEI) per 15 cm plate. To ensure proper posttranslational

modification of the kinase (38), the transfected cells were given fresh media containing 4 mM (\pm) mevalonolactone 16-18 hours post transfection and allowed to grow for 44-48 hours. Subsequently, the transfected cells were harvested in solubilization buffer lacking detergent and protease inhibitors. Cell pellets were washed once in the same buffer, then resuspended in 2 mL of solubilization buffer per plate containing 20 units of DNaseI, 1 mM MgSO₄, and protease inhibitors, and homogenized for 60 strokes using a Dounce homogenizer. Homogenates were solubilized for 1 hour by the addition of 0.125% DDM and nutated at 4°C. The lysates were clarified by centrifugation at 100,000 xg for 45 minutes, and the supernatants were passed through a 0.45 μ m filter before the addition of 1 mM DTT.

The chromatographic purification step involved loading the sample prepared as described above onto a 1 mL Profinity eXact column, equilibrated with Wash Buffer 1. The column is washed with 30 mL Wash Buffer 3, and then washed successively with 15 mL of each of the following: Wash Buffers 4, 5, 6, 7, and 8, then 30 mL Wash Buffer 1, 15 mL Wash Buffer 2, and finally 15 mL Wash Buffer 1. GRK1 was eluted with wash Buffer 1 containing 100 mM Sodium Fluoride. Elution fractions containing purified GRK1 were identified by SDS-PAGE as a band at ~63,000 Daltons. These fractions were pooled, concentrated and buffer exchanged into GRK1 Reaction Buffer with an Amicon ultra 10 kDa centrifugal filter, after which the concentration was calculated based on the absorbance at 280 nm and an extinction coefficient of 64455 (Protparam Swissprot), and stored at 4°C for use.

Isolation of ROS membranes and preparation of urea stripped ROS.

ROS were isolated from bovine retinas as described previously (155, 156). All steps were carried out under dim red light. Rhodopsin concentration was assessed by difference spectra in the presence of hydroxylamine. Stocks were snap-frozen and stored at -80 °C. Urea stripped ROS (USR) was prepared as described (157). Briefly, this involved washing ROS membranes consecutively with 5 M urea in 50 mM Tris pH 8 containing 50 mM EDTA. The membranes were then centrifuged at 13,000 x g for 15 min and washed five times with 50 mM Tris pH 7.4 before snap-freezing in liquid nitrogen.

Expression and Purification of wild-type and mutant rhodopsin.

Wild-type and mutant rhodopsins were transiently expressed in HEK 293S GnTI- cells using the calcium phosphate precipitation method (189). Briefly, 15 cm plates of ~80% confluent cells were transfected with 54 µg of receptor plasmid DNA and 6 µg of pRSVTag plasmid encoding the large T antigen required for translation of the pMT4 vector in this cell line. Plasmid DNA was incubated in a buffer consisting of 50 mM [N,N[bis(2-hydroxyethyl)-2-aminoethanesulphonic acid]], 250 mM NaCl, and 1.5 mM Na₂HPO₄ pH 7.02, then mixed 1:1 with sterile 0.25 M CaCl₂. Transfections were washed after 16 hours with DMEM and fed with naïve DMEM containing FBS, PenStrep, and Glutamine. Receptors were purified using 1D4 immuno-affinity chromatography as described (106).

Rhodopsin kinase activity assay.

Phosphorylation assays containing 1 μ M of DDM-solubilized rhodopsin was incubated with 0.3 μ M GRK1 in GRK1 Reaction Buffer, containing 0.2 mM ATP (with 32 P-ATP as a radioactive tracer) and 1 mM DTT, at room temperature (~ 24 °C), typical reaction volume was 50 μ L. Assays were carried out by illuminating reactions with continuous light passed through a 500 nm long-pass filter, then removing aliquots at different time points (dark, 1, 3, 10, 30, or 90 min) to quench the reaction by addition of TCA to 20% (for filter binding analysis described below). For the “dark” time points, an aliquot of the reaction is set aside before illumination and kept in the dark for the duration of the experiment, and quenched after 95 minutes in the dark.

To determine the phosphorylation kinetics and the average number of phosphates incorporated on to each receptor, a filter-binding method was developed (described below). This involved loading the TCA-precipitated samples onto a 96-well PVDF filter plate followed by extensive washing with GRK1 Reaction Buffer. The filters were removed from the plate and incubated in scintillation fluid. After scintillation counting, the amount of 32 P incorporation was determined by comparing the counts to a standard curve generated using known amounts of 32 P-ATP. The number of phosphates per receptor (# phosphates/receptor) was determined by adjusting for the ratio of 32 P/ 31 P-ATP used in the experiment and dividing total moles of P_i by moles of receptor present in the reaction mix.

Kinetics parameters.

Specific activity was calculated using the average number of phosphates per receptor at the final time point of 90 minutes and the amount of kinase used in each reaction. The total number of phosphates transferred at 1, 3, and 10 minutes were plotted and fit with a straight line, the slope of which is taken to be the initial rate. K_m and V_{max} were calculated from the average of the initial rate of phosphoryl transfer by GRK1 in the presence of 1, 10, 20, or 40 μM DDM-solubilized USR from 3 separate experiments. Unfortunately, the K_m affinity parameter for rhodopsin hydrophobic patch mutants θ L226A or θ V230A could not be reliably assessed as the purified receptor concentrations were too far below the K_m , resulting in very noisy data.

Whole protein mass spectroscopy analysis.

0.5 μg of the Profinity-purified rhodopsin kinase was injected at 20 $\mu\text{L}/\text{min}$ in mobile phase A containing water, 0.1% formic acid and bound to a 5 μL bed volume Opti-Trap protein trap (Optimize Technologies, Oregon City, OR). Following washing for 5 min, the trap was switched on-line to a 1.0 x 250 mm C4 column (214 MS C4, Vydac, Hesperia, CA) and protein eluted using a 30 min linear gradient of 7.5 to 60% mobile phase B containing acetonitrile, 0.1% formic acid. Protein masses were determined by electrospray ionization mass spectrometry using a LTQ linear iontrap mass spectrometer (Thermo Scientific, San Jose, CA), and data collected in profile mode from m/z 400-2000 with averaging of 20 μscans . Spectra from GRK1 eluting at 26 min into the gradient were averaged and processed using Protein Deconvolution 4.0 software (Thermo Scientific).

G_{ta} C-terminal peptide inhibition of phosphorylation.

Reactions were carried out as described above, except that receptors were pre-incubated with 100 μ M high-affinity G_{ta} C-terminal peptide (sequence VLEDLKSGLF (176)) for 20 minutes before adding kinase and subsequent light activation.

GRK1 N-terminal peptide inhibition of phosphorylation.

Reactions were carried out as described above, except that receptors were pre-incubated with 500 μ M GRK1 N-terminal peptide (sequence MDFGSLETVVAV) for 20 minutes before adding kinase and light activation. Initial rates were calculated from phosphate incorporation at 1, 3, and 10 minutes after light activation.

Retinal Release Assay.

The stability of MII rhodopsin was assessed by fluorescence as described previously (21). All fluorescence measurements were made using a PTI fluorescence spectrophotometer fitted with a 295 nm LED (OceanOptics LLS-295) (190). The temperature was held at 20 °C using a water-cooled PTI four-position cuvette turret connected to a circulating water bath (VWR Scientific). The samples were placed in a 4 mm fluorescence cuvette (minimum volume 45 μ L), and the intrinsic tryptophan fluorescence was measured using a λ_{ex} of 295 nm passed through a 98% neutral density filter to prevent photobleaching, and emission monitored at 330nm. After an equilibration of the dark-state fluorescence measurement, the samples were bleached with >500 nm light for 20 s, and fluorescence emission was measured over time. After 90 min,

hydroxylamine (30 mM final concentration) was added to cleave the Schiff base and convert all the remaining photoproducts to opsin and yield the maximal fluorescence.

Assessing visual arrestin binding to rhodopsin via retinal trapping experiment.

The effect of mutating rhodopsin “hydrophobic patch” residues on arrestin binding was studied by a retinal release assay, described above, which is based on the observation that arrestin binding to MII rhodopsin inhibits release of retinal after light activation (22). Constitutively active visual arrestin R175E was added at twice the molar concentration of receptor and incubated with 0.25 μ M “wild-type” (WT₀) or the “hydrophobic patch” mutant rhodopsin in a reaction mixture containing 20 mM HEPES, 140 mM NaCl, 0.05% DDM, and 0.3 mM DOPS (pH 7.4) in the dark for 30 min on ice (109).

Measurement of G_t activation.

G_t activation was monitored by changes in G_t tryptophan fluorescence upon addition of GTP γ S (191). Each measurement contained 250 nM G_t, 10 mM Tris pH 7.4, 100 mM NaCl, 2 mM MgCl₂, 1 mM DTT, 0.01% DDM, and was incubated in a 4 mm jacketed cuvette (minimum volume 225 μ L) with stirring for 5 minutes. Light activated rhodopsin was added to 5 nM final concentration and fluorescence was monitored to ensure a stable baseline. Finally, 500 μ M GTP γ S was added at t=0 and the increase in G_t fluorescence was measured for 20 minutes. Fluorescence was measured using a PTI Quanta Master fluorometer (PTI, New Jersey), with excitation at 295 nm (1 nm slit width) and emission

at 330 nm (6 nm slit width) over time. Reactions were held at 10 °C using a water-jacketed cuvette holder.

PyMPO labeling V250C.

Mutant rhodopsin θ V250C was expressed and purified as described above. V250C was used to detect binding of different peptides to a cleft of the cytoplasmic face of rhodopsin, as the cysteine at site 250 only becomes exposed, and thus reactive to the bulky fluorophore PyMPO, after light activation (176, 192). Experiments involve incubating 2 μ M V250C rhodopsin in the dark-state with 500 μ M peptide (1D4 peptide, Gt α CT peptide, or GRK1 NT peptide) in DMSO (10% final concentration) for 20 minutes in GRK1 reaction buffer, then adding fresh PyMPO fluorophore to 5 μ M, and an aliquot was removed and protected from light. The remaining sample was exposed to >500 nm light for 30 seconds and samples were quenched in 500 mM cysteine at 30 seconds and 90 seconds after light activation. Samples were mixed with SDS-PAGE gel loading buffer and subjected to electrophoresis on an 8% Tris-Tricine gel. Incorporation of fluorophore was measured using a BioRad gel doc using 365 nm light to illuminate the gel, and later Coomassie stained to compare total amount of protein in each lane.

Sequence analysis and modeling of GRK1-rhodopsin binding.

Analysis and visualization of structures was performed using Chimera package from UCSF (193). Human GRK1-7 and bovine GRK1 N-terminal sequences were aligned using Clustal omega from EMBL. Sequence alignment and conservation among human

non-olfactory class-A GPCRs at sites 5.60-5.68 were built using the GPCR database (2, 3, 194, 195) and the sequence logo was generated using the Weblogo server (196, 197).

A 10-mer alpha helix was generated using the N-terminus of bovine GRK1 and manually docked on to the structure of the G_{ta} CT peptide bound to rhodopsin (PDB:4J4Q) (198), and was submitted to the FlexPepDock server (199, 200). Representative structures from the two resulting binding modes of the GRK1 NT 10-mer (G_{ta} CT-like and visual arrestin finger loop-like) were used to generate models of the interaction full-length GRK1 and rhodopsin. To do this, the primary sequence of GRK1 was threaded on to the structure of GRK6 (PDB:3NYN) (83) and the N-terminus of the resulting structure was matched to the peptide conformation in the GRK1 NT peptide binding structure using Chimera from UCSF (193). This structure was submitted to the ROSIE docking server from Rosetta (201-203). Solvent accessibility was calculated using the POPS server from MathBio (204-207).

Results.

The Profinity eXact purification method can be used to rapidly purify tag-free, full-length farnesylated rhodopsin kinase.

GRK1 purified using the Profinity eXact method results in >80% purity from a single step purification, as indicated by Coomassie-stained SDS-PAGE (Figure 4.1B) with a total yield of ~3-5 μg GRK1 per 15 cm plate of transfected COS-1 cells. GRK1 purified using this method elutes from a heparin sepharose column with ≥ 300 mM NaCl (Figure 3.2B), indicating it is almost exclusively GRK1 lacking autophosphorylation (32).

Mass spec analysis of the GRK1 (Figure 3.3) indicates a mass of 62843 Daltons, a value well within experimental error of the expected theoretical mass of 62840.6 Daltons for farnesylated GRK1. Note that the expected mass of farnesylated GRK1 is actually lower than for non-farnesylated protein (62933.9 Daltons), due to the removal of the 3-terminal residues in the CaaX isoprenylation motif and subsequent carboxyl methylation that occurs during the farnesylation process. Based on the results above, we conclude that GRK1 thus produced is fully farnesylated with minimal autophosphorylation.

Purified wild type GRK1 is functional and can phosphorylate DDM-solubilized USR rhodopsin.

The wild type (WT) GRK1 purified using the Profinity method can phosphorylate DDM-solubilized, urea-stripped ROS (USR) rhodopsin, yielding ~8 phosphates per receptor (Figure 4.1C). Further analysis showed a specific activity of 280 ± 53 pmole phosphate $\text{min}^{-1} \text{mg}^{-1}$ of GRK1 and an initial rate of 0.6 phosphates receptor $^{-1} \text{min}^{-1}$ (Table 4.1). The Profinity-purified GRK1 shows a K_m for DDM-solubilized USR of 2.0 ± 1.3 μM (compared to a K_m of ~4 μM for WT GRK1 from bovine retinae (33, 170, 208)), a V_{max} of 2100 ± 620 nmole $\text{min}^{-1} \text{mg}^{-1}$ (compared to a V_{max} of 650-700 nmole $\text{min}^{-1} \text{mg}^{-1}$ for wt GRK1 from bovine retinae (33, 208), and a K_{cat} of $39 \pm 11 * 10^{-3} \text{ s}^{-1}$, resulting in a K_{cat}/K_m of $20 \mu\text{M}^{-1} \text{ s}^{-1}$ (Table 3.1) (compared to K_{cat}/K_m of $0.2 \mu\text{M}^{-1} \text{ s}^{-1}$ for WT GRK1 purified from bovine retinae (208)).

GRK1 phosphorylates DDM-purified bovine rhodopsin almost as efficiently as DDM-solubilized USR.

We next checked the ability of our GRK1 to phosphorylate rhodopsin purified using a 1D4-based immunoaffinity approach. Since rhodopsin is eluted from the 1D4 immunoaffinity column by adding a 9-mer peptide corresponding to the rhodopsin C-terminal tail (the epitope to which 1D4 binds), we had to first assess if any 1D4 peptide remaining in the eluted samples could alter our receptor phosphorylation studies.

To do this, we compared the phosphorylation of two different bovine rhodopsin preparations – neither of which contained 1D4 peptide, DDM-solubilized USR (Figure 4.2A, white bars) and Con-A purified ROS rhodopsin in 0.05% DDM (Figure 4.2A, grey bars) to which we added increasing amounts of 1D4 peptide. No major effect was observed on GRK1-mediated phosphorylation. The results are consistent with the reported ~2-3 orders of magnitude lower affinity of GRK1 for peptides of this region than for the full receptor (33, 148, 170). From these data, we conclude that trace amounts of residual 1D4 peptide in purified samples are unlikely to impact our results. However, there was an overall reduction in the amount of phosphorylation in the DDM-purified sample to ~ 5 phosphates/rhodopsin, presumably due to the loss of the ROS lipids (compare Figure 4.2A white bars to grey bars).

Both the G_{α} C-terminal and the GRK1 N-terminal peptides block efficient GRK1 phosphorylation of rhodopsin.

To localize interaction sites between GRK1 and rhodopsin, we next tested if a transducin G_{α} C-terminus (G_{α} CT) peptide-mimetic could inhibit GRK1 phosphorylation

of rhodopsin. We chose this small peptide because, as noted in the Introduction, it binds directly inside a small area formed in the cytoplasmic cleft during rhodopsin activation (209), and induces no substantial changes in the protein backbone (142, 143, 198, 210-212). As shown in Figure 4.2B, pre-incubation with the G_{ta} CT peptide significantly blocks phosphorylation of the receptor, consistent with the idea that GRK1 needs access to the same site on rhodopsin in order to bind and phosphorylate the receptor. This inhibition is unlikely to be the result of the peptide acting directly on the kinase, since the G_{ta} CT peptide has been shown to also inhibit GRKs 2, 4, 5, and 7-mediated phosphorylation of rhodopsin but to not affect their ability to phosphorylate tubulin (213).

We next tested if a peptide corresponding to the GRK1 N-terminus (GRK1 NT) could similarly block the kinases' ability to phosphorylate rhodopsin. The GRK1 NT peptide inhibits initial rate of phosphorylation (Figure 4.2C), but does not strongly decrease the total number of phosphates per receptor ultimately achieved (Figure 4.2B), presumably because of a starkly lower affinity of the non-optimized GRK1 NT peptide for the receptor. These results suggest that both GRK1 NT and the G_{ta} CT peptide bind to the same site, but with the due to the fact that the GRK1 NT peptide could potentially be acting directly on the kinase itself, we next turned to a site-directed fluorescent labeling approach that avoided this issue.

Site-directed labeling studies suggest the G_{ta} C-terminus and GRK1 N-terminus share the same binding site.

We further tested the possibility of a shared binding site using a chemical labeling approach, in which we tested the ability of these peptides to protect a unique cysteine introduced on the inner face of rhodopsin TM6, at position 250. This mutant, V250C, constructed in a minimal-cysteine rhodopsin mutant background, called θ (214, 215), is only labeled by the cysteine-reactive fluorophore, PyMPO, when in the light-activated state (176, 192). Because we have previously found that the G_{ta} CT peptide binding protects this cysteine from labeling (176, 192), we tested if the GRK1 NT peptide could similarly block PyMPO labeling of V250C. Indeed, as shown in Figure 4.3B & C, both peptides blocked light-activated V250C PyMPO labeling, indicating that they both bind in a similar enough fashion to protect the cysteine at site 250.

We next used this approach to test if both the G_{ta} CT peptide and the GRK1 NT peptide require interactions with a key residue in a “hydrophobic patch” on TM5. Mutations of this residue in rhodopsin, L226, dramatically impair transducin activation (176, 216) and reduce affinity of G_{ta} CT peptide binding (176), presumably due to the loss of direct contact interactions between L226 and hydrophobic residues (L344 and L349) on the G_{ta} CT peptide seen in crystal structures (142, 143, 198, 210-212).

As can be seen in Figure 4.3B & C, introducing the L226A mutation reduced the ability of both peptides to protect V250C from PyMPO labeling. The effect was much more dramatic for the GRK1 NT peptide, consistent with its lower affinity for rhodopsin. These results support the idea that both peptides bind to the same area on the receptor,

and use a similar interaction for their binding affinity. We further explored this concept using functional assays and full-length proteins, as described below.

Mutations in a conserved hydrophobic patch used for G_t and visual arrestin binding block GRK1-mediated receptor phosphorylation.

We next tested the idea that all three affiliate proteins (G_t , visual arrestin, and GRK1) require a “hydrophobic patch” in the rhodopsin cytoplasmic cleft, made up of hydrophobic residues L226, T229, and V230 (Figures 4.3C & 4.5C). As noted above, some of these residues have already been shown to play a role in the binding affinity (176) and activation of G_t (Figure 4.4B), as well as arrestin binding (154). These experiments compared the ability of all three full length proteins to act on the hydrophobic patch mutants L226A, T229A and V230A, as well as wildtype (WT), all in the same limited-cysteine background (θ) used in Figure 3. Importantly, all three “hydrophobic patch” rhodopsin mutants are WT-like in their ability to bind retinal and form chromophore (106, 154), and show normal retinal release rates, indicating similar WT-like stability for their active states (Figure 4.4A).

Intriguingly, despite being WT-like in their basic properties, the hydrophobic patch rhodopsin mutants show marked differences in their ability to activate G_t (Figure 4.4B), be phosphorylated by GRK1 (Figure 4.4C), and be bound by visual arrestin (Figure 4.4D). For example, the WT θ receptor and T229A mutant activate G_t at similar rates (Figure 4.4B), are phosphorylated robustly by GRK1, and exhibit similar rates of phosphorylation (initial rates of 0.2 phosphates receptor⁻¹ min⁻¹, specific activities of 190 ± 30 and 170 ± 26 pmole phosphate per minute per mg of kinase, and K_m of 3.1 ± 0.12

and $3.2 \pm 0.24 \mu\text{M}$, respectively). Both WT₀ and, to a lesser degree, T229A rhodopsin are also bound by visual arrestin R175E, as indicated in the visual-arrestin mediated “retinal trapping” shown in Figure 4.4D.

In contrast, neither L226A nor V230A rhodopsin are able to robustly activate G_t (Figure 4.4B), and phosphorylation of the L226A and V230A mutants was strikingly decreased, with initial rates of 0.02 and 0.06 phosphates receptor⁻¹ min⁻¹ and specific activities of 49 ± 11 and 64 ± 14 pmole phosphate min⁻¹ mg⁻¹ of kinase, respectively (Table 4.1 and Figure 4.4C). Interestingly, while visual arrestin R175E binding was also impaired for the L226A mutant (unable to trap retinal in the L226A rhodopsin mutant), as judged by this assay, the V230A rhodopsin mutant was able to bind arrestin (Figure 4.4D). The implications of these results are discussed below.

Discussion.

Below, we discuss our results in developing a new way to purify highly functional GRK1 and testing if it uses the same binding site on rhodopsin as G_t and visual arrestin.

A rapid way to purify fully functional GRK1.

We find the Profinity eXact purification method yields full-length GRK1 that has wildtype-like functionality. A key advantage of this approach (Figure 4.1) is that it yields a tag-free, full length GRK1, since during the elution step the prosubtilisin purification tag remains on the column after proteolytic cleavage by the resin-bound protease (40-42, 52). Thus, any complications of a remaining “tag” might have on kinase interactions with rhodopsin are avoided. Moreover, the presence of the full C-terminus enables proper

isoprenyl post-translational modification, avoiding the decreased activity seen for kinase lacking this critical farnesylation site (38). We find the GRK1 expressed in the presence of mevalonolactone (43, 53, 54) and purified with the Profinity eXact method is properly farnesylated, exhibiting a mass of 62843 Daltons (Figure 3.3), compared to a theoretical mass of 62840.6 Daltons for the modified protein (38, 55).

The GRK1 thus expressed and purified also has native-like ability to phosphorylate wild-type rhodopsin, incorporating ~ 8 phosphates per rhodopsin on average (Figure 4.1C), well above the reported 3 phosphates required for high affinity arrestin binding (56-58). Compared to the WT GRK1 purified from bovine retina (1, 50, 51), our GRK1 exhibits a similar K_m for DDM-solubilized USR ($2.0 \pm 1.3 \mu\text{M}$, Table 1). It also displays a V_{max} ($2200 \pm 620 \text{ nmole min}^{-1} \text{ mg}^{-1}$) that is at the high-end of the range of maximal reaction velocities for WT GRK1 from other recombinant expression and purification systems (14, 59), and is higher than reported values for bovine GRK1 ($650\text{-}700 \text{ nmole min}^{-1} \text{ mg}^{-1}$ (33, 208)). Interestingly, we find that our purified rhodopsin in DDM micelles shows decreased average phosphorylation levels compared to DDM-solubilized ROS rhodopsin (~ 5 phosphates/receptor vs ~ 8), perhaps due in part to the lack of native ROS lipids and sterols present in the former. Based on these results we conclude that the Profinity-purified GRK1 behaves fully like wild-type kinase. We next used this protein to identify a key interaction between GRK1 and its substrate, rhodopsin.

GRK1 shares a common site of binding on rhodopsin with the G_{ti} C-terminus.

Our overarching goal here was to test the hypothesis that GRK1, G_t, and visual arrestin all share a common binding site on rhodopsin—a cleft that becomes exposed on the cytoplasmic face of the receptor upon activation. First, we tested if GRK1 activity is blocked by a high-affinity peptide mimetic of the transducin (G_t) G_α C-terminus (called G_{ti} CT) (106, 142, 177, 178, 210) and a peptide fragment of the GRK1 N-terminus. Because the G_{ti} CT 9-mer binds tightly within the exposed cytoplasmic cleft and does not protrude (80, 142, 143, 210-212), the impact of this peptide's potential competition with GRK1 is limited to the ~1300 Å³ space it occupies within the cytoplasmic cleft. The fact that this peptide dramatically inhibits rhodopsin phosphorylation (Figure 4.2B) supports the hypothesis that GRK1 needs access to this same specific site on rhodopsin. We assume this inhibition is due to direct competition with this binding site on rhodopsin and not to some effect of the G_{ti} CT on GRK1 itself, since this peptide has also been shown to inhibit the ability of other GRK family members (GRK2, GRK5, GRK6, and GRK7) ability to phosphorylate rhodopsin, but not tubulin (213).

We used a site-directed labeling approach to further resolve this interaction. As shown in Figure 4.3, incubation with a 12-mer peptide corresponding to the N-terminus of GRK1 protects rhodopsin V250C from labeling with the bulky fluorophore PyMPO. This inhibition is similar to the previously observed effect of the G_{ti} CT peptide (176), also shown in Figure 4.3. These results further suggest that the binding site for G_{ti} CT and the GRK1 NT overlap on rhodopsin. The fact that binding of both peptides was ablated by a single leucine to alanine mutation (L226A) within this cleft suggests that both share a

similar mechanism of binding, a concept we next explored using full length proteins (discussed below).

GRK1 requires residues L226 and V230 on the rhodopsin cytoplasmic face for efficient receptor phosphorylation.

We further localized where GRK1 and rhodopsin interact by testing the idea that GRK1 requires a “hydrophobic patch” within the rhodopsin cleft for binding. Previously, we found that this site, comprising residues L226 and V230, and to a lesser extent T229 (Figures 4.3 and 4.5C) plays a role in the binding affinity of G_t . Mutating any of these residues to alanine reduces the affinity between the $G_{t\alpha}$ CT peptide and rhodopsin by ~ 3 kcal/mol (176). Importantly, the fact that these mutations do not block binding, but simply shift affinity, argues that differences are not likely due to altered conformation of the cytoplasmic face upon activation, although we have not directly ruled that out. Similarly, we previously found that visual arrestin binding, which involves insertion of its “finger loop” into the rhodopsin cytoplasmic cleft (154, 181, 186, 217-219), also derives part of its binding affinity due to interactions with residue L226 (154).

Thus we compared the ability of GRK1 to phosphorylate hydrophobic patch mutants, L226A, T229A and V230A, as well as WT θ , and compared these results with the ability of these receptor mutants to activate G_t and bind visual arrestin. As reported previously (106, 154) and reconfirmed here, all three hydrophobic patch rhodopsin mutants are WT-like in their ability to bind retinal and form chromophore, and all show normal retinal release rates, indicating similar WT-like stability for their active states (Figure 4.4A).

We first re-tested if these hydrophobic residues are required for full G_t activation. As expected, the L226A mutation caused the greatest impairment followed by V230A, with much less effect for T229A. In contrast, although the L226A mutation impaired arrestin binding, the T229A and V230A mutations appear to have little effect, at least as determined by their ability to induce retinal “trapping” (Figure 4.4D), suggesting that arrestin binding may not require direct interaction with the latter two residues.

GRK1 phosphorylation of the rhodopsin hydrophobic patch mutants show striking differences. Both the WT θ and mutant T229A rhodopsins are robustly phosphorylated, with initial rates, specific activities, and affinities comparable to DDM-solubilized USR (Figure 4.4C, Table 4.1). In contrast, GRK1 phosphorylation of mutants L226A and V230A were dramatically impaired, with very little phosphorylation, decreased initial rates of phosphorylation, and lowered observed specific activity of the kinase (Table 4.1).

Together these results, coupled with the direct evidence that residue L226 is needed for GRK1 NT binding (Figure 4.3), suggest that the GRK1 N-terminus requires interactions with residues in the rhodopsin “hydrophobic patch” to enable receptor phosphorylation. Interestingly, these results also indicate that GRK1, G_t and arrestin all require residue L226 for efficient coupling with rhodopsin, GRK1 and G_t also require V230, suggesting subtle differences in how these proteins bind and orient in the cytoplasmic cleft of rhodopsin, a concept also proposed previously based on multi-alanine mutagenesis studies of rhodopsin’s intracellular loops (220, 221). We used modeling studies to explore this further.

Modeling studies incorporating our data suggest that the GRK1 N-terminus binds in the same location and orientation as the G α C-terminus.

Comparing GPCR sequences supports the idea that L226 and V230 in rhodopsin are key residues for all three signaling partners— as shown in Figure 4.5A, hydrophobic residues are highly conserved at the equivalent of these sites among non-olfactory class A GPCRs (5.61 and 5.65 in Ballesteros-Weinstein nomenclature). Moreover, as noted by Tesmer and colleagues, alignment of GRK family N-termini also indicates several highly conserved hydrophobic residues, highlighted in Fig 4.5B (83, 84). Mutation of these residues (L6, V9, V10) on GRK1 and their counterparts on GRK6 (L3, I6, V7) strongly decreases the phosphorylation of full-length rhodopsin but not a peptide comprising the C-terminal tail of rhodopsin, suggesting that these conserved residues are critical for interactions with the receptor and not catalytic activity (13, 16).

We used these observations and our new data to model how the GRK1 N-terminus could bind to the crevice formed in light-activated rhodopsin. Our logic for creating this model was simple. The G α C-terminus forms a helix upon binding rhodopsin (222, 223), with residues L349, L344 and I340 making direct contact with residues L226 and V230 on rhodopsin (224). The GRK1 N-terminus is also thought to form an alpha helix (83, 174, 175). Thus we reasoned that, since both the GRK1 N-terminus and G α C-terminus bind at the same site on rhodopsin, adopt the same secondary structure (84, 145), and require interaction with two of the same residues on rhodopsin (L226 and V230), they likely bind in such an orientation that enhances their use of these same types of hydrophobic contacts, a concept also proposed by Tesmer and colleagues (83, 84, 225).

With this in mind, we set about modeling how the GRK1 N-terminus can bind into the cytoplasmic cleft in rhodopsin, consistent with these constraints. First, we converted the sequence of the first ten residues in the GRK1 N-terminus into a helix, and then docked it onto the rhodopsin structure by manually aligning residues L6 and V9 on GRK1 with L344 and I340 of the G_{α} CT peptide. We then submitted this structure to FlexPepDock (199, 200).

Interestingly, the top 10 orientations for GRK1 NT in the binding pocket that resulted could be split in to two general populations. In one group, the orientation of the peptide aligns with how the G_{α} CT peptide binds to the cytoplasmic face of rhodopsin (Figure 4.5C, top). In the other orientation, the GRK1 NT peptide aligns with the same orientation as the visual arrestin finger loop (FL) from the recent crystal structure of rhodopsin bound by visual arrestin (Figure 4.5C, bottom) (188), an orientation which is at a $\sim 45^{\circ}$ angle to the position of the G_{α} CT peptide (Figure 5.2).

In these models, the GRK1 NT oriented like G_{α} CT blocks solvent accessibility to site V250 from the cytoplasm (Table 4.2), supporting the results of our site-directed labeling experiments shown in Figure 4.3. Importantly, this binding orientation also shows potential interactions between its conserved hydrophobic residues on GRK1 (L6, V9, and V10) with the two “hydrophobic patch” residues on rhodopsin (V230 and L226), residues that dramatically impaired rhodopsin phosphorylation when mutated to alanine (Figure 4.4C). This alignment also indicates that no GRK1 residues come within contact of T229 on rhodopsin, consistent with the lack of effect we observe for the T229A mutant.

We next extrapolated these models to assess which would be consistent with binding of full length GRK1 to rhodopsin. To do this, we began by aligning the GRK1 NT with a

GRK crystal structure. Unfortunately, the N-termini of GRKs are rarely crystallized, so we threaded the GRK1 sequence on to a GRK6 structure (83) that showed density for nearly the entire N-terminus, then submitted this manually docked structure to ROSIE from Rosetta (201-203). The result allows GRK1 to bind the cytoplasmic face of rhodopsin with very few structural changes (Figure 4.5D). Intriguingly, this docking model even allows for a plausible approximation of how the rhodopsin C-terminus could bind in the GRK1 catalytic cleft and positions the GRK1 C-terminus at the expected membrane bilayer, showing one way in which the membrane-anchoring farnesyl group could be positioned, although it is important to note that in the original GRK6 structure, the C-terminus is bound to a neighboring crystal contact. A similar result was also observed by Boguth et al (83) in their analysis of the GRK6 crystal structure.

In contrast, a GRK1 NT peptide bound like that of the visual arrestin FL can be ruled out for several reasons. First, such binding does not block solvent accessibility to site V250, and only shows one site of potential overlap/interaction between site L226 on rhodopsin and site V10 in the GRK1 N-terminus, no contacts with L6 or V9 are observed, or with V230 on rhodopsin. Second, this type of binding orients the GRK1 N-terminus in the “wrong direction,” such that it does not enable full length kinase to bind the receptor without requiring extensive structural rearrangement, including inducing a bend in the N-terminal α -helix that would then align itself between the base of TM6 and TM7.

Thus, given the highly conserved nature of both hydrophobic residues in the N-terminus of GRKs, as well as the cytoplasmic face of GPCRs (Figures 4.5A and B), as well as our data and analysis presented here, we propose the GRK1 binding is more like

that of G_{ta} C-terminus, an orientation that could be a universal, shared feature for how GRKs can interact with GPCRs.

Conclusion—rhodopsin uses a common binding pocket and hydrophobic residues to bind all three affiliate signaling proteins; G_b , visual arrestin and GRK1.

In summary, although additional experiments and higher resolution data are needed to determine the precise binding of the GRK1 N-terminus to rhodopsin, our present data, coupled with results from previous studies, indicate all three GPCR affiliate proteins: G_t , arrestin, and GRK1 recognize and utilize the cytoplasmic cleft as a common binding site on rhodopsin. Moreover, our data and modeling suggest that binding of all three proteins employ complementary hydrophobic- interactions with a “hydrophobic patch” exposed in the cytoplasmic cleft upon activation (especially residue L226), suggesting this region may provide a “hot spot of binding energy” (226) for coupling between GPCRs and their affiliate proteins. Finally, we note that the straightforward, rapid, simple way to obtain functional, tag-free GRK1 that has wildtype-like activity should be applicable to studying other GRKs.

Tables

Table 4.1: GRK1 activity parameters for WT rhodopsin and rhodopsin constructs

	specific activity	initial rate*	Km
	pmole P/min/mg	#P/min	μM
DDM-USR	280 \pm 53	0.20	2.0 \pm 1.3
‡ Θ	190 \pm 30	0.2	3.1 \pm 0.12
Θ L226A	49 \pm 11	0.02	ND
Θ T229A	170 \pm 27	0.2	3.2 \pm 0.24
Θ V230A	64 \pm 14	0.06	ND

*R² values for initial rate calculations were all greater than 0.9

‡ Θ is a minimal-cysteine rhodopsin mutant previously described (214, 215)

Table 4.2 Solvent accessibility* of rhodopsin site V250 when bound to G_{τα} CT and GRK1 NT peptides.

Residue	Peptide		Hydrophobic SA Å ²	Hydrophilic SA Å ²	Total SASA‡ Å ²
V250	GRK1 NT	<i>G_{τα} CT-like</i>	26.2	2.61	28.81
	GRK1 NT	<i>FL-like</i>	38.54	2.61	41.15
	G _{τα} CT		18.22	2.74	20.97
	none		43.3	2.74	46.04
L226	GRK1 NT	<i>G_{τα} CT-like</i>	18.81	2.31	21.12
	GRK1 NT	<i>FL-like</i>	23.61	2.4	26.01
	G _{τα} CT		19.15	2.02	21.17
	none		24.43	2.4	26.8
T229	GRK1 NT	<i>G_{τα} CT-like</i>	30.91	14.34	45.24
	GRK1 NT	<i>FL-like</i>	40.13	14.55	54.68
	G _{τα} CT		21.85	14.5	36.35
	none		27.4	15.2	42.6
V230	GRK1 NT	<i>G_{τα} CT-like</i>	15.92	2.75	18.67
	GRK1 NT	<i>FL-like</i>	36.13	3.36	39.49
	G _{τα} CT		17.3	2.59	19.89
	none		30.7	3.2	33.9

* Solvent accessibility (SA) calculated using the POPS server from MathBio

‡SASA stands for solvent-accessible surface area

PDB:4A4M was used for the rhodopsin-G_{τα} CT bound crystal structure

PDB: 3CAP was used for the "none," active-state rhodopsin crystal structure

Figures

Figure 4.1 Design and protocol for rapid purification of Rhodopsin kinase (GRK1) in a functional, tag-free form using the Profinity eXact Fusion Tag method.

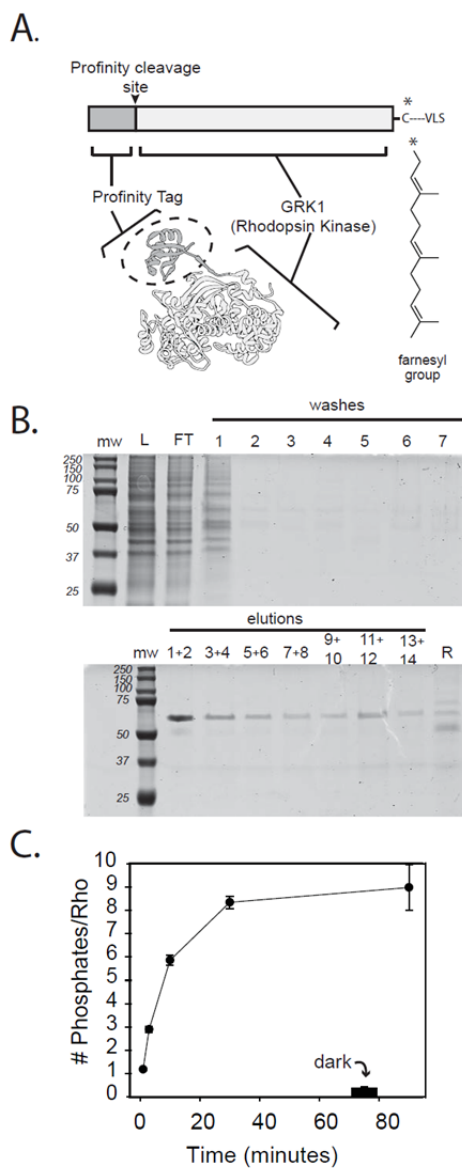


Figure 4.1 Design and protocol for rapid purification of Rhodopsin kinase (GRK1) in a functional, tag-free form using the Profinity eXact Fusion Tag method. **(A)** Schematic diagram (top) and structural model of GRK1 (bottom) show the N-terminal location of the “tag” (subtilisin prodomain, grey). Note that the subtilisin cleavage site is located between the prodomain tag and GRK1. The CaaX farnesylation site is also indicated. Models were made using UCSF Chimera (193), and PDB:3CO0 for the prodomain, and PDB:4PNI for GRK1. **(B)** SDS-PAGE analysis indicates GRK1 purified using the Profinity eXact method produces >80% pure protein in one step. In the top gel, L is the fraction loaded on the column, FT is the flow through, and the numbered fractions (1-7) refer to column washes. The bottom gel shows combined elutions from the column and the results from regeneration of the column, indicated by R. **(C)** The Profinity eXact-purified GRK1 shows robust phosphorylation of DDM-solubilized USR rhodopsin in a light-dependent manner, with ~8 phosphates per receptor, and essentially no phosphorylation in the dark using a 96-well filter binding assay to rapidly quantify GRK1-mediated receptor phosphorylation. For dark experiments, an aliquot was removed and stored in the dark for the entirety of the experiment before quenching.

Figure 4.2 The ability of GRK1 to phosphorylate rhodopsin is not dramatically impacted by presence of 1D4 peptide, but is blocked by the presence of 500 μM GRK1 NT peptide and 100 μM G_{ta} C-terminal peptide (G_{ta} CT), suggesting both affiliate proteins need access to the same sites on the receptor.

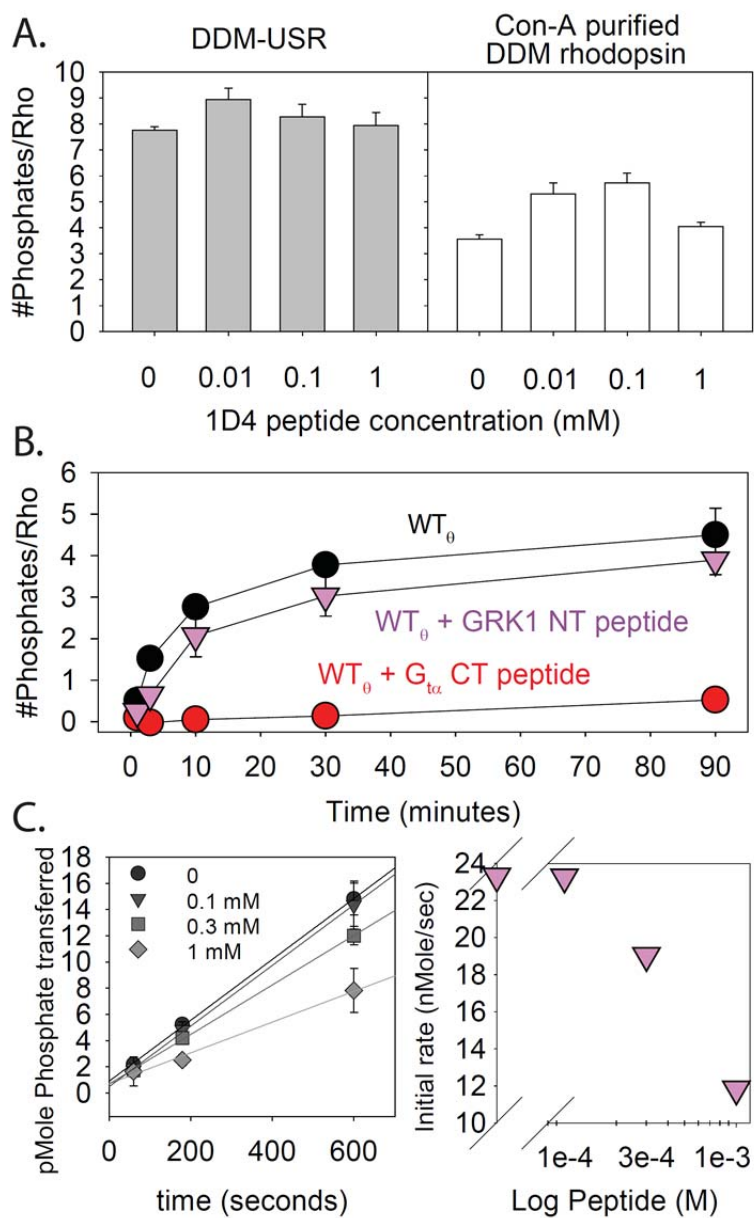


Figure 4.2 The ability of GRK1 to phosphorylate rhodopsin is not dramatically impacted by presence of 1D4 peptide, but is blocked by the presence of 500 μ M GRK1 NT peptide and 100 μ M G_{ta} C-terminal peptide (G_{ta} CT), suggesting both affiliate proteins need access to the same sites on the receptor. **(A)** Ability of GRK1 to phosphorylate DDM-solubilize USR rhodopsin (white bars) as well as Con-A purified DDM rhodopsin (grey) in the presence of excess 1D4 peptide. These experiments were carried out to determine if residual 1D4 peptide present after 1D4-immuno chromatography purification would affect subsequent GRK1 activity studies with recombinantly expressed and purified rhodopsin mutants. The rhodopsins were phosphorylated by GRK1 in the presence of 0, 0.01, 0.1, or 1 mM 1D4 peptide. No dramatic impact on receptor phosphorylation was observed, even in 1 mM 1D4 peptide, consistent with the known higher affinities of GRK1 for rhodopsin compared to C-terminal tail rhodopsin peptides (33, 148, 170). **(B)** In contrast, a high affinity peptide comprising the C-terminal residues of G_{ta} subunit, G_{ta} -CT (red circles), substantially blocks GRK1's ability to phosphorylate a non-cysteine reactive rhodopsin mutant, WT₀ (black circles). This peptide has previously been shown to block GRK-family phosphorylation of GPCRs by working directly on the receptor and not by inhibiting the kinase itself (213). Incubation with a peptide corresponding to the GRK1 N-terminus does not have a dramatic effect on over all phosphorylation level (purple triangles) **(C)** The GRK1 NT peptide blocks the initial rate of GRK1-mediated rhodopsin phosphorylation, as indicated on the left by the decreased slope of phosphate transferred in the presence of 0.1 (dark grey triangles), 0.3 (grey squares) and 1 mM GRK1 NT (light grey diamonds). Initial rates shown on the right were calculated by

fitting the 1, 3, and 10 minute data points for rhodopsin pre-incubated with 0, 0.1, 0.3, and 1 mM GRK1 NT peptide.

Figure 4.3 Site-directed labeling studies of rhodopsin mutant V250C suggest the N-terminus of GRK1 binds to the same site on rhodopsin as the G_{α} C-terminus and requires similar interactions with a key hydrophobic residue, L226. **(A)** A model of the cytoplasmic face of rhodopsin without (left) and with (red) the G_{α} CT peptide bound (143). The site-directed labeling studies measured reactivity of a unique cysteine introduced at site 250 (grey). This cysteine is inaccessible to the fluorescent label PyMPO in dark state rhodopsin, but is rapidly labeled upon receptor activation (192). Incubation with the G_{α} CT peptide blocks this reaction (176). Residues that comprise a “hydrophobic patch” known to influence Gt activation as well as visual arrestin binding, L226 (orange), T229 (green) and V230 (blue) are also shown. **(B)** PyMPO labeling of V250C detected by fluorescence imaging of unstained SDS-PAGE gel (top), where PyMPO incorporation is indicated as white bands. Total protein present is indicated by the subsequent Coomassie staining of the same gel (below). Labeling experiments were carried out on V250C in the presence of 1D4 peptide (negative control), G_{α} CT peptide (positive control), and GRK1 N-terminal 12-mer peptide. Both G_{α} CT and GRK1 NT peptide block PyMPO labeling at V250C, consistent with the idea that the peptides share a binding site. Interestingly, a single mutation in a “hydrophobic patch” on rhodopsin, L226A, disrupts the ability of the GRK1 N-terminal peptide to protect V250C, whereas the higher affinity G_{α} CT peptide still blocks labeling. **(C)** Plot of fluorescent band intensities adjusted for total protein concentration for 3 separate experiments. Grey bars represent PyMPO labeling of V250C in the presence of 1D4 peptide, red bars G_{α} CT peptide, and purple bars GRK1 NT peptide.

Figure 4.4 Functional evidence that GRK1, G_i , and visual arrestin all require some of the same “hydrophobic patch” residues for optimal activity.

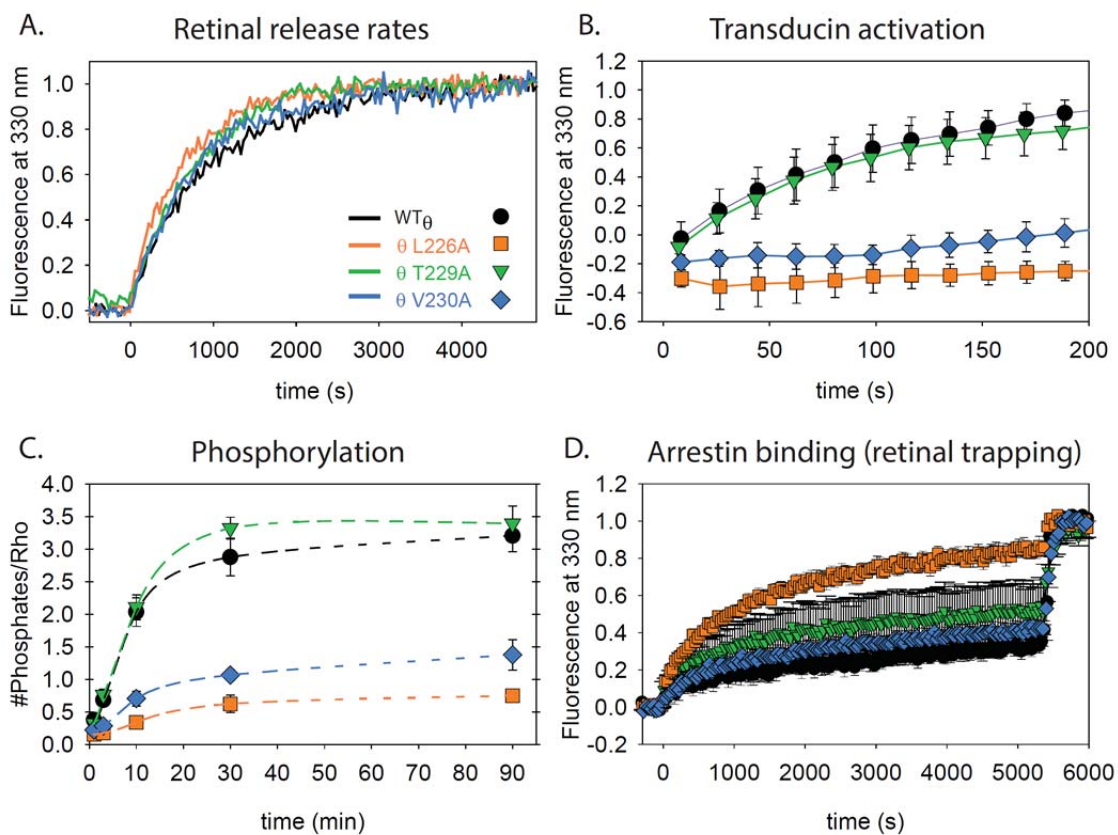


Figure 4.4 Functional evidence that GRK1, G_t , and visual arrestin all require some of the same “hydrophobic patch” residues for optimal activity. **(A)** Retinal release measurements show rhodopsin hydrophobic patch mutants L226A (orange), T229A (green), and V230A (blue) all show similar MII stability to WT_θ (black) receptor (21). **(B)** Hydrophobic patch mutants show different abilities to activate transducin (G_t), as determined by measuring the increase in G_t fluorescence that occurs upon GDP \rightarrow GTP γ S exchange (23, 191). Briefly, 500 nM G_t was incubated in a cuvette at 10 °C with stirring, and then light-activated rhodopsin is added at a final concentration of 5 nM. After 5 min equilibration, GTP γ S was added (at $t=0$) to a final concentration of 5 μ M and the fluorescence increase monitored. Note that mutants L226A and V230A show impaired transducin activation compared to WT_θ or mutant T229A construct. Plot shows the initial rate of G_t activation for 3 experiments with each receptor mutant. **(C)** Hydrophobic patch mutants show different levels of phosphorylation by GRK1. The data indicate GRK1 requires L226 & V230 for efficient phosphorylation, as indicated by reduced phosphorylation of mutants L226A and V230A, in contrast to mutant T229A and WT_θ , data shown are the average of 3-6 experiments. **(D)** Visual arrestin binding (as assessed by measuring the ability to trap retinal release (22)) shows a similar deficiency for one of the hydrophobic patch mutants. As can be seen, constitutively active visual arrestin mutant R175E induces “retinal trapping” for the WT_θ rhodopsin, as well as the V230A hydrophobic patch mutant. In contrast, the visual arrestin R175E only partially traps retinal in T229A rhodopsin, and shows no trapping for L226A rhodopsin, indicating binding to the latter two is impaired. Results are the average of at least 4 experiments.

Figure 4.5 Sequence analysis and structural modeling support the hypothesis that GRKs, G-proteins and arrestins all interact with GPCRs through hydrophobic interactions within a conserved “hydrophobic patch” on TM5 of the receptor.

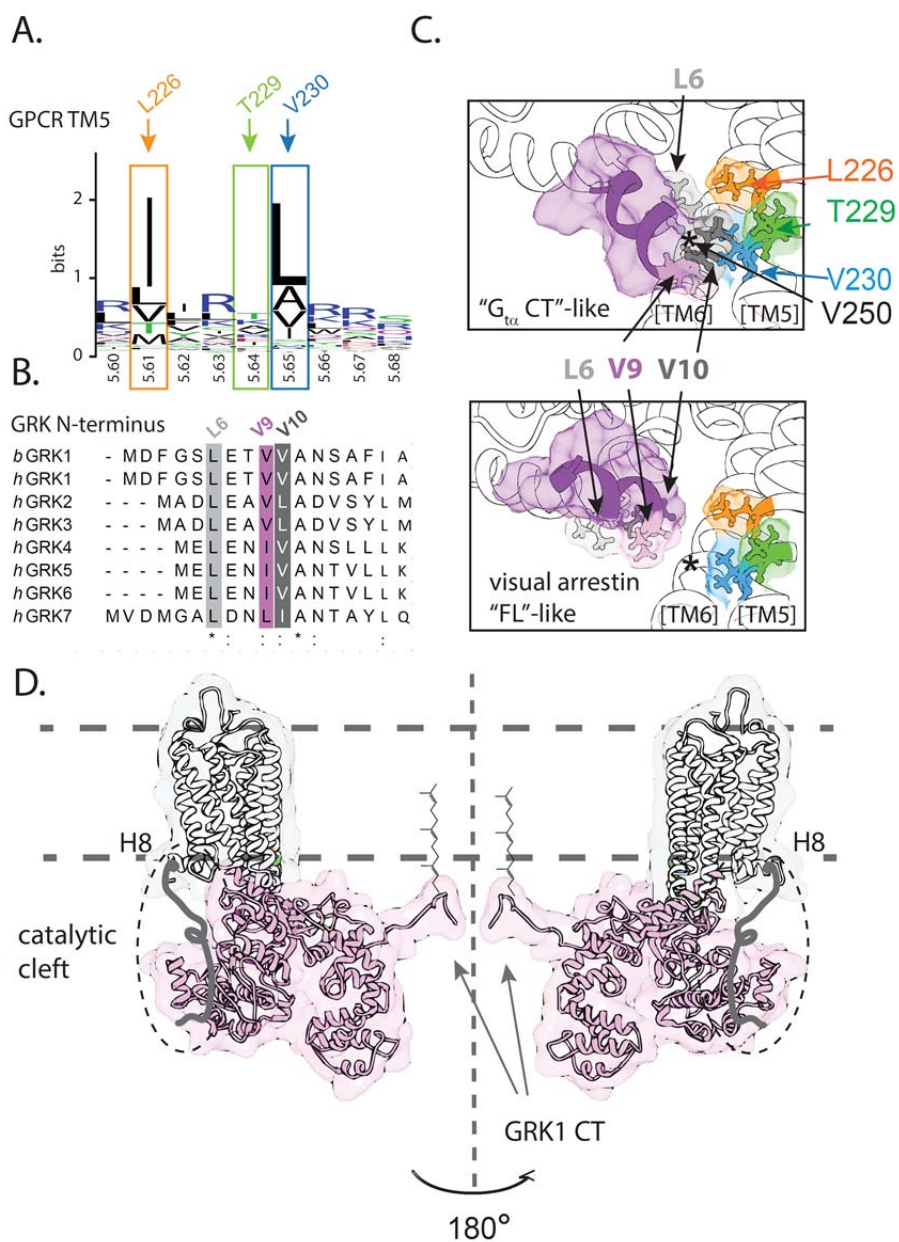


Figure 4.5 Sequence analysis and structural modeling support the hypothesis that GRKs, G-proteins and arrestins all interact with GPCRs through hydrophobic interactions within a conserved “hydrophobic patch” on TM5 of the receptor. **(A)** Sequence alignments show hydrophobic residues are conserved among GPCRs on TM5 at the equivalent of the rhodopsin “hydrophobic patch” (sites 226 and 230, or 5.61 and 5.65 in Ballesteros-Weinstein nomenclature). **(B)** The N-termini of GRK family members also contain several highly conserved hydrophobic residues (83, 84). A shared mode of binding with G_t would suggest these residues interact with residues in the TM5 hydrophobic patch on GPCRs, as do hydrophobic residues in the G_α C-terminus. **(C)** Model of a helical GRK1 N-terminus docked onto the same site as the $G_{t\alpha}$ CT peptide, in brief, a helix corresponding to the GRK1 first ten residues was manually docked onto the structure of $G_{t\alpha}$ CT peptide bound to rhodopsin, then submitted to the FlexPepDoc server from Rosetta (199, 200), and the resulting top 10 structures further analyzed. One group of peptide conformations showed a similar conformation as the $G_{t\alpha}$ CT peptide (top), while the other group had a similar conformation as the structure of rhodopsin bound to the finger loop of visual arrestin (bottom). Both groups of orientations show conserved GRK1 N-terminal residue V10 is in near contact with hydrophobic patch residue L226 on rhodopsin, a residue for which alanine substitutions abrogated rhodopsin phosphorylation. However, only the $G_{t\alpha}$ CT-like conformation also shows the conserved GRK1 N-terminal residues L6 and V9 in near contact to residue V230 to the rhodopsin hydrophobic patch, and shields site 250 (* represents V250 C α position) from solvent access and thus ability to be labeled by PyMPO. **(D)** Only the $G_{t\alpha}$ CT-like alignment can be extrapolated with a full length kinase to yield a reasonable docking model for both

proteins, providing a reasonable model for how the rhodopsin C-terminus can interact with the catalytic cleft of GRK1, black dashed circle. This model also provides a satisfying possible positioning of the GRK1 C-terminus near the membrane, which would enable putative farnesyl group anchoring. The highly conserved nature of both sets of hydrophobic residues in GRKs and GPCRs suggest this could reflect a shared feature for how GRKs interact with GPCRs. Full-length docking models generated by threading the GRK1 sequence on to PDB:3NYN, matching the N-terminal helix of this structure to the position of the “Gt α CT”-like conformation in Figure 5C, docking was optimized using ROSIE from Rosetta (201-203), see methods for additional details.

Chapter 5: Conclusions and Future Directions.

Improvement and expansion of the TrIQ/TyrIQ method for mapping interactions within and between proteins.

This work was built on the work of my mentor, Dr. David Farrens, and several of his previous lab members, primarily, Dr. Steve Mansoor. The previous work examined the ability of Trp residues to quench bimane in a distance dependent manner. In the years of using the TrIQ method, it had been noted that tyrosine residues were known to be capable of quenching bimane (114), but the effect had not been calibrated. During my rotation in the Farrens lab, I was given the opportunity to determine whether tyrosine was also able to quench bimane in a distance dependent manner akin to tryptophan, and if so, if there were differences in this interaction. I found that tyrosine does indeed quench bimane, and in several ways is a better quencher for the purposes of mapping interactions within and between proteins: it quenches over a shorter range ($C\alpha$ - $C\alpha$ distance) than does tryptophan, increasing the resolution of the method, and tyrosine only differs in a hydroxyl group from the “non-quenching” control residue used, phenylalanine.

The work presented in Chapter 2 presents several improvements to the TrIQ method, summarized below. Firstly, from a production perspective, I developed a much faster way to purify and label proteins for SDFL studies. The previous method for purifying the T4 lysozyme for these studies involved several chromatographic steps over two to three days, with fluorescent labeling of the T4 lysozyme after purification followed by removal of unreacted fluorescent label. As the number of proteins and controls increased, it

became clear that faster method was needed. Thus, I invested in optimizing the purification method, utilizing the Profinity eXact method, that relies on the picomolar affinity between a resin-bound protease and its prodomain that has been cloned on the N-terminus of the protein of interest, in this case T4 lysozyme. This affinity results in a stable complex that allows for extensive washing and even fluorescent labeling “on-column” followed by free label removal by additional subsequent washing. Thus, I was able to multiplex the production of six T4 lysozyme mutant proteins in a single day, involving one chromatographic step.

Secondly, in the previous work with TrIQ, the “unquenched sample” used whatever original residue was present in native T4 lysozyme before a tryptophan was introduced at that site. In my work, I instead compared the quenching effect of tryptophan or tyrosine to a phenylalanine residue at the same position. This comparison is optimal because of the shared aromaticity of this non-quenching control. Interestingly, in response to reviewer’s comments, I compared the effect of Asp, Phe, Tyr, and Trp on bimane absorbance, and found that the Phe residue shifted the absorbance of the nearby bimane residue to the same degree as the quenching residues (compared to the Asp residue), indicating that Phe physically interacts with bimane in a comparable manner to Tyr and Trp. In other words Phe also has a “static” interaction with the bimane at this closest C α -C α distance (7.5 Å), but does not quench. Further, Phe and Tyr differ only by a hydroxyl group, which allows for a more direct comparison of the quenched and unquenched sample.

The addition of Tyr to the TrIQ method allows for semi-quantitative distance assessment of dynamic protein movements and interactions using bimane. This is

demonstrated in the T4 lysozyme active site mutant data presented in Figure 2.10. Having previously defined the distance-dependent limits of Trp and Tyr to dynamically quench bimane, at ~ 15 Å and ~ 10 Å ($C\alpha-C\alpha$), respectively, the fact that Tyrosine did not substantially quench T4 lysozyme in either the “open” or “substrate-bound form,” and that Tryptophan could quench the “open” but not the “substrate-bound” form indicated that the “open” form placed the quencher and bimane ≥ 10 Å apart but less than ~ 15 Å apart, and that the “substrate-bound” form place the quencher and bimane ≥ 15 Å apart. Previously, the distance resolution was limited to “very close” (touching in a static complex), “close” (able to dynamically quench), and “not close.” Now, with the combination of TyrIQ and TrIQ, one can further resolve the “close” (but not touching) interaction observed from dynamic quenching and resolve between “not touching” ~ 10 Å (both Trp and Tyr dynamically quench) and between ~ 10 - 15 Å (Trp but not Tyr dynamically quench).

In addition to different distance constraints between Trp and Tyr quenching, Tyr, unlike Trp, does not quench the fluorescence of BODIPY 507/545. With the proper controls, this difference in quenching ability could be exploited to further delineate a particular interaction. For example, to demonstrate that a specific Trp residue was responsible for quenching BODIPY 507/545 at a particular site, one can also use a protein in which that Trp residue has been substituted with a Tyr residue and test to see if quenching persists. My work dealt with only two fluorophores, monobromobimane and BODIPY 507/545, but there are several chemical varieties of both of these fluorophores—each with slightly different chemistries—as well as a large variety of other fluorophores. Thus, a future direction of this work might involve testing the quenching

ability of Tyr residues for multiple other fluorophores in order to understand the applicability of TyrIQ to non-bimane quenching studies.

Another untested line of inquiry is the ability of phosphotyrosine to quench the emission of certain fluorophores. If the phosphorylation of a specific tyrosine altered the ability of the tyrosine to quench a fluorophore, the TyrIQ method would then be a unique sensing method to monitor the actions of tyrosine kinases.

The most impactful future directions of this work are in the application of the method. An example of the application of the TrIQ method is the work Dr. Abhinav Sinha, of a previous graduate student in the Farrens lab, who identified a second site on visual arrestin that comes in to contact with rhodopsin upon binding. A role for this site, called the “160 loop” was previously unappreciated, but our work showed that it comes in to direct physical contact with sites on rhodopsin TM6, as indicated by clear evidence of TrIQ-induced static quenching. At the time of publication (*154*), we were not able to distinguish whether these results were caused by a monomeric interaction between arrestin and rhodopsin that involved multiple binding modes, or a single binding mode that involved a large conformational change that would simultaneously satisfy the distance constraints produced by TrIQ static quenching. Nor were we able to discount the possibility that the visual arrestin in our study was interacting with a dimer of rhodopsins. About a year after our publication, a crystal structure of a rhodopsin visual arrestin complex showed that a monomeric interaction can satisfy all of the distance constraints derived from our work (*188*). An example is shown in Figure 5.1. Thus, the TrIQ method is demonstrably able to map interactions between proteins.

My next goal was to apply this method to study the interaction between rhodopsin and its kinase, GRK1. Since, the use of SDFL techniques requires that one can reliably purify the protein of interest, and assess the impact of mutations on the protein's function and interactions, I began by continuing the effort to optimize the purification of GRK1 from recombinant expression systems.

A rapid method for GRK1 purification that produces highly function kinase, and enables future GRK-GPCR studies.

The Profinity eXact purification approach has also proven to be ideal for purifying GRK1, as it requires only one chromatographic step to produce full length, tag free, farnesylated GRK1, and can be completed in one day. As shown in the purification of multiple T4 lysozyme samples in Chapter 2, the effort involved in this process easily accommodates multiplexed sample handling, which is critical when using site-directed labeling approaches, since multiple quencher/probe locations are required.

Given the relatively straight-forward methods for assessing a productive interaction between rhodopsin and GRK1, as well as other GPCRs and GRKs in general, there is relatively little recent information on these interactions. One possible explanation is that receptor phosphorylation can be seen as a binary process and the number and location of phosphoryl groups do not have a meaningful effect on rhodopsin signaling. In fact, this hypothesis has, in a way, been a prevailing model for a number of years in the rhodopsin community. In 1994 Ohguro, et al reported that serines at positions 334, 338, and 343 were the initial phosphorylation sites (227, 228), and suggested that previously observed higher levels of rhodopsin phosphorylation was an experimental artifact due to the lack of

visual arrestin in the purified system, which would otherwise rapidly bind the phosphorylated rhodopsin and occlude additional phosphorylation (229).

Despite the plausibility of this model, I find the conservation of so many potential sites of phosphorylation, each of which requires ATP consumption when phosphorylated, puzzling. Further, a recent report from Azevedo et al. suggests that threonine, and not serine, phosphorylation is the signal for visual arrestin binding in transgenic mice studies (138). Thus, we cannot rule out the physiological importance of high gain rhodopsin phosphorylation. Regardless of the physiological impact of high-gain rhodopsin phosphorylation, as a measure of purified kinase quality, full rhodopsin phosphorylation in a purified assay indicates the purified GRK likely has interactions that can be described as “wild type.”

This new purification approach not only enabled the biochemical mapping of the GRK1:rhodopsin interaction described in Chapter 4 and discussed later, it also allowed us to identify previously unappreciated biology of GRK1. Previous work using a truncated, and thus not isoprenylated, GRK1 concluded that GRK1 activity is not sensitive to the addition of acidic phospholipids (230). In our work with the full length GRK1, we found that DDM-purified rhodopsin had lower overall phosphorylation levels and that addition of acidic phospholipids restored full GRK1 activity. Future work on GRK1 activity should investigate the causes of this increased activity: is there a lipid binding site in GRK1, as there is for other GRK family members? Additionally, while it is widely accepted that GRK1 can exist in both a soluble and a membrane anchored protein due to the farnesyl group at its C-terminus, little is understood about the structural positioning of the farnesyl group in the soluble form of GRK1. Is the farnesyl group buried within

GRK1 when it is not membrane-anchored? What role does GRK1 autophosphorylation play in farnesyl group occlusion/membrane anchoring?

Potential expansion of the profinity eXact purification method to other GRKs.

Beyond rhodopsin, it is clear that the amount and location of GPCR phosphorylation is a critical marker for both receptor internalization as well as a phenomenon called biased signaling (59-62, 231-234), wherein binding by some ligands bias a receptor for primarily G protein-mediated signaling pathways and other ligands biases the same receptor for arrestin-mediated signaling pathways. Early work shows that receptor phosphorylation and arrestin binding are linked events, and some studies have shown that the number and location of phosphates can direct the intracellular response (59-62), and further, that distinct phosphorylation patterns can be incorporated by different GRK subtypes (61, 63-66). Thus, in order to fully understand and manipulate targeted biased responses in GPCR signaling, we need a robust biochemical production of individual GRK subtypes and the Profinity eXact purification approach is ideal in order to insure that the foundational studies with under-studied GRK subtypes are full length and fully active.

Use full-length, farnesylated GRK1 to phosphorylate non-rhodopsin GPCRs.

Previous studies have demonstrated that GRK1 will phosphorylate non-visual GPCRs in an agonist-dependent manner, although to a lesser degree than rhodopsin (39, 44). In Chapter 3, I describe an experiment I undertook with the help of Dr. Jon Fay, in which we tested the ability of GRK1 to phosphorylate the human cannabinoid receptor CB1, a ligand-binding GPCR. We found the GRK1 phosphorylation of CB1 was agonist dependent, and that incubation with antagonist blocked receptor phosphorylation. GRK1

is an ideal GRK due the way that it associates with membranes—its farnesyl group—allows GRK1 to be soluble or membrane-bound, and this transition is dependent on rhodopsin activation. GRKs 2 and 3 require association with the G $\beta\gamma$ subunits for membrane anchoring (GRK2/3), which means that, for these kinases, in order to achieve native-like experimental conditions one needs to either include G $\beta\gamma$ or add a non-native isoprenylation site to the C-terminus (39). Given the GRK subtype specific phosphorylation patterns, an important caveat of this approach is that GRK1 phosphorylation pattern will differ from the other subtypes, but experiments are needed to demonstrate whether GRK1-mediated phosphorylation of non-rhodopsin GPCRs results in a physiologically relevant pattern and quantity.

Further, future experiments might want to develop a method to detect the specific sites of phosphorylation on the active GPCR. Thus, one can ask if a certain mutation or agonist causes an overall increase or decrease in the position of GRK-mediated phosphorylation, or results in fewer receptors receiving full phosphorylation.

Identification of a shared binding site on rhodopsin, used by the G protein transducin, arrestin, and rhodopsin kinase.

This work used site-directed labeling techniques to demonstrate that the N-terminus of GRK1 binds directly in a cytoplasmic cleft on rhodopsin that becomes exposed after light activation of the receptor. This same cleft binds discrete positions on both G α CT(C-terminus) and visual arrestin (the finger loop), as was shown using biochemical and spectroscopic methods (109, 154, 156, 176, 186, 217, 235) and confirmed using X-ray crystallography (142, 143, 188, 198, 210-212). Intriguingly, as shown in Figure 5.2, the

Gat CT (red) and the visual arrestin finger loop (blue), bind at $\sim 45^\circ$ angles to each other, demonstrating that the active cytoplasmic face of rhodopsin can accommodate starkly different binding angles.

Using this site-directed-labeling approach we first demonstrated that a peptide corresponding to the N-terminus of GRK1 binds to this cleft and protects a buried site from fluorescent labeling, and that mutating a single leucine residue located in a “hydrophobic patch” within the rhodopsin cytoplasmic cleft to an alanine ablates this binding. We then used full-length GRK1 to assess the ability of GRK1 to phosphorylate this L226A rhodopsin mutation and found that the L226A mutation on rhodopsin severely impaired phosphorylation by GRK1. Thus, not only is site L226 on rhodopsin a shared critical interaction between rhodopsin and its three binding partners, but that binding of the cytoplasmic face of rhodopsin by the GRK1 N-terminus is necessary for receptor phosphorylation. This relationship between binding and activation is also true for transducin, wherein rhodopsin L226A shows less ability to activate transducin and less ability to bind a C-terminal peptide of transducin.

We next used this new data in conjunction with modeling approaches to create a plausible model of the rhodopsin-GRK1 interaction. As shown in Chapter 4 figure 4.5, we created a model of the GRK1 N-terminus docked in the cytoplasmic face of rhodopsin and extrapolated this model for docking of the full-length GRK1. We used our existing data to propose which of the possible models were consistent with our results.

Unfortunately, due to time constraints, I was not able to use the models to direct future experiments. However, such future experiments could test the modeling results using several approaches, which I will discuss below. As noted in the discussion of Chapter 4,

sites in the N-terminus of GRK1 protects the rhodopsin site V250 from solvent accessibility. Thus, I would start by using the same V250C rhodopsin mutant constructed in a minimal cysteine background used in Chapter 4 and attempt crosslinking with N-terminal GRK1 cysteine mutants.

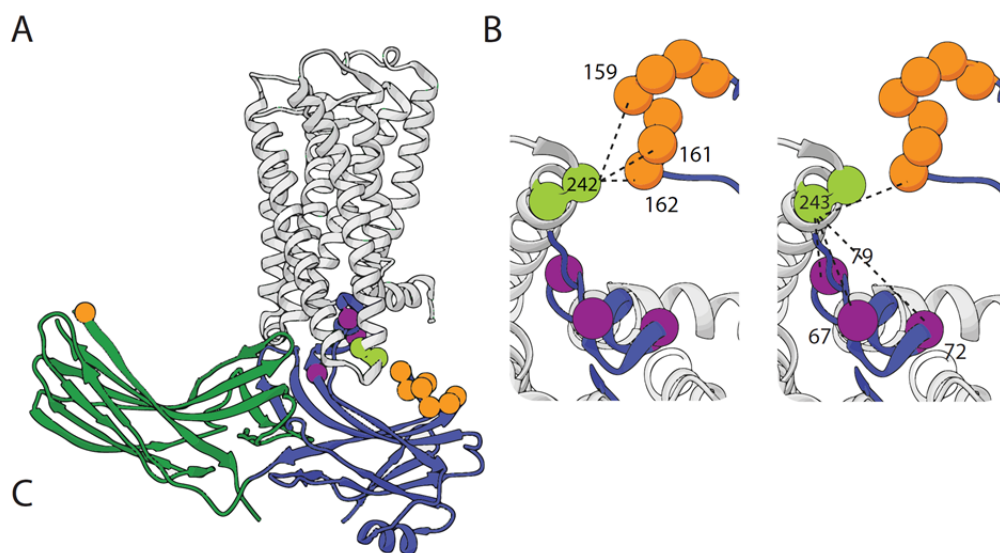
The preliminary work for this set of experiments is already done, I have created mutant GRK1 with a cysteine at each of the first 20 residues of the N-terminus. As described in Appendix 2, I have also expressed and purified several of the N-terminal cysteine mutant GRK1s, and done initial functional experiment, as shown in Figure A2.3 and A2.4. In fact, I have tested the ability of N-terminal cysteine GRK1 mutants to phosphorylate the “wild-type” minimal cysteine mutant rhodopsin (called θ) in DDM micelles both without and supplemented with DOPS and found that, as with WT GRK1 (Chapter 3 and Table A2.1), the N-terminal cysteine GRK1 mutants were better able to phosphorylate θ rhodopsin in the presence of DOPS (Table A2.1, Figs A2.3), and that GRK1 L6C, in particular had nearly WT-like function. In the models generated in Chapter 4, L6 is pointing toward V250, which is an intriguing place to begin this line of inquiry.

Ideally, I would have liked to study the rhodopsin:GRK1 project using SDFL approaches, combining the TyrIQ aspect of my work with the biophysical analysis of this interaction. As noted in earlier chapters, SDFL approaches are powerful for residue-specific resolution of interactions, but do require effort before mapping begins to insure that the mutations made to the proteins involved do not substantively alter the structure or function of the protein. Fortunately, rhodopsin has been well studied over the years, and the mutations have been well catalogued.

Future experiments in this line of inquiry will need to put some effort in to creating GRK1 constructs with Trp or Tyr residues in defined locations. As was demonstrated in chapter 2 of this dissertation, the unquenched control would ideally be a Phe residue. Given the experimental evidence from others (83-87) and presented in Chapter 4, the logical first step would be to create GRK1 N-terminal Trp and Tyr constructs. Conveniently, there is a natural Phe residue at site 15 of GRK1, which could be used as a starting place.

Figures

Figure 5.1 Model of full length visual arrestin fused to opsin (PDB 4ZWJ) shows that a monomeric interaction between the two proteins simultaneously satisfies the distance restraints produced from our TrIQ study.



◇	Bimane Location	Trp Location	C α -C α Distance	Quenching Results	Bimane Location	Trp Location	C α -C α Distance	Quenching Results
		158	13.4	*		158	19.4	<i>d</i>
		159	10.1	<i>s,d</i>		159	16.8	<i>d</i>
		160	10.4	<i>s,d</i>		160	13.5	<i>d</i>
	T242B	161	8.4	<i>s,d</i>	T243B	161	14.1	<i>d</i>
		162	6.3	<i>s,d</i>		162	12.5	<i>d</i>
		67	14.9	<i>nq</i>		67	14.2	<i>d</i>
		72	16.7	<i>nq</i>		72	17.1	<i>nq</i>
		79	10.4	<i>nq</i>		79	8.6	<i>d</i>

◇ Data from Sinha, A., Jones Brunette, A. M., Fay, J. F., Schafer, C. T., and Farrens, D. L. Biochemistry. 2014

s = static quenching

d = dynamic quenching

nq = no quenching detected

* = small amount of quenching detected

Figure 5.1 Model of full length visual arrestin fused to opsin (PDB 4ZWJ) shows that a monomeric interaction between the two proteins simultaneously satisfies the distance restraints produced from our TrIQ study. (A) In this structure (188) opsin N2C/N282C E113Q/M257Y (thermostabilized and constitutive activation mutations, respectively) is shown in grey ribbons, sites 242 and 243 are shown in bright green at the base of TM5. Visual arrestin 3A (constitutive activation is achieved by three consecutive alanine mutations at 374/375/376) is shown in blue (N-domain) and dark green (C-domain). Purple spheres in the finger loop show the sites of Trp incorporation tested in our 2014 publication (154), the N-domain TrIQ sites are shown in orange spheres, the red sphere is site 344 in the C-domain. (B) Close up view of the proximity of sites in visual arrestin and sites 242 (left) and 243 (right) on opsin. Some C α -C α distances are indicated. (C) A table of the C α -C α distances separating the sites of bimane incorporation on rhodopsin from our TrIQ study and the tryptophan positions on visual arrestin are consistent with the distance constraints of tryptophan's ability to quench bimane fluorescence from ~5-15 Å. The type of quenching observed in our TrIQ study are indicated by an *, for small amount of quenching, s for static quenching, d for dynamic quenching, and nq for not quenched.

Figure 5.2 The cytoplasmic face of active rhodopsin can accommodate starkly different binding angles of the α -helices of the G α C-terminal peptide and visual arrestin finger loop.

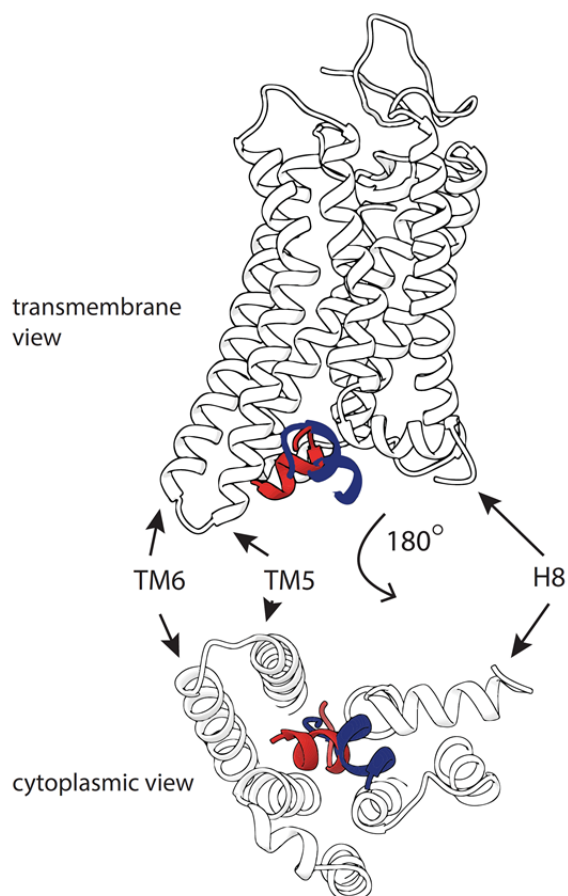


Figure 5.2 The cytoplasmic face of active rhodopsin can accommodate starkly different binding angles of the α -helices of the G α C-terminal peptide and visual arrestin finger loop. PDB 4A4M and 4ZWJ were aligned using the matchmaker function in Chimera. Opsin from 4ZWJ is shown in white, with the visual arrestin finger loop shown in blue and the G α C-terminal peptide shown in red (the opsin from this structure is not shown but is nearly identical to that of the visual arrestin-opsin fusion structure). The angle of binding differs between the two structures, $\sim 45^\circ$.

Bibliography

1. Fidom, K., Isberg, V., Hauser, A. S., Mordalski, S., Lehto, T., Bojarski, A. J., and Gloriam, D. E. (2015) A new crystal structure fragment-based pharmacophore method for G protein-coupled receptors, *Methods* 71, 104-112.
2. Isberg, V., de Graaf, C., Bortolato, A., Cherezov, V., Katritch, V., Marshall, F. H., Mordalski, S., Pin, J. P., Stevens, R. C., Vriend, G., and Gloriam, D. E. (2015) Generic GPCR residue numbers - aligning topology maps while minding the gaps, *Trends Pharmacol Sci* 36, 22-31.
3. Isberg, V., Mordalski, S., Munk, C., Rataj, K., Harpoe, K., Hauser, A. S., Vroiling, B., Bojarski, A. J., Vriend, G., and Gloriam, D. E. (2016) GPCRdb: an information system for G protein-coupled receptors, *Nucleic Acids Res* 44, D356-364.
4. Lagerstrom, M. C., and Schioth, H. B. (2008) Structural diversity of G protein-coupled receptors and significance for drug discovery, *Nature reviews. Drug discovery* 7, 339-357.
5. Rosenbaum, D. M., Rasmussen, S. G., and Kobilka, B. K. (2009) The structure and function of G-protein-coupled receptors, *Nature* 459, 356-363.
6. Oldham, W. M., Van Eps, N., Preininger, A. M., Hubbell, W. L., and Hamm, H. E. (2006) Mechanism of the receptor-catalyzed activation of heterotrimeric G proteins, *Nature structural & molecular biology* 13, 772-777.
7. Simon, M. I., Strathmann, M. P., and Gautam, N. (1991) Diversity of G proteins in signal transduction, *Science* 252, 802-808.
8. Oldham, W. M., and Hamm, H. E. (2008) Heterotrimeric G protein activation by G-protein-coupled receptors, *Nat Rev Mol Cell Biol* 9, 60-71.
9. Sorkin, A., and von Zastrow, M. (2009) Endocytosis and signalling: intertwining molecular networks, *Nat Rev Mol Cell Biol* 10, 609-622.
10. Luttrell, L. M., and Lefkowitz, R. J. (2002) The role of beta-arrestins in the termination and transduction of G-protein-coupled receptor signals, *J Cell Sci* 115, 455-465.
11. Eichel, K., Jullie, D., and von Zastrow, M. (2016) beta-Arrestin drives MAP kinase signalling from clathrin-coated structures after GPCR dissociation, *Nat Cell Biol* 18, 303-310.
12. Shonberg, J., Lopez, L., Scammells, P. J., Christopoulos, A., Capuano, B., and Lane, J. R. (2014) Biased agonism at G protein-coupled receptors: the promise and the challenges--a medicinal chemistry perspective, *Med Res Rev* 34, 1286-1330.

13. Wald, G. (1951) The photochemical basis of rod vision, *J Opt Soc Am* 41, 949-956.
14. Palczewski, K. (2006) G protein-coupled receptor rhodopsin, *Annu Rev Biochem* 75, 743-767.
15. Sandberg, M. N., Greco, J. A., Wagner, N. L., Amora, T. L., Ramos, L. A., Chen, M. H., Knox, B. E., and Birge, R. R. (2014) Low-Temperature Trapping of Photointermediates of the Rhodopsin E181Q Mutant, *SOJ Biochem* 1.
16. Ernst, O. P., and Bartl, F. J. (2002) Active states of rhodopsin, *ChemBiochem* 3, 968-974.
17. Wald, G. (1951) The chemistry of rod vision, *Science* 113, 287-291.
18. Wald, G., and Clark, A. B. (1937) Visual Adaptation and Chemistry of the Rods, *J Gen Physiol* 21, 93-105.
19. Schoenlein, R. W., Peteanu, L. A., Mathies, R. A., and Shank, C. V. (1991) The first step in vision: femtosecond isomerization of rhodopsin, *Science* 254, 412-415.
20. Yoshizawa, T., and Wald, G. (1963) Pre-lumirhodopsin and the bleaching of visual pigments, *Nature* 197, 1279-1286.
21. Farrens, D. L., and Khorana, H. G. (1995) Structure and function in rhodopsin. Measurement of the rate of metarhodopsin II decay by fluorescence spectroscopy, *J Biol Chem* 270, 5073-5076.
22. Sommer, M. E., and Farrens, D. L. (2006) Arrestin can act as a regulator of rhodopsin photochemistry, *Vision Res* 46, 4532-4546.
23. Farrens, D. L., Altenbach, C., Yang, K., Hubbell, W. L., and Khorana, H. G. (1996) Requirement of rigid-body motion of transmembrane helices for light activation of rhodopsin, *Science* 274, 768-770.
24. Kuhn, H., Cook, J. H., and Dreyer, W. J. (1973) Phosphorylation of rhodopsin in bovine photoreceptor membranes. A dark reaction after illumination, *Biochemistry* 12, 2495-2502.
25. Bownds, D., Dawes, J., Miller, J., and Stahlman, M. (1972) Phosphorylation of frog photoreceptor membranes induced by light, *Nat New Biol* 237, 125-127.
26. Weller, M., Virmaux, N., and Mandel, P. (1975) Light-stimulated phosphorylation of rhodopsin in the retina: the presence of a protein kinase that is specific for photobleached rhodopsin, *Proc Natl Acad Sci U S A* 72, 381-385.
27. Stadel, J. M., Nambi, P., Shorr, R. G., Sawyer, D. F., Caron, M. G., and Lefkowitz, R. J. (1983) Catecholamine-induced desensitization of turkey erythrocyte adenylate cyclase is associated with phosphorylation of the beta-adrenergic receptor, *Proc Natl Acad Sci U S A* 80, 3173-3177.

28. Sibley, D. R., Strasser, R. H., Caron, M. G., and Lefkowitz, R. J. (1985) Homologous desensitization of adenylate cyclase is associated with phosphorylation of the beta-adrenergic receptor, *J Biol Chem* 260, 3883-3886.
29. Day, P. W., Carman, C. V., Sterne-Marr, R., Benovic, J. L., and Wedegaertner, P. B. (2003) Differential interaction of GRK2 with members of the G alpha q family, *Biochemistry* 42, 9176-9184.
30. Day, P. W., Tesmer, J. J., Sterne-Marr, R., Freeman, L. C., Benovic, J. L., and Wedegaertner, P. B. (2004) Characterization of the GRK2 binding site of Galphaq, *J Biol Chem* 279, 53643-53652.
31. Day, P. W., Wedegaertner, P. B., and Benovic, J. L. (2004) Analysis of G-protein-coupled receptor kinase RGS homology domains, *Methods Enzymol* 390, 295-310.
32. Buczylo, J., Gutmann, C., and Palczewski, K. (1991) Regulation of rhodopsin kinase by autophosphorylation, *Proc Natl Acad Sci U S A* 88, 2568-2572.
33. Palczewski, K., Buczylo, J., Kaplan, M. W., Polans, A. S., and Crabb, J. W. (1991) Mechanism of rhodopsin kinase activation, *J Biol Chem* 266, 12949-12955.
34. Palczewski, K., Buczylo, J., Van Hooser, P., Carr, S. A., Huddleston, M. J., and Crabb, J. W. (1992) Identification of the autophosphorylation sites in rhodopsin kinase, *J Biol Chem* 267, 18991-18998.
35. Palczewski, K., Ohguro, H., Premont, R. T., and Inglese, J. (1995) Rhodopsin kinase autophosphorylation. Characterization of site-specific mutations, *J Biol Chem* 270, 15294-15298.
36. Horner, T. J., Osawa, S., Schaller, M. D., and Weiss, E. R. (2005) Phosphorylation of GRK1 and GRK7 by cAMP-dependent protein kinase attenuates their enzymatic activities, *J Biol Chem* 280, 28241-28250.
37. Osawa, S., Jo, R., Xiong, Y., Reidel, B., Tserentsoodol, N., Arshavsky, V. Y., Iuvone, P. M., and Weiss, E. R. (2011) Phosphorylation of G protein-coupled receptor kinase 1 (GRK1) is regulated by light but independent of phototransduction in rod photoreceptors, *J Biol Chem* 286, 20923-20929.
38. Inglese, J., Glickman, J. F., Lorenz, W., Caron, M. G., and Lefkowitz, R. J. (1992) Isoprenylation of a protein kinase. Requirement of farnesylation/alpha-carboxyl methylation for full enzymatic activity of rhodopsin kinase, *J Biol Chem* 267, 1422-1425.
39. Inglese, J., Koch, W. J., Caron, M. G., and Lefkowitz, R. J. (1992) Isoprenylation in regulation of signal transduction by G-protein-coupled receptor kinases, *Nature* 359, 147-150.
40. Maltese, W. A. (1990) Posttranslational modification of proteins by isoprenoids in mammalian cells, *FASEB J* 4, 3319-3328.

41. Moores, S. L., Schaber, M. D., Mosser, S. D., Rands, E., O'Hara, M. B., Garsky, V. M., Marshall, M. S., Pompliano, D. L., and Gibbs, J. B. (1991) Sequence dependence of protein isoprenylation, *J Biol Chem* 266, 14603-14610.
42. Yokoyama, K., Goodwin, G. W., Ghomashchi, F., Glomset, J. A., and Gelb, M. H. (1991) A protein geranylgeranyltransferase from bovine brain: implications for protein prenylation specificity, *Proc Natl Acad Sci U S A* 88, 5302-5306.
43. Kuhn, H. (1978) Light-regulated binding of rhodopsin kinase and other proteins to cattle photoreceptor membranes, *Biochemistry* 17, 4389-4395.
44. Benovic, J. L., Mayor, F., Jr., Somers, R. L., Caron, M. G., and Lefkowitz, R. J. (1986) Light-dependent phosphorylation of rhodopsin by beta-adrenergic receptor kinase, *Nature* 321, 869-872.
45. Hisatomi, O., Matsuda, S., Satoh, T., Kotaka, S., Imanishi, Y., and Tokunaga, F. (1998) A novel subtype of G-protein-coupled receptor kinase, GRK7, in teleost cone photoreceptors, *FEBS Lett* 424, 159-164.
46. Chen, C. K., Zhang, K., Church-Kopish, J., Huang, W., Zhang, H., Chen, Y. J., Frederick, J. M., and Baehr, W. (2001) Characterization of human GRK7 as a potential cone opsin kinase, *Mol Vis* 7, 305-313.
47. Weiss, E. R., Ducceschi, M. H., Horner, T. J., Li, A., Craft, C. M., and Osawa, S. (2001) Species-specific differences in expression of G-protein-coupled receptor kinase (GRK) 7 and GRK1 in mammalian cone photoreceptor cells: implications for cone cell phototransduction, *J Neurosci* 21, 9175-9184.
48. Weiss, E. R., Raman, D., Shirakawa, S., Ducceschi, M. H., Bertram, P. T., Wong, F., Kraft, T. W., and Osawa, S. (1998) The cloning of GRK7, a candidate cone opsin kinase, from cone- and rod-dominant mammalian retinas, *Mol Vis* 4, 27.
49. Penela, P., Murga, C., Ribas, C., Lafarga, V., and Mayor, F., Jr. (2010) The complex G protein-coupled receptor kinase 2 (GRK2) interactome unveils new physiopathological targets, *Br J Pharmacol* 160, 821-832.
50. Pronin, A. N., Satpaev, D. K., Slepak, V. Z., and Benovic, J. L. (1997) Regulation of G protein-coupled receptor kinases by calmodulin and localization of the calmodulin binding domain, *J Biol Chem* 272, 18273-18280.
51. Chuang, T. T., LeVine, H., 3rd, and De Blasi, A. (1995) Phosphorylation and activation of beta-adrenergic receptor kinase by protein kinase C, *J Biol Chem* 270, 18660-18665.
52. Winstel, R., Freund, S., Krasel, C., Hoppe, E., and Lohse, M. J. (1996) Protein kinase cross-talk: membrane targeting of the beta-adrenergic receptor kinase by protein kinase C, *Proc Natl Acad Sci U S A* 93, 2105-2109.
53. Wedegaertner, P. B., Wilson, P. T., and Bourne, H. R. (1995) Lipid modifications of trimeric G proteins, *J Biol Chem* 270, 503-506.

54. Penela, P., Rivas, V., Salcedo, A., and Mayor, F., Jr. (2010) G protein-coupled receptor kinase 2 (GRK2) modulation and cell cycle progression, *Proc Natl Acad Sci U S A* 107, 1118-1123.
55. Premont, R. T., Koch, W. J., Inglese, J., and Lefkowitz, R. J. (1994) Identification, purification, and characterization of GRK5, a member of the family of G protein-coupled receptor kinases, *J Biol Chem* 269, 6832-6841.
56. Thiyagarajan, M. M., Stracquatano, R. P., Pronin, A. N., Evanko, D. S., Benovic, J. L., and Wedegaertner, P. B. (2004) A predicted amphipathic helix mediates plasma membrane localization of GRK5, *J Biol Chem* 279, 17989-17995.
57. Munday, A. D., and Lopez, J. A. (2007) Posttranslational protein palmitoylation: promoting platelet purpose, *Arterioscler Thromb Vasc Biol* 27, 1496-1499.
58. Li, L., Homan, K. T., Vishnivetskiy, S. A., Manglik, A., Tesmer, J. J., Gurevich, V. V., and Gurevich, E. V. (2015) G Protein-coupled Receptor Kinases of the GRK4 Protein Subfamily Phosphorylate Inactive G Protein-coupled Receptors (GPCRs), *J Biol Chem* 290, 10775-10790.
59. Hausdorff, W. P., Bouvier, M., O'Dowd, B. F., Irons, G. P., Caron, M. G., and Lefkowitz, R. J. (1989) Phosphorylation sites on two domains of the beta 2-adrenergic receptor are involved in distinct pathways of receptor desensitization, *J Biol Chem* 264, 12657-12665.
60. Jin, W., Brown, S., Roche, J. P., Hsieh, C., Celver, J. P., Koo, A., Chavkin, C., and Mackie, K. (1999) Distinct domains of the CB1 cannabinoid receptor mediate desensitization and internalization, *J Neurosci* 19, 3773-3780.
61. Nobles, K. N., Xiao, K., Ahn, S., Shukla, A. K., Lam, C. M., Rajagopal, S., Strachan, R. T., Huang, T. Y., Bressler, E. A., Hara, M. R., Shenoy, S. K., Gygi, S. P., and Lefkowitz, R. J. (2011) Distinct phosphorylation sites on the beta(2)-adrenergic receptor establish a barcode that encodes differential functions of beta-arrestin, *Science signaling* 4, ra51.
62. Prihandoko, R., Alvarez-Curto, E., Hudson, B. D., Butcher, A. J., Ulven, T., Miller, A. M., Tobin, A. B., and Milligan, G. (2016) Distinct phosphorylation clusters determines the signalling outcome of the free fatty acid receptor FFA4/GPR120, *Mol Pharmacol*.
63. Kim, J., Ahn, S., Ren, X. R., Whalen, E. J., Reiter, E., Wei, H., and Lefkowitz, R. J. (2005) Functional antagonism of different G protein-coupled receptor kinases for beta-arrestin-mediated angiotensin II receptor signaling, *Proc Natl Acad Sci U S A* 102, 1442-1447.
64. Ren, X. R., Reiter, E., Ahn, S., Kim, J., Chen, W., and Lefkowitz, R. J. (2005) Different G protein-coupled receptor kinases govern G protein and beta-arrestin-mediated signaling of V2 vasopressin receptor, *Proc Natl Acad Sci U S A* 102, 1448-1453.
65. Kara, E., Crepieux, P., Gauthier, C., Martinat, N., Piketty, V., Guillou, F., and Reiter, E. (2006) A phosphorylation cluster of five serine and threonine residues

in the C-terminus of the follicle-stimulating hormone receptor is important for desensitization but not for beta-arrestin-mediated ERK activation, *Mol Endocrinol* 20, 3014-3026.

66. Shenoy, S. K., Drake, M. T., Nelson, C. D., Houtz, D. A., Xiao, K., Madabushi, S., Reiter, E., Premont, R. T., Lichtarge, O., and Lefkowitz, R. J. (2006) beta-arrestin-dependent, G protein-independent ERK1/2 activation by the beta2 adrenergic receptor, *The Journal of biological chemistry* 281, 1261-1273.
67. Mansoor, S. E., McHaourab, H. S., and Farrens, D. L. (1999) Determination of protein secondary structure and solvent accessibility using site-directed fluorescence labeling. Studies of T4 lysozyme using the fluorescent probe monobromobimane, *Biochemistry* 38, 16383-16393.
68. Mansoor, S. E., Dewitt, M. A., and Farrens, D. L. (2010) Distance mapping in proteins using fluorescence spectroscopy: the tryptophan-induced quenching (TrIQ) method, *Biochemistry* 49, 9722-9731.
69. Mansoor, S. E., and Farrens, D. L. (2004) High-throughput protein structural analysis using site-directed fluorescence labeling and the bimane derivative (2-pyridyl)dithiobimane, *Biochemistry* 43, 9426-9438.
70. Mansoor, S. E., McHaourab, H. S., and Farrens, D. L. (2002) Mapping proximity within proteins using fluorescence spectroscopy. A study of T4 lysozyme showing that tryptophan residues quench bimane fluorescence, *Biochemistry* 41, 2475-2484.
71. Jones Brunette, A. M., and Farrens, D. L. (2014) Distance mapping in proteins using fluorescence spectroscopy: tyrosine, like tryptophan, quenches bimane fluorescence in a distance-dependent manner, *Biochemistry* 53, 6290-6301.
72. Tesmer, J. J. (2016) Hitchhiking on the heptahelical highway: structure and function of 7TM receptor complexes, *Nat Rev Mol Cell Biol*.
73. Ghosh, E., Kumari, P., Jaiman, D., and Shukla, A. K. (2015) Methodological advances: the unsung heroes of the GPCR structural revolution, *Nat Rev Mol Cell Biol* 16, 69-81.
74. Wang, W., Whorton, M. R., and MacKinnon, R. (2014) Quantitative analysis of mammalian GIRK2 channel regulation by G proteins, the signaling lipid PIP2 and Na⁺ in a reconstituted system, *Elife* 3, e03671.
75. Whorton, M. R., and MacKinnon, R. (2011) Crystal structure of the mammalian GIRK2 K⁺ channel and gating regulation by G proteins, PIP2, and sodium, *Cell* 147, 199-208.
76. Whorton, M. R., and MacKinnon, R. (2013) X-ray structure of the mammalian GIRK2-beta gamma G-protein complex, *Nature* 498, 190-197.
77. Ritter, S. L., and Hall, R. A. (2009) Fine-tuning of GPCR activity by receptor-interacting proteins, *Nat Rev Mol Cell Biol* 10, 819-830.

78. Sakmar, T. P., Menon, S. T., Marin, E. P., and Awad, E. S. (2002) Rhodopsin: insights from recent structural studies, *Annu Rev Biophys Biomol Struct* 31, 443-484.
79. Stenkamp, R. E. (2008) Alternative models for two crystal structures of bovine rhodopsin, *Acta Crystallogr D Biol Crystallogr* D64, 902-904.
80. Blankenship, E., Vahedi-Faridi, A., and Lodowski, D. T. (2015) The High-Resolution Structure of Activated Opsin Reveals a Conserved Solvent Network in the Transmembrane Region Essential for Activation, *Structure* 23, 2358-2364.
81. Inglese, J., Freedman, N. J., Koch, W. J., and Lefkowitz, R. J. (1993) Structure and mechanism of the G protein-coupled receptor kinases, *J Biol Chem* 268, 23735-23738.
82. Stoffel, R. H., 3rd, Pitcher, J. A., and Lefkowitz, R. J. (1997) Targeting G protein-coupled receptor kinases to their receptor substrates, *J Membr Biol* 157, 1-8.
83. Boguth, C. A., Singh, P., Huang, C. C., and Tesmer, J. J. (2010) Molecular basis for activation of G protein-coupled receptor kinases, *The EMBO journal* 29, 3249-3259.
84. Huang, C. C., Orban, T., Jastrzebska, B., Palczewski, K., and Tesmer, J. J. (2011) Activation of G protein-coupled receptor kinase 1 involves interactions between its N-terminal region and its kinase domain, *Biochemistry* 50, 1940-1949.
85. Noble, B., Kallal, L. A., Pausch, M. H., and Benovic, J. L. (2003) Development of a yeast bioassay to characterize G protein-coupled receptor kinases. Identification of an NH₂-terminal region essential for receptor phosphorylation, *J Biol Chem* 278, 47466-47476.
86. Pao, C. S., Barker, B. L., and Benovic, J. L. (2009) Role of the amino terminus of G protein-coupled receptor kinase 2 in receptor phosphorylation, *Biochemistry* 48, 7325-7333.
87. Singh, P., Wang, B., Maeda, T., Palczewski, K., and Tesmer, J. J. (2008) Structures of rhodopsin kinase in different ligand states reveal key elements involved in G protein-coupled receptor kinase activation, *The Journal of biological chemistry* 283, 14053-14062.
88. Homan, K. T., Larimore, K. M., Elkins, J. M., Szklarz, M., Knapp, S., and Tesmer, J. J. (2015) Identification and structure-function analysis of subfamily selective G protein-coupled receptor kinase inhibitors, *ACS Chem Biol* 10, 310-319.
89. Tesmer, V. M., Kawano, T., Shankaranarayanan, A., Kozasa, T., and Tesmer, J. J. (2005) Snapshot of activated G proteins at the membrane: the Gα_q-GRK2-Gβ₂γ complex, *Science* 310, 1686-1690.
90. Alexiev, U., and Farrens, D. L. (2014) Fluorescence spectroscopy of rhodopsins: Insights and approaches, *Biochim Biophys Acta* 1837, 694-709.

91. Caputo, G. A., and London, E. (2013) Analyzing transmembrane protein and hydrophobic helix topography by dual fluorescence quenching, *Methods Mol Biol* 974, 279-295.
92. Daggett, K. A., and Sakmar, T. P. (2011) Site-specific in vitro and in vivo incorporation of molecular probes to study G-protein-coupled receptors, *Curr Opin Chem Biol* 15, 392-398.
93. Dekel, N., Priest, M. F., Parnas, H., Parnas, I., and Bezanilla, F. (2012) Depolarization induces a conformational change in the binding site region of the M2 muscarinic receptor, *Proc Natl Acad Sci U S A* 109, 285-290.
94. Gasymov, O. K., Abduragimov, A. R., and Glasgow, B. J. (2012) Tryptophan rotamer distribution revealed for the alpha-helix in tear lipocalin by site-directed tryptophan fluorescence, *J Phys Chem B* 116, 13381-13388.
95. Ho, D., Lugo, M. R., and Merrill, A. R. (2013) Harmonic analysis of the fluorescence response of bimane adducts of colicin E1 at helices 6, 7, and 10, *J Biol Chem* 288, 5136-5148.
96. Kim, Y. J., Hofmann, K. P., Ernst, O. P., Scheerer, P., Choe, H. W., and Sommer, M. E. (2013) Crystal structure of pre-activated arrestin p44, *Nature* 497, 142-146.
97. Raghuraman, H., Islam, S. M., Mukherjee, S., Roux, B., and Perozo, E. (2014) Dynamics transitions at the outer vestibule of the KcsA potassium channel during gating, *Proc Natl Acad Sci U S A* 111, 1831-1836.
98. Rasmussen, S. G., Choi, H. J., Fung, J. J., Pardon, E., Casarosa, P., Chae, P. S., Devree, B. T., Rosenbaum, D. M., Thian, F. S., Kobilka, T. S., Schnapp, A., Konetzki, I., Sunahara, R. K., Gellman, S. H., Pautsch, A., Steyaert, J., Weis, W. I., and Kobilka, B. K. (2011) Structure of a nanobody-stabilized active state of the beta(2) adrenoceptor, *Nature* 469, 175-180.
99. Sasaki, J., Phillips, B. J., Chen, X., Van Eps, N., Tsai, A. L., Hubbell, W. L., and Spudich, J. L. (2007) Different dark conformations function in color-sensitive photosignaling by the sensory rhodopsin I-HtrI complex, *Biophysical journal* 92, 4045-4053.
100. Taraska, J. W. (2012) Mapping membrane protein structure with fluorescence, *Curr Opin Struct Biol* 22, 507-513.
101. Venezia, C. F., Meany, B. J., Braz, V. A., and Barkley, M. D. (2009) Kinetics of association and dissociation of HIV-1 reverse transcriptase subunits, *Biochemistry* 48, 9084-9093.
102. Yao, X., Parnot, C., Deupi, X., Ratnala, V. R., Swaminath, G., Farrens, D., and Kobilka, B. (2006) Coupling ligand structure to specific conformational switches in the beta2-adrenoceptor, *Nat Chem Biol* 2, 417-422.
103. Doose, S., Neuweiler, H., and Sauer, M. (2005) A close look at fluorescence quenching of organic dyes by tryptophan, *Chemphyschem* 6, 2277-2285.

104. Fay, J. F., and Farrens, D. L. (2012) A key agonist-induced conformational change in the cannabinoid receptor CB1 is blocked by the allosteric ligand Org 27569, *J Biol Chem* 287, 33873-33882.
105. Islas, L. D., and Zagotta, W. N. (2006) Short-range molecular rearrangements in ion channels detected by tryptophan quenching of bimane fluorescence, *J Gen Physiol* 128, 337-346.
106. Janz, J. M., and Farrens, D. L. (2004) Rhodopsin activation exposes a key hydrophobic binding site for the transducin alpha-subunit C terminus, *J Biol Chem* 279, 29767-29773.
107. Semenova, N. P., Abarca-Heidemann, K., Loranc, E., and Rothberg, B. S. (2009) Bimane fluorescence scanning suggests secondary structure near the S3-S4 linker of BK channels, *J Biol Chem* 284, 10684-10693.
108. Sinha, A., Brunette, A. M., Fay, J. F., Schafer, C. T., and Farrens, D. L. (2014) Rhodopsin TM6 can Contact two Separate and Distinct Sites on Arrestin: Evidence for Structural Plasticity and Multiple Docking Modes in Arrestin-Rhodopsin Binding, *Biochemistry* 53, 3294-3307.
109. Sommer, M. E., Farrens, D. L., McDowell, J. H., Weber, L. A., and Smith, W. C. (2007) Dynamics of arrestin-rhodopsin interactions: loop movement is involved in arrestin activation and receptor binding, *J Biol Chem* 282, 25560-25568.
110. Tapley, T. L., Cupp-Vickery, J. R., and Vickery, L. E. (2005) Sequence-dependent peptide binding orientation by the molecular chaperone DnaK, *Biochemistry* 44, 12307-12315.
111. Tapley, T. L., and Vickery, L. E. (2004) Preferential substrate binding orientation by the molecular chaperone HscA, *J Biol Chem* 279, 28435-28442.
112. Tsukamoto, H., and Farrens, D. L. (2013) A constitutively activating mutation alters the dynamics and energetics of a key conformational change in a ligand-free G protein-coupled receptor, *J Biol Chem* 288, 28207-28216.
113. Doose, S., Neuweiler, H., and Sauer, M. (2009) Fluorescence quenching by photoinduced electron transfer: a reporter for conformational dynamics of macromolecules, *Chemphyschem* 10, 1389-1398.
114. Sato, E. S., Mari; Kanaoka, Yuichi; Kosower, Edward M. (1988) Novel Fluorogenic Substrates for Microdetermination of Chymotrypsin and Aminopeptidase: Bimane Fluorescence Appears after Hydrolysis, *Bioorganic Chemistry* 16, 298-306.
115. Hayashibara, M., and London, E. (2005) Topography of diphtheria toxin A chain inserted into lipid vesicles, *Biochemistry* 44, 2183-2196.
116. Sathish, H. A., Stein, R. A., Yang, G., and McHaourab, H. S. (2003) Mechanism of chaperone function in small heat-shock proteins. Fluorescence studies of the conformations of T4 lysozyme bound to alphaB-crystallin, *J Biol Chem* 278, 44214-44221.

117. Taraska, J. W., Puljung, M. C., and Zagotta, W. N. (2009) Short-distance probes for protein backbone structure based on energy transfer between bimane and transition metal ions, *Proc Natl Acad Sci U S A* 106, 16227-16232.
118. Vincelli, A. J., Pottinger, D. S., Zhong, F., Hanske, J., Rolland, S. G., Conradt, B., and Pletneva, E. V. (2013) Recombinant expression, biophysical characterization, and cardiolipin-induced changes of two *Caenorhabditis elegans* cytochrome c proteins, *Biochemistry* 52, 653-666.
119. Kuroki, R., Weaver, L. H., and Matthews, B. W. (1993) A covalent enzyme-substrate intermediate with saccharide distortion in a mutant T4 lysozyme, *Science* 262, 2030-2033.
120. Yirdaw, R. B., and McHaourab, H. S. (2012) Direct observation of T4 lysozyme hinge-bending motion by fluorescence correlation spectroscopy, *Biophysical journal* 103, 1525-1536.
121. Abdulaev, N. G., Zhang, C., Dinh, A., Ngo, T., Bryan, P. N., Brabazon, D. M., Marino, J. P., and Ridge, K. D. (2005) Bacterial expression and one-step purification of an isotope-labeled heterotrimeric G-protein alpha-subunit, *Journal of biomolecular NMR* 32, 31-40.
122. Lakowicz, J. R. (2006) *Principles of fluorescence spectroscopy*, 3rd ed., Springer, New York.
123. Closs, G. L., and Miller, J. R. (1988) Intramolecular long-distance electron transfer in organic molecules, *Science* 240, 440-447.
124. McHaourab, H. S., Oh, K. J., Fang, C. J., and Hubbell, W. L. (1997) Conformation of T4 lysozyme in solution. Hinge-bending motion and the substrate-induced conformational transition studied by site-directed spin labeling, *Biochemistry* 36, 307-316.
125. Zhang, X. J., Wozniak, J. A., and Matthews, B. W. (1995) Protein flexibility and adaptability seen in 25 crystal forms of T4 lysozyme, *J Mol Biol* 250, 527-552.
126. Spencer, R. D. (1970) Fluorescence lifetimes: theory, instrumentation, and application or nanosecond fluorometry, PhD dissertation, Department of Chemistry, University of Illinois at Urbana-Champaign.
127. Harriman, A. (1987) Further Comments on the Redox Potentials of Tryptophan and Tyrosine, *The Journal of Physical Chemistry* 91, 3.
128. Torimura, M., Kurata, S., Yamada, K., Yokomaku, T., Kamagata, Y., Kanagawa, T., and Kurane, R. (2001) Fluorescence-quenching phenomenon by photoinduced electron transfer between a fluorescent dye and a nucleotide base, *Anal Sci* 17, 155-160.
129. Marme, N., Knemeyer, J. P., Sauer, M., and Wolfrum, J. (2003) Inter- and intramolecular fluorescence quenching of organic dyes by tryptophan, *Bioconjug Chem* 14, 1133-1139.

130. Weaver, L. H., and Matthews, B. W. (1987) Structure of bacteriophage T4 lysozyme refined at 1.7 Å resolution, *J Mol Biol* 193, 189-199.
131. Shi, X., Duft, D., and Parks, J. H. (2008) Fluorescence quenching induced by conformational fluctuations in unsolvated polypeptides, *J Phys Chem B* 112, 12801-12815.
132. Ghanouni, P., Gryczynski, Z., Steenhuis, J. J., Lee, T. W., Farrens, D. L., Lakowicz, J. R., and Kobilka, B. K. (2001) Functionally different agonists induce distinct conformations in the G protein coupling domain of the beta 2 adrenergic receptor, *J Biol Chem* 276, 24433-24436.
133. Ghanouni, P., Steenhuis, J. J., Farrens, D. L., and Kobilka, B. K. (2001) Agonist-induced conformational changes in the G-protein-coupling domain of the beta 2 adrenergic receptor, *Proc Natl Acad Sci U S A* 98, 5997-6002.
134. Tsukamoto, H., Farrens, D. L., Koyanagi, M., and Terakita, A. (2009) The magnitude of the light-induced conformational change in different rhodopsins correlates with their ability to activate G proteins, *J Biol Chem* 284, 20676-20683.
135. Palczewski, K., McDowell, J. H., and Hargrave, P. A. (1988) Purification and characterization of rhodopsin kinase, *J Biol Chem* 263, 14067-14073.
136. Sokal, I., Pulvermuller, A., Buczylo, J., Hofmann, K. P., and Palczewski, K. (2002) Rhodopsin and its kinase, *Methods Enzymol* 343, 578-600.
137. Wilden, U., and Kuhn, H. (1982) Light-dependent phosphorylation of rhodopsin: number of phosphorylation sites, *Biochemistry* 21, 3014-3022.
138. Azevedo, A. W., Doan, T., Moaven, H., Sokal, I., Baameur, F., Vishnivetskiy, S. A., Homan, K. T., Tesmer, J. J., Gurevich, V. V., Chen, J., and Rieke, F. (2015) C-terminal threonines and serines play distinct roles in the desensitization of rhodopsin, a G protein-coupled receptor, *Elife* 4.
139. Teller, D. C., Okada, T., Behnke, C. A., Palczewski, K., and Stenkamp, R. E. (2001) Advances in determination of a high-resolution three-dimensional structure of rhodopsin, a model of G-protein-coupled receptors (GPCRs), *Biochemistry* 40, 7761-7772.
140. Palczewski, K., Kumasaka, T., Hori, T., Behnke, C. A., Motoshima, H., Fox, B. A., Le Trong, I., Teller, D. C., Okada, T., Stenkamp, R. E., Yamamoto, M., and Miyano, M. (2000) Crystal structure of rhodopsin: A G protein-coupled receptor, *Science* 289, 739-745.
141. Okada, T., Le Trong, I., Fox, B. A., Behnke, C. A., Stenkamp, R. E., and Palczewski, K. (2000) X-Ray diffraction analysis of three-dimensional crystals of bovine rhodopsin obtained from mixed micelles, *J Struct Biol* 130, 73-80.
142. Choe, H. W., Kim, Y. J., Park, J. H., Morizumi, T., Pai, E. F., Krauss, N., Hofmann, K. P., Scheerer, P., and Ernst, O. P. (2011) Crystal structure of metarhodopsin II, *Nature* 471, 651-655.

143. Deupi, X., Edwards, P., Singhal, A., Nickle, B., Oprian, D., Schertler, G., and Standfuss, J. (2012) Stabilized G protein binding site in the structure of constitutively active metarhodopsin-II, *Proc Natl Acad Sci U S A* 109, 119-124.
144. Homan, K. T., Larimore, K. M., Elkins, J. M., Szklarz, M., Knapp, S., and Tesmer, J. J. (2014) Identification and Structure-Function Analysis of Subfamily Selective G Protein-Coupled Receptor Kinase Inhibitors, *ACS Chem Biol*.
145. Singh, P., Wang, B., Maeda, T., Palczewski, K., and Tesmer, J. J. (2008) Structures of rhodopsin kinase in different ligand states reveal key elements involved in G protein-coupled receptor kinase activation, *J Biol Chem* 283, 14053-14062.
146. Tesmer, J. J., Nance, M. R., Singh, P., and Lee, H. (2012) Structure of a monomeric variant of rhodopsin kinase at 2.5 Å resolution, *Acta Crystallogr Sect F Struct Biol Cryst Commun* 68, 622-625.
147. Bruel, C., Cha, K., Reeves, P. J., Getmanova, E., and Khorana, H. G. (2000) Rhodopsin kinase: expression in mammalian cells and a two-step purification, *Proc Natl Acad Sci U S A* 97, 3004-3009.
148. Huang, C. C., Yoshino-Koh, K., and Tesmer, J. J. (2009) A surface of the kinase domain critical for the allosteric activation of G protein-coupled receptor kinases, *J Biol Chem* 284, 17206-17215.
149. Orban, T., Huang, C. C., Homan, K. T., Jastrzebska, B., Tesmer, J. J., and Palczewski, K. (2012) Substrate-induced changes in the dynamics of rhodopsin kinase (G protein-coupled receptor kinase 1), *Biochemistry* 51, 3404-3411.
150. Cha, K., Bruel, C., Inglese, J., and Khorana, H. G. (1997) Rhodopsin kinase: expression in baculovirus-infected insect cells, and characterization of post-translational modifications, *Proc Natl Acad Sci U S A* 94, 10577-10582.
151. Ruan, B., Fisher, K. E., Alexander, P. A., Doroshko, V., and Bryan, P. N. (2004) Engineering subtilisin into a fluoride-triggered processing protease useful for one-step protein purification, *Biochemistry* 43, 14539-14546.
152. Huang, L., Mao, X., Abdulaev, N. G., Ngo, T., Liu, W., and Ridge, K. D. (2012) One-step purification of a functional, constitutively activated form of visual arrestin, *Protein expression and purification* 82, 55-60.
153. Tsukamoto, H., Sinha, A., DeWitt, M., and Farrens, D. L. (2010) Monomeric rhodopsin is the minimal functional unit required for arrestin binding, *J Mol Biol* 399, 501-511.
154. Sinha, A., Jones Brunette, A. M., Fay, J. F., Schafer, C. T., and Farrens, D. L. (2014) Rhodopsin TM6 can interact with two separate and distinct sites on arrestin: evidence for structural plasticity and multiple docking modes in arrestin-rhodopsin binding, *Biochemistry* 53, 3294-3307.
155. Papermaster, D. S. (1982) Preparation of retinal rod outer segments, *Methods Enzymol* 81, 48-52.

156. Sommer, M. E., Smith, W. C., and Farrens, D. L. (2005) Dynamics of arrestin-rhodopsin interactions: arrestin and retinal release are directly linked events, *J Biol Chem* 280, 6861-6871.
157. Shichi, H., and Somers, R. L. (1978) Light-dependent phosphorylation of rhodopsin. Purification and properties of rhodopsin kinase, *J Biol Chem* 253, 7040-7046.
158. Sommer, M. E., Smith, W. C., and Farrens, D. L. (2006) Dynamics of arrestin-rhodopsin interactions: acidic phospholipids enable binding of arrestin to purified rhodopsin in detergent, *J Biol Chem* 281, 9407-9417.
159. Fay, J. F., and Farrens, D. L. (2015) Structural dynamics and energetics underlying allosteric inactivation of the cannabinoid receptor CB1, *Proc Natl Acad Sci U S A* 112, 8469-8474.
160. Fay, J. F., and Farrens, D. L. (2013) The membrane proximal region of the cannabinoid receptor CB1 N-terminus can allosterically modulate ligand affinity, *Biochemistry* 52, 8286-8294.
161. DebBurman, S. K., Ptasienski, J., Benovic, J. L., and Hosey, M. M. (1996) G protein-coupled receptor kinase GRK2 is a phospholipid-dependent enzyme that can be conditionally activated by G protein betagamma subunits, *J Biol Chem* 271, 22552-22562.
162. DebBurman, S. K., Ptasienski, J., Boetticher, E., Lomasney, J. W., Benovic, J. L., and Hosey, M. M. (1995) Lipid-mediated regulation of G protein-coupled receptor kinases 2 and 3, *J Biol Chem* 270, 5742-5747.
163. Onorato, J. J., Gillis, M. E., Liu, Y., Benovic, J. L., and Ruoho, A. E. (1995) The beta-adrenergic receptor kinase (GRK2) is regulated by phospholipids, *J Biol Chem* 270, 21346-21353.
164. Glomset, J. A., Gelb, M. H., and Farnsworth, C. C. (1990) Prenyl proteins in eukaryotic cells: a new type of membrane anchor, *Trends Biochem Sci* 15, 139-142.
165. Gurevich, V. V., and Benovic, J. L. (1993) Visual arrestin interaction with rhodopsin. Sequential multisite binding ensures strict selectivity toward light-activated phosphorylated rhodopsin, *J Biol Chem* 268, 11628-11638.
166. Bayburt, T. H., Vishnivetskiy, S. A., McLean, M. A., Morizumi, T., Huang, C. C., Tesmer, J. J., Ernst, O. P., Sligar, S. G., and Gurevich, V. V. (2011) Monomeric rhodopsin is sufficient for normal rhodopsin kinase (GRK1) phosphorylation and arrestin-1 binding, *J Biol Chem* 286, 1420-1428.
167. Krupnick, J. G., Gurevich, V. V., and Benovic, J. L. (1997) Mechanism of quenching of phototransduction. Binding competition between arrestin and transducin for phosphorhodopsin, *J Biol Chem* 272, 18125-18131.

168. Kunapuli, P., Gurevich, V. V., and Benovic, J. L. (1994) Phospholipid-stimulated autophosphorylation activates the G protein-coupled receptor kinase GRK5, *J Biol Chem* 269, 10209-10212.
169. Pitcher, J. A., Fredericks, Z. L., Stone, W. C., Premont, R. T., Stoffel, R. H., Koch, W. J., and Lefkowitz, R. J. (1996) Phosphatidylinositol 4,5-bisphosphate (PIP₂)-enhanced G protein-coupled receptor kinase (GRK) activity. Location, structure, and regulation of the PIP₂ binding site distinguishes the GRK subfamilies, *J Biol Chem* 271, 24907-24913.
170. Palczewski, K., McDowell, J. H., and Hargrave, P. A. (1988) Rhodopsin kinase: substrate specificity and factors that influence activity, *Biochemistry* 27, 2306-2313.
171. Fay, J. F., Dunham, T. D., and Farrens, D. L. (2005) Cysteine residues in the human cannabinoid receptor: only C257 and C264 are required for a functional receptor, and steric bulk at C386 impairs antagonist SR141716A binding, *Biochemistry* 44, 8757-8769.
172. Palczewski, K., Buczylo, J., Lebioda, L., Crabb, J. W., and Polans, A. S. (1993) Identification of the N-terminal region in rhodopsin kinase involved in its interaction with rhodopsin, *J Biol Chem* 268, 6004-6013.
173. Levay, K., Satpaev, D. K., Pronin, A. N., Benovic, J. L., and Slepak, V. Z. (1998) Localization of the sites for Ca²⁺-binding proteins on G protein-coupled receptor kinases, *Biochemistry* 37, 13650-13659.
174. Ames, J. B., Levay, K., Wingard, J. N., Lusin, J. D., and Slepak, V. Z. (2006) Structural basis for calcium-induced inhibition of rhodopsin kinase by recoverin, *J Biol Chem* 281, 37237-37245.
175. Higgins, M. K., Oprian, D. D., and Schertler, G. F. (2006) Recoverin binds exclusively to an amphipathic peptide at the N terminus of rhodopsin kinase, inhibiting rhodopsin phosphorylation without affecting catalytic activity of the kinase, *J Biol Chem* 281, 19426-19432.
176. Janz, J. M., and Farrens, D. L. (2004) Rhodopsin activation exposes a key hydrophobic binding site for the transducin alpha-subunit C terminus, *The Journal of biological chemistry* 279, 29767-29773.
177. Acharya, S., Saad, Y., and Karnik, S. S. (1997) Transducin-alpha C-terminal peptide binding site consists of C-D and E-F loops of rhodopsin, *J Biol Chem* 272, 6519-6524.
178. Van Eps, N., Anderson, L. L., Kisselev, O. G., Baranski, T. J., Hubbell, W. L., and Marshall, G. R. (2010) Electron paramagnetic resonance studies of functionally active, nitroxide spin-labeled peptide analogues of the C-terminus of a G-protein alpha subunit, *Biochemistry* 49, 6877-6886.
179. Reeves, P. J., Callewaert, N., Contreras, R., and Khorana, H. G. (2002) Structure and function in rhodopsin: high-level expression of rhodopsin with restricted and homogeneous N-glycosylation by a tetracycline-inducible N-

- acetylglucosaminyltransferase I-negative HEK293S stable mammalian cell line, *Proc Natl Acad Sci U S A* 99, 13419-13424.
180. Feuerstein, S. E., Pulvermuller, A., Hartmann, R., Granzin, J., Stoldt, M., Henklein, P., Ernst, O. P., Heck, M., Willbold, D., and Koenig, B. W. (2009) Helix formation in arrestin accompanies recognition of photoactivated rhodopsin, *Biochemistry* 48, 10733-10742.
 181. Hanson, S. M., Francis, D. J., Vishnivetskiy, S. A., Kolobova, E. A., Hubbell, W. L., Klug, C. S., and Gurevich, V. V. (2006) Differential interaction of spin-labeled arrestin with inactive and active phosphorhodopsin, *Proc Natl Acad Sci U S A* 103, 4900-4905.
 182. Kim, M., Vishnivetskiy, S. A., Van Eps, N., Alexander, N. S., Cleghorn, W. M., Zhan, X., Hanson, S. M., Morizumi, T., Ernst, O. P., Meiler, J., Gurevich, V. V., and Hubbell, W. L. (2012) Conformation of receptor-bound visual arrestin, *Proc Natl Acad Sci U S A* 109, 18407-18412.
 183. Krupnick, J. G., Gurevich, V. V., Schepers, T., Hamm, H. E., and Benovic, J. L. (1994) Arrestin-rhodopsin interaction. Multi-site binding delineated by peptide inhibition, *The Journal of biological chemistry* 269, 3226-3232.
 184. Ostermaier, M. K., Peterhans, C., Jaussi, R., Deupi, X., and Standfuss, J. (2014) Functional map of arrestin-1 at single amino acid resolution, *Proc Natl Acad Sci U S A* 111, 1825-1830.
 185. Pulvermuller, A., Schroder, K., Fischer, T., and Hofmann, K. P. (2000) Interactions of metarhodopsin II. Arrestin peptides compete with arrestin and transducin, *J Biol Chem* 275, 37679-37685.
 186. Sommer, M. E., Hofmann, K. P., and Heck, M. (2012) Distinct loops in arrestin differentially regulate ligand binding within the GPCR opsin, *Nat Commun* 3, 995.
 187. Zhuang, T., Chen, Q., Cho, M. K., Vishnivetskiy, S. A., Iverson, T. M., Gurevich, V. V., and Sanders, C. R. (2013) Involvement of distinct arrestin-1 elements in binding to different functional forms of rhodopsin, *Proc Natl Acad Sci U S A* 110, 942-947.
 188. Kang, Y., Zhou, X. E., Gao, X., He, Y., Liu, W., Ishchenko, A., Barty, A., White, T. A., Yefanov, O., Han, G. W., Xu, Q., de Waal, P. W., Ke, J., Tan, M. H., Zhang, C., Moeller, A., West, G. M., Pascal, B. D., Van Eps, N., Caro, L. N., Vishnivetskiy, S. A., Lee, R. J., Suino-Powell, K. M., Gu, X., Pal, K., Ma, J., Zhi, X., Boutet, S., Williams, G. J., Messerschmidt, M., Gati, C., Zatsepin, N. A., Wang, D., James, D., Basu, S., Roy-Chowdhury, S., Conrad, C. E., Coe, J., Liu, H., Lisova, S., Kupitz, C., Grotjohann, I., Fromme, R., Jiang, Y., Tan, M., Yang, H., Li, J., Wang, M., Zheng, Z., Li, D., Howe, N., Zhao, Y., Standfuss, J., Diederichs, K., Dong, Y., Potter, C. S., Carragher, B., Caffrey, M., Jiang, H., Chapman, H. N., Spence, J. C., Fromme, P., Weierstall, U., Ernst, O. P., Katritch, V., Gurevich, V. V., Griffin, P. R., Hubbell, W. L., Stevens, R. C., Cherezov, V.,

- Melcher, K., and Xu, H. E. (2015) Crystal structure of rhodopsin bound to arrestin by femtosecond X-ray laser, *Nature* 523, 561-567.
189. Reeves, P. J., Thurmond, R. L., and Khorana, H. G. (1996) Structure and function in rhodopsin: high level expression of a synthetic bovine opsin gene and its mutants in stable mammalian cell lines, *Proc Natl Acad Sci U S A* 93, 11487-11492.
190. Schafer, C. T., and Farrens, D. L. (2015) Conformational selection and equilibrium governs the ability of retinals to bind opsin, *J Biol Chem* 290, 4304-4318.
191. Phillips, W. J., and Cerione, R. A. (1988) The intrinsic fluorescence of the alpha subunit of transducin. Measurement of receptor-dependent guanine nucleotide exchange, *J Biol Chem* 263, 15498-15505.
192. Dunham, T. D., and Farrens, D. L. (1999) Conformational changes in rhodopsin. Movement of helix f detected by site-specific chemical labeling and fluorescence spectroscopy, *J Biol Chem* 274, 1683-1690.
193. Pettersen, E. F., Goddard, T. D., Huang, C. C., Couch, G. S., Greenblatt, D. M., Meng, E. C., and Ferrin, T. E. (2004) UCSF Chimera--a visualization system for exploratory research and analysis, *J Comput Chem* 25, 1605-1612.
194. Isberg, V., Vroling, B., van der Kant, R., Li, K., Vriend, G., and Gloriam, D. (2014) GPCRDB: an information system for G protein-coupled receptors, *Nucleic Acids Res* 42, D422-425.
195. van der Kant, R., and Vriend, G. (2014) Alpha-bulges in G protein-coupled receptors, *Int J Mol Sci* 15, 7841-7864.
196. Crooks, G. E., Hon, G., Chandonia, J. M., and Brenner, S. E. (2004) WebLogo: a sequence logo generator, *Genome Res* 14, 1188-1190.
197. Schneider, T. D., and Stephens, R. M. (1990) Sequence logos: a new way to display consensus sequences, *Nucleic Acids Res* 18, 6097-6100.
198. Park, J. H., Morizumi, T., Li, Y., Hong, J. E., Pai, E. F., Hofmann, K. P., Choe, H. W., and Ernst, O. P. (2013) Opsin, a structural model for olfactory receptors?, *Angew Chem Int Ed Engl* 52, 11021-11024.
199. London, N., Raveh, B., Cohen, E., Fathi, G., and Schueler-Furman, O. (2011) Rosetta FlexPepDock web server--high resolution modeling of peptide-protein interactions, *Nucleic Acids Res* 39, W249-253.
200. Raveh, B., London, N., and Schueler-Furman, O. (2010) Sub-angstrom modeling of complexes between flexible peptides and globular proteins, *Proteins* 78, 2029-2040.
201. Chaudhury, S., Berrondo, M., Weitzner, B. D., Muthu, P., Bergman, H., and Gray, J. J. (2011) Benchmarking and analysis of protein docking performance in Rosetta v3.2, *PloS one* 6, e22477.

202. Lyskov, S., Chou, F. C., Conchuir, S. O., Der, B. S., Drew, K., Kuroda, D., Xu, J., Weitzner, B. D., Renfrew, P. D., Sripakdeevong, P., Borgo, B., Havranek, J. J., Kuhlman, B., Kortemme, T., Bonneau, R., Gray, J. J., and Das, R. (2013) Serverification of molecular modeling applications: the Rosetta Online Server that Includes Everyone (ROSIE), *PLoS one* 8, e63906.
203. Lyskov, S., and Gray, J. J. (2008) The RosettaDock server for local protein-protein docking, *Nucleic Acids Res* 36, W233-238.
204. Fraternali, F., and Van Gunsteren, W. F. (1996) An efficient mean solvation force model for use in molecular dynamics simulations of proteins in aqueous solution, *J Mol Biol* 256, 939-948.
205. Fraternali, F., and Cavallo, L. (2002) Parameter optimized surfaces (POPS): analysis of key interactions and conformational changes in the ribosome, *Nucleic Acids Res* 30, 2950-2960.
206. Cavallo, L., Kleinjung, J., and Fraternali, F. (2003) POPS: A fast algorithm for solvent accessible surface areas at atomic and residue level, *Nucleic Acids Res* 31, 3364-3366.
207. Kleinjung, J., and Fraternali, F. (2005) POPSCOMP: an automated interaction analysis of biomolecular complexes, *Nucleic Acids Res* 33, W342-346.
208. Palczewski, K., McDowell, J. H., and Hargrave, P. A. (1988) Purification and characterization of rhodopsin kinase, *The Journal of biological chemistry* 263, 14067-14073.
209. Janz, J. M. (2004) Structural Dynamics of Rhodopsin: Relationships between Retinal Schiff Base Integrity and Receptor Signaling States, In *Biochemistry and Molecular Biology*, Oregon Health & Science University.
210. Scheerer, P., Park, J. H., Hildebrand, P. W., Kim, Y. J., Krauss, N., Choe, H. W., Hofmann, K. P., and Ernst, O. P. (2008) Crystal structure of opsin in its G-protein-interacting conformation, *Nature* 455, 497-502.
211. Singhal, A., Ostermaier, M. K., Vishnivetskiy, S. A., Panneels, V., Homan, K. T., Tesmer, J. J., Vepriyev, D., Deupi, X., Gurevich, V. V., Schertler, G. F., and Standfuss, J. (2013) Insights into congenital stationary night blindness based on the structure of G90D rhodopsin, *EMBO reports*.
212. Standfuss, J., Xie, G., Edwards, P. C., Burghammer, M., Oprian, D. D., and Schertler, G. F. (2007) Crystal structure of a thermally stable rhodopsin mutant, *J Mol Biol* 372, 1179-1188.
213. Baameur, F., Hammit, R. A., Friedman, J., McMurray, J. S., and Clark, R. B. (2014) Biochemical and Cellular Specificity of Peptide Inhibitors of G Protein-Coupled Receptor Kinases, *Int J Pept Res Ther* 20, 1-12.
214. Resek, J. F., Farahbakhsh, Z. T., Hubbell, W. L., and Khorana, H. G. (1993) Formation of the meta II photointermediate is accompanied by conformational changes in the cytoplasmic surface of rhodopsin, *Biochemistry* 32, 12025-12032.

215. Resek, J. F., Farrens, D., and Khorana, H. G. (1994) Structure and function in rhodopsin: covalent crosslinking of the rhodopsin (metarhodopsin II)-transducin complex--the rhodopsin cytoplasmic face links to the transducin alpha subunit, *Proc Natl Acad Sci U S A* 91, 7643-7647.
216. Yang, K., Farrens, D. L., Hubbell, W. L., and Khorana, H. G. (1996) Structure and function in rhodopsin. Single cysteine substitution mutants in the cytoplasmic interhelical E-F loop region show position-specific effects in transducin activation, *Biochemistry* 35, 12464-12469.
217. Hirsch, J. A., Schubert, C., Gurevich, V. V., and Sigler, P. B. (1999) The 2.8 Å crystal structure of visual arrestin: a model for arrestin's regulation, *Cell* 97, 257-269.
218. Vishnivetskiy, S. A., Gimenez, L. E., Francis, D. J., Hanson, S. M., Hubbell, W. L., Klug, C. S., and Gurevich, V. V. (2011) Few residues within an extensive binding interface drive receptor interaction and determine the specificity of arrestin proteins, *J Biol Chem* 286, 24288-24299.
219. Vishnivetskiy, S. A., Hosey, M. M., Benovic, J. L., and Gurevich, V. V. (2004) Mapping the arrestin-receptor interface. Structural elements responsible for receptor specificity of arrestin proteins, *The Journal of biological chemistry* 279, 1262-1268.
220. Raman, D., Osawa, S., and Weiss, E. R. (1999) Binding of arrestin to cytoplasmic loop mutants of bovine rhodopsin, *Biochemistry* 38, 5117-5123.
221. Shi, W., Osawa, S., Dickerson, C. D., and Weiss, E. R. (1995) Rhodopsin mutants discriminate sites important for the activation of rhodopsin kinase and Gt, *J Biol Chem* 270, 2112-2119.
222. Kisselev, O. G., Kao, J., Ponder, J. W., Fann, Y. C., Gautam, N., and Marshall, G. R. (1998) Light-activated rhodopsin induces structural binding motif in G protein alpha subunit, *Proc Natl Acad Sci U S A* 95, 4270-4275.
223. Brabazon, D. M., Abdulaev, N. G., Marino, J. P., and Ridge, K. D. (2003) Evidence for structural changes in carboxyl-terminal peptides of transducin alpha-subunit upon binding a soluble mimic of light-activated rhodopsin, *Biochemistry* 42, 302-311.
224. Farrens, D. L. (2010) What site-directed labeling studies tell us about the mechanism of rhodopsin activation and G-protein binding, *Photochem Photobiol Sci* 9, 1466-1474.
225. Huang, C. C., and Tesmer, J. J. (2011) Recognition in the face of diversity: interactions of heterotrimeric G proteins and G protein-coupled receptor (GPCR) kinases with activated GPCRs, *J Biol Chem* 286, 7715-7721.
226. Clackson, T., and Wells, J. A. (1995) A hot spot of binding energy in a hormone-receptor interface, *Science* 267, 383-386.

227. Ohguro, H., Johnson, R. S., Ericsson, L. H., Walsh, K. A., and Palczewski, K. (1994) Control of rhodopsin multiple phosphorylation, *Biochemistry* 33, 1023-1028.
228. Ohguro, H., Palczewski, K., Ericsson, L. H., Walsh, K. A., and Johnson, R. S. (1993) Sequential phosphorylation of rhodopsin at multiple sites, *Biochemistry* 32, 5718-5724.
229. Vishnivetskiy, S. A., Raman, D., Wei, J., Kennedy, M. J., Hurley, J. B., and Gurevich, V. V. (2007) Regulation of arrestin binding by rhodopsin phosphorylation level, *J Biol Chem* 282, 32075-32083.
230. Bayburt, T. H., Vishnivetskiy, S. A., McLean, M. A., Morizumi, T., Huang, C. C., Tesmer, J. J., Ernst, O. P., Sligar, S. G., and Gurevich, V. V. (2011) Monomeric rhodopsin is sufficient for normal rhodopsin kinase (GRK1) phosphorylation and arrestin-1 binding, *The Journal of biological chemistry* 286, 1420-1428.
231. Busillo, J. M., Armando, S., Sengupta, R., Meucci, O., Bouvier, M., and Benovic, J. L. (2010) Site-specific phosphorylation of CXCR4 is dynamically regulated by multiple kinases and results in differential modulation of CXCR4 signaling, *J Biol Chem* 285, 7805-7817.
232. Reiter, E., Ahn, S., Shukla, A. K., and Lefkowitz, R. J. (2012) Molecular mechanism of beta-arrestin-biased agonism at seven-transmembrane receptors, *Annu Rev Pharmacol Toxicol* 52, 179-197.
233. Patel, C. B., Noor, N., and Rockman, H. A. (2010) Functional selectivity in adrenergic and angiotensin signaling systems, *Mol Pharmacol* 78, 983-992.
234. Butcher, A. J., Prihandoko, R., Kong, K. C., McWilliams, P., Edwards, J. M., Bottrill, A., Mistry, S., and Tobin, A. B. (2011) Differential G-protein-coupled receptor phosphorylation provides evidence for a signaling bar code, *The Journal of biological chemistry* 286, 11506-11518.
235. Szczepek, M., Beyriere, F., Hofmann, K. P., Elgeti, M., Kazmin, R., Rose, A., Bartl, F. J., von Stetten, D., Heck, M., Sommer, M. E., Hildebrand, P. W., and Scheerer, P. (2014) Crystal structure of a common GPCR-binding interface for G protein and arrestin, *Nat Commun* 5, 4801.
236. Mathiasen, S., Christensen, S. M., Fung, J. J., Rasmussen, S. G., Fay, J. F., Jorgensen, S. K., Veshaguri, S., Farrens, D. L., Kiskowski, M., Kobilka, B., and Stamou, D. (2014) Nanoscale high-content analysis using compositional heterogeneities of single proteoliposomes, *Nature methods* 11, 931-934.
237. Kobashi, K. (1968) Catalytic oxidation of sulfhydryl groups by o-phenanthroline copper complex, *Biochim Biophys Acta* 158, 239-245.

Appendix 1: Supplementary Results and Discussion for TyrIQ.

Opening statement.

This appendix includes the supplementary results and discussion from our 2014 manuscript expanding the TrIQ method to include tyrosine as a quenching residue for the fluorophore bimane. In this work, we used time-correlated single photon counting to measure the fluorescent decay of bimane when unquenched and when quenched by tryptophan and tyrosine at various C α -C α distances. The resolution of the instrument used, and the fitting program utilized, allowed us to fit the decay curves with alternative kinetic models. Whereas the decay of bimane is well described by an exponential decay model, we were also able to fit the decay with a Lorentzian distribution for the multiple lifetimes within the population of quenched bimane-labeled T4 lysozyme. The results and implications of this treatment are discussed below.

I have also included data I generated in collaboration with another laboratory working to expand TrIQ/TyrIQ to fluorescence imaging applications. In pursuit of this goal, I tested the ability of tryptophan and tyrosine to quench the fluorophores Atto488 and Oxa11.

The fluorescence decay curves can be fit with a Lorentzian Distribution kinetic model.

The fluorescence decay data were all subjected to a lifetime distribution analysis with the goal of assessing whether the quenched bimane exhibited distinct short and long lifetime components, which could be used to further analyze the dynamic quenching data from our TrpIQ and TyrIQ experiments. These analyses show the unquenched, Phe-containing samples are well fit by a single lifetime distribution (Table A1.1, and Figure A1.1), and the resulting lifetimes span approximately the same range as the exponential fits (Table 2.1).

For the Trp-containing samples, only the sample that did not show static quenching (11.0 Å) could be well fit to a single Lorentzian distribution. The remaining Trp-containing samples required use of a bimodal distribution, and we note that these also showed considerable amounts of quenching. Interestingly, in almost all cases, the longer lifetime component fluctuated in these bimodal lifetime distributions (with the longer lifetime component getting shorter as the distance between the Trp and bimane decreased), whereas the shorter lifetime was approximately 1 ns or less. The exception to this trend is the 7.5 Å Trp sample, in which the longer lifetime component is shifted closer to the unquenched lifetime, possibly due to the larger relative contribution of static quenching at this distance (Figure 2.6), which removes fluorophores from the observable lifetime measurement.

A similar pattern is observed for the Tyr samples. The lifetime data for the 11.0 and 10.7 Å distances can be fit to a single lifetime distribution, consistent with the fact that

these sites also show no quenching of the emission intensity (Figures 2.4, 2.6). However, the samples that do show Tyr-induced quenching of the bimane are also best fit to a bimodal distribution, also with one long lifetime component shorter than the unquenched sample and a short component, often of less than 1 ns.

Lifetime decays analyzed using a Lorentzian distribution kinetic model provide insights into the dynamic quenching component in TrIQ and TyrIQ studies.

The pattern of lifetime distributions that emerges from a distribution fit is intriguing (see Figure A1.1). A single lifetime distribution is observed for all the control (unquenched) Phe-containing samples (top row). In cases of substantial quenching the decay data are best fit using a bimodal lifetime distribution, resulting in a long lifetime component that is always shorter than the corresponding value from the unquenched (Phe containing) sample. Moreover, the degree to which it is decreased (left shifted in Figure A1.1) seems to correlate with the relative presence of dynamic quenching (see Figure 2.6). In fact, there seems to be a correlation between the relative decrease in long lifetime components and $C\alpha$ - $C\alpha$ separation for the 8.4, 10.1, 10.7, and 11 Å samples, the 7.5 Å shows primarily static quenching and does not fit this trend.

We propose these data might be interpreted as follows. The longer component reflects longer-range dynamic quenching because the relative shortening of the longer lifetime component correlates well with the relative presence of dynamic quenching components. The very short lifetimes are due to very fast quenching caused by probe-quencher pairs that are very close together, but not quite touching at the moment of light

excitation. This population of probe-quencher pairs could be considered to be yet a 4th conformation that is not explicitly accounted for in the equations given in Figure 2.2, and the ability to detect such events will depend highly on the time resolution of the instrument and ability to separate them from scattering events. Thus, the use of a Lorentzian analysis approach may help to identify and separate potential “pseudo static quenching” interactions from the calculation of dynamic quenching events. Taken together, these analyses suggest it may be possible to investigate dynamic quenching by simply focusing on the longer-lifetime component in a bimodal Lorentzian lifetime distribution analysis, and this possibility should potentially be explored further.

Analysis of two fluorophores well suited for fluorescence imaging, Atto488 or Oxa11.

The TrIQ/TyrIQ method is powerful for assessing real-time dynamic interactions within and between proteins. To date, we have only used this for measuring fluorescence of samples in a cuvette, resulting in data that applies to bulk conformational changes. However, a rapidly emerging method for resolving single molecule dynamics uses the instrumentation employed in fluorescence imaging, whereby one can detect changes in individual proteins by tracking the fluorescence of single points of light in the field of view (236). The fluorophore we have commonly used in TrIQ/TyrIQ studies is bimeans, which has several benefits including its small size—being not much larger than a Trp residue—but unfortunately, bimeans is not well suited for fluorescence imaging. Another favored fluorophore in our lab is BODIPY, which is larger than bimeans (Figure 2.1) is red-shifted and has better quantum yield, but is not well suited to fluorescence imaging

due to photobleaching (from communications with the Stamou lab). In order to test the applicability of TyrIQ/TrIQ to fluorescence imaging techniques, in collaboration with the Stamou lab, I tested the ability of both Trp and Tyr to quench Atto 488 and Oxa11 using the closest Fluorophore/Quencher pair in T4L N116X/N132C that has a C α -C α distance of 7.5 Å, illustrated in Figure 2.1, as well as the F4X/K60C T4L construct that has a 10.5 Å C α -C α separation distance, illustrated in Figure 2.10.

Atto 488 is quenched appreciably by tryptophan, and to a lesser degree by tyrosine.

T4L samples were matched for Atto 488 fluorophore concentration by absorbance and the fluorescence was measured as described in the methods section for Chapter 2. At the 7.5 Å C α -C α separation, tryptophan quenches the fluorescence emission with a Fo/F of ~3 and a τ_0/τ of 1.9 (Figure A1.2A), which indicates that the quenching is comprised of both dynamic and static components. Indeed, when the relative contributions of dynamic and static quenching are calculated it is clear that about half of the observed quenching is due to static quenching and half is due to dynamic quenching (Figure A1.2A).

At the 10.5 Å C α -C α distance, there was less quenching, as shown in Figure A1.2B. The emission quenching ratio is 1.4 and the lifetime quenching ratio is 1, or no effect on the lifetime. This results in a small amount of quenching that is only attributed to static quenching, but further studies would be required to validate this finding.

Despite the relatively small emission quenching ratio for Atto 488 and tryptophan, this fluorophore:quencher pair could be ideal if, as this study suggests, the strong quenching is distance dependent. In fact, the sharp decline in quenching ability would make this pair more usable because of the increased apparent resolution of this quenching, meaning that

even small conformational changes could be monitored by changes in Atto 488 fluorescence.

Tyrosine does show a small amount of quenching for Atto 488 at the 7.5 Å C α -C α separation distance, with a Fo/F of 1.3 and a τ_0/τ of 1.2 (Figure A1.2A), values that are similar enough to indicate that the small amount of quenching is likely dynamic in nature. The components of fluorescence analysis show a minor presence of static quenching, but given the relative low amount of total quenching, this could be explained by error. The small amount of quenching observed at the shortest separation distance is absent at the 10.5 Å C α -C α distance (Figure A1.2B). In order for tyrosine to be a useful quenching residue for Atto 488, additional C α -C α distances would need to be tested to see if there are orientations of quencher and Atto 488 that does result in substantive amounts of quenching.

Oxa11 is weakly quenched by tryptophan, but not by tyrosine.

Oxa11 is a derivative of Atto 665, and differs in linker length, but not in chemical structure of the fluorophore. The 2010 Mansoor, *et al* study found that tryptophan was able to quench Atto665 in a distance dependent manner (68), with Fo/F of \sim 3 for the 7.5 Å C α -C α separation, and the mode of quenching was predominantly attributed to static quenching. In this study, I found that tryptophan only slightly quenched Oxa11, with an Fo/F of 1.5 at the 7.5 Å C α -C α distance (Figure A1.3A). I also tested the ability of tryptophan to quench Oxa11 at the 10.5 Å C α -C α separation (Figure A1.3B), and found the emission quenching ratio was 1.8, which is slightly higher than the emission quenching ratio observed for the much shorter C α -C α distance. Unfortunately, our

TCSPC instrument was not equipped with an appropriate light source to excite Oxa11, so the fluorescence decay was not analyzed. The disparity in tryptophan quenching amount between the Atta 665 and Oxa11 dyes could be due to steric issues arising from decreased linker length, as well as differences in the behavior of the two fluorophores in their excited states.

Tyrosine did not appreciably quench Oxa11 at the 7.5 Å C α -C α distance, but did show a small amount of quenching in the 10.5 Å C α -C α distance sample. The relatively small emission quenching ratio in this case, without a concomitant quenching ability at the shorter distance, does not strongly support the utility of TyrIQ for quenching studies using Oxa11, but a full analysis would be required to fully rule out this fluorophore:quencher pair.

In summary, in the course of the collaboration between the Farrens lab at OHSU and the Stamou lab in Denmark, we began to assess if the TrIQ/TyrIQ quenching methods would translate to fluorescence imaging techniques. The results are mixed but still promising; we find that Trp can measurably quench Atto 488 at relatively close distances, but additional experiments will be needed to better define this observation.

Tables

		C α -C α Distance							
		7.5	8.4	10.1	10.7	11			
<i>Phe</i>	τ	10.48	13.51	9.19	11.08	8.45			
	%	100.00	100.00	100.00	100.00	100.00			
	FWHM	2.42	3.98	1.42	3.06	1.47			
	χ^2	1.04	1.03	0.95	0.99	0.92			
<i>Tyr</i>	τ	7.38	2.38	5.89	0.06	7.06	11.09	8.37	
	%	58.67	41.33	9.99	90.01	100.00	100.00	100.00	
	FWHM	3.60	6.30	4.93	0.42	3.20	2.29	1.73	
	χ^2	1.03		0.96		1.03	1.03	1.03	
<i>Trp</i>	τ	6.08	0.09	6.08	0.09	4.39	0.81	8.73	6.60
	%	9.32	90.68	23.85	76.15	37.70	62.30	100.00	100.00
	FWHM	7.94	0.75	7.94	0.75	6.12	1.03	2.59	0.00
	χ^2	1.10		1.00		0.95		1.09	1.00

Bimane fluorescent decay data were fit with a Lorentzian distribution model using FluoFit software from PicoHarp. τ is the center of the distributed lifetime component, % is the relative percentage of the distributed component, FWHM is the distribution width (full width at half maximum) of the distributed component, and χ^2 is the chi-squared goodness of fit parameter.

Figures

Figure A1.1: Results from fitting Bimane decays with a Lorentzian distribution model.

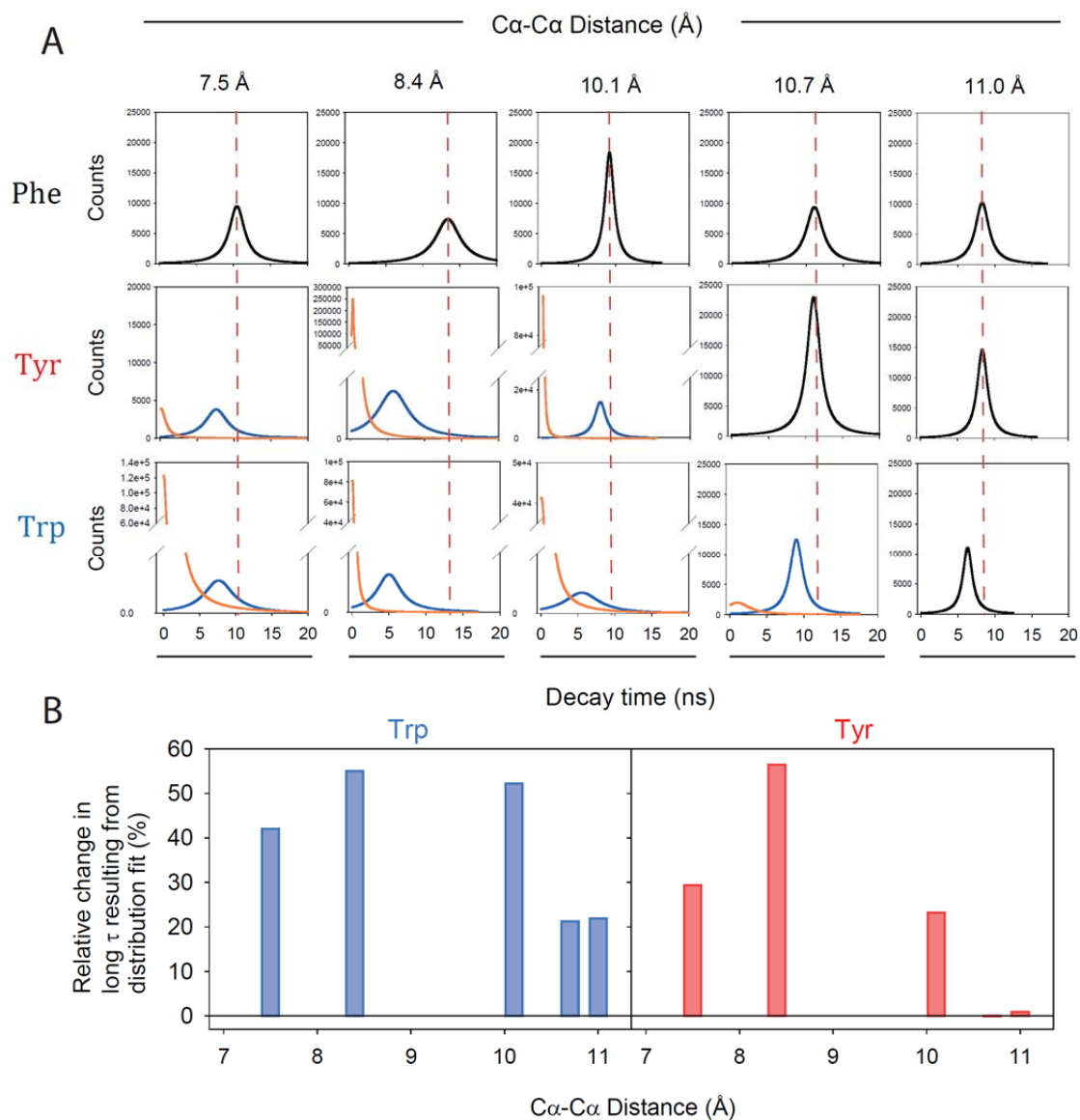


Figure A1.1: Results from fitting Bimane decays with a Lorentzian distribution model.

(A) Lorentzian distribution fitting of bimane-labeled T4 lysozyme lifetime decay curves when the probe is unquenched (Phe containing samples, top row) or is quenched by Tyrosine (middle row) or Tryptophan (bottom row) residues located at different distances from the bimane probe. Each graph is a distribution with amplitude in counts as the y-axis and decay time in nanoseconds as the x-axis. Each column is a different C_{α} - C_{α} distance (\AA) separating quencher and probe (labeled at the top). The vertical red dotted lines act as a reference for the peak lifetime of the unquenched samples containing a Phe residue at each C_{α} - C_{α} distance. (B) The relative change in the long lifetime component of bimane quenched by Trp or Tyr was calculated using $(\tau_0 - \tau) / \tau_0 * 100$. The relative shift in the long lifetime follows a general increasing trend with decreasing C_{α} - C_{α} distances, except for the shortest distance, 7.5 \AA , which has a very large static quenching component.

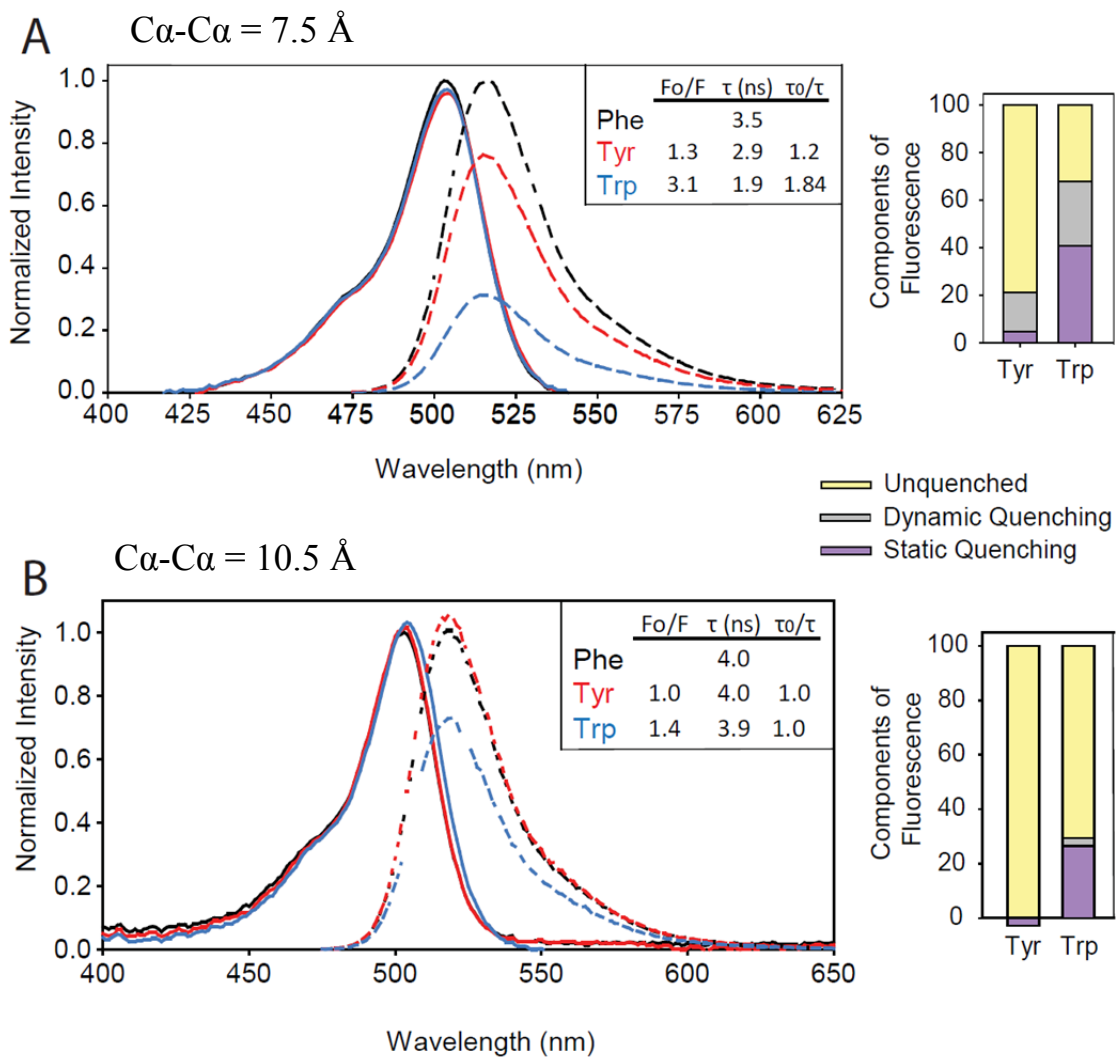
Figure A1.2 Ability of Tyrosine and Tryptophan to quench Atto 488 fluorescence.

Figure A1.2 Ability of Tyrosine and Tryptophan to quench Atto 488 fluorescence. (A) T4L N116X/N132-Atto 488 (7.5 Å separation) were matched for fluorophore concentration, as illustrated in the solid lines at ~425-540 nm, with the unquenched, Phe-containing construct in black, the Tyr-containing construct in red, and the Trp-containing construct in blue. The fluorescence emission is shown on the right of the graph shown in dashed lines, with the same color coding as previous. This analysis shows that Tyr can minimally quench Atto 488 but to a lesser extent than Trp, which quenches Atto 488 with a F_0/F of ~3. The inset shows the emission quenching ratios, the calculated lifetimes, and the lifetime quenching ratios. In the graph on the right, the emission and lifetime quenching ratios were combined to calculate the relative contributions of dynamic and static quenching to the observed reduction in Atto 488 fluorescence and it was found the Trp quenching is about half static quenching. (B) Analysis of T4L F4X/K60-Atto 488 (10.5 Å separation) shows an emission quenching ratio of 1.4 from Trp, but no observable lifetime quenching, resulting in predominantly static quenching. Tyr does not quench Atto 488 at this distance.

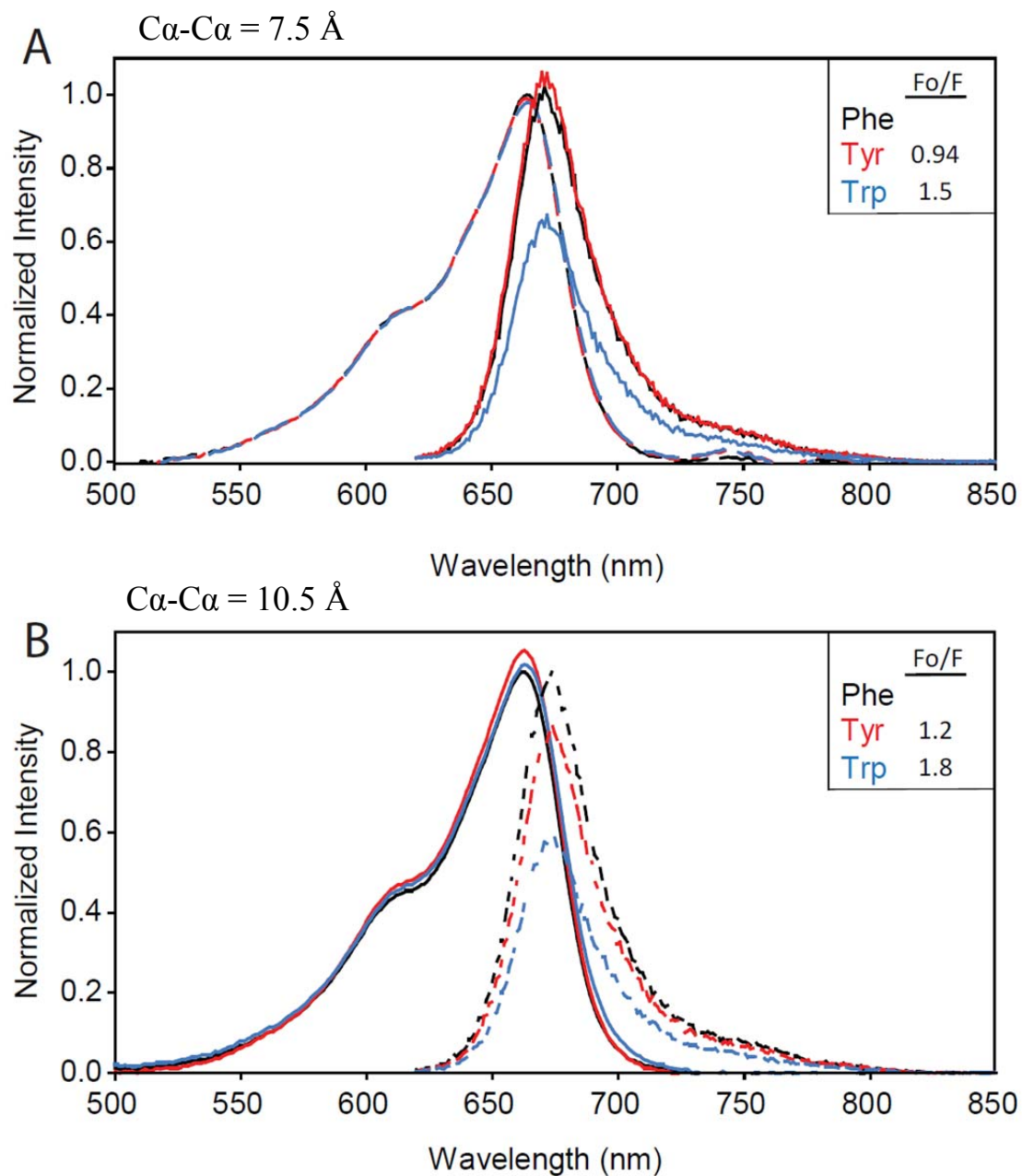
Figure A1.3 Ability of Tyrosine and Tryptophan to quench Oxa 11 fluorescence

Figure A1.3 Ability of Tyrosine and Tryptophan to quench Oxa 11 fluorescence. (A) T4L N116X/N132-Oxa 11(7.5 Å separation) were matched for fluorophore concentration, as illustrated in the solid lines at ~525-740 nm, with the unquenched, Phe-containing construct in black, the Tyr-containing construct in red, and the Trp-containing construct in blue. The fluorescence emission is shown on the right of the graph shown in dashed lines, with the same color coding as previous. This analysis shows that Tyr does not quench Oxa11 at this C α -C α distance or conformation but that Trp Oxa11 with a Fo/F of 1.5. The inset shows the emission quenching ratios. (B) Analysis of the T4L F4X/K60-Oxa11 (10.5 Å separation) shows a slightly increased emission quenching ratio for Trp, at 1.8. At this distance separation, Tyr shows a slight ability to quench Oxa11, with an emission quenching ratio of 1.2.

Appendix 2: Preliminary GRK1:rhodopsin crosslinking experiments.

Introduction.

While I spent much of my time optimizing the purification and activity of WT GRK1, I was also looking ahead to higher resolution methods for mapping the interaction between rhodopsin and GRK1. The work presented in Chapters 3 and 4 of this dissertation leverages decades of research into individual rhodopsin mutations that have been well characterized and could thus be used as a comparative standard for WT GRK1 activity with Gt activation and visual arrestin binding using site-direct labeling techniques, which were critical for identification of a binding interface on rhodopsin that is shared by all three intracellular binding partners of rhodopsin. The next step in utilizing site-directed labeling techniques in general is to start working with mutants of GRK1.

Previous studies from the Tesmer lab used GRK1 mutants to show the mechanism of kinase activation involves interaction between the N- and C-lobes of the kinase (84, 148). Work from the same group used point mutations in the N-terminus of GRK1 and GRK6 to show that mutation of certain hydrophobic residues in the N-terminus of GRKs almost completely impairs its ability to phosphorylate rhodopsin (32, 84, 87).

The mutagenesis work that is required to utilize site-directed labeling approaches, such a minimal cysteine mutants, is still in an early phase. A previous graduate student, Dr. Abhinav Sinha, contributed to this effort by mutating surface cysteine residues on GRK1. When this “cys-less” GRK1 is expressed and purified, however, it can still react

with the sulfhydryl-reactive probe monobromobimane, indicating that there is still at least one reactive cysteine present in the protein.

In this appendix I describe my efforts to produce various cysteine mutant GRK1s and to assess their functionality. Fortunately, I discovered that GRK1 L6C has WT-like functionality on a minimal cysteine rhodopsin mutant, as well as two cysteine-mutant rhodopsins, V250C and V139C. I undertook this endeavor prior to modeling the interaction between rhodopsin and the GRK1 N-terminus. The crosslinking experiments I chose used a rhodopsin mutant with a cysteine at site 242, which is located in intracellular loop 3, which connects TM5 and TM6. Site 242 is a threonine in the native structure. Mutation of site T242 starkly inhibits rhodopsin's ability to activate transducin (216) but does not affect phosphorylation by GRK1 (220, 221), thus, I surmised that site 242 was ideal for initial attempts at crosslinking GRK1 to rhodopsin.

I used two crosslinking approaches. The first employed copper-phenanthroline-mediated direct di-sulfide crosslinking (237) by redox mechanism (Figure A2.1). The second approach used a bis-maleimide crosslinker with an ethyl linker group (BMOE), resulting in a ~ 8 Å linker that allows for less discretion (Figure A2.1). Unfortunately, I was unable to observe crosslinked complexes using either approach.

Nevertheless, I was able to optimize our methods for electrophoretic analyses of these experiments. In particular, I borrowed an easy and accessible method for silver staining my SDS-PAGE gels from Dr. Jessica Martin, which helped me to maintain low protein concentrations in my reactions and small loading volumes in each gel well (given that rhodopsin does not stain well with Coomassie blue and usually requires larger total protein per gel well for visualization). This method was also ideal because the silver-

development step was slow (up to 20 minutes), which avoids a common technical challenge with silver staining: overdevelopment. The other method optimization was a dual probe western blot detection system that allowed me to simultaneously probe my transferred blot with a monoclonal antibody raised against the rhodopsin C-terminus in mice, called 1D4 (OHSU monoclonal antibody core), and a monoclonal antibody for the C-terminus of GRK1 raised in rabbits (Santa Cruz Biotech).

Materials & Methods.

Preparation of rhodopsin mutants.

Rhodopsin mutant constructs were expressed in HEK 293S GnTI- cells, as described in Chapters 3 and 4 of this dissertation.

Purification and activity assays of site-directed GRK1 cysteine mutants.

GRK1 cysteine mutant DNA was produced using the overlap-extension PCR cloning method, and mutations were confirmed by DNA sequencing before expression in COS-1 cells and purification as described in Chapters 3 and 4 of this dissertation. Activity assays were performed as described in Chapter 3.

Copper phenanthroline crosslinking.

Crosslinking reactions contained 1 μ M rhodopsin T242C₀, 0.3% DOPS, 0.05% DDM, 5 mM MES, 20 mM HEPES pH 7.2, 75 mM MgCl₂, 2 mM EDTA, 1 mM Cu²⁺, 3 mM 1,10 phenanthroline. The reaction volume was 35 μ L, and reactions were set up in an 8-strip of PCR tubes, to allow for simultaneous initiation and quenching of parallel

crosslinking experiments using a multichannel pipette. The order of the experiment involved pre-incubation of the rhodopsin, buffers, and kinase for 20 minutes.

The copper-phenanthroline was prepared as follows. A 450 mM 1,10 phenanthroline was freshly prepared by dissolving 0.09 g of 1,10 phenanthroline crystals in 1 mL 100% ethanol. The copper and phenanthroline (CuP) were pre-chelated for 10 minutes at room temperature at a concentration of 1 mM Cu^{2+} and 3 mM 1,10 phenanthroline in rhodopsin kinase buffer. Before addition to the rhodopsin/kinase mixture, the pre-chelated CuP was diluted 1:100, again in rhodopsin kinase buffer, such that the addition of 3.5 μL of this CuP pre-chelation to a final reaction volume resulted in the desired final concentration of 1 μM Cu^{2+} and 3 μM phenanthroline.

Reactions were quenched before light activation and then 15 and 60 minutes after light excitation in 66 mM N-ethyl maleimides (freshly prepared). Quenched samples were mixed with Applebury SDS-PAGE loading buffer containing either no or 500 mM DTT and separated by electrophoresis on two identical 8% Tris-tricine polyacrylamide gels. One gel was silver stained, and the other was transferred to PVDF for subsequent Western blotting.

BMOE crosslinking.

The BMOE crosslinking experiments were carried out under the same conditions as the copper phenanthroline experiments, but instead of adding the CuP pre-chelation to the pre-incubated rhodopsin/kinase mixture, BMOE was added to 10 or 50 μM final concentrations. The BMOE was freshly prepared by dissolving 1 mg of powder in 1 mL DMSO to make a 5 mM solution and serially diluting until a suitable concentration is

reached. Reactions are quenched in Cysteine before addition of Applebury SDS-PAGE buffer and analyzed as described above.

SDS-Page and silver staining.

Samples were separated on 8% Tris-tricine polyacrylamide gels. After electrophoresis, gels were fixed by incubation in 30% ethanol and 10% acetic acid for 45 minutes, then more of the same mixture overnight. The next day, gels were washed twice in 20% ethanol for 10 minutes, then in deionized water twice for 10 minutes each. Next, gels were briefly incubated in 0.02% sodium thiosulfate, and rinsed twice in deionized water for 1 minute each. Gels were incubated for 2 hours in 12 mM silver nitrate. After removing the silver nitrate solution, gels were briefly rinsed in deionized water for 10 seconds. Gels were developed in 2% sodium carbonate, 0.00125% sodium thiosulfate, and 0.00925% formaldehyde until protein bands were sufficiently developed. This process was stopped by first draining the developing buffer then adding the stop solution comprised of 330 mM Tris base and 0.5% acetic acid.

Western blot transfer and dual antibody labeling.

The contents of separated SDS-PAGE gels were transferred to immobilon-P PVDF membranes and blocked in PBSSC and 50% Aquablock overnight at 4° C with rocking. Blots were then incubated for 1-2 hours at room temperature in 1° antibody mix that contained 1:10,000 dilution of mouse α -rhodopsin 1D4 antibody and 1:250 dilution rabbit α -GRK1 C-terminus (purchased from Santa Cruz biologicals) in PBSSC, 10% Aquablock, and 0.05% Tween-20. The 1° antibody mix was carefully removed and saved, and then blots were washed with PBSSC and 0.05% Tween-20 three times for 10

minutes each. The blots were then incubated for 1-2 hours at room temperature with secondary antibody mix containing 1:25,000 dilution of α -mouse and α -rabbit infrared antibodies, followed by three washes in PBSSC containing 0.05% Tween-20 then PBSSC alone to reduce background infrared signal from Tween-20. Blots were imaged using the LiCor odyssey system.

Results.

Purified GRK1 L6C has wild type-like activity.

The functionality of the purified GRK1 L6C (Figure A2.2) was assessed by measuring its ability to phosphorylate wild-type rhodopsin in the form of the minimal cysteine recombinantly expressed rhodopsin mutant θ , and two cysteine mutant rhodopsins, in a θ background, V139C θ and V250C θ , using the 96-well filter binding plate assay described in Chapter 3. I found that GRK1 L6C and WT GRK1 showed similar activity towards DDM-purified θ rhodopsin, with total receptor phosphorylation of ~4-5 phosphates/receptor (Figure A2.3). GRK1 L6C activity, like that of WT GRK1, is increased when the acidic phospholipid DOPS is incorporated in the DDM-rhodopsin micelles, to ~6 phosphates/receptor (Figure A2.3).

Similar phosphorylation efficiencies are observed for the rhodopsin cysteine mutants tested V139C θ and V250C θ in DDM-DOPS mix are phosphorylated by both GRK1 L6C and WT GRK1 with ~6-8 phosphates per receptor (Figure A2.4). Specific activities and initial rates of phosphorylation can be found in Table A3.1.

GRK1 T8C and S13C are less active than wild type GRK1.

GRK1 T8C and GRK1 S13C both show limited ability to phosphorylate DDM-solubilized θ rhodopsin with ~ 2 phosphates per receptor, which increases to $\sim 3-4$ phosphates per receptor in the presence of DOPS (Figure A2.3). Similarly, both GRK1 T8C and GRK1 S13C can add $\sim 3-4$ phosphates per V139C $_{\theta}$ in DOPS mix and $\sim 4-5$ phosphates per V250C $_{\theta}$ in DOPS mix (Figure A2.4), specific activities and initial rates are reported in Table A2.1.

GRK1 T8C and V9C were not crosslinked to rhodopsin T242C $_{\theta}$ in the presence of 10 or 50 μ M BMOE.

No crosslinked bands were observed for either GRK1 T8C or GRK1 V9C with rhodopsin T242C $_{\theta}$ using either 50 μ M BMOE (Figure A2.5, left) or 10 μ M BMOE (Figure A2.5, right). The quenched crosslinked experiments were analyzed using SDS-PAGE followed by either silver staining (top gels) or doubly probed western blotting (bottom blots) with the red channel showing rhodopsin bands and the green channel showing GRK1 bands. While there are visible higher molecular weight bands for lanes containing rhodopsin T242C $_{\theta}$ incubated with either GRK1 T8C or V9C visible by both silver staining and western blot analysis, all of the higher molecular weight bands are also present in the lanes containing a receptor only or kinase only control, indicating that these bands are most likely self-dimers and not crosslinks between the two proteins.

GRK1 T8C and V9C were not crosslinked to rhodopsin T242C₀ in the presence of copper phenanthroline.

As with my crosslinking attempts with BMOE, I did not observe any crosslinked bands of GRK1 T8C or GRK1 V9C with rhodopsin T242C₀ (Figure A2.6, right) that were not present in the kinase or receptor control lanes (Figure A2.6, left).

Discussion and future directions.

GRK1 N-terminal cysteine mutant L6C has WT activity towards rhodopsin and rhodopsin mutants.

Previous GRK mutation studies have demonstrated that certain mutations to the extreme N-terminus can have a negative effect on phosphorylation of rhodopsin. It should be noted that the GRK1 construct that was used in these studies was the C-terminally truncated construct called wt $\Delta 535$ -His₆. A 2008 study by Singh, et al.(87) reported that mutations to the N-terminus reduced that K_m affinity and V_{max} of the mutant GRK1 for rhodopsin, specifically S5A, and T8E had K_m values of 5.1, 1.5, and 4.8 μ M compared to a value of 2.1 μ M for the wt $\Delta 535$ -His₆. The T8A GRK1 mutant had a comparable K_m of 1.5 μ M, but, like S5A and T8E, had reduced V_{max} values: S5A is 1600 nmol/min/mg, T8A is 1200 nmol/min/mg, and T8E is 1700 nmol/min/mg compared to a V_{max} of 2300 nmol/min/mg for WT $\Delta 535$ -His₆ (87). In a more recent manuscript, in 2011 Huang, et al. reported that GRK1 N-terminal mutants had reduced activity as reported a fold decreases in K_{cat}/K_m compared to wt $\Delta 535$ -His₆, L6A fold decrease was 18, E7A fold decrease was 12, fold decrease was 55, and V10A fold decrease was 130 (84). The

latter results were also controlled by testing the N-terminal GRK1 mutants' ability to phosphorylate a control peptide and found very little difference in this measurement, which indicated that the reduced ability to phosphorylate rhodopsin was due to reduced affinity for the receptor and not a change in catalytic ability.

In my initial work with N-terminal cysteine mutations of GRK1, I found that the L6C mutation had similar activity to the full length WT GRK1 as assessed by specific activity. This similar activity was true for the minimal cysteine rhodopsin mutant θ purified in DDM and in a mixture of DDM and DOPS, and also for the rhodopsin cysteine mutants V139C θ and V250C θ (Table 3.1, Figures A2.3 and A2.4). These parameters were calculated from the phosphorylation experiments shown in Figure A3.4 and A3.5, in which it is clear that the GRK1 L6C mutant is able to fully phosphorylate DDM-solubilized USR, θ , V139C θ , and V250C θ .

GRK1 N-terminal cysteine mutants T8C and S13C have reduced activity towards rhodopsin and rhodopsin mutants.

Unlike GRK1 L6C, GRK1 T8C and S13C, both show decreased specific activity for DDM-purified rhodopsin θ . Incubation of the DDM-purified rhodopsin θ with DOPS increases the specific activity of these N-terminal mutants (Table A2.1) and increases the total phosphate incorporation to ~ 4 phosphates per receptor, well above the reported minimum 3 phosphates necessary for visual arrestin binding (165, 167, 230), but below the full phosphorylation of ~ 8 phosphates per receptor for DDM-solubilized USR by WT GRK1. Both GRK1 T8C and S13C display decreased total phosphorylation level for the rhodopsin mutants V139C θ and V250C θ , but again, the phosphorylation level is well

within the published minimum value, and indicates that, despite their lower activity, these mutants should be usable for future crosslinking experiments.

Attempts to crosslink rhodopsin T242C_θ were unsuccessful, but our binding model suggests sites for future crosslinking experiments.

Attempts to crosslink GRK1 T8C and V9C with rhodopsin T242C_θ failed using both approaches, direct disulfide crosslinking with copper phenanthroline (Figure A2.6) and the extended bis-maleimide BMOE (Figure A2.5). Unfortunately, there are several factors that could have contributed to this lack-of-results. First, I did not test the activity of the GRK1 V9C on any receptor, nor was GRK1 T8C activity measured for the T242C_θ, thus, a lack of crosslinking could simply be an inability to bind and phosphorylate the substrate that is present. There also seems to have been EDTA in my reaction buffer for the copper-phenanthroline crosslinking studies, which would inhibit disulfide formation. Similarly, the concentrations I chose to use to crosslink via BMOE were both too high, and likely resulted in dead-end reactions in which each of the cysteines had reacted with a BMOE before they could cross react between the two proteins.

In Chapter 4 of this dissertation we modeled the interaction between GRK1 and rhodopsin, shown in Figure 4.5. From this model, it seems that a cysteine at site GRK1 L6C should come in to crosslinking distance with site V250C on rhodopsin. Similarly, site V9C on GRK1 comes within crosslinking distance of site T243C on rhodopsin (Figure A2.7). Thus, the next step in pursuit of crosslinking between GRK1 and rhodopsin should begin with preparing GRK1 L6C and GRK1 V9C, and first testing their activity on rhodopsin V250C_θ and T243C_θ to make confirm that they are able to

phosphorylate these rhodopsin mutants. If they are active, I would begin with copper phenanthroline crosslinking, as the separation between the modeled sulfhydryl groups should be close enough for direct crosslinking. If a crosslinked complex can be made, this complex could eventually be used in cryo-EM structural studies.

Tables

Table A2.1: Kinetic parameters of GRK1 cysteine mutants for rhodopsin mutants.

kinase construct	rhodopsin construct	detergent/ phospholipid	specific activity	initial rate
			nmole P/min/mg	#P/min
GRK1wt	\emptyset	<i>DM</i>	160 ± 41	0.75
	\emptyset	<i>DM/DOPS</i>	180 ± 51	0.93
	<i>V139C₀</i>	<i>DM/DOPS</i>	270 ± 21	1.3
	<i>V250C₀</i>	<i>DM/DOPS</i>	200 ± 25	1.2
GRK1 L6C	\emptyset	<i>DM</i>	140 ± 34	0.49
	\emptyset	<i>DM/DOPS</i>	190 ± 64	1.0
	<i>V139C₀</i>	<i>DM/DOPS</i>	260 ± 54	1.3
	<i>V250C₀</i>	<i>DM/DOPS</i>	230 ± 69	1.3
GRK1 T8C	\emptyset	<i>DM</i>	52 ± 15	0.07
	\emptyset	<i>DM/DOPS</i>	120 ± 45	0.35
	<i>V139C₀</i>	<i>DM/DOPS</i>	120 ± 24	0.25
	<i>V250C₀</i>	<i>DM/DOPS</i>	170 ± 32	0.67
GRK1 S13C	\emptyset	<i>DM</i>	66 ± 24	0.10
	\emptyset	<i>DM/DOPS</i>	110 ± 28	0.27
	<i>V139C₀</i>	<i>DM/DOPS</i>	120 ± 31	0.20
	<i>V250C₀</i>	<i>DM/DOPS</i>	130 ± 28	0.35

Figures

Figure A2.1 Crosslinking studies used copper phenanthroline for direct crosslinking and BMOE for an 8 Å linker arm.

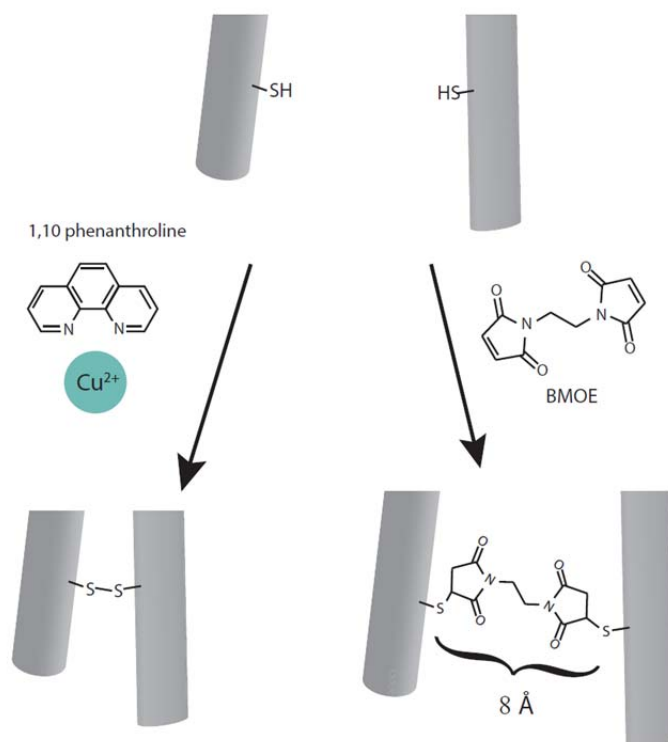


Figure A2.1 Crosslinking studies used copper phenanthroline for direct crosslinking between two sulfhydryl groups, shown on the left. In order to widen the range of distances crosslinked I also used a bis-maleimide connected by an ethane group (BMOE), which leaves an 8 Å linker between sulfur atoms.

Figure A2.2 SDS-PAGE analysis shows that the Profinity eXact purification method yields highly pure GRK1 L6C, T8C, and S13C.

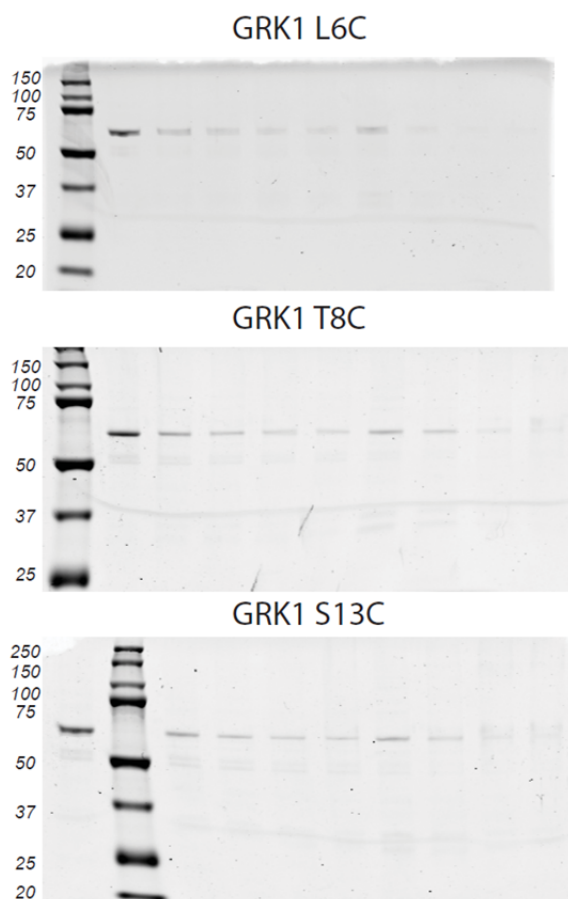


Figure A2.2 SDS-PAGE analysis shows that the Profinity eXact purification method yields highly pure GRK1 L6C (top), T8C (middle), and S13C (bottom). Gels were stained with Coomassie blue, molecular weight standards are indicated on the left.

Figure A2.3 Addition of DOPS to DDM-purified θ rhodopsin increases the activity of GRK1 cysteine mutants.

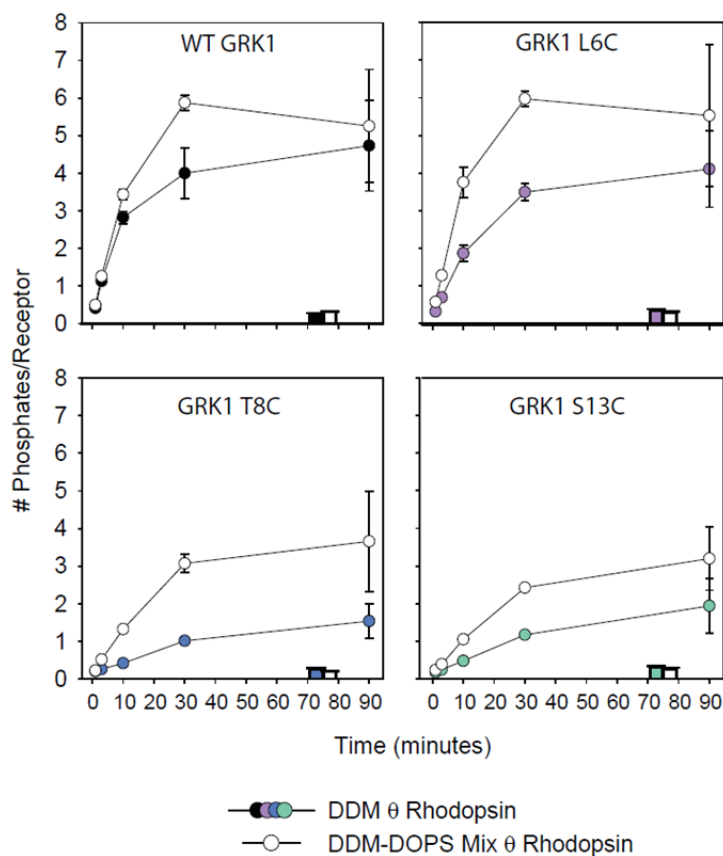


Figure A2.3 Addition of DOPS to DDM-purified θ rhodopsin increases the activity of GRK1 cysteine mutants. GRK1 L6C has activity comparable to that of WT GRK1, and is able to phosphorylate DDM-purified θ rhodopsin with ~ 4 phosphates/receptor, which increases to ~ 6 phosphates/receptor when DOPS is added. GRK1 T8C and GRK1 S13C show low activity in phosphorylating θ rhodopsin, only adding ~ 2 phosphates/receptor, which increases to ~ 4 phosphates/receptor when DOPS is added.

Figure A2.4 Cysteine substitutions at sites V139 and V250 do not affect the phosphorylation of these DDM-DOPS purified rhodopsins by GRK1 cysteine mutants.

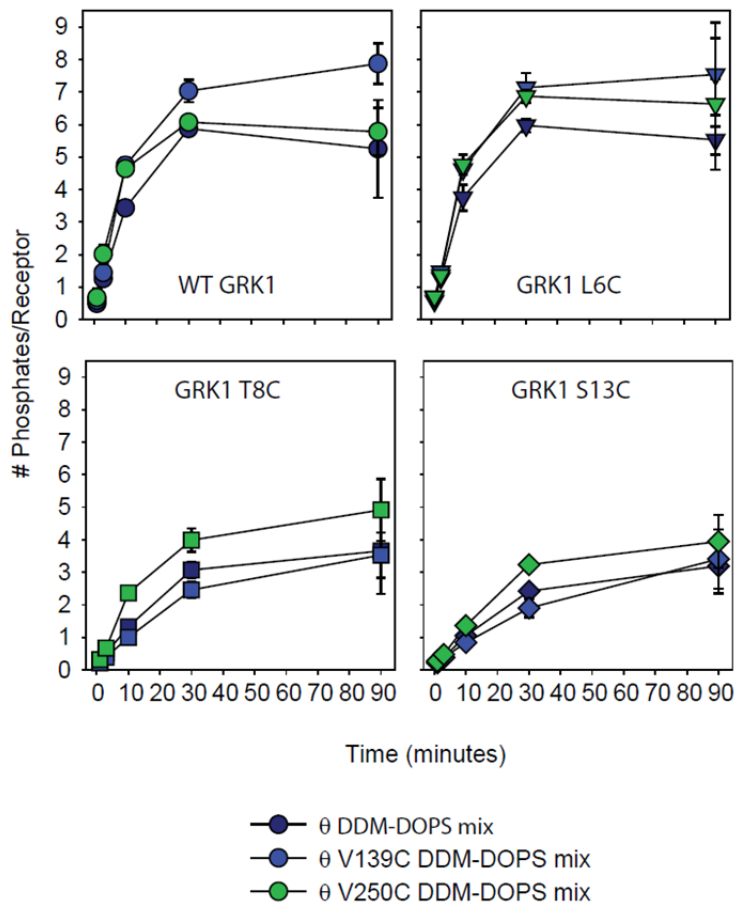


Figure A2.4 Cysteine substitutions at sites V139 and V250 do not affect the phosphorylation of these DDM-DOPS purified rhodopsins by GRK1 cysteine mutants.

Figure A2.5 GRK1 T8C and GRK1 V9C did not crosslink to rhodopsin T242C₀ with BMOE.

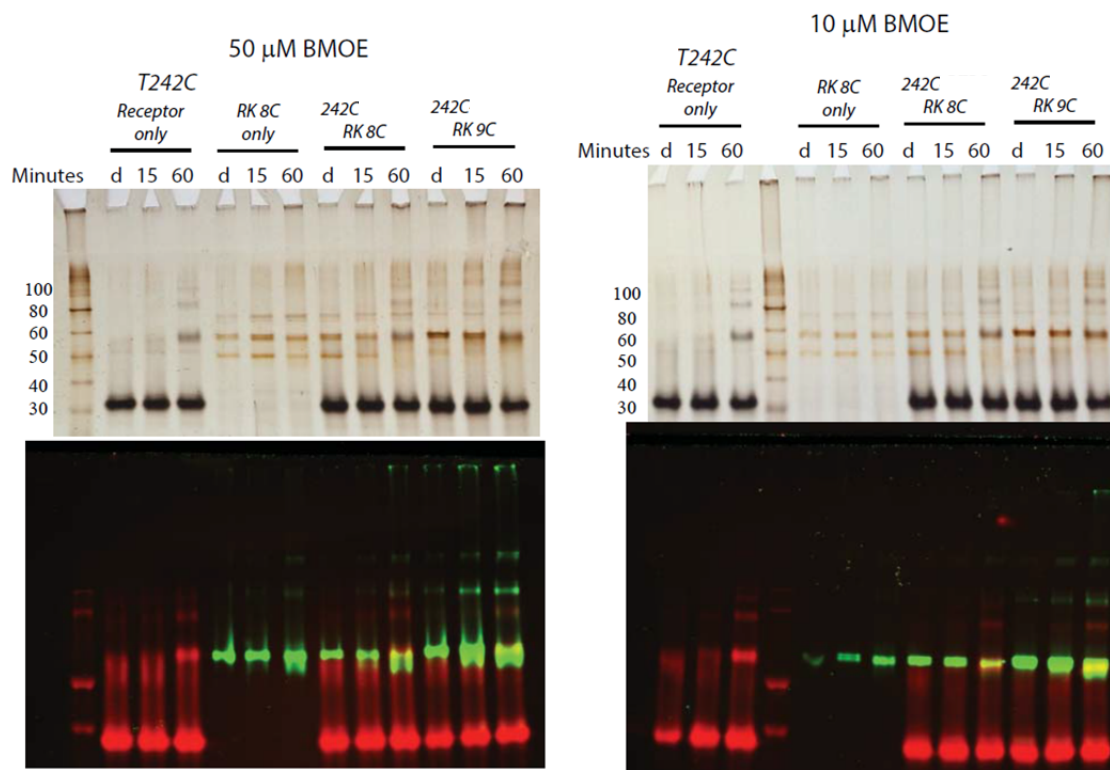


Figure A2.5 GRK1 T8C and GRK1 V9C did not crosslink to rhodopsin T242C₀ with BMOE. Reactions were carried out by pre-incubating rhodopsin T242C₀ with GRK1 T8C or V9C or a buffer control, in the dark. BMOE was added to either 50 μ M (left) or 10 μ M final concentrations, which was a mistake. The maximum molar equivalent should be 1/2 that of the proteins to be crosslinked, otherwise one ends up with doubly labeled monomers. Crosslinked compounds were not observed using SDS-PAGE analysis followed by silver staining (top) or Western blotting of a transferred gel (bottom). In the Western blots, GRK1 is indicated in green bands and rhodopsin is indicated in red bands. Importantly, which the rhodopsin T242C₀ + GRK1 9C reactions do show higher molecular weight bands for the GRK1 (green) channel, these bands are not co-localized with rhodopsin and cannot be interpreted as crosslinks.

Figure A2.6 GRK1 T8C and GRK1 V9C did not crosslink to rhodopsin T242C₀ using copper phenanthroline.

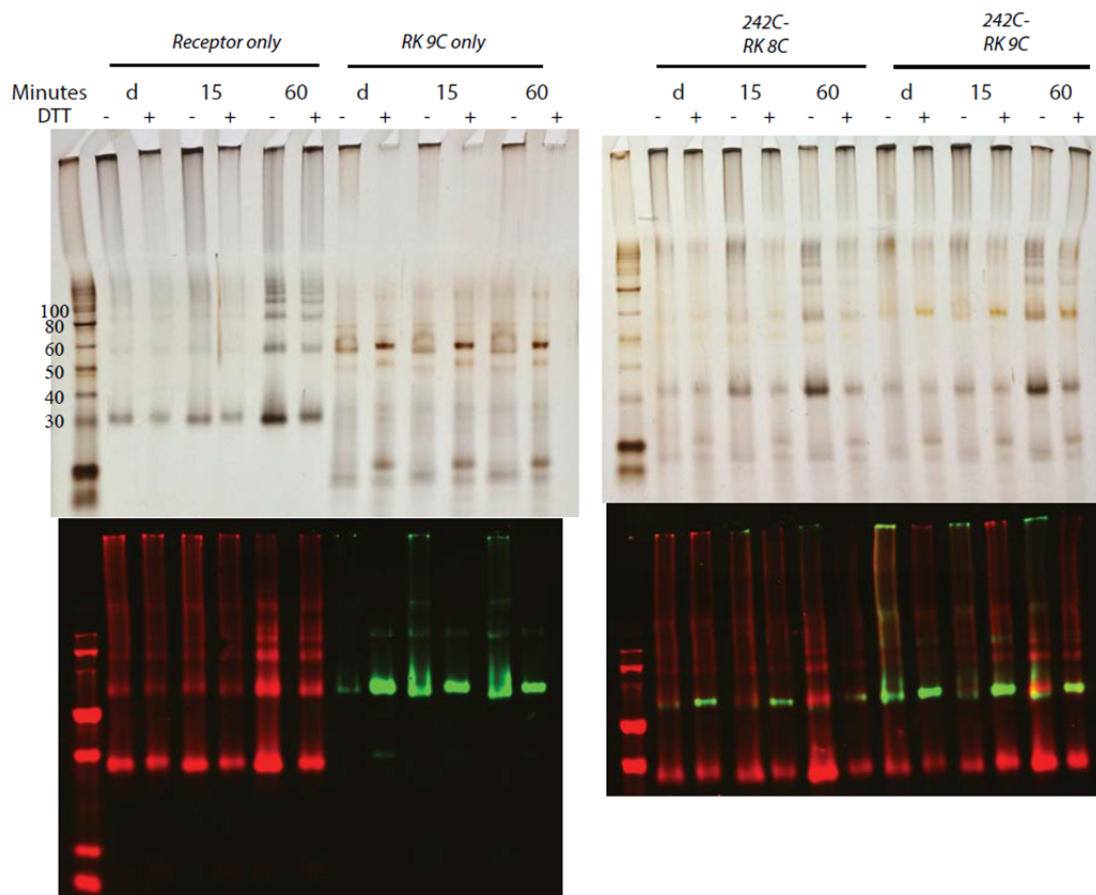


Figure A2.6 GRK1 T8C and GRK1 V9C did not crosslink to rhodopsin T242C₀ using copper phenanthroline. Reactions were carried out by pre-incubating rhodopsin T242C₀ with GRK1 T8C or V9C or a buffer control, in the dark. Pre-chelated copper phenanthroline was added at 3X molar excess. Crosslinked compounds were not observed using SDS-PAGE analysis followed by silver staining (top) or Western blotting of a transferred gel (bottom). In the Western blots, GRK1 is indicated in green bands and rhodopsin is indicated in red bands.

Figure A2.7 A model of the GRK1 N-terminus bound to the cytoplasmic face of rhodopsin predicts that GRK1 L6 and V9 bind near rhodopsin site V250 and T243.

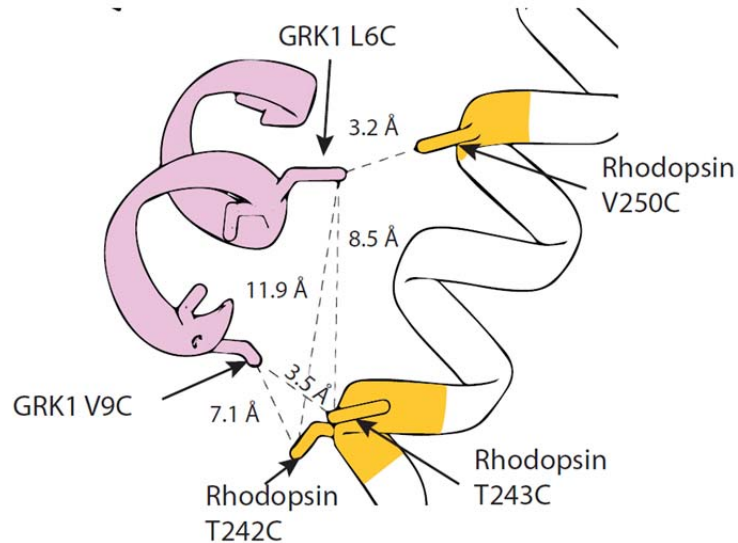


Figure A2.7 A model of the GRK1 N-terminus bound to the cytoplasmic face of rhodopsin predicts that GRK1 L6 and V9 bind near rhodopsin site V250 and T243. The model generated in Chapter 4 predicts that certain N-terminal sites in GRK1 align with sites on rhodopsin that should allow for successful disulfide crosslinking. In particular, the match of L6 on GRK1 and V250 on rhodopsin (these sites have been mutated to cysteine in this model) would be ideal given the high activity of the former for the latter.